UNIVERSIDAD NACIONAL AUTÓNOMA DE MÉXICO

PROGRAMA DE POSGRADO EN ASTROFÍSICA

INSTITUTO DE ASTRONOMÍA

Física de la formación estelar y el ensamblaje bariónico de las galaxias de baja masa en el escenario cosmológico ΛCDM

TESIS

QUE PARA OPTAR POR EL GRADO DE:
DOCTOR EN CIENCIAS (ASTROFÍSICA)

PRESENTA:
ALEJANDRO GONZÁLEZ SAMANIEGO

TUTORES:
DR. VLADIMIR ANTÓN AVILA REESE, IA-UNAM
DR. OCTAVIO VALENZUELA TIJERINO, IA-UNAM

MÉXICO, D.F OCTUBRE DE 2014

Física de la formación estelar y el ensamblaje bariónico de las galaxias de baja masa en el escenario cosmológico ΛCDM

por

ALEJANDRO GONZÁLEZ SAMANIEGO

A la memoria de mi padre,

que se fue cuando apenas empezaba este proyecto.

Física de la formación estelar y el ensamblaje bariónico de las galaxias de baja masa en el escenario cosmológico ΛCDM

por

ALEJANDRO GONZÁLEZ SAMANIEGO
Universidad Nacional Autónoma de México

Resumen

Se presenta primero un estudio semi-empírico del ensamblaje de masa oscura y luminosa de las galaxias en función de su masa, en el contexto del modelo cosmológico estándar de materia oscura fría con constante cosmológica. Galaxias formadas en halos de masas similares al de la Vía Láctea (VL) son los más eficientes en formar estrellas a todas las épocas. El ensamblaje estelar de galaxias masivas es frenado, más antes mientras más masivo es el halo; encontramos que la fase de cuasar podría ser responsable de este proceso. El ensamblaje estelar de galaxias poco masivas se retrasa sistemáticamente, más mientras menos masiva es la galaxia. Este comportaniento no es fácil de explicar y lo estudiamos a través de simulaciones de N-cuerpos+hidrodinámica.

En las simulaciones de galaxias menores a la VL se observa la tendencia a retrasar el ensamblaje estelar mientras menor es la galaxia (debido principalmente al efecto de la eyección de gas por supernovas), aunque no al nivel que sugiere el enfoque semi-empírico y algunas observaciones. Con re-simulaciones de alta resolución de galaxias de baja masa vimos que el ensamblaje estelar no se separa lo suficiente del ensamblaje de masa de sus halos. Mostramos que aumentando más la eyección de gas se estaría en desacuerdo con las altas fracciones de gas observadas en galaxias pequeñas, por lo que mecanismos complementarios deben ser introducidos (p. ej. retroalimentación preventiva más que eyectiva).

Por otra parte, hemos hecho simulaciones magneto-hidrodinámicas para estudiar las propiedades físicas del medio interestelar (MIE) que determinan el proceso de formación estelar a las escalas de nubes moleculares (NMs). Los resultados sugieren que un flujo isotérmico y continuamente turbulento no representa correctamente el flujo del medio en las NMs reales; las teorías que presuponen este régimen estarán perdiendo un aspecto clave de las propiedades del MIE. Sugerimos que un escenario más realista puede ser el del colapso gravitacional jerárquico.

Star formation physics and the baryonic assembly of low mass galaxies in the cosmological ΛCDM scenario

by

ALEJANDRO GONZÁLEZ SAMANIEGO
Universidad Nacional Autónoma de México

Abstract

First of all, we present a semi-empirical study of dark and luminous mass assembly of galaxies as a function of its mass in the context of the standard Λ cold dark matter cosmology. Galaxies formed in Milky Way-sized halos are the most efficient in forming stars at all epochs. The stellar mass assembly of high-mass galaxies is quenched more as more massive is its halo; we found the quasar stage might be the reason of this process. The stellar mass assembly of low-mass galaxies is systematically delayed, more as less massive is the galaxy. Since is not clear what physical processes may produce this behavior, we have studied the evolution of low-mass galaxies by means of N-body + hydrodynamics simulations.

In numerical simulations of galaxies smallerr than the Milky Way, we have found that they delay on average their stellar mass assembly with respect to the halo one (mainly due to the ejection of gas by supernovae), but not as strong as it is suggested by semi-empirical results and observations. By using zoom-in numerical simulations with high resolution we have found the stellar mass assembly follows closely the assembly mass of the halos. We showed that introducing more intense SN-driven outflows would be in disagreement with the high gas fractions observed in low-mass galaxies, so additional mechanisms should be introduced within the cosmological codes (e.g., preventive feedback instead of ejective feedback).

Finally, we performed magnetohydrodynamic simulations with the aim to study the physical properties of the interstellar medium that characterize star formation at scales of molecular clouds. Our results suggest that randomly driven isothermal turbulence may not correctly represent the flow within actual clouds, and that theories that assume this regime may be missing a fundamental aspect of the flow. We suggest that a more realistic regime may be that of hierarchical gravitational collapse.

Artículos

Asociados directa o parcialmente a este trabajo de tesis se publicaron o remitieron a publicación los siguientes artículos:

1.- Avila-Reese, V., Colín, P., **González-Samaniego, A.,** Valenzuela, O., Firmani, C., Velázquez, H., & Ceverino D.: "The Specific Star Formation Rate and Stellar Mass Fraction of Low-mass Central Galaxies in Cosmological Simulations". ApJ, 736, 134, 2011

2.- De Rossi, M. E., Avila-Reese, V., Tissera, P.B., **González-Samaniego, A.,** Pedrosa, S.E.: "On the mass assembly of low-mass galaxies in hydrodynamical simulations of structure formation"; MNRAS, 435, 2736, 2013

3.- **González-Samaniego, A.,** Colín, P., Avila-Reese, V., Rodríguez-Puebla, A., Valenzuela, O.: "Simulations of Isolated Dwarf Galaxies Formed in Dark Matter Halos with Different Mass Assembly Histories"; ApJ, 785, 58, 2014a

4.- **González-Samaniego, A.,** Vázquez-Semadeni, E., González, R. F., Kim, J.: "Testing assumptions and predictions of star formation theories"; MNRAS, 440, 2357, 2014b

5.- Colín, P., Avila-Reese, V., **González-Samaniego, A.,** & Velázquez, H.: "Simulations of galaxies formed in warm dark matter halos of masses at the filtering scale". Submitted in September 2014 to *The Astrophysical Journal*.

7.- **González-Samaniego, A.** & Avila-Reese, V.: "On the stellar and halo mass assembly of galaxies"; in preparation.

Proceedings:

8.- **González-Samaniego, A.** & Avila-Reese, V.: "On the mass assembly of sub-Milky-Way galaxies"; AAABS, Workshop Series of the Argentine Astronomical Society, vol.4, p.83-86, 2013.

9.- De Rossi, M. E., Avila-Reese, V., **González-Samaniego, A.**, Pedrosa, S. E.: "Downsizing of galaxies vs upsizing of dark-halos in a LCDM cosmology"; Boletín de la Asociación Argentina de Astronomía (BAAS), vol.55, p.273-277, 2012.

Agradecimientos

Este trabajo de tesis doctoral es el resultado de mucho esfuerzo y dedicación a un proyecto que me resultó muy gratificante. Éste no habría sido posible sin el apoyo, la asesoría, y el acompañamiento de muchas personas e instituciones. Así, quiero agradecer:

A mi mamá, Carmen, y a mis hermanos todos, su apoyo incondicional durante todo este tiempo ha sido fundamental para que yo pudiera seguir adelante y sobreponerme en los momentos más adversos. A mis sobrinos, en particular a Mariana, Alex, y Leo, su curiosidad y sus "porras" siempre estuvieron allí.

A mis amigos y compañeros de la *UNAM*, ustedes hicieron que el Doctorado fuera una experiencia mucho más agradable de lo que imaginé. A Eva, por su amistad y paciencia al aguantarme como compañero de cubículo durante TODO el Doctorado. A mis compañeros extranjeros, que en su paso por la *UNAM*, compartieron su amistad y cultura conmigo. A Luis Fernando y a Lola, por distraerme cuando fue necesario, y por el incondicional apoyo durantes estos, a veces difíciles, pero no por eso menos divertidos últimos años.

A los investigadores del CRyA, Luis F. Rodríguez, Laurent Loinard, y Paola D'Alessio, que con su ejemplo y enseñanza en las aulas, me motivaron para concluir los estudios de maestría y empezar el Doctorado. Al Dr. Enrique Vázquez, que me abrío las puertas al supercómputo y a la investigación en Astrofísica. Los resultados del trabajo en colaboración con Enrique son parte de esta tesis. En particular, quiero agradecer el apoyo y seguimiento que hizó a mi proyecto el Dr. Pedro Colín, como profesor, colaborador y evaluador de mi desempeño durante mi Doctorado, fue parte importante de este proyecto de tesis doctoral.

A mis asesores, el Dr. Octavio Valenzuela y el Dr. Vladimir Ávila Reese, por ofrecerme y dirigir este proyecto que ahora concluyo con gusto. A Octavio, por compartirme su pasión por el supercómputo, las largas y continuas discusiones de ideas nuevas, han sido siempre estimulantes. Gracias Vladimir, por ese ejemplo de pasión por la Astronomía y la ciencia en general; sin duda, esto propició un ambiente de trabajo siempre estimulante. Con infinita paciencia y mucho más talento, has sido responsable no solo de que concluya con éxito este proyecto, sino además, de mi entusiasmo por continuar en la investigación científica.

A los miembros del jurado de examen: Dra. Maria Emilia De Rossi, Dr. Héctor Velázquez, Dr. Javier Sánchez, Dr. Pedro Colín y Dr. Vladimir Avila Reese, por tomarse el tiempo para leer, comentar y sugerir correcciones al trabajo de tesis, sin duda, sus comentarios ayudaron a mejorar el escrito final.
A la CEP-UNAM y al Conacyt por su apoyo económico, sin el cual, me hubiera sido imposible realizar mis estudios de posgrado. Al personal de supercómputo del CRyA, el IA, y DGTIC-UNAM, el uso de los "clusters" Nostromo, Atócatl, Kambalam, y Miztli, fue esencial para mi investigación doctoral.

Índice general

Capítulo 1

Introducción

1.1. El contexto cosmológico

El estudio sistemático del Universo como un todo, objetivo principal de la *Cosmología*, requiere del planteamiento de modelos teóricos capaces de reproducir la imagen de Universo que nos han dado las observaciones astronómicas realizadas principalmente en las últimas décadas. Dichas observaciones son compatibles con el hecho de que el Universo local es isótropo y homogéneo a grandes escalas y prácticamente a todas las escalas en el remoto pasado. El postulado de homogeneidad e isotropía de la métrica del espacio se denomina *Principio Cosmológico*. La teoría de la *Relatividad General* (RG), presentada por A. Einstein en 1915, junto con el Principio Cosmológico, han brindado el marco teórico para formular la dinámica del Universo. Es el caso de las soluciones a las ecuaciones de campo de la RG encontradas por A. Friedmann, mismas que describen un Universo en constante evolución. La ecuación de Friedmann con constante cosmológica que describe la tasa de cambio del factor de escala de la métrica espacial, $a(z)$, se escribe en términos de observables así:

$$\left(\frac{\dot{a}}{a}\right)^2 = H_0^2[a^{-4}(z)\Omega_r + a^{-3}(z)\Omega_m + a^{-2}(z)(\Omega_k) + \Omega_\Lambda], \tag{1.1}$$

donde H_0 el parámetro de Hubble en el presente ($a_0 = 1$), $a = 1/(1+z)$, Ω_m, Ω_Λ y Ω_r los parámetros de densidad adimensionales en el presente para la materia, la constante cosmológica Λ y la radiación respectivamente, y Ω_k representa el término que tiene que ver con la curvatura del espacio.

De acuerdo con la ec. (1.1), si la geometría es plana, entonces $\Omega_k = 0$ y la suma de los parámetros de densidad, $\Omega_{total} = \Omega_m + \Omega_\Lambda + \Omega_r$, da la unidad. El caso de geometría plana es el que mejor se describe por una serie de sondeos observacionales de alta precisión (ver por ej. Komatsu et al. 2009; Planck Collaboration et al. 2013a, , y referencias ahí). El factor de escala $a(t)$ en este caso es una función monotónicamente creciente siempre. El

comportamiento de esta función para $z < 1000$ y hacia el futuro depende significativamente sólo de los valores de Ω_m y Ω_Λ. Los sondeos observacionales han mostrado también que el valor de Ω_Λ es significativo en el presente (≈ 0.70) y lo fue desde $z \approx 0.6$ lo cual implica que desde entonces la expansión en vez de frenarse se está acelerando (ver por ej. resultados recientes con las SNs Ia en Riess et al. 2009).

En los modelos cosmológicos de Friedmann, en épocas más tempranas la distancias propias en el Universo siempre fueron menores, las densidades promedio de materia y energía mayores y la radiación de fondo más caliente. La descripción de las propiedades físicas de la materia y radiación en estas condiciones tempranas del Universo caliente se enmarcan dentro de la así llamada *Teoría de la Gran Explosión* (TGE), misma que ha sido comprobada observacionalmente en repetidas ocasiones. No obstante, esta Teoría tiene limitaciones para la épocas más tempranas del universo que han sido superadas con la propuesta del *modelo inflacionario*, mismo que complementa a la TGE al describir el Universo en épocas extremádamente tempranas ($t \lesssim 10^{-32}$ s) y ofrece una explicación al problema de la planitud, del horizonte y del origen de las perturbaciones que luego evolucionarán hacia las estructuras cósmicas actuales.

En los últimos años, a través de diversos sondeos cosmológicos, se ha logrado determinar con buena precisión que la contribución actual de la materia bariónica a la densidad total de materia-energía en el Universo es sólo de $\approx 5\,\%$, la contribución de la materia oscura (materia que no interactúa electromagnéticamente) es de $\approx 25\,\%$, y la de la constante cosmológica es de ≈ 0.70 (ver resultados reciente por ej. en Planck Collaboration et al. 2013a). Entonces, la densidad de energía asociada a la constante cosmológica domina la dinámica del Universo actual. De hecho, se ha generalizado la naturaleza de esta componente repulsiva a propuestas con ecuaciones de estado diferentes a la de la constante cosmológica (interpretada como un remanente del vacío cuántico de la época inflacionaria). El nombre genérico que recibió el medio repulsivo fue el de "energía oscura". Las ecuaciones de Friedmann con los valores de los parámetros mencionados y el de la constante de Hubble de 71 $\mathrm{Kms^{-1}Mpc^{-1}}$, implican una edad actual del Universo de 13.75 mil millones de años.

El modelo cosmológico que se ha consolidado como el más exitoso, siempre enmarcado dentro de la RG + TGE + Inflación y del cual ya mencionamos sus principales parámetros, se le ha bautizado como el modelo de *Materia Oscura Fría con* Λ (ΛCDM por Λ Cold Dark Matter en inglés). En el contexto de esta cosmología se ha podido desarrollar un escenario de formación y evolución de estructuras cósmicas que ha servido de marco teórico para interpretar un gran cuerpo de observaciones tanto del Universo local como de alto corrimiento al rojo. Los elementos básicos de este escenario son: (1) la generación de perturbaciones de la métrica del espacio-tiempo en la época inflacionaria, cuyo espectro de potencias es aproximadamente invariante de escala al cruzar el horizonte de causalidad, y (2) el dominio de la materia oscura fría (MOF), lo cual garantiza la supervivencia de las perturbaciones primigenias durante la época caliente del universo. Estos elementos

permiten predecir que las estructuras cósmicas luminosas (galaxias, grupos y cúmulos de galaxias) se formarán tras ser atrapado el gas en los pozos de potencial gravitacional trazados por la MOF.

El *espectro de potencias* procesado a la época de la Recombinación es el punto de partida para la evolución ulterior (no lineal) de las fluctuaciones. Desde el punto de vista más general, la misma será tal que las estructuras oscuras de menor escala (masa) colapsan primero y las estructuras de mayor escala se ensamblan posteriormente por la agregación de las estructuras menores. Este proceso de ensamblaje de lo chico a lo grande se denominó *jerárquico*.

Mientras que el proceso no lineal de ensamblado de la MOF es únicamente gravitacional (no colisional y posiblemente sin ningún tipo de autointeracción significativa por parte de la MOF), el de la materia bariónica es mucho más complejo: además de seguir el proceso gravitacional dominado por la MOF, es suceptible de procesos hidrodinámicos, termodinámicos, de transporte radiativo, de formación estelar, de retroalimentación, etc. (denominados genéricamente como procesos "gastrofísicos"). Tres aspectos relevantes del gas bariónico son que: (1) es colisional y disipativo, (2) se puede transformar en estrellas, cambiando así sus características dinámicas y termodinámicas y (3) introduce fuentes de energía (aparte de la gravitacional) a través de la retroalimentación, tanto de estrellas como de los Núcleos Activos Galácticos (NAGs).

El escenario jerárquico ΛCDM de formación de estructuras cósmicas ha servido para interpretar innumerables conjuntos de observaciones así como para estimular el desarrollo de la astronomía, cosmología y la física de partículas y altas energías a través de las predicciones que hace. Sus éxitos han sido muchos, principalmente en lo que concierne a las grandes escalas. Por ejemplo: la explicación y descripción detallada de las anisotropías observadas en la Radiación Cósmica de Fondo en Microondas, la fiel descripción de la función de correlación de dos puntos reconstruida de los grandes catastros de galaxias, la función de correlación angular local y altos corrimientos al rojo reconstruidas de catastros de galaxias, la explicación de algunas relaciones de escala de las galaxias y cúmulos de galaxias, etc. (ver reseñas en Avila-Reese 2006; Bower et al. 2010; Frenk & White 2012).

No obstante, el escenario jerárquico ΛCDM tiene también en frente varios retos y dificultades por resolver a diferentes niveles. En este contexto, recientemente se ha dado un explosivo incremento de inferencias observacionales de propiedades físicas de las galaxias en un amplio rango de corrimientos al rojo (entre $z \sim 0$ y $z \sim 7-8$). Como resultado está emergiendo un cuadro semi-empírico de cómo ensamblan las galaxias sus masas estelares en función de sus masas, tipo, entorno, etc. Por otro lado, la cuestión de las historias de ensamblaje de los halos de materia oscura es algo relativamente bien predicho por la teoría y las simulaciones numéricas de N cuerpos (v.gr. Avila-Reese, Firmani & Hernández 1998; Wechsler et al. 2002; Maulbetsch et al. 2007; Fakhouri, Ma & Boylan-Kolchin 2010; Boylan-Kolchin et al. 2010; Genel et al. 2010; Behroozi et al. 2013; Knebe et al. 2013, y más referencias ahí).

1.2. Controversias a pequeñas escalas

El escenario de formación de galaxias en los halos oscuros en crecimiento hasta ahora desarrollado (el cual incluye toda la complejidad de la gastrofísica con diferentes niveles de aproximación) parece toparse con posibles problemas a escalas pequeñas al compararse con las inferencias observacionales más recientes: las observaciones muestran que mientras menos masiva es la galaxia, más tardiamente ensambló sus estrellas, presentando al día de hoy todavía altas tasas de formación estelar específica ($TFEE \equiv TFE/M_s$), algo que se denominó como "downsizing" en la TFEE, mientras que las predicciones de los modelos tienen dificultad en reproducir algo así debido a la naturaleza jerárquica ("upsizing") del ensamblaje de la masas M_h de los halos oscuros (Santini et al. 2009; Colín et al. 2010; Firmani & Avila-Reese 2010; Avila-Reese et al. 2011a; Weinmann et al. 2012; De Rossi et al. 2013, ver por ej.).

A este potencial conflicto se le suman otros que han sido ampliamente discutidos en la literatura especializada en la última década y que siempre se refieren a las escalas galácticas más pequeñas (masas de halos menores a $\sim 10^{11} - 10^{10}\ M_\odot$), así como a la subestructura dentro de los halos galáctivos (satélites). Estas controversias son, entre otras, el problema de los satélites enanos perdidos en halos tipo Vía Láctea, el de los núcleos picudos de los halos, el del exceso de satélites brillantes en halos tipo Vía Láctea ("too-big-too-fail problem"), etc. (ver reseñas recientes en Weinberg et al. 2013; Del Popolo et al. 2014, y las referencias ahí).

Ante estas controversies, es natural formularse preguntas como: ¿Existe un problema intrínseco (de modelo cosmológico) en el sentido de que el ensamblaje de masa oscura trazado por el de la masa estelar no es jerárquico como lo predice el escenario ΛCDM? ¿Son reales los problemas de satélites perdidos, núcleos picudos, exceso de satélites luminosos o tienen que ver con limitaciones observacionales o tal vez efectos gastrofísicos aún no entendidos bien? ¿Son más bien esos procesos gastrofísicos los que invierten la jerarquía al pasar de masa de halo a masa estelar? ¿Cuáles son estos procesos y cómo operan en diferentes escalas? ¿Qué predicen modelos y simulaciones numéricas de formación y evolución de galaxias que incluyen la gastrofísica? En el caso de que sean reales los problemas a pequeñas escalas, ¿se resuelven con escenarios cosmológicos alternativos como el de Materia Oscura Tibia (MOT)?

Todas estas son preguntas abiertas que se han abordado en el presente trabajo de Tesis, *dando especial énfasis a la cuestión del "downsizing" en TFEE de las galaxias menos masivas*. Será también importante encontrar los aspectos de las inferencias empíricas que más directamente estén relacionados con las predicciones del escenario en su parte medular que es la de materia oscura. En su defecto, a través de la modelación, intentar, encontrar las "desviaciones" relevantes del ensamblaje galáctico con relación al de materia

oscura y así poder constreñir los procesos astrofísicos de la evolución galáctica. En esto ayudan mucho modelos de juguete o paramétricos que se constriñen con la información empírica.

Es en este contexto que, en el presente trabajo de Tesis Doctoral, *nos hemos propuesto (a) explorar los comportamientos promedio de ensamblaje de la masa estelar en los halos de ΛCDM en constante crecimiento, y (b) el cómo se lleva a cabo el ensamblaje de la materia bariónica de las galaxias de baja masa que se forman en halos de materia oscura (fría y tibia) a través de simulaciones numéricas de hidrodinámica y N cuerpos*. Esto último con el objetivo general de entender el proceso de formación y evolución de galaxias de baja masa en los contextos cosmológicos de formación de estructuras cósmicas.

1.3. Procesos de formación estelar

El ensamblaje de la masa estelar de las galaxias está claramente ligado al proceso de formación estelar. Este proceso se sabe ocurre principalmente en nubes moleculares en el medio interestelar (MIE) a escalas de parsecs. Dichas escalas son difíciles de resolver en las simulaciones numéricas de galaxias en un contexto cosmológico. Así, los estudios teóricos de formación de galaxias siempre suponen como válidas ciertas recetas y correlaciones de las propiedades del MIE para modelar o simular el complejo proceso de formación estelar y crecimiento de la masa estelar de las galaxias. No obstante la formación estelar es una teoría que dista mucho de estar acabada.

Las teorías de formación estelar actuales dependen fuertemente de ciertas suposiciones acerca de la estructura de nubes moleculares (NMs), siendo estas los lugares donde se forman las estrellas. Una de las suposiciones más comunes es que los anchos supersónicos de las líneas observadas en NMs constituyen turbulencia supersónica (Zuckerman & Evans 1974a), y que esta turbulencia causa una presión neta que provee soporte en contra de la autogravedad de la nubes, manteniéndolas en un aproximado equilibrio virial (v. gr. Larson 1981a; Myers & Goodman 1988a; Blitz 1993). Aquí es importante hacer notar que para que los movimientos no térmicos sean capaces de dar soporte en contra de la autogravedad, el campo de velocidades turbulento debe ser esencialmente aleatorio. Esta propiedad es extremadamente difícil de medir observacionalmente, ya que normalmente se tiene información solamente de una componente del vector del campo de velocidades (aquella a lo largo de la línea de visión). Esto se complica aún más porque ni siquiera tenemos información acerca de la estructura espacial de esta componente a lo largo de la línea de visión.

En la contraparte teórica, en años recientes han aparecido en la literatura teorías (Krumholz & McKee 2005; Padoan & Nordlund 2011; Hennebelle & Chabrier 2011,

hereafter KM05, PN11 and HC11 respectively) que tratan de describir la dependencia de la TFE de los principales parámetros físicos de las NMs, a decir, el cociente de energía cinética entre la energía gravitacional, caracterizado por el parámetro virial α (KM05), el número de Mach turbulento $\mathcal{M}_{\rm s}$, el número de Mach Alfvénico $\mathcal{M}_{\rm A}$ y el cociente de los modos solenoidales entre los modos compresivos inyectados a la turbulencia, caracterizados estos por el así llamdo *parámetro-b* (Federrath, Klessen & Schmidt 2008a). Una revisión detallada de estas teorías se encuentra en Federrath & Klessen (2012a,b).

Estas tres recientes teorías parten de la hipótesis fundamental de que los movimientos supersónicos no-térmicos constituyen turbulencia isotrópica que, mientras localmente induce compresiones que pueden llegar a ser inestables gravitacionalmente[1] y colapsen, globalmente produzca una presión turbulenta que puede oponerse a la autogravedad de los núcleos densos que se forman en las NMs. Más aún, dos de éstas teorías (KM05 y PN11) dependen de la suposición de que núcleos densos que son subsónicos y que a su vez tienen masa superior a su masa de Jeans juegan un papel fundamental en el proceso de formación estelar. Estas dos suposiciones han sido ya cuestionadas en un estudio basado en simulaciones numéricas hidrodinámicas sin campo magnético (Vázquez-Semadeni et al. 2008a). En este contexto es importante verificar sí estas suposiciones básicas para entender la formación estelar son auto consistentes en simulaciones numéricas ahora en el caso magnetohidrodinámico. Y tratando de ir un poco más allá, también será importante poner a prueba las prediciones que de la TFE hacen estas teorías.

1.4. Objetivos y Contenido

Así, de acuerdo con lo analizado y planteado previamente, en esta Tesis se pretende abordar un estudio semi-empírico y numérico del proceso de ensamblado de las galaxias en los halos de materia oscura en constante crecimiento en un contexto cosmológico. Debido a que potenciales problemas se debaten activamente a escalas de galaxias de bajas masas, nuestro estudio numérico se centrará en estas galaxias de baja masa. Por otro lado, siendo el proceso de formación estelar clave para entender la evolución de las galaxias, el estudio de este proceso a nivel detallado de nubes moleculares será también abordado. En concreto, los objetivos de la presente Tesis se pueden formular así:

- Hacer compatible el cuadro empírico emergente de ensamblaje de la masa estelar de las galaxias con las predicciones del escenario jerárquico ΛCDM y así constreñir los principales procesos gastrofísicos en juego en función de la masa de halo y de la época.

[1] Por inestabilidad gravitacional nos referimos a que una cierta estructura alcance en su evolución una masa $\mathcal{M}$ superior a su masa de Jeans $\mathcal{M}_{\rm J}$, lo cual provocaría que ante ausencia de algún agente no gravitacional que provea soporte, dicha estructura eventualmente se colapse.

- Explorar en detalle con simulaciones cosmológicas de N cuerpos + hidrodinámica la formación y evolución de galaxias de baja masa ($M_s \lesssim 3 \times 10^{10} M_{\odot}$) pues es para ellas donde aparentemente se revela una dificultad de importancia para el ΛCDM: el "downsizing" en la tasa de formación estelar específica y las bajas fracciones de masa estelar y bariónica mientras menos masiva es la galaxia. Explorar en consecuencia, simulaciones de galaxias de bajas masas en el contexto del escenario de materia oscura tibia (ΛWDM).

- Como complemento al estudio del ensamblaje de masa de las galaxias de baja masa, abordar el estudio de las propiedades del MIE que se postula caracterizan el proceso de formación estelar. En particular estudiaremos las hipótesis que se plantean como punto de partida para que ocurra la formación estelar, así como las predicciones de teorías actuales de la formación estelar en un medio turbulento y magnetizado. Esto nos permitirá conceptualizar un poco como sería el enlace entre el cómo se da la FE a escalas de NMs y su influencia en el ensamblaje de masa global en las galaxias.

La Tesis está estructurada de la siguiente manera: en el Capítulo 2 se presenta un estudio (compilación observacional y modelo parámetrico) del ensamblaje de masa de las galaxias en el modelo ΛCDM. En el Capítulo 3 presentamos un análisis de simulaciones numéricas de galaxias de baja masas relativo principalmente al problema "downsizing" en la TFEE. En el Capítulo 4 analizamos las historias de ensamblaje de masa (estrellas, gas, y materia oscura) de galaxias enanas simuladas con alta resolución, y la respectiva influencia de las diferentes historias (parte de la estocasticidad del campo de fluctuaciones primigenio) sobre las propiedades globales de dichas galaxias a $z\ 0$. El Capítulo 5 se estudian algunas de estas galaxias enanas pero simuladas en el contexto del escenario ΛWDM con el objeto de explorar los efectos del filtrado en el espectro de potencias sobre las galaxias de masas cercanas a la escala de filtrado. El estudio de las propiedades del MIE que modelan el proceso de FE se estudian vía simulaciones hidrodinámicas en un medio turbulento en el Capítulo 6. Finalmente en el Capítulo 7 presentamos las conclusiones generales de esta tesis doctoral.

Es importante mencionar que los Capítulos 4 y 6 corresponden enteramente a artículos ya publicados en revistas con arbitraje, donde el candidato a Doctor es el primer autor. Los Capítulos 3 y 5 corresponden también a artículos (uno publicado y otro enviado para su arbitraje) donde participé como coautor. En estos casos, se presentan los resultados relevantes de estos artículos y se los discute en el contexto de la presente Tesis.

Capítulo 2

Ensamblaje de las galaxias en el escenario jerárquico ΛCDM

Como se mencionó, las fluctuaciones primordiales de materia oscura fría evolucionan de tal forma que al colapsarse gravitacionalmente forman los pozos de potencial en los cuales los bariones se acretan y eventualmente se condensan para formar las galaxias que hoy en día vemos. Dicha acreción y la consiguiente formación galáctica es un proceso por demás complejo: intervienen un conjunto de procesos astrofísicos e hidrodinámicos que en sí mismos son todavía materia de una activa investigación. Dentro de dichos procesos físicos podemos mencionar: la generación del fondo UV y su acción de inhibición de acreción de gas en los halos más pequeños, los procesos disipativos propios del gas, el transporte de momento angular, la formación estelar, la retroalimentación por SNs y los vientos galácticos que producen, la retroalimentación preventiva de las estrellas masivas, la turbulencia del medio interestelar, las fusiones de galaxias, la retroalimentación debida a los NGAs, etc.

Los procesos astrofísicos mencionados pueden operar de tal manera que separan considerablemente la historia de ensamblaje de la masa bariónica y estelar de las galaxias de la historia de sus respectivos halos de materia oscura, algo que podría explicar el "downsizing"de las galaxias con relación al “upsizing"de sus halos. *¿Cómo actúan dichos fenómenos y procesos para lograr tal efecto de separación? ¿Con qué eficiencia y con qué dependencia de la masa y de la época operan?* Estas son preguntas claves diréctamente relacionadas con la física de la evolución de las galaxias en el contexto cosmológico. Por lo pronto, es de gran relevancia el poder inferir de manera heurística la separación de las historias de ensamblaje galáctico de las de sus halos oscuros y así cuantificar la eficiencia de formación galáctica en función de la masa.

Con la idea de explorar qué tanto se desvía el ensamblaje de la masa estelar galáctica del de la materia oscura es que planteamos un modelo paramétrico (“Modelo de juguete”) en el cual, si bien no se modelan en particular los mecanismos físicos antes mencionados, sí se parametrizan por una función que trata de englobar la gran complejidad que estos

representan. Los parámetros de dicha función se constriñen tras confrontar con un cuerpo de observaciones relevantes para el caso. Nuestro enfoque consistirá en conectar la tasa de agregación de materia de los halos ΛCDM galácticos en función de su masa y de la época con la tasa de crecimiento de masa estelar de la galaxia. Esta última se debe tanto a la tasa de formación estelar (TFE) in situ como a la incorporación de masa estelar ex situ, por fusiones. El modelo paramétrico nos servirá para estudiar la consistencia entre el ensamblaje de la masa estelar instantáneo o diferencial (por TFE y fusiones) y el ensamblaje acumulativo o integral (reflejado en la M_s acumulada); ambas son cantidades que se logran inferir de las observaciones en función de la masa y el corrimiento al rojo.

En este Capítulo se presenta primero una compilación de resultados observacionales que nos ilustran cómo se da el ensamblaje de masa estelar de las galaxias a nivel empírico (Sección 2.1). Dicha compilación forma parte importante del artículo Avila-Reese et al. (2011) y fue parte de mi contribución al mismo. Las relaciones empíricas presentadas a diferentes épocas son las que se usan para constreñir el modelo paramétrico que se presenta en la sección 2.3. En esta Sección se discute también, a la luz del modelo, cómo afectan cambios en un dado plano empírico sobre otros. En la Sección 2.5, se usan los resultados del modelo paramétrico mejor constreñido para analizar diversos aspectos de la conexión galaxia-halo y su evolución. En la Sección 2.6 se discute el concepto de masa de transición en el contexto del apagado ("quenching") de galaxias y su conexión con la evolución de quasares. Finalmente, en la Sección 2.7 presentamos las conclusiones obtenidas con nuestro modelo paramétrico.

2.1. Las relaciones empíricas

2.1.1. Tasa de formación estelar específica vs. masa estelar

Aparentemente mientras menos masivas son las galaxias, más tardiamente tienen su ensamblaje de masa estelar, siendo éste a la inversa del ensamblaje de la masa de sus halos oscuros. Este comportamiento se ha reportado no sólo para muestras locales (v.gr. Salim et al. 2007; Schiminovich et al. 2007; Bauer et al. 2013) sino que hasta corrimientos al rojo $z \approx 1-2$ (v.gr. Bauer et al. 2005; Noeske et al. 2007b; Bell et al. 2007; Damen et al. 2009b,a; Santini et al. 2009; Oliver et al. 2010; Rodighiero et al. 2010; Speagle et al. 2014). En esencia, dichos estudios observacionales muestran una anticorrelación entre la TFE específica ($TFEE \equiv TFE/M_s$) de las galaxias y su respectiva M_s asociada. Para clarificar esto, y con el objetivo de realizar un estudio sistemático de dichas inferencias, hemos realizado una compilación de resultados observacionales en los que se reporta justamente la dependencia de la $TFEE$ con la M_s y su correspondiente evolución con el corrimiento al rojo z.

En la figura 2.1 (Figura 5 de Avila-Reese et al. 2011a) graficamos los resultados observacionales compilados de tal manera que podamos compararlos. Las inferencias de M_s (y TFE) hechas a partir de las luminosidades observadas o la distribución espectral de energía (SED) de las galaxias están basadas en resultados de modelos estelares de sintésis de poblaciones (SPS). En todos los trabajos analizados se supuso una función de masa inicial (IMF) universal; pero como cada autor habría usado diferentes IMFs, homogenizamos todos los resultados observacionales a la IMF de Chabrier (2003). En la tabla 2.1 presentamos un resumen de todas las fuentes usadas en la figura 2.1. En todos los casos h=0.70 o 0.71. En las columnas 2 y 3 se reportan los trazadores usados para estimar la TFE y la IMF empleada respectivamente. Las columnas 4 y 5 dan las correciones promedio (en dex) que aplicamos aquí para homogeneizar tanto la M_s como la TFE a la IMF de Chabrier (2003). Hay que hacer notar que de acuerdo con Bell et al. (2007), las masas estelares y las TFEs calculadas con las IMFs de Chabrier (2003) y Kroupa (2001) (cuando se usa $L_{IR} + L_{UV}$ como trazador) son consistentes dentro de $\leq 10\,\%$, de tal forma que en estos casos no aplicamos corrección alguna; conclusiones similares son planteadas por Salim et al. (2007) y Karim et al. (2011) cuando usan a H_α y $L_{1400MHz}$ como trazadores. Para ver detalles de las muestras y carcaterísticas particulares de las distintas estimaciones observacionales ver el apéndice A de Avila-Reese et al. (2011a).

Los resultados observacionales compilados y contrastados en la figura 2.1 muestran con claridad el fenómeno del "downsizing" en la $TFEE$ discutido previamente: *a todas las épocas, mientras más pequeña es la galaxia, mayor es su TFEE promedio*. Además se aprecia que las galaxies más pequeñas a cada época están en su fase activa de crecimiento; la línea punteada horizontal en cada panel representa la $TFEE$ a esa época que tendría una galaxia que durante toda su historia formó estrellas a una TFE constante, es decir:

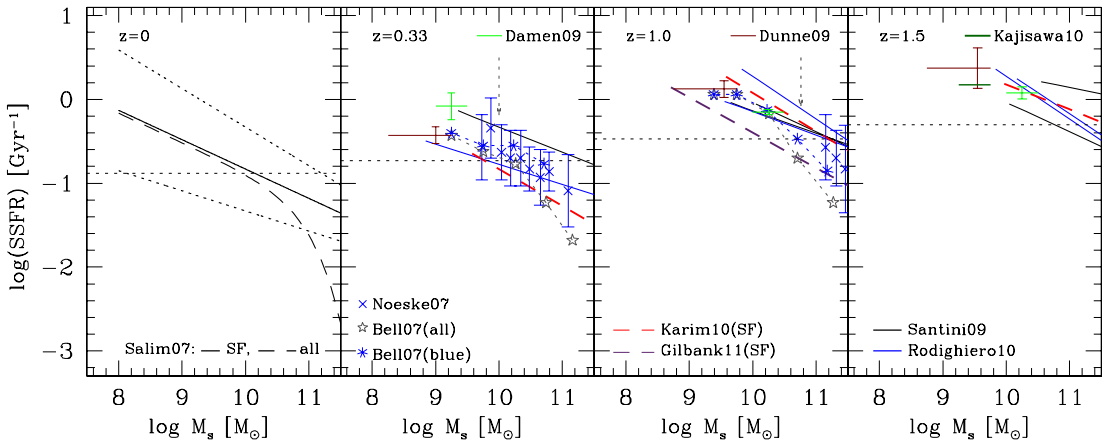

Figura 2.1: Tasas de formación estelar por unidad de masa estelar de la galaxia (TFEE) como función de la masa estelar M_s para $z = 0, 0.33, 1.0, 1.5$. Los asteriscos en azul y las estrellas en gris representan datos observacionales determinados para las galaxias azules y todas las galaxias de la muestra en el CDFS respectivamente,(Bell et al. 2007). Cruces con barras de error: datos observacionales reportados por Noeske et al. (2007b) que muestran la media y la desviación estandar de la muestra (AEGIS) para la TFEE en el rango donde la muestra es 95 % completa. Las líneas representan ajustes a observaciones dados por los autores indicados en los paneles.

Cuadro 2.1: Resumen de referencias y correcciones

Referencia	Trazador de TFE	IMF	M_s Offset	SFR Offset
Salim et al. (2007)	L_{UV}, H_α	Chabrier (2003)	0.0	0.0
Bell et al. (2007)	$L_{IR} + L_{UV}$	Chabrier (2003)	0.0	0.0
Noeske et al. (2007b)	$L_{24\mu m}$+ emission lines	Kroupa (2001)	0.0	0.0
Santini et al. (2009)	$L_{IR} + L_{UV}$	Salpeter (1955)	–0.25	–0.176
Damen et al. (2009b)	$L_{IR} + L_{UV}$	Kroupa (2001)	0.0	0.0
Dunne et al. (2009)	$L_{1400MHz}$	Salpeter (1955)	–0.25	–0.176
Kajisawa et al. (2010)	L_{UV}(corrected)	Salpeter (1955)	–0.25	–0.176
Karim et al. (2011)	$L_{1400MHz}$	Chabrier (2003)	0.0	0.0
Rodighiero et al. (2010)	$L_{IR} + L_{UV}$	Salpeter (1955)	–0.25	–0.176
Gilbank et al. (2011)	[O II]-(H_α)	Baldry & Glazebrook (2003)	–0.08	–0.18

TFE/M_s= 1/[(1 – R)($t_H(z)$ – 1 Ga)], donde $R = 0.4$ es el factor promedio de reciclado de gas debido a la pérdida de masa estelar, t_H es el tiempo cósmico y se sustrae 1 Ga a fin de tomar en cuenta el inicio de la formación galáctica. Las galaxias por debajo de la línea punteada tienen una TFE menor al promedio de su pasado, mientras que aquellas por encima, en el momento tienen una TFE más alta que el promedio del pasado. Es interesante notar que a medida que z es menor, cada vez galaxias de menores masas caen por encima de la línea punteada; esto es también evidencia del "downsizing": con el tiempo galaxias cada vez más pequeñas se van apagando.

Aunque el resultado presentado en la Fig. 2.1 parece ser robusto, es importante tener en cuenta que las inferencias observacionales tienen sus propias problemáticas que debemos considerar. En particular, vale la pena remarcar que dada la imposibilidad para poder resolver observacionalmente las poblaciones estelares de las galaxias, la estimación de su masa estelar está basada en, y por lo tanto depende de, los modelos de síntesis de poblaciones estelares. Estos modelos son limitados principalmente por las incertidumbres en la evolución estelar (por ej. en la TP-AGB) y por el poco conocimiento de la IMF, así como por las degeneraciones que se presentan en dichos modelos entre la edad y la metalicidad de las galaxias (para una discusión ver por ej. Maraston et al. 2006; Bruzual 2007; Tonini et al. 2009; Conroy, Gunn & White 2009; Santini et al. 2009; Salimbeni et al. 2009). Por ejemplo, Conroy, Gunn & White (2009) estimó que al incluir incertidumbres en la evolución estelar, la M_s a $z \sim 0$ acarreaba errores de ~ 0.3 dex a un $95\,\%$ de nivel de confianza con poca dependencia en la luminosidad o el color. Salimbeni et al. (2009) han encontrado que las masas obtenidas con los modelos de Maraston (2005) (M05) y Charlot & Bruzual 2007 (CB07, ver Bruzual 2007) (que toman en cuenta la fase TP-AGB) son en promedio más pequeñas que las obtenidas con el modelo de sintesis de poblaciones de Bruzual & Charlot (2003) (BC03). En el rango en z's $0.4 < z < 0.8$ el cociente que ellos encontraron entre las masa estimadas por BC03 y CB07 es ~ 0.3 dex para $M_s < 10^{9.5} M_\odot$ y ~ 0.05 dex para $M_s > 10^{11} M_\odot$, mientras que para BC03 y M05 la razón es de ~ 0.2 dex para todas las masas.

Todas las relaciones $TFEE - M_s$ compiladas aquí y mostradas en la figura 2.1 fueron inferidas usando el modelo BC03. Aún así, si suponemos una corrección conservadora debido a la fase TP-AGB de 0.2 dex en la M_s para todas las masas y una pendiente de -0.5 en el plano $log(TFEE) - log(M_s)$ (en la mayoría de los casos la pendiente es menos pronunciada), entonces dicha relación se ve desplazada por 0.1 dex($\approx 25\,\%$) hacia la parte alta de la TFEE. Por lo tanto, el resultado que se obtiene al considerar las correciones a la sobrestimación de la M_s por los modelos de sintésis de poblaciones "viejos" es en un desplazamiento neto hacia la parte superior del plano $log(TFEE) - log(M_s)$. Esto no cambia el comportamiento ya discuitido en el plano $log(TFEE) - log(M_s)$ y, como se discutirá más adelante, no hace sino acentuar aún más la discrepancia entre las inferencias observacionales y los resultados de simulaciones numéricas de galaxias reportadas por diversos grupos de investigación.

Es importante señalar que desde que se acuñó el término "downsizing" (Cowie et al. 1996), el mismo ha sido utilizado confusamente en la literatura para caracterizar en realidad diferentes tipos de resultados observacionales y a diferentes escalas. Así, en general, se puede dividir el fenómeno del "downsizing" en dos manifestaciones distintas, una de ensamblaje de masa que aplica a las galaxias masivas, las que se van apagando (frenando su tasa de ensamblaje de masa estelar), más temprano las más masivas, y otra de tasa de TFEE que aplica a las galaxias menos masivas, las que muestran una TFEE activa, de tal modo que mientras más pequeña la galaxia, más tardíamente está teniendo sus fases activas de crecimiento por formación estelar. Ver detalles de los aspectos observacionales de estas manifestaciones del "downsizing" en la Sección 2.2

2.1.2. Historia de la TFE cósmica

Desde el trabajo pionero de Madau et al. (1996), se ha medido cada vez con más completez y precisión lo que es la TFE por unidad de volumen comóvil a diferentes épocas, desde $z \approx 0$ hasta $z \sim 7-8$. Esta cantidad integra la TFE producida por todas las galaxias a cada z y su principal característica es que desde $z \sim 2-3$ decrece hacia el día de hoy por un factor 10–15; la actividad de formación estelar, y por ende galáctica, tuvo su máximo hacia esas épocas tempranas del Universo y actualmente está en proceso de extinción. A $z's$ mayores parece decrecer aunque, dadas las incertidumbres observacionales y el trazador de TFE usado, es debatible si este decrecimiento es pronunciado o débil. La historia de TFE cósmica es una observable valiosa que integra toda la complejidad del proceso de formación y evolución de galaxias por lo que suele usarse para constreñir modelos y simulaciones (ver una reseña y un ejemplo de estos modelos en Muñoz-Gutíerrez 2010, y referencias ahí). En particular, la historia de TFE cósmica será relevante para constreñir nuestro modelo de juguete paramétrico.

La recopilación más reciente de múltiples estudios observacionales (posteriores a 2006) fue realizada por Madau & Dickinson (2014). En está sólo se incluyeron sondeos que hayan medido la TFE a partir del lejano UV (FUV) (generalmente 1500 Å) o en el mediano y lejano infrarrojo, en este último caso, con preferencia por observaciones en el lejano infrarrojo de *Spitzer* y *Herschel* sobre los basados solo en el mediano infrarrojo de *Spitzer* a 24 μm. Los respectivos valores para la TFE cósmica se muestran en el panel superior de la Figura 2.2.

Como se menciona en Madau & Dickinson (2014), el "estado del arte" de los datos observacionales nos presenta una clara fotografía de lo que ha sido la historia de TFE cósmica: una fase de crecimiento sostenido a altos corrimientos al rojo ($z > 3$), que alcanza su máximo entre $z = 2$ y $z = 1.5$, para después empezar una nueva etapa en la que cae hasta el día de hoy, con una pendiente ligeramente menor a la que creció en sus etapas tempranas. En particular, se muestra que la TFE co-móvil a $z \approx 7$ es del orden de la que se mide en el Universo local.

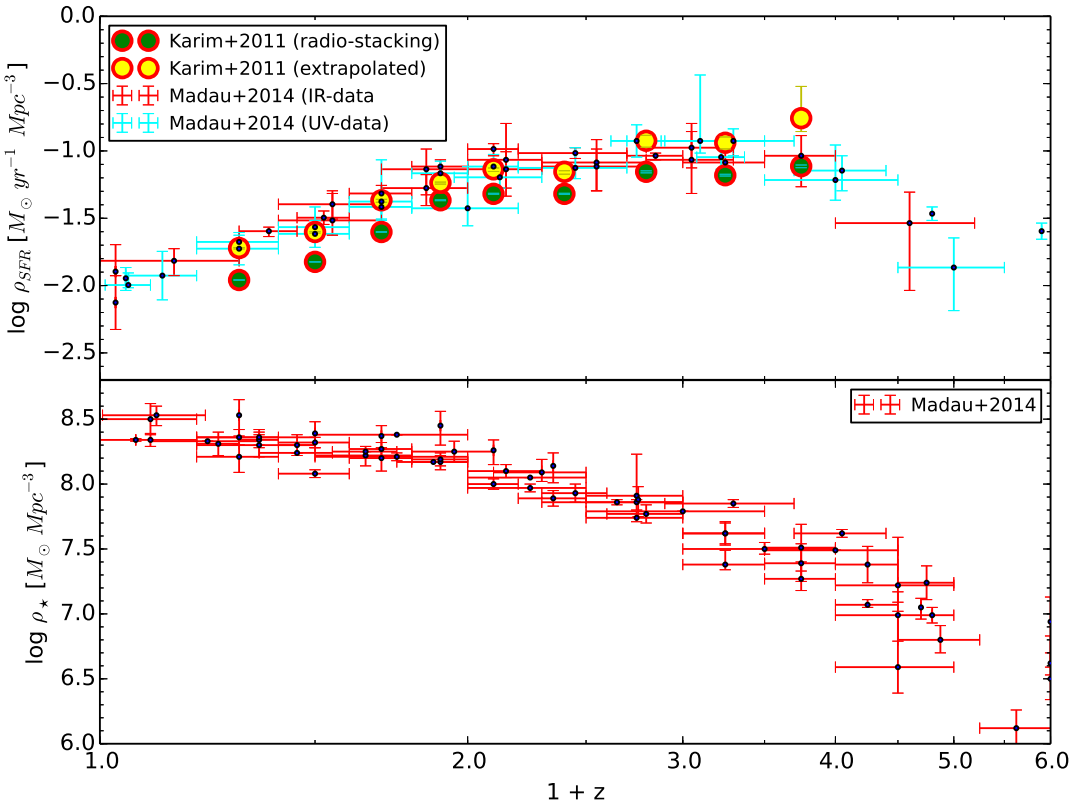

Figura 2.2: Panel superior: Densidad de la tasa de formación estelar como función de z (Madau plot). Los datos observacionales obtenidos con trazadores UV (infrarrojos) compilados por Madau & Dickinson (2014) están graficados con barras de error en color cyan (rojo). Los círculos verdes son datos observacionales obtenidos por Karim et al. (2011) del VLA-COSMOS survey, considerando solo datos hasta donde la muestra es completa. Los círculos en amarillo son los respectivos resultados al considerar datos extrapolados hasta el límite de bajas masas donde la muestra deja de ser completa. Panel inferior: Densidad de masa estelar como función de z. Los datos observacionales compilados por Madau & Dickinson (2014) están representados con cruces en rojo.

La integración de la historia de TFE cósmica, tomando en cuenta el factor de reciclado por pérdida de masa estelar, da lo que sería la historia de densidad estelar (DE) cósmica, es decir la densidad comóvil de estrellas en el Universo a diferentes épocas. Esta cantidad es también una observable que se obtiene de integrar las funciones de masa estelar galáctica medidas a diferentes épocas. En el panel inferior de la Fig. 2.2 se presenta una compilación de datos recientes (posteriores al 2006) realizada por Madau & Dickinson (2014). Las estimaciones locales están basadas en datos del SDSS (Gallazzi et al. 2008; Li & White 2009; Moustakas et al. 2013). La mayoría de las estimaciones a $0.1 < z < 4$ incluyen datos con fotometría en el infrarrojo del Spitzer IRAC (e.g., Pérez-González et al. 2008;

Kajisawa et al. 2009; Marchesini et al. 2009; Pozzetti et al. 2010; Ilbert et al. 2013); a muy alto redshift ($z > 4$) las estimaciones se hacen a partir de observaciones de LBG en el UV (e.g., Yabe et al. 2009; González et al. 2011; Lee et al. 2012; Labbé et al. 2013). Para una descripción más detallada de la compilación ver Madau & Dickinson (2014).

En la literatura se ha discutido sobre una posible inconsistencia entre las historia DE cósmica obtenida de integrar la historia de TFE cósmica y la medida a partir de las funciones de masa estelar galácticas a diferentes z's. De acuerdo a Madau & Dickinson (2014) este problema, a la luz de las estimaciones más recientes, no es tan importate como se creía, aunque ellos también encuentran un ligera sobrestimación de la DE cósmica de ~ 0.2 dex sobre un rango amplio de z's.

2.1.3. Relación masa de halo–masa estelar

En el escenario de formación de estructuras de la cosmología ΛCDM se supone que las galaxias se forman al enfriarse el gas que cae en los pozos de potencial de los halos de materia oscura (MO). Dicho gas frío y su eventual transformación en estrellas son los trazadores básicos de las propiedades estructurales y dinámicas de las galaxias. En particular, se sabe que la luminosidad (en especial infrarroja) de una galaxia correlaciona muy bien con su masa en estrellas (M_s), algo que ya hemos discutido en la Sección 2.1. Sin embargo, la determinación de la masa virial del halo ($M_{\rm v}$) en que viven dichas galaxias es algo que no se puede aún realizar de manera rutinaria, especialmente a altos corrimientos al rojo. Así, los esfuerzos para lograr una medición directa de las masas viriales están restringidos a z's no muy altos, para lo cual en general se emplean técnicas de lente gravitacional débil o vía la cinemática de satélites. Estas determinaciones de la relación M_s–$M_{\rm v}$, por cuestiones de señal a ruido, se hacen con métodos de apilamiento (stacking) y son dependientes de modelo por el momento. Como alternativa, métodos indirectos (semi-empíricos), pero que cubren intervalos más grandes de masa y corrimiento al rojo, han sido exitosamente desarrollados en los últimos años (ver una reseña en Rodríguez-Puebla 2013).

A pesar de que existen una gran variedad de métodos semi-empíricos, en general todos están basados en constreñir funciones que permiten conectar las distribuciones estadísticas de las galaxias observadas (p.ej. las funciones de masa estelar galáctica y las de correlación de dos puntos) con las distribuciones estadísticas de los halos y subhalos obtenidos en simulaciones cosmológicas de N cuerpos. Los dos formalismos más usados son el *modelo de ocupación de halos*[1] y el que emplea la *técnica de correlación de abundancias*[2]. No es el objetivo de este trabajo entrar en los detalles de sus fortalezas y debilidades. Lo que sí es importante señalar es que ambos esquemas han probado ser muy útiles para restringir la realación M_s–$M_{\rm v}$ y su evolución con z.

[1] Este modelo es mejor conocido por sus siglas en inglés como Halo Occupation Distribution (HOD).
[2] Este modelo se conoce en la literatura como Abundance Matching Technique (AMT).

En los últimos años se han publicado una gran cantidad de trabajos en los que se reportan inferencias semi-empíricas para la relación M_s–$M_{\rm v}$, o su equivalente F_s–$M_{\rm v}$, con $F_s \equiv M_s/M_{\rm v}$ (ver p. ej., Conroy & Wechsler 2009; Moster et al. 2010; Behroozi, Conroy & Wechsler 2010; Firmani & Avila-Reese 2010; Yang et al. 2012; Behroozi, Wechsler & Conroy 2013b; Moster, Naab & White 2013). En estos trabajos no sólo se determina la F_s a un época dada, sino que además se infiere su evolución con z. En la Figura 2.3 se muestran las inferencias semi-empíricas en el plano F_s–$M_{\rm v}$ obtenidas por Firmani & Avila-Reese (2010); Yang et al. (2012); Behroozi, Wechsler & Conroy (2013b); Moster, Naab & White (2013) para el intervalo $0 \lesssim z \lesssim 4$. En esta figura se pueden apreciar ciertas coincidencias cualitativas:

1. En los cuatro casos existe una masa característica, ${M_{\rm v}}^{max}$, que identifica la masa de halo que tienen una F_s máxima. El valor a $z \sim 0$ de ${M_{\rm v}}^{max}$ es $\approx 10^{11.8} M_\odot$ para todos los casos, aunque para esta masa en particular, cada autor reporta distintos valores de la fracción F_s.

2. A cada z, mientras más pequeño sea el halo con respecto a ${M_{\rm v}}^{max}$, menor es la F_s asociada con este. Esto ocurre en todas las inferencias reportadas independientemente del corrimiento al rojo.

3. Para todo z, mientras más grande sea el halo con respecto a ${M_{\rm v}}^{max}$, menor es también la F_s que se le asocia a dicho halo, aunque el decrecimiento es menos pronunciado que a las bajas masas.

4. En general, las pendientes de las relaciones M_s–$M_{\rm v}$, tanto a bajas como altas masas, no cambian mucho con z; el caso extremo a bajas masas es el de Moster, Naab & White (2013) y a altas masas, el de Yang et al. (2012). A bajas masas, la relación M_s–$M_{\rm v}$, hasta por lo menos $z \sim 2$, decrece en el sentido de que a paridad de $M_{\rm v}$, las masas estelares son menores para z's más altos. En algunos casos el decrecimiento es fuerte (evolución pronunciada) y en otros es muy ligero (es de hecho tema de debate si la relación M_s–$M_{\rm v}$ evoluciona mucho o no); a altas masas, el cambio es menor que a bajas masas en todos los casos.

Las diferencias entre las distintas inferencias semi-empíricas son más notables en la Figura 2.4, donde en cada uno de los paneles, correspondientes a $z = 0.1$, 1, 2 y 4, se grafican las cuatro inferencias mostradas en la Figura 2.3. Ahora los distintos colores en las curvas denotan las distintas inferencias reportadas por los citados autores. Hay que notar que las estimaciones de la dispersión *intrínseca* de la mayoría de estas determinaciones (desviación estándard) son del orden de 0.15-0.20 dex. A $z \sim 0.1$ parece estar bien restringida la relación F_s–$M_{\rm v}$, aunque hay ciertas diferencias en el valor máximo para F_s. Lo cierto es que cuando comparamos el valor máximo para F_s reportado por Moster, Naab & White (2013) y Behroozi, Wechsler & Conroy (2013b), la diferencia es menor a un factor 2, lo que implica es que ésta es menor que la incertidumbre *sistemática* en la

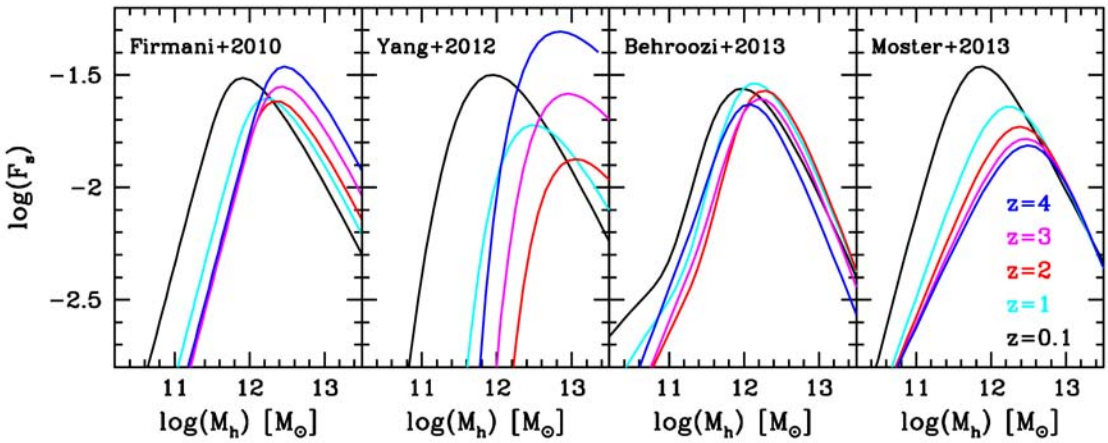

Figura 2.3: Fracción de masa estelar F_s como función de la masa del halo $M_{\rm v}$ para cuatro inferencias independientes según se indica en cada panel respectivamente. En cada panel se muestran en curvas de colores las F_s's a distintos corrimientos al rojo, desde $z \sim 0.1$, hasta $z \sim 4$.

estimación de la M_s de las galaxias. El único punto por resaltar es la diferencia cualitativa en el comportamiento de la F_s reportado por Behroozi, Wechsler & Conroy (2013b) a bajas masas; ese cambio en la pendiente puede tener implicaciones muy relevantes al momento de restringir los modelos paramétricos de formación de galaxias de bajas masas. Según se menciona en Behroozi, Wechsler & Conroy (2013b), este aplanamiento de la curva viene de restringir el modelo de método de abundancias con una función de masa estelar que a las bajas masas tiende a empinarse y tener una curva más pronunciada, algo que es aún incierto.

Claramente las diferencias entre las distintas inferencias para la F_s empiezan a ser más significativas conforme las vamos comparando a z's cada vez más grandes. A $z \sim 4$ los valores para la F_s máxima llegan a diferir hasta por un factor 3. Y dada la distinta evolución característica de cada inferencia, a paridad de masa de halo las diferencias llegan a ser enormes, sobre todo si comparamos la F_s reportada por Yang et al. (2012), que ya desde $z \sim 1$, para un halo con $M_{\rm v} \sim 10^{10.6} M_{\odot}$, la F_s llega a ser al menos un factor 6 menor que la reportada por los otros autores. Esto indica que las inferencias de la relación M_s–$M_{\rm v}$ a $z > 2$ se tornan muy inciertas.

2.1.4. Enfoque semi-empírico

La relación M_s–$M_{\rm v}$ y su evolución proporcionan información valiosa para inferir el proceso de ensamblaje de las galaxias a diferentes escalas. Por ejemplo, si se hace uso de las historias de agregación de masa (HAM) promedio de los halos ΛCDM, se

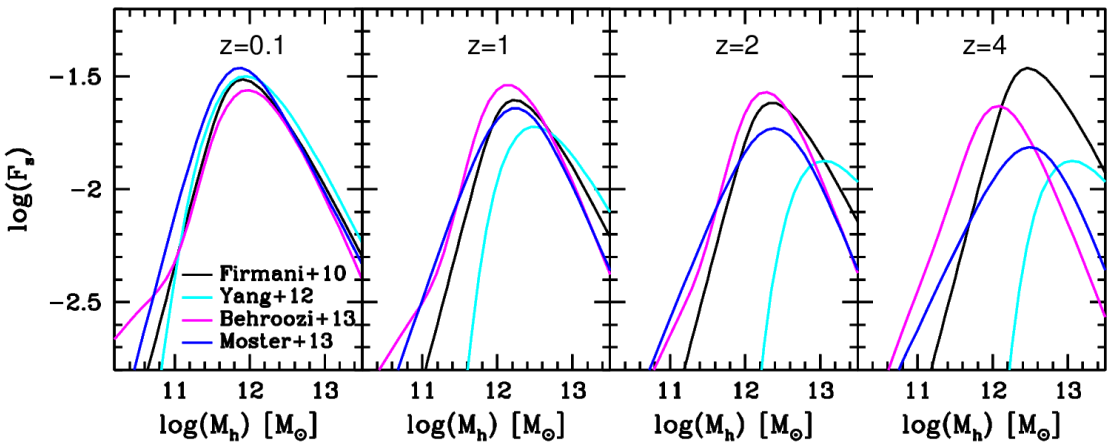

Figura 2.4: Fracción de masa estelar F_s como función de la masa del halo $M_{\rm v}$ para cuatro inferencias independientes para cuatro corrimientos al rojo: desde $z \sim 0.1$ (primer panel a la izquierda), hasta $z \sim 4$ (cuarto panel a la derechsa). En cada panel se muestran en curvas de colores las F_s's que reportan los distintos autores, líneas en color: negro, Firmani+2010; en cyan, Yang+2012; en magenta, Behroozi+2013, y en azul Moster+2013.

pueden entonces aislar trazas evolutivas promedio de crecimiento de M_s conectando las relaciones M_s–$M_{\rm v}$ a diferentes z's de la Fig. 2.3 (isócronas). Este enfoque fue desarrollado originalmente en Conroy & Wechsler (2009) y Firmani & Avila-Reese (2010) con resultados novedosos en cuanto al ensamblaje de M_s de las galaxias de acuerdo a su masa. Las derivadas temporales de las HAM de la masa de halo y estelar están asociadas a las tasas de agregación de masa de halo y de formación estelar (y en menor grado, a la tasa de fusiones), respectivamente. Es de esperar que las trazas evolutivas de los sistemas galaxia-halo en el plano de las relaciones M_s–$M_{\rm v}$ a diferentes z's estén íntimamente conectadas con las relaciones $TFEE - M_s$ a diferentes z's. A su vez la integración de las TFE de toda la población de los sistemas galaxia-halos, se traduce en las historias de TFE y DE cósmicas. Un modelo paramétrico que conecte la tasa de agregación de masa de los halos con la TFE de las galaxias, es capaz de proyectarse en todas estas relaciones empíricas; al fijar los parámetros de la función de conexión de tal manera que se obtengan resultados consistentes con las relaciones empíricas, se obtienen historias evolutivas de la masa estelar de las galaxias de acuerdo a su masa y se cuantifica el grado de desviación del ensamblaje galáctico del oscuro, algo que da valiosa información sobre los procesos físicos de la evolución de galaxias y las escalas y épocas en que operan unos y otros. Es el enfoque que seguiremos a continuación.

Las secciones por venir en lo que resta del presente Capítulo forman parte de un artículo que esta en proceso de ser enviado para su arbitraje a una revista, por lo cual dichas secciones están redactadas en idioma inglés.

2.2. On the stellar and halo mass assembly of galaxies

With the advent in the last decade of large and uniform surveys of local and high-redshift galaxies, it is now possible to reconstruct empirically the main evolutionary trends of the galaxy population as a function of mass and other galaxy properties. Among the main observational determinations at different redshifts that allowed this achievement we should mention: (a) the galaxy stellar mass function ($GSMF$) decomposed into different galaxy types, (b) the star formation rate (SFR) as a function of stellar mass, M_s, and galaxy type, and (c) the galaxy merging rates at different masses.

Based on these determinations, the empirical picture of the galaxy assembly process that emerged (see e.g., Bell et al. 2007; Drory & Alvarez 2008; Pozzetti et al. 2010), has as a general result that $\sim 50\,\%$ of the local stellar mass density was assembled since $z = 1$, and $\sim 90\,\%$ since $z = 3.5$ (e.g., Pérez-González et al. 2008). The main new concept distilled from this empirical picture is that of *cosmic downsizing*, a term coined by Cowie et al. (1996) to describe the decline with cosmic time of the maximum rest-frame $K-$band luminosity of galaxies undergoing active SF. This term has been more recently used to describe a number of trends of the galaxy population as a function of mass that imply in general a galaxy buildup from top to down. However, these different trends are actually related to different scales, astrophysical phenomena, and galaxy evolutionary stages (Fontanot et al. 2009). From the most general point of view, the many downsizing manifestations can be separated into those that refer to the evolution of (A) massive early-type, red, quenched galaxies, and of (B) less massive late-type, blue, star forming galaxies:

- (A) *Downsizing in the mass assembly.* Observations show that the high-mass end of the $GSMF$ was in place since high z (e.g., Fontana et al. 2004, 2006; Drory et al. 2005; Cimatti, Daddi & Renzini 2006; Marchesini et al. 2009; Pérez-González et al. 2008), and provide evidence of a decrease with cosmic time of the characteristic mass at which the SFR is dramatically quenched or at which the $GSMF$s of early- and late-type galaxies cross, i.e. less and less massive galaxies migrate with time to the red sequence, being today in this process those of masses $M_s \sim 3 - 5 \times 10^{10}$ $M_\odot$ (e.g., Cowie et al. 1996; Bundy et al. 2006; Borch et al. 2006; Bell et al. 2007; Hopkins, Richards & Hernquist 2007; Drory & Alvarez 2008; Vergani et al. 2008; Pozzetti et al. 2010). This is in line with "archaeological" inferences,[3] which show an earlier mass assembly as more massive are the (elliptical) galaxies (archaeological downsizing; e.g., Daddi et al. 2004; Thomas et al. 2005; Panter et al. 2007).

- (B) *Downsizing in specific SFR (sSFR = SFR/M_s).* Although the observations of less luminous (massive) galaxies suffer incompleteness as z increases due to the flux limits, at least up to $z \sim 1 - 2$, most of observational studies have found that the sSFR of galaxies with $M_s \lesssim 3 \times 10^{10}$ $M_\odot$, which are mostly late-type, star-forming

[3]The archaeological inference is based on the reconstruction of the SF and metallicity evolution of galaxies by applying models of stellar population synthesis to spectro-photometric observations of local galaxies.

galaxies, is surprisingly high even at $z \sim 0$ and, on average, the lower the mass, the higher the SSFR (e.g., Baldry et al. 2004; Bauer et al. 2005; Zheng et al. 2007; Noeske et al. 2007a; Bell et al. 2007; Elbaz et al. 2007; Salim et al. 2007; Chen et al. 2009; Damen et al. 2009a; Santini et al. 2009; Oliver et al. 2010; Kajisawa et al. 2010; Rodighiero et al. 2010; Karim et al. 2011; Gilbank et al. 2011; Huang et al. 2012; Bauer et al. 2013; Speagle et al. 2014). This means that the smaller the galaxies, the later they enter to the active phase of growth by SF. This applies at least for central galaxies, i.e. those that are not satellites. Recently, Geha et al. (2012) have found in a complete sample from the SDSS DR7 that practically all isolated galaxies of masses $M_s \lesssim 10^9\ M_\odot$ have H_α line widths that evidence active SF.

By combining the evolution of the $GSMF$ with the measured SFR–M_s relations at different z, the contribution of in situ SF and ex situ accretion (by mergers) to the stellar mass build up has been constrained (Bell et al. 2007; Drory & Alvarez 2008; Pozzetti et al. 2010), showing clearly the downsizing trends mentioned above. It is important to remark that these as well as direct –but yet limited– observational determinations of the merging rate (e.g., Lotz et al. 2008; Bundy et al. 2009; Bluck et al. 2012; López-Sanjuan et al. 2013; Conselice et al. 2013; Ferreras et al. 2014) show that the in situ SF channel completely dominates in low- and intermedium-mass galaxies at all epochs, while (dry) mergers may play a moderate role for massive ($M_s \gtrsim 10^{11} M_\odot$, mainly red) galaxies at later epochs ($z \lesssim 1$), contributing on average up to 50 % of the assembled present-day mass of these galaxies.

Although important efforts have been made already in order to constrain the dynamical evolution of galaxies (e.g., from observational studies at high redshifts of the Tully-Fisher and Faber-Jackson relations, galaxy-galaxy weak lensing, etc.), direct constraints of the galaxy-halo connection as a function of mass are yet very limited. This kind of observations together with those regarding the gas mass of galaxies at high z are necessary to complete the whole picture of galaxy stellar, baryonic, and dark mass assembly. In the meantime, semi-empirical methods were introduced in order to get the whole evolutionary connection in the context of the ΛCDM scenario and constrain in this way the average *individual* trends of the galaxy evolution process as a function of halo mass (e.g., Conroy & Wechsler 2009; Hopkins et al. 2009; Firmani & Avila-Reese 2010; Bouché et al. 2010a; Leitner 2012; Yang et al. 2012).

2.2.1. Connecting galaxies to dark halos

In the semi-empirical approach, the information provided by direct observations at different epochs (mainly the $GSMF$ and spatial correlation function) is combined in a statistical way with predicted properties for the ΛCDM halos in order: (1) to attain a connection between galaxies and halos, and (2) to infer *individual* (average) galaxy evolutionary tracks. An schematic idea of the approach is as follows:

(1) Global galaxy-halo connection.- Statistical approaches like the abundance matching technique, halo occupation distribution, and conditional luminosity function, allow us to connect the statistics of halos and subhalos measured in the cosmological N-body simulations with the statistics of observed central and satellite galaxies, in the understanding that each halo hosts a central galaxy with a population of satellites, and that each subhalo hosts a satellite. As the result, a link between M_s and $M_{\rm v}$ is obtained, including its intrinsic scatter, and, more recently, the link has been obtained even for blue and red galaxies separately (Rodriguez-Puebla et al. 2014, see therein also a review of the different statistical methods for the galaxy-halo connection, and more references).

The halo masses of galaxies can be actually determined by direct methods as galaxy-galaxy weak lensing and satellite kinematics (e.g., Mandelbaum et al. 2006; More et al. 2011). Nevertheless, in current studies, due to the low signal-to-noise ratios, the analysis can be performed only by stacking a large number of galaxies; this introduces biases and significant statistical uncertainties in the inferences, and limits the inferences to relatively small mass ranges. However, in the mass ranges where comparisons are feasible, these direct methods and the semi-empirical statistical approaches give M_s–$M_{\rm v}$ relations at $z \sim 0$ compatible among them within a factor of ~ 2 (see BCW10; Moster et al. 2010; Guo et al. 2010; More et al. 2010; Rodríguez-Puebla et al. 2011,2013).

The obtained stellar mass fractions, $F_s \equiv M_s/M_{\rm v}$, are very low with respect to the universal baryon fraction ($F_{b,U} \equiv \Omega_b/\Omega_M \approx 0.17$), i.e. galaxy SF inside ΛCDM halos seems to be a very inefficient process. Besides, the efficiency is strongly dependent on mass: it peaks around $M_{\rm v} = 8 \times 10^{11}\ M_\odot$, decreasing significantly towards lower ($F_s \propto {M_{\rm v}}^a, a \approx 1.25$) and higher ($F_s \propto {M_{\rm v}}^b, b \approx -0.6$) masses. The $GSMF$ determinations at higher redshifts allow now to use methods like the AMT to infer the M_s–$M_{\rm v}$ relation at different epochs (e.g., Behroozi, Conroy & Wechsler 2010; Moster et al. 2010; Wang & Jing 2010; Yang et al. 2012; Moster, Naab & White 2013; Behroozi, Wechsler & Conroy 2013b). The latter authors extended the AMT out to $z \approx 7$ and found that (a) the $M_{\rm v}$ at wich F_s peaks shifts little to higher masses (by ≈ 0.6 dex out to $z \approx 4$), and (b) the peak value remains roughly constant. For masses below (above) the peak at a given epoch, F_s is smaller (slightly larger) than at earlier epochs for a given $M_{\rm v}$. This implies that galaxy SF in massive halos should have been slightly more efficient in the past, while in low-mass halos it should have been even less efficient. *This is a manifestation of the cosmic downsizing discussed above.*

(2) Individual $M_{\rm v}$ and M_s evolutionary tracks.- In the ΛCDM scenario, the individual mass aggregation histories (MAHs) of halos are known. By using averages of them and combining with the semi-empirical M_s–$M_{\rm v}$ relations at different z, the evolutionary M_s tracks corresponding to the average MAHs can be inferred (Conroy & Wechsler 2009; Firmani & Avila-Reese 2010, hereafter FA10). The results are encouraging and show that at each epoch there is a characteristic mass that separates galaxies into two rough

populations: (a) galaxies more massive than $M_s(z=0) \approx 3 \times 10^{10}\ M_\odot$ are on average quiescent/passive (their M_s growth slowed down or stopped completely), besides the more massive is the galaxy, the earlier it has transited from the active (blue, star-forming) to the passive (red, quenched) population ("downsizing"); (b) galaxies less massive than $M_s(z=0) \approx 3 \times 10^{10}\ M_\odot$ are on average active (blue), and the less massive the galaxy, the faster its late M_s growth, driven likely by local SF ("downsizing in sSFR").

As FA10 showed, the shapes of the average stellar and halo mass assembling histories are quite different. For galaxies with $M_s(z) < 3 \times 10^{10}\ M_\odot$, their halo MAHs at later epochs grow slightly slower as smaller is the mass, while their stellar MAHs grow much faster. For $M_s(z{=}0) > 3\ 10^{10}\ M_\odot$, as the system is more massive, the stellar assembly of the galaxy occurs earlier in time with respect to the corresponding halo. Only for systems that attained at a given epoch masses $M_s \approx 3-5 \times 10^{10}\ M_\odot$ ($M_{\rm v} \approx 1-2 \times 10^{12}\ M_\odot$), both the M_s and $M_{\rm v}$ assembly history shapes are similar; these systems are namely those in the peak efficiency (maximum $M_s/M_{\rm v}$ ratio).

The previous studies have shown that the semi-empirical approaches are a powerful tool for constraining key aspects of the galaxy population assembly in the cosmological context. *These constrains are very useful*: (a) for confronting them to semi-analytic models and numerical simulations in order to explore for systematical deviations, which would point out to the necessity of improving or introducing new astrophysical processes, and/or of changing the cosmological context to alternative models; (b) for making further predictions regarding particular aspects of galaxy evolution at concrete galaxy scales and epochs; (c) for isolating the key physics of galaxy formation and evolution within the growing CDM halos as a function of scale and time.

Recently, appeared several works which use simple parametric models trying to mimic and explain the behavior of different dependences and evolutionary features of the observed galaxy population (Bouché et al. 2010a; Leitner 2012; Weinmann et al. 2012; Moster, Naab & White 2013; Behroozi, Wechsler & Conroy 2013b; Mutch, Croton & Poole 2013; Peng et al. 2014). Here, we introduce a parametric model that can be constrained by the semi-empirically inferred M_s–$M_{\rm v}$ relations at different redshifts, the SFR–M_s correlation at different redshifts, and the cosmic SFR history. The model starts by proposing a parametric function that describes the relation between the rates of (cosmological) halo mass aggregation and galaxy SF as a function of $M_{\rm v}$ and z. Then, by using the average halo MAHs taken from the Millennium Simulations I and II (Fakhouri, Ma & Boylan-Kolchin 2010), as well as the abundance of halos of all masses at each epoch, the SFR and stellar mass growth histories of individual (average) galaxies can be predicted along with their overall contributions to the cosmic SFR and stellar density.

By means of our parametric model we aim to explore (1) how compatible are between them the empirical SSFR– M_s and M_s–$M_{\rm v}$ relations at different redshifts and how the

evolution of one affects over the other; (2) to constrain the main average in situ and ex situ stellar mass growth histories as a function of mass, as well as the main features of the (stellar) galaxy assembly efficiency as a function of halo mass and epoch; (3) to constrain the stellar mass and comoving density of galaxies that are transiting from active to passive at each redshift and explore whether the quenching process is related to the quasar phase of (massive) galaxies.

2.3. The model

2.3.1. The efficiency of galaxy stellar mass growth

Semi-empirical inferences of the stellar-to-halo mass relation, F_s–$M_{\rm v}$, state that, since high redshift ($z \sim 4$), this relation shows a "bell-shaped" behavior (see Figs. 2.3 and 2.4). Then, at each z, there is a characteristic halo mass ${M_{\rm v}}^{\rm max}$ at which the relation reach its maximum, in such a way that as lower or higher is the mass with respect to ${M_{\rm v}}^{\rm max}$, the lower is the average F_s for a halo with this $M_{\rm v}$. The low values for F_s at the high-mass regime can be explained mainly by a combined effect of: i) the long radiative cooling times for the larger halos, which makes inefficient the accretion of cold gas to form stars and, ii) the AGN feedback, which heats, and eventually ejects gas from the galaxy, quenching the SF. On the other hand, the capture of satellites (mergers) by a given galaxy, something that is more probable in more massive systems, works in the direction of increasing F_s.

Regarding the low-mass regime, the strong decreasing of F_s as $M_{\rm v}$ is smaller, is commonly explained by the effects of SN-driven outflows (e.g., Benson et al. 2003; Firmani, Avila-Reese & Rodríguez-Puebla 2010), while also preventive forms of stellar-driven feedback may play a crucial role in delaying and lowering the stellar mass growth of low-mass galaxies (e.g, Hopkins et al. 2013; Trujillo-Gomez et al. 2013). For the smallest halos, it is proposed that the gas is even not captured by them due to its photoheating produced by the fresh UV background after reionization.

The different astrophysical mechanisms proposed in both the low- and high-mass regimes are actually not yet well constrained, since the high complexity of each of this mechanisms makes difficult to join them in a simple unified model describing galaxy formation and evolution. It is not the aim of this work to study the astrophysical processes that shape the M_s–$M_{\rm v}$ or F_s–$M_{\rm v}$ relation. Rather, we are interested in constraining semi-empirically how should be the efficiency of galaxy stellar mass growth as a function of halo mass and z in order to give rise to the M_s–$M_{\rm v}$ and sSFR–M_s relations at different epochs. This way, we obtain valuable constraints to the effects of each one the mentioned astrophysical mechanisms.

We assume that the deviation of the stellar mass assembly from the halo mass assembly

is given by a function of mass and redshift that we call the "galaxy efficiency function", $G_{\rm SFE}(M_{\rm v},\ z)$. Guided by semi-empirical results of the M_s–$M_{\rm v}$ relation, which many authors interpret as an efficiency function[4], we assume $G_{\rm SFE}$ to be a ("bell-shaped") double power law. In the following we describe the procedure to construct the parametric "toy" model.

2.3.2. The procedure

We start by assuming that the baryon accretion rate $\dot{M}_b$ is proportional to the DM accretion rate $\dot{M}_{DM}$:

$$\dot{M}_b = f_{b,u}\dot{M}_{DM} \tag{2.1}$$

where

$$f_{b,u} \equiv \frac{\Omega_b}{\Omega_m - \Omega_b} \approx 0.17 \tag{2.2}$$

represents the universal baryon fraction. For $\dot{M}_{DM}$ we use the averages as a function of $M_{\rm v}$ and z obtained by Fakhouri, Ma, & Boylan-Kolchin (2010) from analizing the merger trees of thousands of halos from the Millenium Simulations,

$$\dot{M}_{DM} =< \dot{M} >_{mean}= 46.1 M_\odot yr^{-1} \left(\frac{M_{\rm v}}{10^{12}M_\odot}\right) \times (1+1.11z)\sqrt{\Omega_m(1+z)^3+\Omega_\Lambda}. \tag{2.3}$$

However, as discussed above, observational and theoretical pieces of evidence show that either not all baryons are trapped by the galaxy and/or transformed into stars or a fraction of them are expelled from the galaxy due to several feedback–driven processes. Therefore, the SFR efficiency is expected to depart from the "cosmological" (halo) baryon infall rate. As mentioned above, we define a "galaxy efficiency function", $G_{\rm SFE}(M_{\rm v},\ z)$ that encodes the great complexity and interconnection of the different astrophysical phenomena, which could cause that the stellar mass assembly differs from the the dark matter assembly. By introducing this function, we estimate the SFR as a function of the halo mass at a given epoch as:

$$\text{SFR}(M_{\rm v}) = \dot{M}_b(M_{\rm v}) \times G_{\rm SFE}(M_{\rm v}). \tag{2.4}$$

We propose $G_{\rm SFE}(M_{\rm v})$ to be defined at a given epoch as:

$$G_{\rm SFE}(M_{\rm v}) \equiv G'_{\rm SFE}(M_{\rm v}, z) \times \epsilon. \tag{2.5}$$

where ϵ is the normalization factor and $G'_{\rm SFE}$ is the shape function, which we propose as a double-power law:

$$G'_{\rm SFE}(M_{\rm v}) = \frac{2G_0}{\left(\frac{M_{\rm v}}{M_1}\right)^{-\alpha} + \left(\frac{M_{\rm v}}{M_1}\right)^{\beta}}. \tag{2.6}$$

[4]It is more correct to define an efficiency function in terms of differential (instantaneous) quantities instead of integral (cumulative) ones, as it is the case of the M_s–$M_{\rm v}$ relation.

The dependence with z is implicit in each one of the parameters. The function can be expressed with only three parameters if we assume that it is normalized to 1 at its maximum, i.e., $G'_{\rm SFE}(M_{\rm max}, z) = 1$, where $M_{\rm max}$ is the mass at which this maximum is attained. In this case, by taking the condition that $\frac{\partial G'_{\rm SFE}}{\partial M_{\rm v}} = 0$, it is easy to show that:

$$M_{\rm max} = f_1(\alpha, \beta) \times M_1, \quad with \quad f_1(\alpha, \beta) = \left(\frac{\alpha}{\beta}\right)^{\frac{1}{\alpha+\beta}}, \tag{2.7}$$

and

$$G_0 = \frac{1}{2}\left(f_1(\alpha, \beta)^{-\alpha} + f_1(\alpha, \beta)^{\beta}\right), \tag{2.8}$$

so finally, the the shape function can be expressed as

$$G'_{\rm SFE}(M_{\rm v}) = \frac{(f_1(\alpha, \beta))^{-\alpha} + (f_1(\alpha, \beta))^{\beta}}{\left[\left(\frac{f_1(\alpha,\beta)M_{\rm v}}{M_{\rm max}}\right)^{-\alpha} + \left(\frac{f_1(\alpha,\beta)M_{\rm v}}{M_{\rm max}}\right)^{\beta}\right]}, \tag{2.9}$$

where the *three free parameters* are α, β, and $M_{\rm max}$, responsible for the low-mass end, the high-mass end, and the "peak" of the bell-shaped function, respectively. These parameters are expected to change with redshift as well as the normalization parameter ϵ, in such a way that $G'_{\rm SFE}$ is actually a function of $M_{\rm v}$ and z.

Our main aim is to reproduce with our "evolutionary" model different (semi)empirical isochrones, namely the relations sSFR–M_s (the differential plane of the stellar mass build-up) and F_s–$M_{\rm v}$ (the integral plane of the stellar mass build-up) at different redshifts, as well as the cosmic SFR density at different redshifts. For this, one needs to parametrize the free parameters of the "galaxy efficiency" function, $G_{\rm SFE}$, as a function of z, with as simple as possible laws. The proposed dependences are as follow:

$$\epsilon(z) = \epsilon_0 + \epsilon_1 \log(1+z) \tag{2.10}$$

$$\alpha(z) = \alpha_0 + \alpha_1 \log(1+z) \tag{2.11}$$

$$\beta(z) = \beta_0 - \beta_1(1+z) \tag{2.12}$$

$$M_{max}(z) = (M_0 + M_{1z} \times (z-3)^2) \times 10^{11} M_{\odot} \tag{2.13}$$

The parameters in these dependences will be constrained by the (semi)empirical relations at each z (isochrones). Note that it is not the aim of the present work to obtain formal best fits to these (semi)empirical relations (which on its own are yet uncertain and diverse among different authors) *but to recover the most significative and general trends of*

them in a self-consistent way.

For computing the cumulative average individual growth of the galaxy stellar mass (evolutionary tracks), we assume that this occurs by two different modes: (a) by an in-situ SF process, and (b) by an ex-situ mode. The first mode refers to the M_s increase by the SF that takes place in the galaxy as defined above. The ex-situ mode refers to the M_s increase from stars formed outside the main galaxy and incorporated to the galaxy by mergers. Accordingly, we define the average stellar mass increase of a halo of mass $M_{\rm v}$ at a given z as:

$$\Delta M_s(M_{\rm v}, z) \equiv {M_s}^{\rm in-situ}(M_{\rm v}, \Delta z) + {M_s}^{\rm ex-situ}(M_{\rm v}, \Delta z). \tag{2.14}$$

The first term is calculated as:

$${M_s}^{in-situ}(M_{\rm v}, z) = SFR(M_{\rm v}, z) \times \Delta t \times (1 - f_{loss}(t)), \tag{2.15}$$

where Δt is the cosmic time interval corresponding to Δz (we will use $\Delta t = 0.1$ Gyr), and $f_{loss}(t)$ is the stellar mass loss factor[5], which evolves with cosmic time (see Moster, Naab & White 2013) as:

$$f_{loss}(t) = 0.05 \times \log\left(1 + \frac{t}{3 \times 10^5 yr}\right). \tag{2.16}$$

The second term is calculated as follows:

$${M_s}^{ex-situ}(M_{\rm v}, z) = a_0 \left[1 + \log\left(\frac{M_{\rm v}}{5 \times 10^{10} M_\odot}\right)\right](1+z)^b, \tag{2.17}$$

The smaller the mass, the smaller is the mass increase due to the ex-situ contribution. For the very low masses at which ${M_s}^{ex-situ}$ becomes negative, we fix ${M_s}^{ex-situ} = 0$. In fact, several pieces of evidence (e.g., Bluck et al. 2012; López-Sanjuan et al. 2013; Conselice et al. 2013; Ferreras et al. 2014) show that galaxies do not assemble a significant fraction of their stellar masses by (dry) mergers; only the most massive ones seem to have acquired up to 30-50 % of their present-day masses by mergers since $z \sim 2 - 1$. Therefore, the term due to ex-situ mass growth is not of special worry for us. We will take care that the parameters in eq. (2.17) are such that only for the most massive galaxies the fraction of the present-day M_s assembled by this mode attains relatively significant values but not larger than $\sim 50\,\%$; for the smaller masses, these fractions are expected to be so small that accurate constrains to the parameters are not of relevance.

Our procedure starts by selecting a given individual average halo MAH taken from the Fakhouri, Ma & Boylan-Kolchin (2010) fits. Then, we fix an initial epoch, at a high redshift, and from that epoch we calculate the halo mass accretion rate at each redshift, $\dot{M}_{DM}(M_{\rm v}, z)$, according to eq. (2.3). Given $\dot{M}_{DM}(M_{\rm v}, z)$, we calculate the corresponding

[5]This factor, called also the recycling factor and denoted as R in the literature, takes into account the mass loss during the stellar evolution due to different mechanisms such as stellar winds and SN ejection.

SFR at each z (eq. 2.4) as well as the total stellar mass growth rate (eq. 2.14) given by the in-situ (eq. 2.15) and ex-situ (eq.2.17) contributions. By integrating in time, we calculate the accumulated M_s up to a given z, i.e., we obtain the individual average stellar MAH corresponding to the average halo MAH. The above described procedure is applied to a mesh of halo MAHs that today end with masses from 10^{10} to 10^{14} $M_\odot$. Therefore, we are able to calculate several relations at any epoch (isochrones), for instance, the F_s–M_v and sSFR–M_s relations, $F_s(M_\mathrm{v};\, z)$ and sSFR(M_s; z), respectively. *The free parameters in the toy model are namely constrained in order that these relations at different redshifts were reproduced.*

Besides, by using the ΛCDM halo mass functions at each epoch, we calculate the comoving number density of galaxies of any mass at any epoch associated to their halos. The halo mass function can be written as

$$M_\mathrm{v}\frac{dn}{dM_\mathrm{v}} = \Omega_{m0}\rho_{cr,0}\frac{d\sigma(M_\mathrm{v})}{\sigma(M_\mathrm{v})dM_\mathrm{v}}f(\sigma), \tag{2.18}$$

where $\sigma(M)$ is the rms mass density fluctuation computed by integrating the power spectrum of perturbations, $P(k)$. We use the approximations for $\sigma(M)$ and $f(\sigma)$ given for the cosmological parameters of the Bolshoi simulation (see appendix B in Klypin, Trujillo-Gomez & Primack 2011). The shape of $f(\sigma)$ is given by the Sheth-Tormen function (Sheth & Tormen 2002). Since each halo of mass M_v at each epoch z has an associated galaxy described by its stellar mass M_s and SFR, through the halo mass function, we can calculate the comoving abundances of galaxies by their M_s (the galaxy stellar mass function, $GSMF$) or SFR. By integrating in mass, we calculate then the total comoving SFR and stellar mass (SM) densities and their changes with z. Thus, the observed *cosmic SF history is also used to constrain the values of the model parameters.*

2.4. Connections between the two relations

By means of the parametric "toy" model described above we are able to explore the (evolutionary) connection between the sSFR(M_s; z) and $F_s(M_\mathrm{v};\, z)$ (or $M_s[M_\mathrm{v};\, z]$) relations. Recall that the semi-empirical inferences of how the F_s–M_v relation does change with redshift is yet a matter of debate (see Section 2.1.3). From the most general point of view, one can bracket most of cases between that we call the "low-evolution" and "high-evolution" regimes, according to the rate at which changes the low-mass side of the F_s–M_v relation (from the maximum in F_s towards lower masses) across the cosmic time. We will explore how these two regimes are connected to the sSFR–M_s relation and its change with z.

Our first exercise is to reproduce the observed sSFR(M_s; z) relations, in particular the one at $z \sim 0$, not taking into account the $F_s(M_\mathrm{v};\, z)$ relations for constraining the model parameters. In this way, we explore the effects of the sSFR(M_s; z) function on the $F_s(M_\mathrm{v};$

z) function. In the upper panel of Figure 2.5, we show with blue solid lines our model results, which were constrained to reproduce the observational sSFR–M_s relation for all galaxies given in Salim et al. (2007) at $z \approx 0$ (grey solid line for the average and dotted lines for the 1σ scatter in the case of only star forming galaxies, and gray dashed line for the average of all the galaxies), as well as this relation for all galaxies at higher redshifts (z =0.5,1.0, and 2.0) as given in Bell et al. (2007); Bauer et al. (2011); Karim et al. (2011) (black circles and grey solid lines as indicated inside the panels). We also reproduce the recent observational determinations of the sSFR(M_s; z) relations for only star-forming galaxies by Speagle et al. (2014, black dashed lines surrounded by a grey band); at low masses, by far most of galaxies are star forming.

In the bottom panels of Figure 2.5, we plot the corresponding model $F_s(M_{\rm v}; z)$ relations (blue solid lines). They evolve strongly in the low-mass side. For comparison, we plot the semi-empirical $F_s(M_{\rm v}; z)$ function given in Firmani & Avila-Reese (2010), based on the Behroozi, Conroy & Wechsler (2010) results (black long-dashed lines). As discussed in Section 2.1.3, this function represents a moderate evolution for the M_s–$M_{\rm v}$ relation as compared to others in the literature. Determinations that show a strong evolution of the F_s–$M_{\rm v}$ relation are, for instance, those of Yang et al. (2012) and Moster, Naab & White (2013) (see Fig. 2.3 above). The strong low-mass side evolution of the model F_s–$M_{\rm v}$ relation is necessary in order to reproduce the sSFR(M_s,z) relations at low redshifts. In particular, after many experiments, we have concluded that in order to reproduce the increase at low masses of the sSFR at low redshifts, the stellar mass of low–mass galaxies should grow very rapidly since $z \sim 1.0$ in such a way that the M_s-to-$M_{\rm v}$ ratio ($\equiv F_s$) increases much faster than the corresponding $M_{\rm v}$ growth. This produces a significant increasing with time of the low-mass side of the F_s–$M_{\rm v}$ relation, giving rise even to a bend in the relation for halos with $log(M_{\rm v}/M_{\odot}) < 11.0$.

The high-evolution model, aimed to reproduce the observed sSFR(M_s; z) relations, implies also a moderate shift of the F_s peak to lower halo masses as z decreases, as well as an increasing of the value of F_s for masses around and larger the one corresponding to the peak. The peaks in this model are related to the bending at high masses of the sSFR–M_s relations; the mass at which the bending happens decreases as z is lower. The model predicts relatively high amplitudes in the high-mass end of the F_s–$M_{\rm v}$ relation since $z \sim 2$. This is because we attempt to fit the massive end of the observed sSFR–M_s relations. While there is a clear bending at these masses, it seems that is not enough as to avoid that the stellar mass grew up by in-situ SF in massive halos ending with relatively high values of F_s in the high-mass side of the F_s–$M_{\rm v}$ relation.

As discussed in Section 2.1.3, there are some semi-empirical inferences of the $M_s(M_{\rm v}$; z) relations that change little with z and can be regarded as the low-evolution case (Behroozi, Wechsler & Conroy 2013a,b). We use again our model to explore this case. The results are represented by the black curves in Figure 2.5. This model is in rough agreement

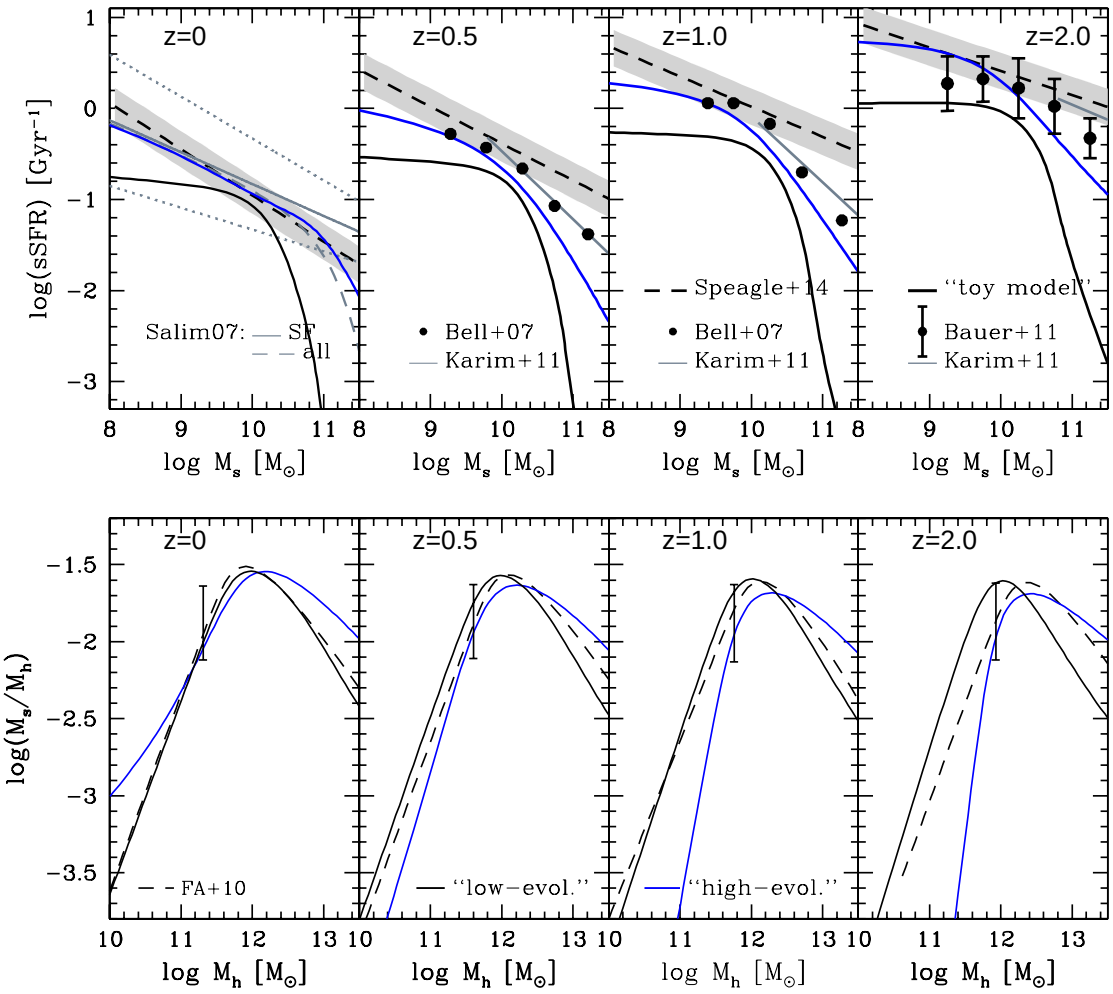

Figura 2.5: *Upper panels:* sSFR as a function of M_s for $z = 0$, 0.5, 1.0 and, 2.0. Black (blue) solid lines is for the model which parameters have been adjusted to reproduce the behavior of a low-evolution (high-evolution) M_s–$M_{\rm v}$ relation according to semi-empirical evidence discussed in Section 2.1.3. Observations are also shown. Note that the high-evolution model reproduces well them. *Bottom panels:* M_s–$M_{\rm v}$ ratios as function of $M_{\rm v}$ for the same z's given in the upper panels. The low (high)–evolution model is represented by black (blue) solid lines. Semi-empirical inferences given by Firmani & Avila-Reese (2010), which represent a "moderate-evolution" model, are plotted with black long-dashed lines. Note that the high-evolution model departs strongly from these semi-empirical inferences.

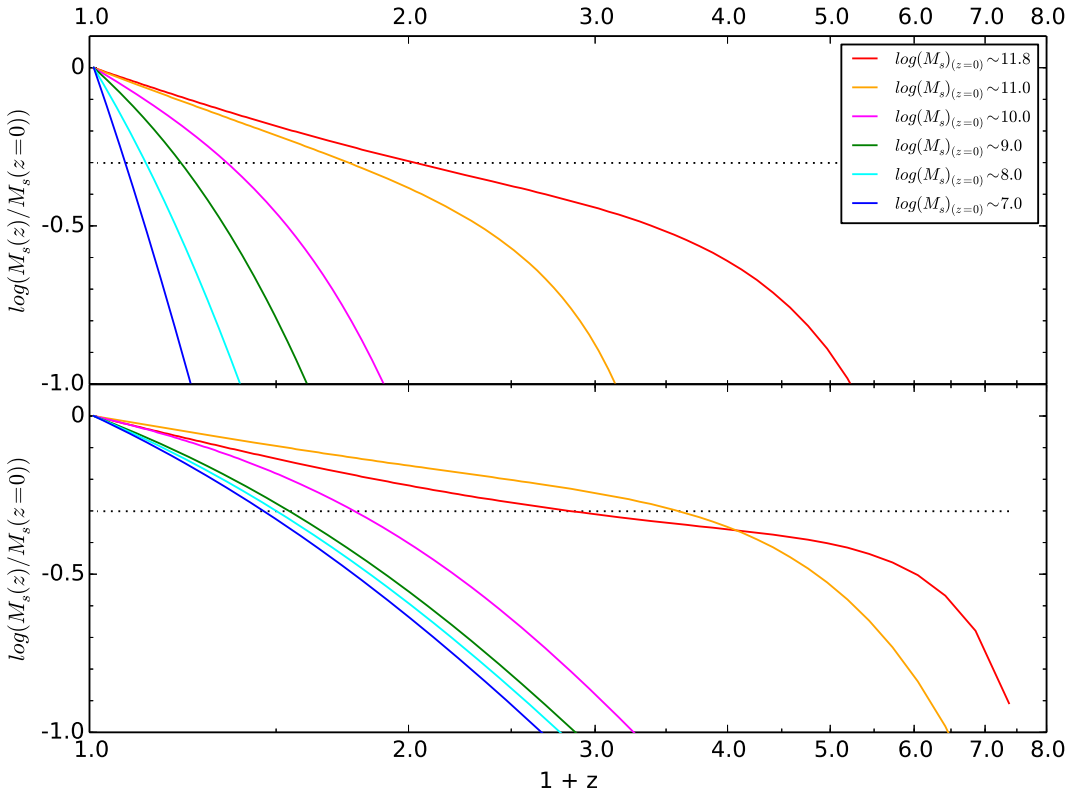

Figura 2.6: Stellar MAHs normalized to their mass at $z = 0$. The corresponding present-day masses are indicated in the inset. *Upper panel:* for the high-evolution model. *Lower panel:* for the low-evolution model.

with the results presented by Behroozi, Wechsler & Conroy (2013b) up to $z \sim 2$, except for the bend at the lowest masses obtained by these authors, and it evolves slightly less than the function provided by Firmani & Avila-Reese (2010). Under our parametrization, this case of low-evolution in the F_s–$M_{\rm v}$ relation is in conflict with the observed sSFR–M_s relations at different z's (see Figure 2.5): the predicted relations are too flat for galaxies smaller than $M_s < 10^{10}\ M_\odot$ since high redshifts, and the overall amplitude of the relations changes too little, as compared to the observations.

How are the individual average stellar MAHs of the high- and low-evolution cases presented above? Our model provides these histories or evolutionary tracks. Figure 2.6 shows the average M_s tracks for galaxies that end at $z = 0$ with $\log(M_s/M_\odot) \approx$ 7, 8, 9, 10, 11, and 12. In order to appreciate the differences in the shapes, the tracks were normalized to their present day M_s. The high- and low-evolution cases are shown in the top and bottom panels, respectively. The difference between these two cases is evident: the stellar masses in the low-evolution case are assembled much earlier than in the high-evolution case. For exam-

ple, the redshifts at which half the present-day masses were assembled for the mentioned above mass range are from $z \approx 0.5$ to 2 and from $z \approx 0.1$ to 1 for the former and latter cases, respectively (see the horizontal dotted lines in Fig. 2.6). The low-mass galaxies ($M_s < 10^{10}\ M_\odot$ at $z = 0$) that describe well the observed sSFR(M_s,z) relations (high-evolution case) assemble late and today are yet in their active growing phases, specially the smallest ones, while the corresponding galaxies in the low-evolution case, assemble earlier, being those of masses $M_s \sim 10^{10}\ M_\odot$ already in process of quenching.

2.4.1. Is there a conflict between the two relations?

The analysis of the two extreme cases presented above, show that, under our parametrization, there is a tight connection between the sSFR(M_s; z) and $M_s(M_\mathrm{v}; z)$ relations. By changing the results in one "plane", also change the results in the other "plane", in such a way that attempting to fit both set of observations seems to be a difficult task. Since the stellar mass M_s can grow also by the ex-situ mode, some detaching between both relations can be attained in the direction of having the possibility to increase M_s or F_s (by mergers) without increasing the SFR. However, the role that this mode plays is strongly constrained by observational inferences of the dry mergers rates. These inferences show that the stellar mass of galaxies did not grow significantly by dry mergers; only the most massive ones could have grown up to $\sim 30 - 50\,\%$ of their masses in dry mergers since $z \sim 1$. Even more, there are some pieces of evidence that the most massive galaxies, $M_s > 10^{11}\ M_s$, at $1.5 < z < 3$ assembled most of their stellar masses by gas accretion and consequent in-situ SF rather than by mergers (Conselice et al. 2013). Therefore, in our models we fix the parameters related to the ex-situ mode (see eq. 2.17) to values such that the most massive galaxies increased their M_s since $z \sim 1.5 - 2$ by no more than 50 %, decreasing with mass and z the role of this mode. Thus, *there is no room for significantly changing the $F_s(M_\mathrm{v}; z)$ relations (through the ex-situ mode) without changing significantly the sSFR(M_s; z) relations*.

With the ex-situ mode constrained to only a minor role in the growth of the stellar mass of galaxies, in particular the less massive ones, our results showed that the observed increasing of sSFR as M_s is smaller (downsizing in sSFR) can be attained only if the low-mass side of the F_s–M_s relation strongly increases since $z \sim 2$. This increasing is extremum, even as compared to those inferences of the $M_s(M_\mathrm{v}; z)$ relations that imply strong evolution. At this point, it should be said that both determinations of the sSFR and the $GSMF$ (necessary for inferring the M_s-to-M_v ratio) are uncertain at low masses and higher redshifts. Low-mass galaxies seem to have actually very bursty SFR histories both in observations (e.g., Kauffmann 2014) and simulations (González-Samaniego et al. 2014) so that the scatter around the means in the sSFR–M_s and F_s–M_v relations are expected to be large; this can introduce important biases in the observational samples used to determine these relations.

Another implication of the high-evolution model aimed to reproduce the observed

sSFR(M_s; z) relations since high redshifts, is that it implies relatively shallow F_s–$M_{\rm v}$ relations at their high-mass side at redshifts lower than $z \sim 1$ (blue solid lines in Fig. 2.5). This is because (i) galaxies below the peak mass grow significantly by in-situ SF, becoming later more massive than the peak mass and with relatively high value of F_s, and (ii) because the bending at the highest masses in the observed sSFR–M_s relations at high redshifts seems not to be too strong, in such a way that these galaxies grow yet significantly by in-situ SFR, having then at $z \rightarrow 0$ relatively high values of F_s. As shown for the low-evolution case, the F_s–$M_{\rm v}$ relation at its high-mass side can be kept steeply decreasing if the sSFR–M_s relations strongly decrease at high masses (strong bending; black solid lines in Fig. 2.5). At this point, we note that it could be that the observational determinations of the sSFR–M_s relation at high redshifts is biased to star forming galaxies. If this is the case, then the mean or median values reported in the observational works do not take into account the possible presence of passive, quenched galaxies, which tend to be massive, being then these values higher than the real mean or median. Recently, Hayward et al. (2014) have shown also that inferences of the SFR based on IR luminosities may be highly overestimated (up to two orders of magnitude) in (massive) post-starbust galaxies. The reason for this overestimation is that although the SFR decreases rapidly from its maximum, there is still significant IR emission from dust heated by the stars formed during, and even before, the starburst. The magnitude of the overestimate is greater for lower sSFR values. As the authors write, "this overestimation may have significant implications for e.g. the SFR-M_s relation. In particular, it may cause the number of quenched galaxies and degree to which galaxies are quenched to be underestimated". The overestimation, as the authors discuss, applies even when UV is added to IR as a tracer of the SFR.

On the other hand, it should be said that the high-mass end of the local $GSMF$ seems to have a shallower decay than previously thought, which would imply a shallower F_s–$M_{\rm v}$ relation at the high-mass end. This is because, as several recent studies have pointed out, there is a systematical underestimation of luminosity and stellar mass-to-light ratios of large galaxies due to the commonly used aperture limits in the SDSS (see Bernardi et al. 2013, and more references therein; see also Mendel et al. 2014). Surface brightness (mass) profiles of galaxies, in particular the central ones in clusters, extend much further away than the commonly used apertures (Kravtsov, Vikhlinin & Meshscheryakov 2014, and more references therein). In Bernardi et al. (2013), luminosity and stellar mass functions were calculated based on different model fits for the surface brightness profiles in the SDSS galaxies. The authors showed that their results preferred $GSMF$s with the most luminous galaxies having larger masses for a given number density than most of the previous published mass functions. Similar conclusions were obtained in He et al. (2013) based on a more sophisticated photometric data reduction from the SDSS DR7 and with morphological classifications from the Galaxy Zoo project (Lintott et al. 2011). Kravtsov, Vikhlinin & Meshscheryakov (2014) have confirmed this by using a compilation of well studied massive central cluster galaxies. These authors have applied the Abundance Matching Technique to their "corrected" at high masses $GSMF$, and inferred the local F_s–$M_{\rm v}$ relation. As

expected, it is shallower at the high-mass end than previous ones.

2.5. Semi-empirical inferences of halo/galaxy mass assembly

The parametric "toy" model presented in Section 2.3.2 allowed us to explore the general connection between the (semi)empirical sSFR(M_s; z) and $M_s(M_{\rm v}; z)$ relations, as well as with the cosmic SFR density (SFRD) and the stellar mass density (SMD) histories. From the analysis carried out in Section 2.4, we conclude that it is difficult to make compatible a given inference of the $M_s(M_{\rm v}; z)$ relations with a given set of observed sSFR(M_s; z) relations and viceversa. We have remarked the main incompatibilities and discussed that they happen at masses, redshifts, and particular objects, where the observational uncertainties can be yet large. Having in mind these uncertainties, we constrain the model parameters in order the model results are consistent with most of the inferences of the average sSFR–M_s and M_s–$M_{\rm v}$ relations at different redshifts as well as with the cosmic SFRD and SMD histories. Note that we do not carry out any formal fitting procedure in order to constrain the best model parameters. Our main criteria for constraining this fiducial model are:

- to reproduce the main trends of the different determinations of the sSFR–M_s relations for all galaxies up to $z \sim 2-3$ and in the $\log(M_s/M_\odot) \approx 9.5-10.5$ range (see the discussion in Section 2.4.1 on caveats for smaller masses, even at $z \sim 0$, and for larger masses at high redshifts);

- to reproduce the main trends of the M_s–$M_{\rm v}$ relations up to $z \sim 3$; since there are actually different inferences of these relations, we choose relations that are in between the cases of low and high evolution (see previous Section), and we do not pay too much attention to the lowest- and highest-mass ends due to several uncertain aspects discussed above;

- to be in agreement with most of the determinations of the cosmic SFRD and SMD at different redshifts.

From a conceptual point of view, we require also that the "galaxy SF efficiencies" as a function of $M_{\rm v}$ (the function $G_{\rm SFE}[M_{\rm v},z]$) started at very high redshifts ($z \sim 7$) being roughly flat at masses larger than $M_{\rm v} \sim 5 \times 10^{10}\ M_\odot$ since there is no a known physical process able to inhibit gas accretion, wet mergers, and bursts of SF in collapsing massive halos at these epochs, halos that are actually very rare and assemble likely through violent major mergers. With the time passing, the SF in most massive halos start to be less efficient due to the long radiative cooling times of the heated gas during the halo assembly, and due to the positive feedback of the AGNs in their quasar phase.

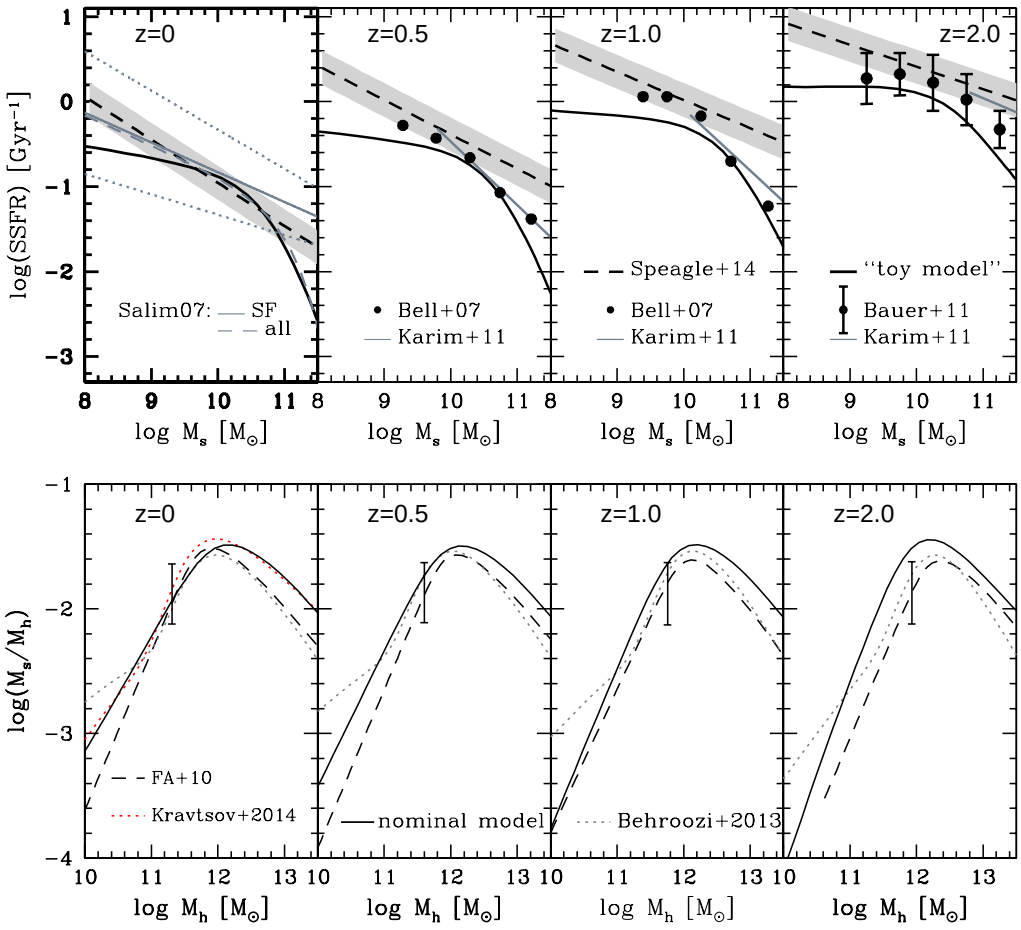

Figura 2.7: Same as Figure 2.5, but for our fiducial model. The semi-empirical inferences by Firmani & Avila-Reese (2010), and Behroozi, Wechsler & Conroy (2013b) are shown in the lower panel. For $z = 0$, the recent inference by Kravtsov, Vikhlinin & Meshscheryakov (2014) (red dotted line) using corrected stellar masses in the $GSMF$ due to aperture issues, is also shown.

The model parameters that we find as optimum for obeying these criteria are presented in Table 2.2. Figure 2.7 shows the sSFR–M_s (upper panels) and M_s–$M_{\rm v}$ relations (lower panels) at four redshifts and compared to some (semi)empirical inferences, as indicated inside the panels. The "toy" model is in reasonable agreement with the sSFR(M_s; z) determinations at different redshifts, in particular at $z \sim 0$. As discussed in the previous Section, in order to roughly reproduce the increasing of sSFR as M_s is smaller at low

Cuadro 2.2: Parameters Model

"Fiducial"	α_0	α_1	β_0	β_1	ϵ_0	ϵ_1	M_0	M_{1z}	a_0	b
Nominal	0.58	1.7	1.7	0.21	0.4	0.1	7.2	-0.3	0.001	0.5

redshifts, significant evolution of the low-mass end of the M_s–$M_{\rm v}$ relation is necessary. For our fiducial model, this low-mass end evolves, since $z \sim 2$, faster than the corresponding to the Behroozi, Wechsler & Conroy (2013b) but slower than other determinations, and it is roughly similar to the Firmani & Avila-Reese (2010) function. Note also that the model reproduces the trend of flattening in the low-mass side of the sSFR–M_s relation as z increases.

At higher z's, the model sSFR decreases more steeply at high masses than the observational determinations; otherwise, the high-mass end of the M_s–$M_{\rm v}$ relation becomes too high and shallow as compared to most of the semi-empirical determinations. It is likely that the $GSMF$s at high masses, which are used to infer the M_s–$M_{\rm v}$ relations, are better constrained at high z's than the high-mass end of the sSFR–M_s relation (see a discussion in Section 2.4.1). Even that, the high-mass ends of the model $M_s(M_{\rm v}; z)$ relations are higher and shallower than most of the semi-empirical determinations. However, at this point it is important to recall that recent studies show that the luminosities and stellar masses of the luminous galaxies seem to have been underestimated due to inaccurate photometric profile fits (see Section 2.4.1 for an explanation of this problem and the references); massive galaxies, in particular those in the center of groups and clusters, have large stellar halos, which typically are not taken into account due to their low-surface brightness. For local galaxies, Kravtsov, Vikhlinin & Meshscheryakov (2014) have taken into account the corresponding corrections to the stellar masses of luminous galaxies and inferred the M_s–$M_{\rm v}$ relation by means of the Abundance Matching Technique. We reproduce their results in Fig. 2.7 (red dotted line). Our fiducial model is in good agreement with this inference.

2.5.1. Individual average evolutionary tracks

The average stellar MAHs of our fiducial model show a pronounced detachment from their corresponding halo MAHs at low and high masses. In the upper panel of Fig. 2.8, we plot these MAHs for three tracks, which end today with $M_{\rm v}$= 10^{10} (black lines), 2.5×10^{12} (magenta lines) and 10^{14} $M_\odot$ (red lines). The solid lines are for the stellar MAHs while the dashed lines are for for the halo MAHs. Both are normalized to their respective halo or stellar mass at $z = 0$. The horizontal dotted line indicates the redshift when half the respective present-day mass has been acquired, $z_{1/2}$. For the lowest-mass object, while the halo assembles early ($z_{1/2} \approx 1.8$), the stellar mass assemble very late ($z_{1/2} \approx 0.3$), i.e., the galaxy growth is strongly delayed with respect to the halo one. The opposite happens for the highest-mass object, that is, the galaxy stellar mass assembles early ($z_{1/2} \approx 2$), while

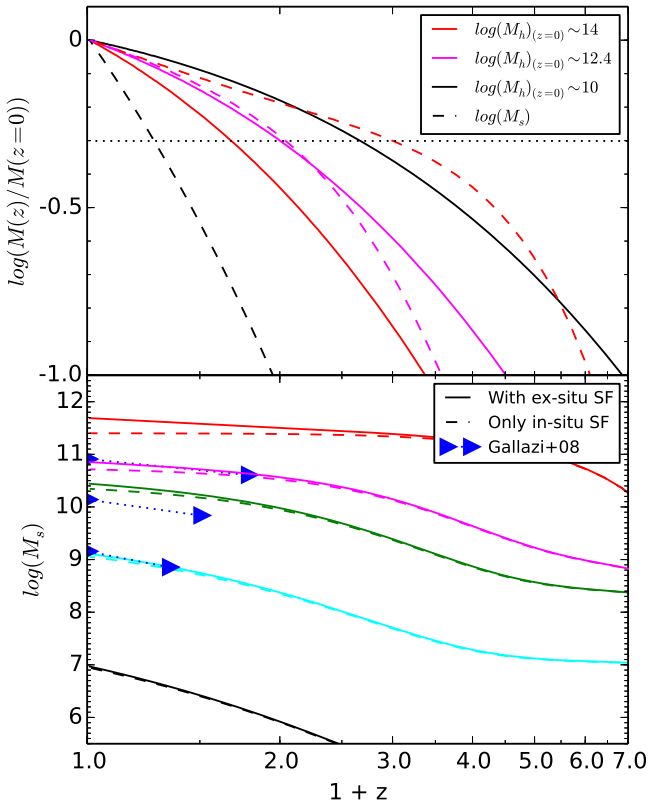

Figura 2.8: *Upper panel:* Three halo and stellar MAHs normalized to their masses at $z = 0$ for our fiducial model (solid and long-dashed lines, respectively). The present-day halo masses of the halos are indicated in the inset. While the the stellar MAH follows closely the halo MAH for the intermedium-mass halo, the stellar MAHs deviate to an earlier (later) assembly for the high-(low-)mass halo. *Lower panel:* Stellar MAHs for the fiducial model (solid lines). The long-dashed lines represent the stellar MAHs considering only the in-situ (star formation) growth mode. The blue dotted lines join the triangles, which represent the average stellar mass at $z = 0$ of SDSS galaxies reported in Gallazzi et al. (2008), and their respective $z_{1/2}$, the epoch when galaxies acquired half of their current stellar mass, obtained from stellar population synthesis (archeological) studies.

the halo mass continues growing actively ($z_{1/2} \approx 0.7$). For the intermedium mass object, both the stellar and halo MAHs are much less detached than for lower- and higher-mass objects. The assembly of galaxies in halos around $M_{\rm v} = 1 - 3 \times 10^{12}\ M_{\odot}$ does not depart significantly from the one of their halos; for example, for the $M_{\rm v} = 2.5 \times 10^{12}\ M_{\odot}$ halo, the stellar and halo half masses are attained roughly at the same redshift ($z_{1/2} \approx 1$).

In the lower panel of Fig. 2.8, we present the stellar MAHs for several average tracks that end at $z = 0$ with masses in between $M_s = 10^7$ and $10^{12}\ M_{\odot}$. The solid lines are

for the total stellar masses (assembled by the in-situ and ex-situ modes), while the dashed lines are for only the in-situ mode. The ex-situ mode (mergers) has no contribution to the M_s growth of the low-mass model galaxies. For the most massive ones, it can contribute up to $\sim 50\,\%$ of the present-day mass and it starts to contribute only since $z \sim 2$. The high-mass side of the semi-empirical $M_s(M_{\rm v}, z)$ relations constrain the ex-situ mode; if this mode is allowed to contribute more, then the model would produce too high values of F_s at large masses, increasing with time, something that would be already in large tension with the semi-empirical inferences. On the other hand, the observational inferences of the merging rate contributions to the growth of galaxies show that these contributions are relevant only for massive galaxies, being responsable for up to half of their present-day masses.

In the lower panel of Fig. 2.8, we reproduce the results of Gallazzi et al. (2008), who inferred by means of stellar population synthesis ("archaeological") reconstruction the average epochs at which local galaxies from the SDSS survey assembled half of their stellar masses. The blue triangles connected with a dotted line show their results for three masses. The MAHs of the fiducial model that are close to these masses follow the same behavior as in Gallazzi et al. (2008). This shows that our results are consistent in general with the "archeological" inferences, at least in the mass range given in Gallazzi et al. (2008), which we extend to lower and higher masses.

In the upper panel of Fig. 2.9, the average SF histories (in-situ mode) of our fiducial model are plotted. High-mass galaxies ($M_s > 10^{11} M_\odot$ at $z = 0$, orange and red lines), had an early phase of active SF (possible in a violent regime) and then, since $z \sim 3$, show a strong exponential decline in their SFRs (quenching). Intermediate-mass galaxies ($10^{10} \lesssim M_s/M_\odot \lesssim 10^{11}$, green and pink lines) show a sustained rise in their SFRs up to ~ 2 and then a weak exponential decline. Low-mass galaxies ($M_s \lesssim 10^{10} M_\odot$, black and cyan lines) have rising SF histories, i.e., they did not attain a maximum, and at $z = 0$ are yet in their active growth phase, more as the less massive is the galaxy (downsizing in sSFR). For galaxies larger than $M_s \sim 10^{10}\ M_\odot$, the larger the galaxy, the earlier attain their peak SFR ("archeological downsizing"). It is interesting to note that the commonly used τ model for the SF histories of galaxies (exponential declining SF histories with different widths), *seems not to be adequate for low-mass galaxies*. This has been actually noted in Pacifici et al. (2013) by applying sophisticated stellar population synthesis models to the spectral energy distribution of blue galaxies in a large mass range at $0.2 < z < 1.4$.

In the lower panel of Fig. 2.9, we compare the observed change of the sSFR of galaxies with redshift to our results. In fact, these observations, obviously, did not refer to the evolution of individual galaxies. Instead, they show how the SFR or sSFR change with z for a fixed stellar mass bin, which is the same at all z's. The blue and black symbols refer to observations in the mass bins around $M_s \sim 5 \times 10^9$ and $\sim 5 \times 10^{10} M_\odot$, respectively, except for the Salim et al. (2007) data at $z \sim 0$, which are the strongest constraints to our model in the sSFR–M_s plane (showed with red triangles). The authors of the different

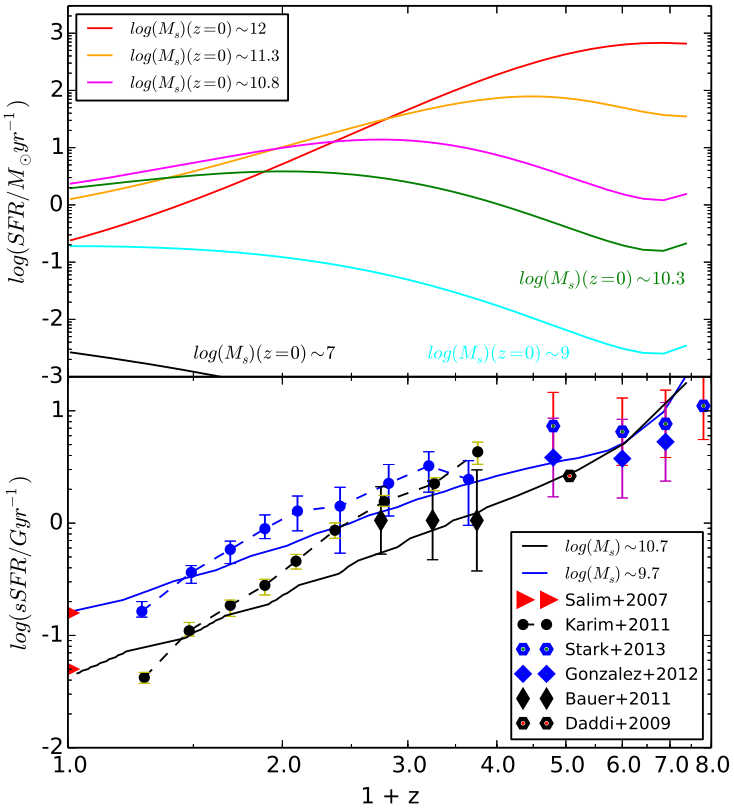

Figura 2.9: *Upper panel:* Individual average SF histories that end at $z = 0$ with the masses indicated in the inset. While massive galaxies have a clear declining SF histories, low-mass galaxies have rising SF histories. *Lower panel:* The sSFR at different z for galaxies with a fixed mass at all epochs, $M_s \sim 5 \times 10^9$ (blue line) and $5 \times 10^{10} M_\odot$ (black line). Blue and black symbols are the respective observational data at different z's given by different authors as labeled in the inset. Red triangles correspond to the observational results from Salim et al. (2007) at $z \sim 0$ for these M_s.

determinations are indicated in the inset. The blue and black lines are the sSFRs of our model galaxies with fixed masses $M_s = 5 \times 10^9$ and $5 \times 10^{10} M_\odot$ at each z, respectively (recall that these are not evolutionary tracks). For the low-mass bin, the agreement with observations is remarkable, even at the highest redshifts, $z \sim 6$. For the high-mass bin, the sSFR of the model are lower than those of Karim et al. (2011) at $z > 1$ (stacking technique with radio observations) but agree roughly with those of Bauer et al. (2011) (UV corrected by dust + infrared data) and Daddi et al. (2009) (radio observations + infrared data).

In Fig. 2.10, the sSFR–M_s relations at different redshifts (color solid lines; isochrones) together with some *individual* average tracks in this plane (dotted lines) are plotted. We see that for very massive galaxies, M_s only slightly increases as z is lower, while the sSFR

strongly decreases, i.e., these galaxies quench, the earlier, the more massive they are (archeological quenching). For these cases, due to the almost constancy of M_s with time (up to $z \sim 2-3$), an observational plot like the lower panel of Fig. 2.9 can be interpreted as the evolution of the sSFR of individual galaxies. However, for lower-mass galaxies, the stellar mass evolution is strong in such a way that the sSFR at a fixed M_s at all z's is far from the individual evolution of galaxies. Galaxies smaller than $\sim 10^{10}$ $M_\odot$ today are yet in their active M_s growth by in-situ SF, the smaller they are, the more active they look (this is the downsizing in sSFR).

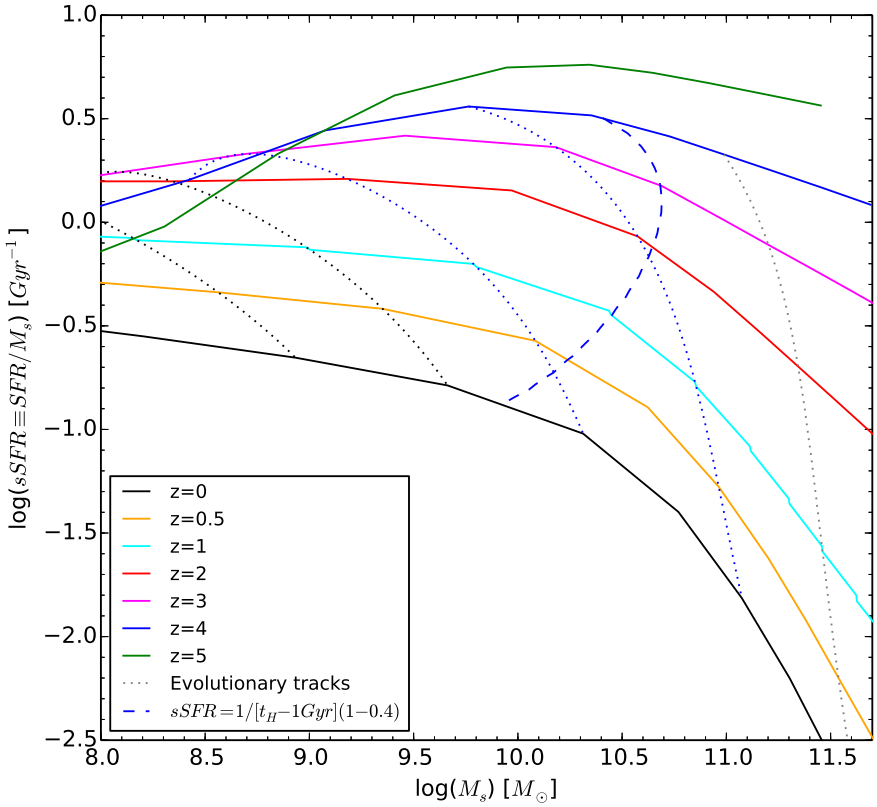

Figura 2.10: Specific star formation rate as function of M_s at different redshifts (isochrones; colored solid lines). Individual average evolutionary tracks are shown with dotted lines. The blue long-dashed line mark the mass at each z that meats the criterion of starting to be quenched, $M_{\rm trans}$ (see text).

We can attempt to quantify the level of SF activity of a galaxy at a given epoch by introducing the time-averaged sSFR in the case of constant SFR:

$$< \text{sSFR} > (z) = \frac{SFR(t[z])}{\int_{t_i}^{t(z)} SFR(t')(1-R)dt'} \approx \frac{1}{(1-R))[t(z)-1]} \qquad (2.19)$$

where R is the stellar mass loss factor and $t(z)$ is the cosmic time as a function of z, given

in Gyr. In eq. (2.19) we considered that the onset of galaxy formation started 1 Gyr after the Big Bang, $t_i = 1$. The average specific star formation rate in this case, $<$ sSFR $>(z)$, is universal, it depends only on the cosmic time. It should be considered just as a model-independent criterion for defining active/passive galaxies. In order to keep this universality and simplicity, we assume that R is constant and equal on average to 0.4. A galaxy with a sSFR at a given z larger (smaller) than $<$ sSFR $>(z)$ is currently forming stars at a rate higher (lower) than the past average of the SFR=const. case, and can be considered it as actively star forming (passive). Hence, we can define the epoch at which a galaxy is transiting from the active to passive mode of growth by SF as that z when its current average sSFR is equal to $<$ sSFR $>(z)$. We define the stellar mass at that epoch as the transition mass, $M_{\rm trans}$. The dashed blue line in Fig. 2.10 indicates the sSFR at each epoch that is equal to $<$ sSFR $>(z)$ and the corresponding mass, $M_{\rm trans}$. This mass grows with z up to $z \sim 2.5$, where it attains a maximum, and then it declines at higher z's. Galaxies much larger at a given z than $M_{\rm trans}(z)$ are expected to be red and death, and those smaller are yet in their active phase of growth by in-situ SF.

2.5.2. Cosmic SFR and SM density histories

As explained in Section 2.3.2, we are able to convolve the model halo MAHs (with their respective galaxies) and the halo mass function at different redshifts in such a way that we obtain the comoving abundances of galaxies as a function of M_s or SFR. By integrating this abundances at a given epoch, we calculate the average comoving SFR and stellar mass (SM) densities at each z. In fact, one of the criteria to constrain the fiducial model was to reproduce the main trends of the observed cosmic SFR and SM density histories. A compilation of data related to the cosmic SF history, mainly extracted from Madau & Dickinson (2014), was presented in Section 2.1.2. In the upper panel of Fig. 2.11 we reproduce this compilation and plot the cosmic SF history from the fiducial model (blue line). The corresponding cosmic SM density history is plotted in the lower panel, along with the corresponding observations as compiled also in Madau & Dickinson (2014). The red line in the upper panel of Figure 2.11 represents the corresponding baryonic accretion rate density across cosmic time for our fiducial model (by construction, it is proportional to the dark matter accretion rate).

Interestingly, since the epoch in which the SFR density peaks up to the present day, it has the same declining as z is smaller than the baryonic accretion rate density. At high redshift, $z > 3$, while the baryonic accretion rate density continues increasing, the SFR density strongly decreases. If we divide the cosmic baryonic accretion rate by the SF rate, then we obtain the global (per comoving volume unit) SFE at each epoch, i.e. the cosmic efficiency of making stars (and of inhibiting this process due to feedback effects) from the cosmologically accreted gas. The result is that *since $z \sim 3$ the global or cosmic SFE is $\approx$ 10 % and constant*. At higher redshifts, this global efficiency decreases, being ≈ 2 % at $z = 5$; the bulk galaxy and SF processes did not take place yet at this epoch.

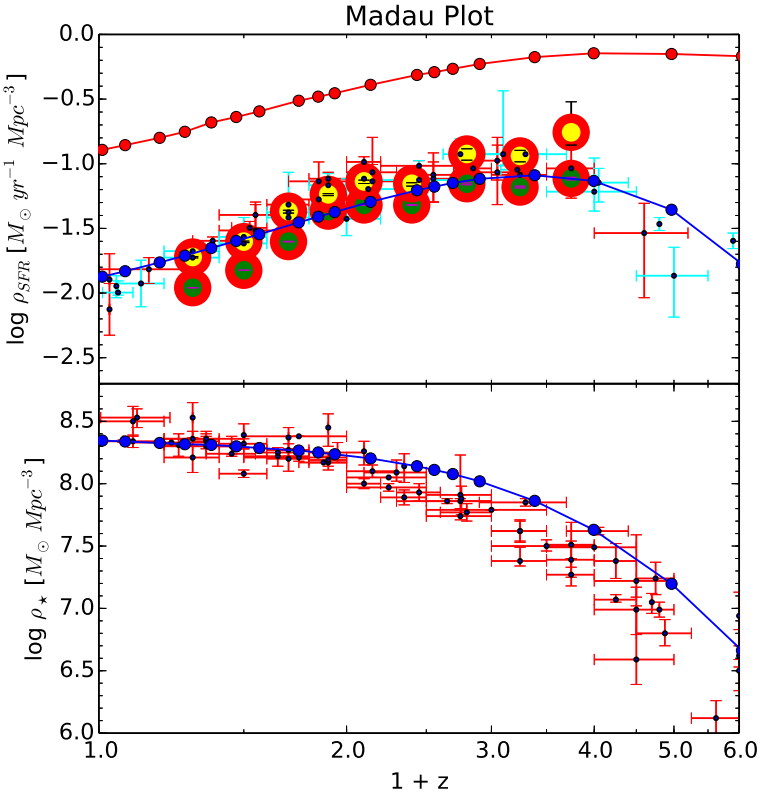

Figura 2.11: *Upper panel:* SFR density as a function of z (cosmic SF history; blue solid line) and the corresponding baryonic accretion rate density history (red line). Observational data obtained by UV (infrared) tracers as compilled by Madau & Dickinson (2014) are plotted with cyan (red) error bars. Green circles are the observational inferences obtained by Karim et al. (2011) by considering only the data up to where the sample is complete. The yellow circles are the respective results by considering data extrapolated to low masses, where its sample is not complete. *Lower panel:* Stellar mass density as a function of z, blue solid line. Observational data compiled by Madau & Dickinson (2014) are plotted with red error bars.

As seen in Fig. 2.11, overall the fiducial model resembles the general features of the observed cosmic SF history. In particular, it reproduces the peak of the SFR density at $z \sim 2.5$. At high redshifts, $z > 3$, the model is consistent with the yet uncertain observations. However, the SFR densities at $1 < z < 3$ are lower than most of the observational determinations and it declines since its peak to $z \sim 0$ less than them (by ≈ 0.7 dex vs ≈ 1.2 dex). On the other hand, the model SM density at different z are also in rough agreement with the main trends of the observed SM density history, though for $z > 1$ it is slightly above the observations (by ~ 0.2 dex on average) and at $z \sim 0$ it is slightly below the

observations (by ~ 0.2 dex). This situation shows the apparent incompatibility between the cosmic SFR and SM density histories at the level of the observations (similar as discussed above between the sSFR(M_s; z) and $M_s(M_{\rm v}; z)$ relations). If we increase the SF efficiency of the model galaxies in order to be in better agreement with the cosmic SFR history at $1 < z < 3$, then the SM density history down to $z \sim 1$ results already too high with respect to observations. Our fiducial model is a compromise case, as it was discussed above.

In fact, several authors noted already that passing from the observed cosmic SFR history to the cosmic SM history produces SM densities at high redshifts larger than those inferred from the observed $GSMF$s at these redshifts. A possible solution to this problem has been proposed to be a top-heavy stellar Initial Mass Function (IMF) in (massive) galaxies at high redshifts. Another effect that may attenuate this problem is the mentioned above results of Hayward et al. (2014) for those inferences of the SFR that make use of IR luminosity. In any case, from their observational compilation and homogenization, Madau & Dickinson (2014) discuss that the apparent discrepancy between the cosmic SFR and SM density histories is present but it is less severe than in previous works. *By means of our evolutionary semi-empirical model, we confirm this discrepancy and extend it to the sSFR(M_s; z) and $M_{\rm v}(M_s; z)$ relations.*

An interesting question is the *dissection of the cosmic SF history by mass* (both stellar and halo masses). What galaxies/halos are contributing more to the global SFR density at each epoch? In the left and and right panels of Fig. 2.12 we plot the contribution of different stellar and halo masses to the SFR density at z =0, 1, 2, 3, and 4, respectively. It is surprising that, *at any redshift, the galaxies that more contribute to the SFR density are those of stellar masses between* ≈ 1 *and* $3 \times 10^{10}\ M_\odot$ *and halo masses between* ≈ 3 *and* $10 \times 10^{11}\ M_\odot$. A combination of the abundances and SFRs of these halo/galaxy systems at each redshift conspires to make them the most important contributors to the SFR per comoving volume at all redshifts. The dissection by stellar mass tends to broaden with time towards the low-mass side, that is, as z is lower, the contribution of low-mass galaxies to the global SFR becomes more important; this is another way of enunciating the downsizing in SFR.

2.5.3. Galaxy SF efficiency through cosmic time

We have shown that our fiducial model is in general consistent with the sSFR–M_s and M_s–$M_{\rm v}$ (semi)empirical relations at different redshifts and with the observed cosmic SFR and SM densities histories, within the diversity of inferences that are in the literature, the scatters around the relations, and the observational uncertainties in the quantities involved in these relations. Since our evolutionary semi-empirical model is based on the connection between the baryonic (halo) mass accretion and star formation rates in ΛCDM halos of different masses across the cosmic time, it constrains in a explicit way the galaxy star formation efficiency, SFE, as a function of mass and time. This SFE, given by the function

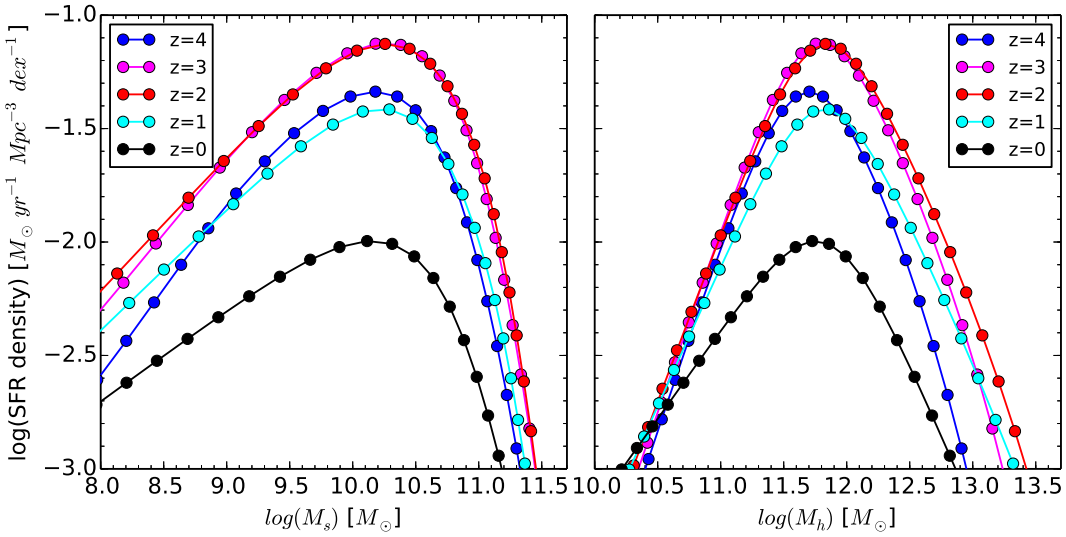

Figura 2.12: Dissection in stellar (left panel) and halo (right panel) mass of the SFR density at $z = 0$, 1, 2, 3, and 4. At all redshifts the stellar (halo) masses that more contribute to the current SFR density are those of $M_s \approx 1 - 3 \times 10^{10}\ M_\odot$ ($M_{\rm v} \approx 3 - 10 \times 10^{11}\ M_\odot$).

$G_{\rm SFE}(M_{\rm v},\ z)\equiv$(SFR/$\dot{M}_b$)($M_{\rm v}$,$z$), encodes the relevant astrophysical processes of galaxy formation and evolution inside the halos, as discussed in the Introduction and subsection 2.5.3. As we have mentioned therein, it has been common in the literature to interpret this galaxy SFE as equal or proportional to the F_s=$M_s/M_{\rm v}$ ratio, in such a way the the $M_s(M_{\rm v}; z)$ relations were used to directly constraint it. Our results are directly related to the galaxy SFE and allow us to infer key aspects of the overall process of galaxy assembly in the ΛCDM halos as a function of mass and time.

In Figure 2.13, we present both the mean $F_s(M_{\rm v})$ and $G_{\rm SFE}(M_{\rm v})$ functions constrained by our fiducial model at different redshifts (isochrones), from $z = 0$ to 6.[6] Even when they share common features and both can be approximated by two-power laws, the shapes in more details and the changes of the functions with z are quite different. Have in mind that the $F_s(M_{\rm v})$ relation is cumulative, while the function $G_{\rm SFE}(M_{\rm v})$ is instantaneous.

[6]We start our evolutionary tracks at $z = 7$. We have experimented with different initial redshifts and found that the results at $z \sim 5$ are already quite insensitive to the initial conditions.

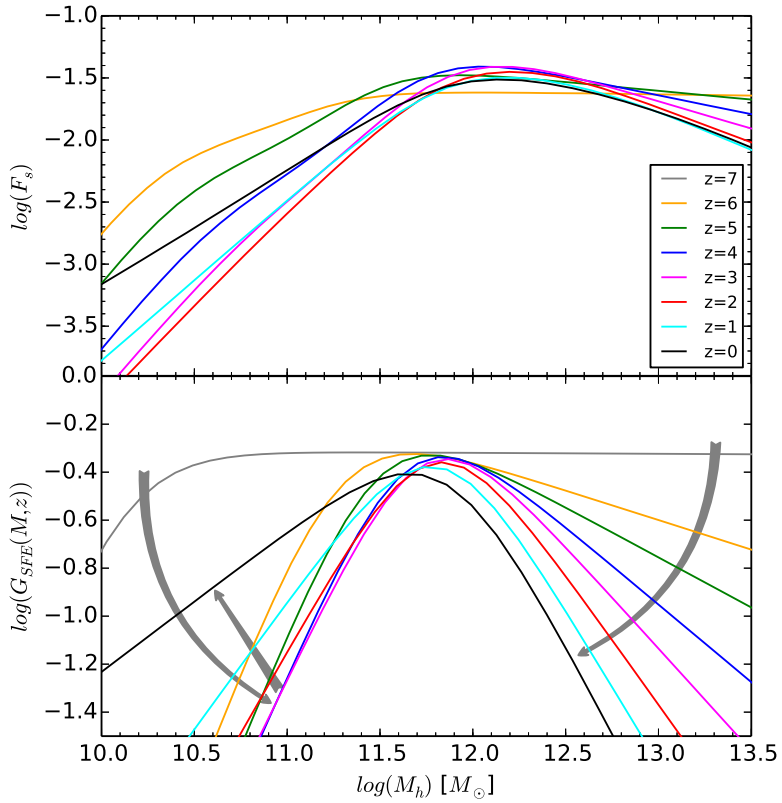

Figura 2.13: *Upper panel:* Stellar-to-halo mass ratio (F_s) as a function of $M_{\rm v}$ for $z = 0$ to 7 as was constrained in our fiducial model. *Lower panel:* The "best" constrained galaxy SFEs (the function $G_{\rm SFE}(M_{\rm v}$,z), eqs. 2.5–2.13) in our fiducial model. See Table 1 for the corresponding parameters.

From Fig. 2.13, we see that the $G_{\rm SFE}(M_{\rm v},\ z)$ functions reach their maxima at $\log(M_{\rm v}/M_{\odot})\approx$ 11.6–11.8, while the $F_s(M_{\rm v};\ z)$ relations attain their maxima at slightly larger masses. The maximum values of SFE at any epoch are around 0.5, that is, even in the most efficient cases, on average only half of the cosmologically accreted gas is transformed into stars "instantaneously". The low–mass side of both functions initially decreases with time down to $z \sim 3$ and 2, respectively. The average SFE in the low-mass halos decreases with time probably due to the SN-driven feedback after some galaxies had bursts of SF during the active halo mass assembly. The low-mass side of the $G_{\rm SFE}(M_{\rm v};\ z)$ function reverses its decreasing at $z \sim 3$, increasing now with time (see the arrows); the same happens in the $F_s(M_{\rm v};\ z)$ relation with some delay, since $z \sim 2$. This behavior is necessary for producing the downsizing in sSFR seen in the observations, and it could be because of a delay in the SFR of low-mass halos due to preventive stellar-feedback effects, no formation of H_2 molecule in low-metallicity, low-gas surface density galaxies, etc. (see

the Introduction for references). Once the halos and galaxies grow and the gas is enriched, then the SF proceeds lately.

Regarding the high–mass side, in the case of $G_{\rm SFE}(M_{\rm v},\, z)$, it significantly decreases with time, i.e., massive halos become less and less efficient in making stars as more massive they are (see the arrow; archeological downsizing). Since M_s is mainly the result of integrating the SFR (taking into account the mass loss factor), in the case of the F_s–$M_{\rm v}$ relation also is seen a decreasing of the F_s ratio at large masses with time, but the variation is small and even it slightly reverses towards $z = 0$, due to the progressive contribution of the ex-situ mode (mergers). Since $z \sim 2$ (the last ≈ 10.4 Gyr), the high-mass end of the F_s–$M_{\rm v}$ relation almost does not change, which implies that the halo/galaxy systems shift with time mainly along the relation. As showed in Fig. 2.8, this shift implies a slow growth of M_s as more massive are the galaxies, growth that is partially due to (dry) mergers and partially due to SF. Thus, the little change with z of the high-mass end of the $F_s(M_{\rm v};\, z)$ relations should not be interpreted as that massive halos have similar SFEs at all epochs; as seen in the lower panel of Fig. 2.13, the SFE of massive halos actually strongly changes (decreases) with time.

From the fiducial model, which reproduces many empirical inferences at different epochs, we can learn how are the average SFEs of galaxies as a function of halo mass at different epochs, as well as how the SFE of *individual* average systems does change with time. This is shown in Fig. 2.14, where color-coded iso-contours of SFE are plotted in the $M_{\rm v}$–cosmic time (or redshift) plane. We have added to this plot several average halo MAHs (dark dotted curves). The maximal SFE is on average for halos of $\approx 10^{12}$ $M_\odot$ at $z = 6$ and $\approx 5 \times 10^{11}$ $M_\odot$ at $z = 0$. Thus, *it is in the narrow halo mass range of* $0.5 - 1 \times 10^{12}$ $M_\odot$ *where the SFE is maximal at all epochs. For larger and lower halo masses, the SFE decreases.*

If we define "inefficient" halos as those with a SFE below 1 %, then we can find the minimal and maximal halo masses, below and above which, the SFE becomes inefficient, that is, less than 1 %, respectively. These masses are indicated with black dashed lines in Fig. 2.14. The maximal mass, $\rm M_{max}$, remains roughly constant up to $z \sim 2$ with a value of $\log(\rm M_{max}/M_\odot)\approx$13.2–13.6, and then it increases with z, attaining $\log(\rm M_{max}/M_\odot)\approx$ 14 and 14.7 at $z = 3$ and 4, respectively. At higher redshifts, at the onset of galaxy formation, all massive (very rare) halos have high (maximal) SFEs (see also Fig. 2.13). The minimal mass $\rm M_{min}$, decreases significantly with time. At $z = 4$, $\log(\rm M_{min}/M_\odot)\approx$ 10.5, while at $z = 0$, only halos below $\approx$ 8.7 are inefficient. This shows that *there is not a constant "floor"mass below which galaxies are inefficient* as proposed in Bouché et al. (2010b). Because of the downsizing in sSFR, with time smaller masses become relatively efficient in forming stars. For low masses, we see in Fig. 2.14 that for a fixed halo mass, the SFE increases with time. The opposite happens for massive halos, i.e., for a given halo mass, the SFE decreases with time. Similar results to our ones were found by Behroozi, Wechsler & Conroy (2013a).

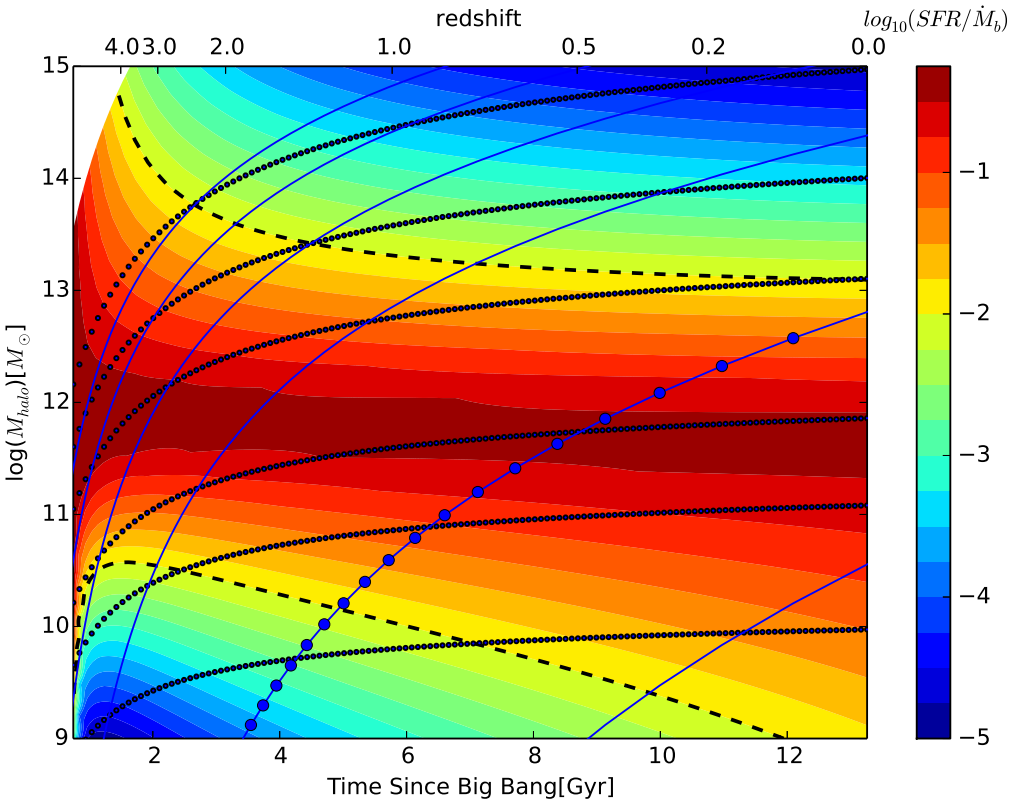

Figura 2.14: Average SFEs ($\equiv SFR/\dot{M}_b$) as a function of $M_{\rm v}$ and z. The SFE is plotted as color-coded iso-countours. The dotted black lines show several average halo MAHs. The thick dashed lines indicate where the SFE falls below 1 %. Therefore, halos above the upper line and below the lower line are inneficient. Blue points connected with the blue solid line represent the $1-\sigma$ halos at each epoch; the upper blue solid lines represent the respective 2, 3 4 and $5-\sigma$ halos and the lower blue line represent the 0.5σ halos.

In Fig. 2.14, we can find the SFEs along the halo MAHs of individual (average) systems. *Halos that end today with masses* $M_{\rm v}\approx 0.3-1\times10^{12}M_\odot$*, had most of the time high SFEs along their MAHs*. Instead, more massive halos change drastically their SFEs with time, being very high at the beginning, and then, as the halo grows, strongly decrease with time. A *quenching mechanism* is at work, the earlier acting as the more massive is the halo today. In the side of low-mass halos, the opposite happens: the SFE along their MAHs increases with time; a mechanism that *delays* SF and the M_s growth seems to be acting; the smaller the system, the more efficient is the delay.

Finally, in Fig. 2.14 we plot the loci of what are called the 1σ halos (blue dots connected with a blue line), i.e., the halos, which mass at a given z obey the criteria

of collapse according to the spherical top-hat model: $\delta_c^2(z) = \nu\sigma^2(M)$, where δ_c is the collapse overdensity, $\sigma^2(M)$ is the mass variance given by the power spectrum of the ΛCDM cosmology, and $\nu = 1$ for the 1σ halos. These halos are expected to be the most common at a given epoch. As ν is higher, the rarer are the halos; these halos are associated to high peaks in the fluctuation field (of height ν), which at the time of collapse are more massive than the average. As ν is smaller than 1, the rarer are also the halos, and they are associated to halos that delayed their collapse, being then less massive than the average collapsing mass at a given epoch. According to Fig. 2.14, the SFE of the 1σ halos is very low at high redshifts, it attains the maximum SFE at $z \sim 0.6$, and it is lower than this SFE at lower redshifts. The SFEs in high-peak (low-peak) halos are high only in time intervals at high (low) redshifts. *The 1σ halos are actually those that most of time have high SFEs, but this happens at relatively late epochs, since $z \sim 1$* (the last ~ 8 Gyr).

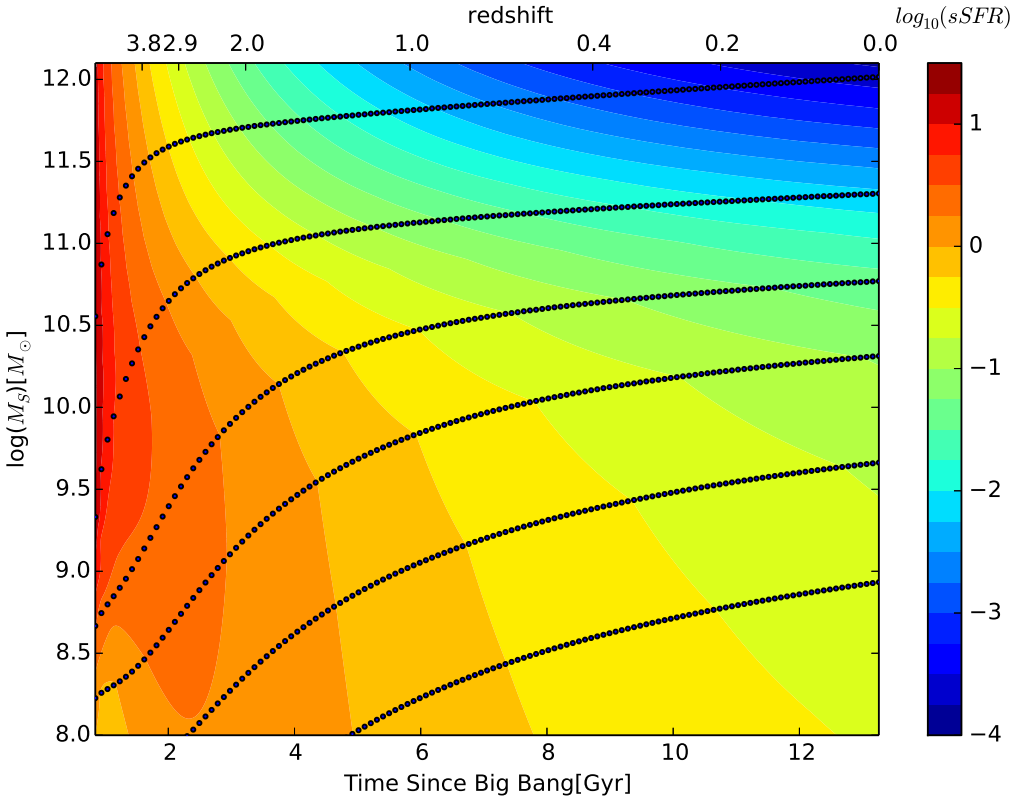

Figura 2.15: Average sSFRs as a function of M_s and z. The sSFR is plotted as color-coded iso-countours. The dotted black lines show several average stellar MAHs.

A purely observational counterpart of Fig. 2.14 is presented in Fig. 2.15. Here the sSFR of galaxies as a function of M_s and epoch is plotted as color-coded iso-contours in the M_s vs cosmic time or z plane. We see that the sSFR decreases in general across the cosmic

time, but much stronger for large stellar masses than for the lower mass ones. Galaxies of masses larger than $M_s \sim 10^{11}\ M_\odot$ are very actively growing by SF (high values of sSFR, $> 2\text{Gyr}^{-1}$) at $z > 4$, but at $z = 0$ are quenched (sSFR< 0.02 Gyr^{-1}). Instead, galaxies smaller than $M_s \sim 10^9\ M_\odot$, have sSFRs not much larger than 2 Gyr^{-1} at $z > 4$ and not smaller than ~ 0.5 Gyr^{-1} at $z = 0$. It is interesting that while at low redshifts the sSFR strongly decreases with M_s, at very high redshifts the sSFR is roughly the same for all masses; the sSFR–M_s relation flattens as z increases. Besides, at the highest z's, galaxies of all masses tend to have an "upper-limit" sSFR, ~ 10 Gyr^{-1}.

In Fig. 2.15, the mean *individual* stellar MAHs (in-situ + ex-situ modes) of several masses are plotted. One clearly sees that the sSFR across the stellar MAHs of massive galaxies strongly changes, and the larger the mass, the earlier it transited to very low values of sSFR (quenching). Instead, for low-mass galaxies, the sSFR did not decreases significantly having even today values not smaller than ~ 0.3 Gyr^{-1} (they are still actively forming stars).

2.6. Galaxy quenching

In subsection 2.5.1, we introduced the concept of transition mass, $M_{\rm trans}$, i.e. the mass of the galaxy that at a given epoch has a sSFR equal to $<$ sSFR $>(z)$, where this average sSFR is the one of a galaxy with current SFR at z equal to its past average SFR, assuming a SFR constant in time. The loci of $M_{\rm trans}$ at different z's in the sSFR–M_s plane has been shown in Fig. 2.10 for the fiducial model. In Fig. 2.16, we show explicitly the change with z of $M_{\rm trans}$ (dashed line). This is a semi-empirical inference of the stellar mass at each z of those galaxies that on average start to be quenched. It is of relevance to understand what are the mechanisms that produce the quenching of galaxies. Our results show that there is a "peak" redshift, $z \sim 2.7$, at which the quenching mechanism affects galaxies of mass $M_{\rm trans}$. At lower redshifts, galaxies of smaller masses enter on average in this process of quenching, down to $M_s \approx 9 \times 10^9\ M_\odot$ at $z = 0$. At redshifts higher than the peak, the quenching mechanism affects galaxies of stellar masses smaller than those at $z \sim 2.7$; the larger masses are already quenched.

In Fig. 2.16, we attempt to compare some direct observational inferences of the quenching mass with our results. Here, we plot the results from different surveys (symbols), where $GSMF$s were inferred for the blue/late-type and red/early-type populations at different redshifts. The mass where both $GSMF$s intercept can be associated to the quenching mass, i.e., the one where the galaxies already became quenched at each epoch. Our transition mass $M_{\rm trans}$ (blue line) is smaller than the quenching mass inferred from observations. This is because $M_{\rm trans}$ is associated to the moment at which the galaxy *initiates to be quenched*, while the quenched mass refers to the case the galaxy is already quenched (red/early-type). This happens probably when the galaxy sSFR decayed already

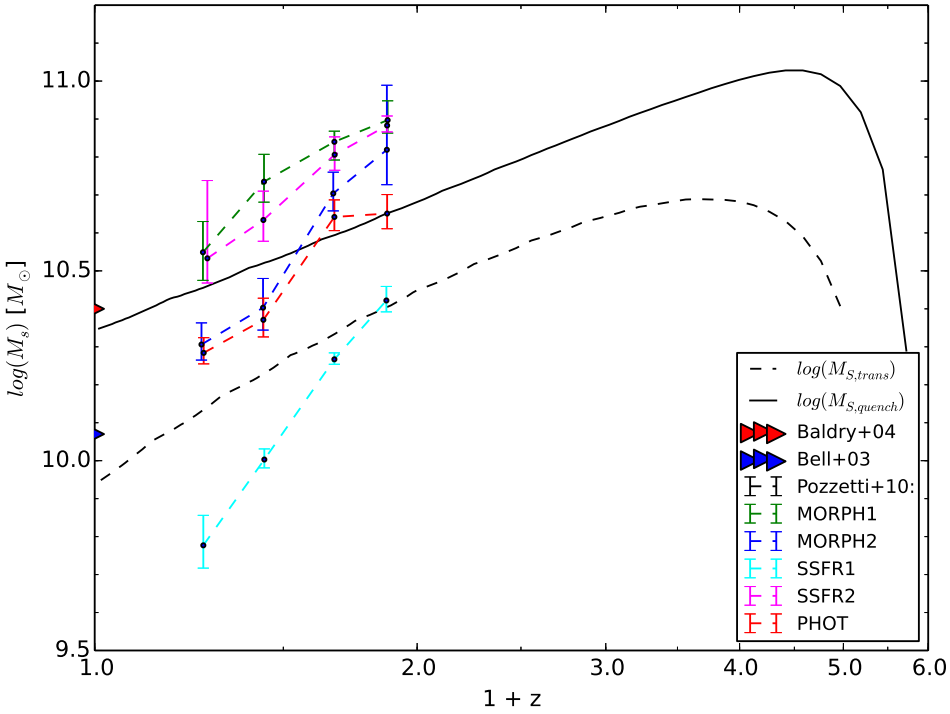

Figura 2.16: Mass at which on average galaxies start to transit from active star forming to passive, $M_{\rm trans}$, as a function of z (dashed line; see also Fig. 2.10). This mass is defined as the stellar mass a galaxy had when its sSFR becomes equal to $< SFR > (z)$ (eq. 2.19). For defining the mass at which the galaxies are already quenched, $M_{\rm quench}$, the criterion is set to a fraction of $< SFR > (z)$. The solid line represents $M_{\rm quench}(z)$ when the fraction was set to 2/3. Several observational inferences of the quenching mass are plotted for comparison (indicated in the inset; see text).

to a fraction of $<$ sSFR $>$. In Fig. 2.16, we plot for our fiducial model, the mean mass at each z for which its sSFR $= \frac{2}{3} <$ sSFR $> (z)$, and call it the *quenched mass*, $M_{\rm quench}$ (solid line). It is encouraging the rough agreement of $M_{\rm quench}(z)$ with the observational inferences up to $z \sim 1$, showing that our semi-empirical approach is able to capture the main galaxy mass assembly trends.

In Fig. 2.16, the data at $z \sim 0$ correspond to criteria for color separation into blue and red based on $(u-r)$ band (Bell et al. 2003a) and $(g-r)$ band (Baldry et al. 2004). At higher redshifts, the results from the COSMOS survey presented in Pozzetti et al. (2010) are used. The lines labeled as MORPH1 and MORPH2 in the inset correspond to a morphological separation of galaxies using two different methods for defining the morphological type

(see Pozzetti et al. 2010, for details). The lines labeled as SSFR1 and SSFR2 correspond to a separation of the galaxies by their sSFR, with values of log(sSFR/Gyr^{-1})=-1 and -2, respectively. While the first case corresponds mostly to galaxies that barely started to be quenched (closer to our $M_{\rm trans}$), the second case refers mostly to galaxies that probably are completely quenched (closer to our $M_{\rm quench}$).

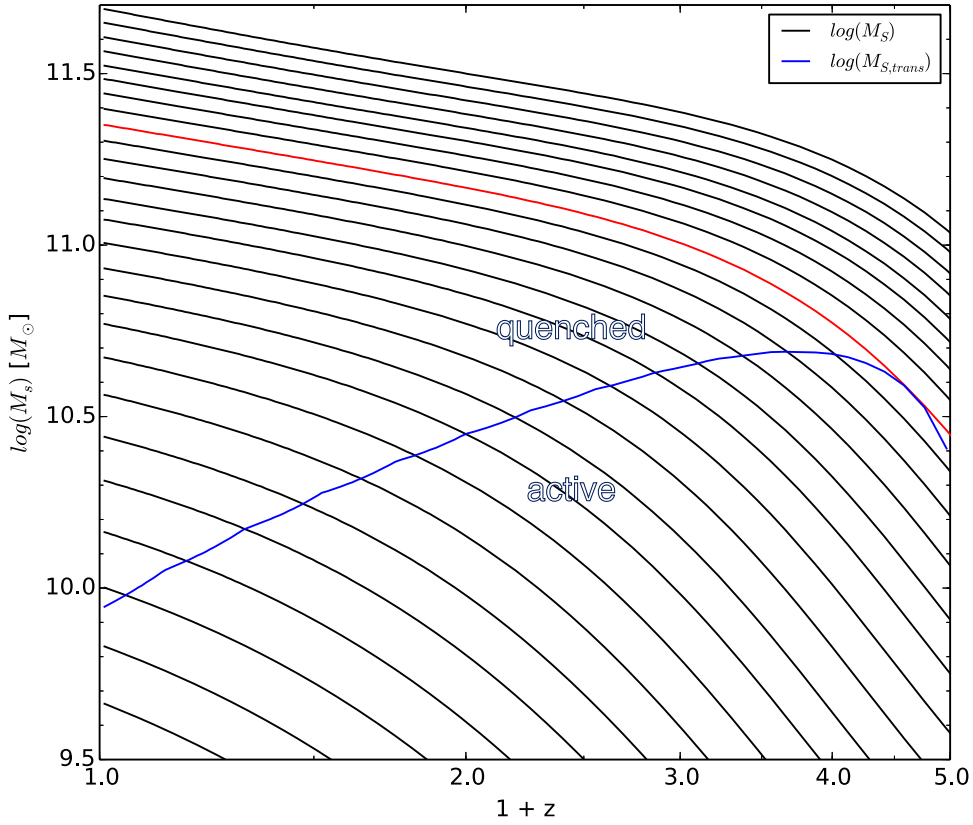

Figura 2.17: Individual mean stellar MAHs (black lines) and $M_{\rm trans}(z)$ (blue line). The individual track highlighted with red line corresponds roughly to a galaxy that barely intersects with $M_{\rm trans}(z)$ at very high z. Galaxies more massive than this one, are already quenched, at least since $z \sim 4-5$. Galaxies less massive start to be quenched (intersect $M_{\rm trans}$) at lower redshifts as less massive they are. Galaxies at $z = 0$ less massive than $\approx 9 \times 10^9\ M_\odot$, on average, were not yet quenched, i.e., they are actively growing by in-situ SF.

The question of what does quench galaxies is widely debated in the current literature. We are not in condition to answer to this question, but our semi-empirical inferences may shed light on it. In Fig. 2.17, we plot several individual mean stellar MAHs obtained from our fiducial model (black lines; see Fig. 2.8) along with $M_{\rm trans}(z)$ (blue line). Recall that the stellar MAHs refer to the growth of M_s by both the in-situ SF growth mode and the

ex-situ (mergers) mode. The latter is important only for the most massive galaxies (see Fig. 2.8). The plot shows that galaxies that today end with masses $M_s \gtrsim 2.2 \times 10^{11}\ M_\odot$ (red track), have masses larger than $M_{\rm trans}(z)$ at any z, since at least $z \sim 4$, which means that these galaxies are already since that epochs quenched. The evolutionary tracks of galaxies of mean masses $M_s(z=0) \approx 2.2 \times 10^{11}\ M_\odot$ and lower are intercepted by $M_{\rm trans}(z)$ since $z \sim 3$, the later, the less massive is the galaxy.

This means that since $z \sim 3$ (the last ~ 11.5 Gyr):

1. there is a common mechanism that produces a systematical quenching of galaxies;
2. this mechanism is able to quench at a given epoch only galaxies above a given stellar mass at that epoch;
3. with time, the mechanism affects smaller and smaller galaxies; and
4. the minimal mean stellar mass affected by this mechanism is the one corresponding to $M_{\rm trans}$ at $z=0$, $M_s = 9 \times 10^9$.

The main reasons for the quenching of massive galaxies have been proposed to be (i) the large radiative cooling time of the gas heated by the gravitational collapse to large temperatures in the case of massive halos, (ii) the negative feedback produced by luminous AGNs (quasars) formed in massive galaxies, and (iii) the effects of the environment, for instance, when a galaxy becomes a satellite in a group/cluster ambient. Several pieces of evidence show that the third mechanism is not relevant for massive galaxies since they have quenched before they became satellites (e.g., van den Bosch et al. 2008). The large gas cooling times in collapsed massive halos certainly may leave the central galaxy without the "cosmological" gas supply, though the previously gas accreted by the galaxy can keep the galaxy forming stars for some time. The cooling time starts to be long for collapsed halos of $\sim 10^{12}\ M_\odot$ and it is only for the most massive ones, $M_{\rm v} > 3 \times 10^{13}\ M_\odot$, for which the "cosmologically" accreted gas can be decreased in the inflow to the galaxy by factors as large as 3-5 at $z=0$ (see e.g., Dutton & van den Bosch 2009). At higher redshifts, these factors are larger as calculations show (Dutton, van den Bosch & Dekel 2010). It could be that the (very rare) most massive galaxies (those that are in high density peaks and therefore assembled early by violent wet major mergers), had highly efficient SF that transformed most of the gas into stars in a bursting mode at early epochs; after the halo massive virialized, the intrahalo gas is heated to high virial temperatures in such a way that further accretion to the galaxy is ceased, and the galaxy quenches since that early epochs. Some stellar mass growth may happen later by dry mergers. This scenario may be consistent with our result that galaxies more massive than $M_s \sim 2.2 \times 10^{11}\ M_\odot$ at $z=0$ appear quenched since redshifts as high as 4–5 (their masses are larger than $M_{\rm trans}$ since that epochs; Fig.2.17).

For lower mass galaxies ($9 \times 10^9 \lesssim M_s \lesssim 2.2 \times 10^{11}\ M_\odot$ at $z=0$), while the long gas cooling times avoids that all the "cosmological" gas cools and infalls to the galaxy, some

fraction of it, which is higher as smaller is the halo, cools and infalls to the galaxy. This cooling gas and the gas remaining inside the galaxy are a sufficient reservoir as to keep the galaxy growing by in-situ SF. Therefore, another mechanism should be responsible for the observed quenching in our results, and which produces the archeological downsizing. This mechanism may be the negative AGN feedback, which was proposed also to avoid a too shallow massive-end in the observed $GSMF$, i.e., the formation of too massive galaxies (e.g., Bower et al. 2006; De Lucia & Blaizot 2007).

The popular scenario of elliptical galaxy formation is as follows: major wet mergers at high redshifts give rise to a spheroid $\rightarrow$ strong star bursts in a dust-obscured regime (submillimeter galaxy) and growth of a super massive black hole (SMBH) $\rightarrow$ feeding of the SMBH and activation of the central machine ("IR excess" quasar) $\rightarrow$ dust sublimation and SF quenching due to the luminous AGN (quasar) $\rightarrow$ gas loss and turn off of the quasar $\rightarrow$ massive stellar spheroid in process of aging (see for a review e.g., Hopkins et al. 2007, and more references therein). The SF quenching by luminous AGNs has been detected in some galaxies at different redshifts (e.g., Cano-Díaz et al. 2012; Cicone et al. 2014).

We will explore whether the mean transition mass $M_{\rm trans}(z)$ is associated to the quasar phase, and therefore, whether this phase is associated to the one producing the quenching of massive galaxies (Hopkins et al. 2007). For this, let us assume that $M_{\rm trans}$ is the host spheroid mass and calculate the corresponding SMBH mass, $\mathrm{M}_\bullet$, from the empirical $\mathrm{M_{sph}}$–$\mathrm{M}_\bullet$ relation. This relation is now relatively well constrained at $z \sim 0$. We use the compilation and best fit given by Kormendy & Ho (2013):

$$\log(M_\bullet/M_\odot) = -4.18 + 1.17\log(M_{\rm sph}/M_\odot). \tag{2.20}$$

The scatter around this relation is 0.29 dex. There is some pieces of evidence that this relation does not significantly change until $z \sim 2$ and for higher z's it seems that the zero-point increases by 0.3-0.5 dex (Kormendy & Ho 2013) up to $z \sim 6$, i.e., for a given SMBH mass, the spheroid mass is smaller than in the present day. This can be understood if at high redshifts, after the violent merger phases, the SMBH is already settled down, while the corresponding galaxy mass may still grow by some in-situ SF (mainly before the quasar quenching phase) and by minor dry mergers. In order to take into account the (slight) evolution in the $\mathrm{M_{sph}}$–$\mathrm{M}_\bullet$ relation, we assume that since $z = 1$ its zero-point increases in such a way that at $z = 5$ is 0.5 dex higher than in eq. (2.20).

Given the SMBH, we follow the common assumptions in order to estimate the quasar bolometric luminosity produced by accretion into the SMBH at the near Eddington regime (see e.g., Croton 2009):

$$L_{\rm QSO}/L_\odot = \eta\, 3.3 \times 10^4 M_\bullet, \tag{2.21}$$

where η represents some fraction of Eddington luminosity. Using our $M_{\rm trans}$ and eq.(2.20), the luminosity calculated in eq. (2.18) is then the quasar luminosity associated to a galaxy

of mass equal to $M_{\rm trans}(z)$. The quasar luminosities follow a distribution at each z that can be described by a double-power law, characterized mainly by the brake luminosity $L^\star$ (see Hopkins, Richards & Hernquist 2007, and the references therein). This is the characteristic luminosity of quasars at each epoch. The abundance of quasars more luminous than $L^\star$ strongly decreases. The abundance of less luminous quasars remains constant or slightly increases as L is smaller. However, most of these objects are already faint AGN, which are being fed at a much weaker regime than the Eddington one. It is likely that their feedback is not enough as to quench the SF of their respective hosts.

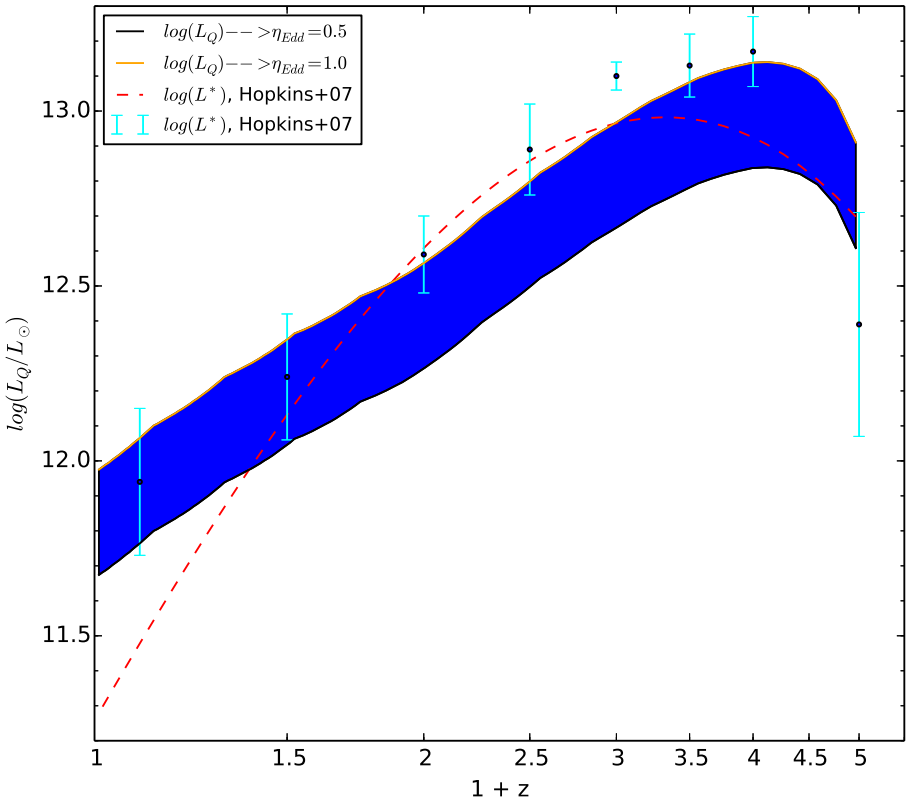

Figura 2.18: Quasar luminosity associated to a (spheroid) stellar mass equal to $M_{\rm trans}$ at different redshifts. The blue band corresponds to values from 0.5 to 1 for the η parameter (see eq. 2.21). The characteristic (brake) quasar luminosity, $L^\star$, from observations at different z is also shown: error bars are from a compilation by Hopkins, Richards & Hernquist (2007) and dashed line is for an overall fit at all redshifts assuming the PLE model (Hopkins, Richards & Hernquist 2007). The approximate coincidence between $L^\star(z)$ and the quasar luminosity associated to the transition mass $M_{\rm trans}(z)$ strongly suggest that is the quasar (AGN) feedback the responsible of quenching massive galaxies since $z \sim 4$.

In Fig. 2.18, we plot the quasar luminosity as a function of z associated to the transition

mass $M_{\rm trans}(z)$ inferred by means of our semi-empirical model. Here, we also plot the best fitting to the the brake luminosity $L^{\star}$ of the observed luminosity functions at different redshifts as obtained in Hopkins, Richards & Hernquist (2007). It is well known that the quasar luminosity function evolves and it is at $z \approx 2.5$ where quasar abundance has its peak. For the shapes of the observed luminosity functions at different z's, this translates meanly in a evolution of $L^{\star}$; the normalization density, $\phi^{\star}$, remains roughly constant (see Hopkins, Richards & Hernquist 2007).

It is quite encouraging that *the characteristic luminosity of observed quasars follows so closely the quasar luminosity associated to the mean transition mass*, i.e., the characteristic mass at which the massive galaxies start to quench. This "coincidence", within the large uncertainties and the actually broad distributions and scatters not taken into account here, provides an important evidence in favor of *the quasar feedback as a key mechanism for quenching massive galaxies*.

2.7. Conclusions

We have presented a parametric "toy" model for the average mass assembly histories of galaxies as a function of mass. The model assumes that the galaxy SFR is proportional to the "cosmological" halo mass aggregation rate multiplied by an efficiency that is function of halo mass $M_{\rm v}$ and redshift. This function, $G_{\rm SFE}(M_{\rm v},z)$, encodes the main astrophysical processes of gas cooling and infall within the dark matter halos, galaxy SF, and stellar and AGN feedbacks (both preventive and ejective). The parameters of the function $G_{\rm SFE}(M_{\rm v},z)$ are constrained in order to reproduce observational or semi-empirical inferences at different redshifts: the sSFR(M_s;z) and $M_s(M_{\rm v};z)$ relations, and the cosmic SFR and SM density histories. Only the means of the relations are used, that is, we do not take into account the scatters, and for the halo MAHs, we use average histories as measured in the Millennium Simulations (Fakhouri, Ma & Boylan-Kolchin 2010). Therefore, our results refer only to mean trends of galaxy mass assembly as a function of mass. The main virtue of the model is that allows to infer *individual* mean galaxy evolutionary tracks from the observations at different redshifts, as well as to connect the different observational inferences one to another. Our approach is therefore semi-empirical.

By means of our approach, we first explored the connection between the sSFR(M_s;z) and $M_s(M_{\rm v};z)$ mean relations. There is a tight connection between both relations. From our analysis, we remark two potential issues for the current inferences of these relations:

- In order to reproduce an increasing sSFR as M_s is smaller (for instance a slope of -0.3 at the low-mass side of the relation as observations show at low redshifts; down-sizing in sSFR), a strong evolution of the low-mass side of the $M_s(M_{\rm v};\, z)$ relations is required, at least since $z \sim 1$ to 0. For a given $M_{\rm v}$, M_s should strongly increase as z is smaller. This is in conflict with even those semi-empirical inferences that show

high evolution in the M_s–$M_{\rm v}$ relation. A very bursty SF of galaxies at low masses may introduce biases in the determination of the mean of the sSFR–M_s relation, as well as to invalidate the main assumption (at these small masses) of the abundance matching method used to infer the M_s–$M_{\rm v}$ relation.

- In order the high-mass side of the $M_s(M_{\rm v};\, z)$ relations did not change too much with time (as the semi-empirical inferences show), a strong declining (bending) of the sSFR–M_s relation at the high mass-end at high redshifts is necessary. The latter is not seen in the average from the few observational measures at $z > 2-3$. It could be that the SFR measures of massive, post-merger (post-star-burst) galaxies at high redshifts are actually overestimated.

Given the apparent inconsistencies mentioned above, as well as the variety of (semi)empirical inferences and observational uncertainties, we have constrained the parameters of our model by searching for an overall consistency with these diverse inferences of the sSFR–M_s and $M_s(M_{\rm v};\, z)$ relations, as well as the cosmic SFR and SM density histories, and the galaxy merger rate histories. We follow some reasonable criteria for giving more or less weight to the different "observables" at different epochs (see Section 2.5). Once the model parameters were constrained, the mean *individual* evolutionary tracks as a function of mass are obtained. We refer to these results as our fiducial model, and the main implications from it are as follow:

• The SFE ($G_{\rm SFE} \equiv$SFR/$\dot{M}_b$) encodes the relevant astrophysical processes of galaxy formation and evolution inside the halos. We find that from $z \sim 6$ to 0, the halos that *at each epoch* have the highest SFEs are those of masses $0.3-1\times10^{12}\ M_\odot$, not changing significantly they SFEs across the cosmic time (Figs. 2.13 and 2.14). Instead, the SFE in low-mass halos is higher as z is lower (since $z \sim 3-4$), and in high-mass halos, the SFE is all the time much lower as z is smaller. The minimal and maximal halo masses for which the SFE becomes less than 1 % ("inefficient" halos) change with z, specially at the low-mass side: for instance, at $z = 3$, halos less massive than $\approx 4\times10^{10}\ M_\odot$ are inefficient, while at $z = 0$, this happens only for $M_{\rm v} \lesssim 5\times10^{8}\ M_\odot$. At the same redshifts, $z = 3$ and 0, halos more massive than $\approx 10^{14}$ and $10^{13}\ M_\odot$ are already inefficient, respectively.

• The evolution of the SFE along the *individual* average halo MAHs depends strongly on the present-day mass of the system (Fig. 2.14). Halos that end today with masses $M_{\rm v} \approx 0.3-1\times10^{12} M_\odot$, had most of the time high SFEs. More massive halos, start with the highest SFEs ever but as the halo grows, the SFE strongly decreases. A *quenching mechanism* is at work, the earlier acting as the more massive is the halo today. For the less massive halos, the opposite happens: the SFE along their MAHs increases with time; a mechanism that *delays* SF and the M_s growth seems to be acting; the smaller the system, the more efficient is this delay.

• The sSFR (=SFR/M_s) of galaxies at $z > 4$ are very high ($\gtrsim 3-10$ Gyr^{-1}) and is roughly the same for all galaxies with $M_s \gtrsim 3\times10^{9}\ M_\odot$; hence, the sSFR–$M_s$ relation at high redshifts is roughly flat (Figs. 2.15 and 2.10). For a fixed M_s, if this mass is large,

the sSFRs strongly decrease as z is smaller, while if this mass is small, the sSFR decreases weakly. For example, for galaxies of $M_s = 10^{11}\ M_\odot$, sSFR ≈ 2 Gyr^{-1} at $z = 4$ and $\approx$ 0.02 Gyr^{-1} at $z = 0$, while for galaxies of $M_s = 3 \times 10^9\ M_\odot$, sSFR ≈ 3 and 0.18 Gyr^{-1} at these redshifts, respectively.

• By defining the transition from active to passive stellar growth by SF as the one when the current SFR is equal to the past average $< SSFR > (z)$, we find at each z the typical stellar mass that is in this transition process, $M_{\rm trans}$. This mass is $9 \times 10^9\ M_\odot$ at $z = 0$, increases up to $5 \times 10^{10}\ M_\odot$ at $z = 2.7$, and then it slightly decreases at higher redshifts. We can define also the mass where the galaxies are already quenched, $M_{\rm quench}$, for instance, when their sSFR declined to a fraction (e.g., 2/3) of $< SSFR > (z)$. The predicted $M_{\rm quench}(z)$ agrees with observational determinations of the mass where the $GSMF$ of red/early-type galaxies start to dominate at different z.

• Galaxies that today end with $M_s = 5 - 8 \times 10^{10}$ ($M_{\rm v} \approx 2 - 3 \times 10^{12}$) $M_\odot$ have stellar MAHs that follow closely their halo MAHs, at least since $z \sim 2$ (Fig. 2.8). The stellar mass assembly of these galaxies, in the mean, is driven mainly by the "cosmological" mass aggregation rate. For larger and smaller galaxies, their stellar and halo MAHs detach significantly in different directions:

- For larger galaxies, the stellar growth slows down while their halos continue growing; the more massive is the system, the earlier is "quenched" its stellar mass growth by in-situ SF (this gives rise to the archeological downsizing). The most massive galaxies ($M_s(z = 0) > 10^{11}\ M_\odot$) may grow up to 50 % their present-day M_s by the ex-situ mode (mergers).

- For smaller galaxies, their halo MAHs slow down early but their stellar MAHs grow late; the smaller the galaxy, the more "delays" the stellar growth with respect to its halo growth (this gives rise to the downsizing in sSFR).

• The model results agree with the main features of the observed cosmic SFR and Stellar Mass (SM) density histories (per comoving volume; Fig 2.11). However, we confirm the potential problem that passing from the observed cosmic SF history to the cosmic SM history produces SM densities at $z > 1$ larger than those inferred from integrating the observed $GSMF$s. Our fiducial model is a compromise in between both "observables". This potential problem resembles the one between the sSFR(M_s; z) and $M_{\rm v}(M_s; z)$ relations.

• The dissection by mass of our cosmic SF history surprisingly shows that, at any redshift, the galaxies that more contribute to the SFR density are those of stellar masses between $\approx 1 - 3 \times 10^{10}\ M_\odot$ and halo masses $\approx 3 - 10 \times 10^{11}\ M_\odot$ (Fig. 2.12). A combination of the abundances and SFRs of these halo/galaxy systems at each redshift conspires to make them the most important contributors to the SFR per comoving volume at all redshifts. The contribution of low-mass galaxies to the global SFR becomes more important as z is smaller; this is another way of enunciating the downsizing in SFR.

The overall picture of halo/galaxy mass assembly across the cosmic time that emerges from our fiducial semi-empirical model suggests several key implications. We remark two

of them:

- The inferred mean SF histories of galaxies vary strongly as a function of the present-day galaxy M_s (Fig. 2.9). For massive galaxies, $M_s > 10^{11}\ M_\odot$, the SFR was very high at early epochs and since high redshifts, $z > 3$, it strongly declines (quenching). For intermediate mass galaxies, $2 \times 10^{10} \lesssim M_s/M_\odot \lesssim 7 \times 10^{10}$, the SFR rises up to $\sim 2-1$ and then weakly declines. For low-mass galaxies, $M_s < 7\times10^9 M_\odot$, the SFR is rising all the time and at $z = 0$ they are yet in their active growth phase, more as the less massive is the galaxy (downsizing in SSFR). For galaxies with $M_s > 10^{10} M_\odot$, the larger they are, the earlier attain their peak SFR (archaeological downsizing). The commonly used τ model (exponential declining SF histories with different widths) in models as the stellar population synthesis ones, seems not to be adequate for low-mass galaxies.

- Galaxies more massive than $\sim 2 \times 10^{11}\ M_\odot$ at $z = 0$, do not intersect $M_{\rm trans}(z)$ in their (at least up to $z \sim 5-6$) , which means that they became passive (quenched) very early. This is consistent with a scenario where many wet mergers produced strong bursts of SF that exhausted all the available gas, and the violent collapse of the massive halo heated the gas to temperatures that can not cool in times shorter than the cosmic time; the central galaxy can not grow anymore unless by late dry mergers. Galaxies less massive that $\sim 2 \times 10^{11}\ M_\odot$ at $z = 0$ intersect $M_{\rm trans}(z)$ in the past, i.e. they start to quench (since ~ 3), besides the later, the smaller they are, producing the archeological downsizing. If we associate $M_{\rm trans}(z)$ to a SMBH mass through the stellar mass–$M_\bullet$ relation, and assume that the accretion disk around the SMBH radiates at the Eddington limit (quasar), then the obtained quasar luminosity at each z is similar in amplitude and in evolution to the characteristic (brake) luminosity of quasars at different z. This "coincidence" between the typical mass that is starting to quench with the characteristic quasar luminosity, strongly favors the scenario of quenching massive (post-merger) galaxies by the quasar (AGN) feedback.

An important caveat of the approach presented here is that does not take into account any scatters in the observational relations nor in the halo MAHs. The only parameter in play at all times is the halo mass and its associated stellar mass. We are aware that galaxy evolution is affected by many other factors than only the mass and this is why the different observable correlations with mass have scatters. These scatters likely can be explained by the stochastic nature of the halo MAHs, the dependences with environment, etc. On its own, this give rise to different types of galaxies, which are characterized not only by mass but by color, sSFR, morphology, etc. Our study here ignores all this diversity and focus only on the main and mean aspects of galaxy evolution. It is a first-th order approach based on only the dependences on mass and therefore, for consistency, it takes into account only the means of the mass-depending observable relations.

Finally, we remark that the overall consistency of our model with a large body of empirical local and high-redhsift inferences, shows that the ΛCDM cosmology, which has been used as backbone in our approach, is consistent with the mean statistical and evolutionary properties of observed galaxies. This consistency comes from assuming that galaxy formation and evolution inside the hierarchically growing ΛCDM halos is described by SFEs as a function of $M_{\rm v}$ and z as those we have constrained here. Several known astrophysical processes are likely to be responsible for shaping these SFEs. However, the rising SF histories of present-day galaxies smaller than $M_s \sim 7 \times 10^9\ M_\odot$, which imply a strong delaying mechanism of stellar mass growth for these galaxies, remains as a challenge for our current understanding of low-mass galaxy formation and evolution.

How are the mass assembly and SF histories of low-mass galaxies in numerical simulations? Do they predict the downsizing behavior as in our semi-empirical results? Are the SN-driven outflows able to produce this behavior? How bursty are the SF histories of low-mass galaxies and how much they follow the assembly of their halos? Are the simulations missing yet some key physical processes at these small scales? Or is the ΛCDM paradigm in trouble at these scales?

With the aim to address these and other questions, in the following Chapters of the Thesis, we will present several studies we have carried out regarding the formation and evolution of low-mass galaxies in the cosmological context (Λ Cold and Warm Dark Matter cosmologies) by means of high-resolution numerical simulations.

Capítulo 3

Ensamblaje de galaxias de baja masa en simulaciones cosmológicas

Ya hemos visto que mientras menos masivas las galaxias, más tardiamente tienen su ensamblaje de masa estelar, siendo éste a la inversa del ensamblaje de la masa de sus halos oscuros. Modelos semi-analíticos y semi-numéricos han mostrado preliminarmente que el "downsizing" en TFEE parece constituir un problema para los mismos (dentro del escenario ΛCDM y con la gastrofísica que se suele introducir hasta ahora; Fontanot et al. 2009; Santini et al. 2009; Firmani & Avila-Reese 2010).

De manera preliminar, en Colín et al. (2010) se ha mostrado que este problema también se observa en simulaciones numéricas de N cuerpos + hidrodinámica de galaxias de baja masa. En Avila-Reese et al. (2011),[1] corroboramos que este es el caso al comparar un conjunto de simulaciones de galaxias de baja masa con la compilación observacional ya mencionada en el capítulo anterior. En este trabajo presentamos un conjunto de galaxias simuladas con el código H+ART con la técnica "zoom-in". Este esquema nos permite tener simulaciones en las que conocemos el detalle de las propiedades de las galaxias a escalas de cientos de parsecs, pero tiene la desventaja de que debido al alto costo de computo para realizarlas, solo se cuenta con pocas galaxias.

Una alternativa es el realizar un simulación de una "caja cosmológica", la cual es una representación de una región del Universo en la cual viven muchas galaxias. La ventaja de este enfoque es que dado que tenemos un gran número de galaxias dentro de la caja cosmológica simulada, podemos hacer estadística y obtener valores promedios de las propiedades de las galaxias. Claramente la desventaja es que dichas galaxias estan pobremente resueltas espacialmente, así que solo podemos estudiar sus propiedades globales y no así su estructura. Ambas aproximaciones son complementarias entre sí con respecto a la información que nos pueden dar acerca de la formación y evolución

[1] Primer trabajo en el que presentamos resultados producto de mi proyecto de Tesis Doctoral.

de galaxias. Con esto en mente, emprendimos el análisis de una caja cosmológica de 14 Mpcs en la cual se encontraron ~ 250 galaxias de baja masa. Esta simulación se realizó con el código GADGET-3 y los resultados aparecen en De Rossi et al. (2013). Dichos resultados son contrastados con el "modelo de juguete" presentado en el capítulo anterior, y encontramos que aunque para estas galaxias su ensamblaje de masa estelar se desviaba levemente del de los halos en los que residen, no lo era suficiente cmo para explicar el "downsizing" inferido por las observaciones. A continuación mostramos un resumen de lo reportado en ambos artículos[2] que es pertinente para los objetivos del presente trabajo de tesis.

[2]Dada la relevancia de este artículo para el entendimiento de los capítulos 2 y 3 es que lo incluyo como apéndice 1 al final de la Tesis.

3.1. Simulaciones numéricas de alta resolución ("zoom-in")

En este trabajo hemos estudiado un alto número de simulaciones cubriendo un intervalo amplio de masas, resoluciones y parámetros sub-malla. Nuestro objetivo es explorar la evolución de la tasa de formación estelar (TFE), M_s, y $M_{\rm v}$ de galaxias aisladas de baja masa en simulaciones numéricas, y compararlas con inferencias observacionales actuales de galaxias centrales de baja masa a diferentes corrimientos al rojo. Esto se hizo usando el código ART (Adaptive Refinement Tree, Kravtsov, Klypin & Khokhlov 1997a) con hidrodinámica (Kravtsov 2003a). Dentro de los procesos físicos incluidos en ART están el enfriamiento de gas y su subsecuente conversión en estrellas, retroalimentación estelar térmica, y una fuente de fondo de calentamiento UV. Las tasas de calentamiento y enfriamiento incorporan calentamiento/enfriamiento Compton, atómico, y molecular, y son tabulados para un rango de temperaturas de $10^2K < T < 10^9K$ y una malla de densidades, metalicidades, y corrimientos al rojo usando el código CLOUDY (Ferland et al. 1998a); para una descripción más detallada de cómo se implementan en el código los diferentes procesos físicos mencionados ver el artículo Avila-Reese et al. (2011a), para una discusión más detallada ver Kravtsov (2003a); Kravtsov, Nagai & Vikhlinin (2005).

3.1.1. Esquema de las simulaciones

Las simulaciones que forman parte de este estudio tienen como antecedente un trabajo previamente emprendido por Colín et al. (2010) donde se exploraron diferentes esquemas de retroalimentación estelar y parámetros sub-malla para galaxias de baja masa ($M_h \approx 7 \times 10^{10} M_\odot$ a $z = 0$) que desarrollaban un disco. Aquí continuamos con esta línea de tal manera que estudiamos diez simulaciones cosmológicas de alta resolución (*N-cuerpos + hidrodinámica*) de galaxias de baja masa. Estas galaxias se formaron en halos aislados con masas en el rango $2.5 \lesssim M_{\rm v}/10^{10} M_\odot \lesssim 50$ a $z = 0$.

En estas simulaciones la formación estelar ocurre en las regiones más densas y frías, carcaterizadas por $T < T_{\rm SF}$ y $n_g > n_{\rm SF}$, donde T y n_g son la temperatura y la densidad del gas respectivamente, y $T_{\rm SF}$ and $n_{\rm SF}$ son los umbrales de temperatura y densidad de formacón estelar. Así, una partícula estelar de masa m_* es colocada en una celda de la malla donde se satisfacen simultáneamente estas condiciones, y esta masa es removida de la masa de gas en la celda. La partícula subsecuentemente sigue una dinámica de N-cuerpos. La masa de la partícula estelar, m_*, es determinada en cada celda y paso temporal suponiendo que $\dot{\rho}_*$ es proporcional a una ley de potencias de la densidad del gas, $\dot{\rho}_* \propto \rho_g^\alpha$ (nosotros usamos $\alpha = 1$; ver Colín et al. (2010) para más detalles). En la mayoría de las simulaciones presentadas aquí, m_* es calculada suponiendo que una dada fracción (factor de eficiencia local de FE $\epsilon_{\rm SF}$) de la masa de gas de la celda, m_g, es

convertida en estrellas; es decir, $m_* = \epsilon_{\rm SF} m_g$, donde $\epsilon_{\rm SF}$ es tratado como un parámetro libre. En este trabajo usamos $\epsilon_{\rm SF} = 0.5$, valor sugerido por el estudio realizado por Colín et al. (2010), donde encuentran que dicho valor en las simulaciones da resultados rasonables. En este mismo artículo los autores experimentaron con una implementación "estocástica" para definir los momentos cuando se daba la formación estelar. Bajo este esquema, las partículas estelares son creadas en una celda con una función de probabilidad proporcional a la densidad del gas. Así, se permite la posibilidad de formar estrellas en regiones de baja densidad promedio en las cuales las nubes densas características del medio interestelar no se resuelven. En este trabajo solo en una de las simulaciones se usa dicho esquema probabilístico, en todos los demas casos se sigue la implementación determinística suponiendo un unmbral de densidad de $n_{\rm SF} = 6\ {\rm cm}^{-3}$, lo cual corresponde a una densidad columnar de $N \sim 10^{21}$ cm^{-2}.

Las partículas estelares inyectan energía en forma de calor a las celdas en las que nacen. La mayor parte de esta energía térmica es radiada hacia afuera al menos que el enfriamiento sea apagado temporalmente. Este mecanismo, de la mano con el alto valor de $\epsilon_{\rm SF}$ permite que el gas se expanda alejándose de la región de formación estelar. Así, para permitir el que se generen vientos galácticos, en este trabajo se adoptó la estrategia de apagar el enfriamiento durante un tiempo $t_{\rm off}$ en las celdas donde se forman las partículas estelares (ver Colín et al. 2010). En la mayoría de las simulaciones presentadas en este trabajo, apagamos el enfriamiento por $t_{\rm off} = 40$, 20, y 10 Myr dependiendo de la resolución; sin embargo, es importante aclarar que hemos encontrado que variar este parámetro no afecta nuestros resultados.

Para maximizar la eficiencia en la resolución, se usó la técnica "zoom-in": primero se corre una simulación cosmológica de baja resolución solo con partículas de materia oscura, después se seleccionan las regiones (halos de materia oscura) de interés para finalmente ser re-simulados con alta resolución y con la inclusión de la física del gas. Las simulaciones de baja resolución se corrieron con 128^3 partículas dentro de una caja de $10h^{-1}$Mpc por lado, con la caja inicialmente cubierta por una malla de 128^3 celdas. El número de partículas de materia oscura en la región de alta resolución depende del número de especies de materia oscura y de la masa del halo. Para modelos con cuatro especies (alta resolución) este varía de $\sim$ medio millon (modelo Ah) a alrededor de 4.7 millones (modelo Ih), el halo menos masivo y el segundo halo más masivo, respectivamente. La correspondiente masa de MO por partícula de las galaxias simuladas ($m_{\rm dm}$) está indicada en la Tabla 1.

En ART, la malla numérica que inicialmente es uniforme, se refina recursivamente al evolucionar la distribución de materia. El criterio elegido para el refinamiento se basa en las densidades de gas o de MO. Así, una celda es refinada cuando la masa en las partículas de MO excede $1.3(1 - F_{b,U})m_p$ o la masa en gas es más grande que $13.0F_{b,U}\ m_p$, donde $m_p = m_{dm} + m_g = m_{dm}/(1 - F_{b,U})$ y $F_{b,U}$ es la fracción bariónica universal, $F_{b,U}$= 0.15 para la cosmología usada aquí. Para las simulaciones presentadas en este artículo, usando

múltiples masas para la partícula de MO, la malla siempre se refina incondicionalmente hasta el tercer nivel (cuarto nivel), correspondiendo a un tamaño de malla efectiva de 512^3 (1024^3). Por otra parte, el nivel máximo de refinamiento permitido se ajustó a 9 y 10, para simulaciones de baja y alta resolución respectivamente. Esto implica tamaños espaciales para la parte más fina del mallado de $\ell_{\rm max} = 218$ y 109 pc (comóvil), respectivamente.

Siguiendo el procedimiento ya descrito, hemos resimulado la evolución de diez sistemas individuales galaxia/halo cubriendo un rango en masa del halo total (bariones + materia oscura) desde $M_{\rm v} \approx 2 \times 10^{10}\ M_\odot$ hasta $M_{\rm v} \approx 4 \times 10^{11}\ M_\odot$ a $z = 0$. Para la mayoría de los sistemas hemos corrido dos o mas simulaciones variando la resolución, el parámetro de eficiencia local de formación estelar $\epsilon_{\rm SF}$, el tiempo durante el cual se apaga el enfriamiento (después de eventos de formación estelar), $t_{\rm off}$, y, en un caso, el esquema de formación estelar. La tabla 4.4.2 resume las características de las simulaciones estudiadas en este trabajo. Hay tres simulaciones maracadas con el símbolo "*". En las simulaciones con "h" y "*" son de alta resolución en el sentido del número de partículas de MO y en términos del número de celdas de la malla.

Cuadro 3.1: Parámetros de las Simulaciones

Name	$M_h(z=0)$ ($10^{10}\ M_\odot$)	M_{part} ($10^4\ M_\odot$)	l_{max} (pc)	$\epsilon_{\rm SF}$	t_{off} (10^6 yr)
A_{h1}	1.97	9.41	109	0.5	20
A^*_{h1}	2.01	9.41	109	0.5	20
B_{h1}	2.32	9.41	109	0.5	20
B^*_{h1}	2.46	9.41	109	0.5	20
C_{l1}	2.80	65.7	218	0.5	20
C_{h1}	2.48	8.28	109	0.5	20
C^*_{h1}	2.84	8.28	109	0.5	20
D_{h1}	3.65	9.40	109	0.5	20
E_{l1}	5.94	76.0	218	0.5	40
E_{h1}	5.11	9.40	109	0.5	10
E_{h2}	5.31	9.40	109	0.5	40
E_{h3}	5.76	9.40	109	0.2	40
F_{l1}	7.79	65.7	218	0.5	20
F_{h1}	6.56	8.28	109	0.5	20
G_{l1}	8.37	76.0	218	0.66	40
G_{l2}	9.52	76.0	218	—	40
H_{l1}	14.5	46.5	218	stoch.	r.a.
I_{l1}	30.4	76.0	218	0.5	40
I_{h1}	30.5	9.40	109	0.5	40
J_{l1}	35.8	76.0	218	0.66	40
J_{l2}	40.4	76.0	218	—	40

3.1.2. Resultados y comparación con las observaciones

La mayoría de las galaxias simuladas que estudiamos en este trabajo tienen propiedades dinámicas, estructurales, y del medio interestelar que están rasonablemente en acuerdo con las observaciones de galaxias centrales de baja masa. Las principales propiedades a $z = 0$ para todas las corridas se muestran en la Tabla 3.2. El nombre de la simulación y la masa virial del halo están dados en las Columnas 1 y 2. Las Columnas 3 y 4 presentan la masa estelar y la fracción de masa de gas (frío) de la galaxia, M_s y f_g=M_g/(M_s+ M_g), respectivamente, donde M_g es la masa contenida en las partículas de gas con $T \leq 10^4$ K. Ambas, M_s and M_g están definidas como la masa estelar y de gas contenidas dentro de $5R_e$. R_e está definido a su vez como el radio donde está contenida la mitad de la masa estelar de la galaxia (Columna 5). Esta definición considera la masa asociada con un posible halo estelar muy extendido; las galaxias satélites también serían consideradas pero esto no hace mucha diferencia para el cálculo de las propiedades en general ya que su contribución a la masa total es $\lesssim$ 5 %. La velocidad circular máxima. $V_{\rm max}$, esta dada en la Columna 6; la velocidad circular es calculada como $V_{\rm c} = \sqrt{GM(R)/R}$, donde $M(R)$ es la masa total (oscura, estelar, y gas). Finalmente, las Columnas 7 y 8 dan las fracciones de masa estelar y bariónica de las galaxias, definidas como F_s= M_s/$M_{\rm v}$ y F_b= M_b/$M_{\rm v}$, donde M_b= M_s+ M_g y $M_{\rm v}$ es la masa virial total (oscura + bariones).

Los resultados relevantes para este proyecto de tesis se muestran en las Figuras 2.1 y 3.2. Antes de empezar con su descripción es importante indicar la simbología usada para representar el conjunto de galaxias simuladas en estas figuras. Los símbolos geométricos grandes (chicos) son usados para representar galaxias simuladas con alta (baja) resolución. Los símbolos abiertos se usan cuando $t_{\rm off} = 40$ Myr y sólidos cuando $t_{\rm off} = 20$ o 10 Myr. Los círculos, pentágonos y cuadrados se usan para corridas donde $\epsilon_{\rm SF}$= 0.5, 0.2, y 0.67, respectivamente; un triángulo es usado cuando la masa de la partícula estelar es calculada en lugar de la asignación que se haría como una fracción de la masa en gas de la celda (ver Sección anterior). Las corridas que corresponden al mismo sistema galaxia/halo tienen el mismo color. Los símbolos tachados por una cruz corresponden a las simulaciones de alta resolución con más celdas (A^*_{h1}, B^*_{h1}, and C^*_{h1}). El triángulo abierto invertido corresponde a la simulación con el esquema de formación estelar "estocástico" y en el que además no se apaga el enfriamiento.

En la Figura 2.1 se reporta la *TFEE* de las simulaciones a cuatro épocas ($z = 0.0, 0.3, 1.0$, y 1.5) como función de la correspondiente M_s a dicha época (símbolos geométricos). Aquí la TFE a un corrimiento al rojo dado es calculada sumando la contribución de la masa de todas las partículas estelares con edades menores que 0.1 Gyr localizadas en un cilindro con 1.0 h^{-1}kpc (propio) de alto por 20.0 h^{-1}kpc de radio, centrado en el disco gaseoso. Esta masa dividida por 0.1 Gyr es entonces la TFE. El ancho temporal de 0.1 Gyr es suficientemente amplio para evitar pequeñas fluctuaciones en los valores de la TFE.

Cuadro 3.2: Propiedades físicas a $z = 0$ de las Galaxias Simuladas

Name	$M_{\rm v}$	M_s	f_g	R_e	$V_{\rm max}$	SFR	F_s	F_b
(1)	(2)	(3)	(4)	(5)	(6)	(7)	(8)	(9)
	(10^{10} $M_\odot$)	(10^9 $M_\odot$)		(kpc h^{-1})	(km s^{-1})	($M_\odot$ yr^{-1})		
A_{h1}	1.97	0.17	0.051	0.45	50.8	0.000	0.009	0.009
A^*_{h1}	2.01	0.30	0.058	0.31	52.9	0.000	0.015	0.016
B_{h1}	2.32	0.22	0.440	0.59	49.4	0.003	0.009	0.017
B^*_{h1}	2.46	0.21	0.690	0.50	55.9	0.009	0.009	0.027
C_{l1}	2.80	0.10	0.850	0.66	57.1	0.000	0.004	0.023
C_{h1}	2.48	0.21	0.480	0.94	44.2	0.006	0.009	0.016
C^*_{h1}	2.84	0.16	0.760	0.74	51.4	0.012	0.006	0.024
D_{h1}	3.65	0.44	0.620	0.66	60.9	0.013	0.012	0.032
E_{l1}	5.94	3.47	0.100	0.55	126.0	0.110	0.058	0.065
E_{h1}	5.11	1.84	0.048	0.83	82.2	0.016	0.036	0.038
E_{h2}	5.31	2.02	0.340	1.05	84.0	0.044	0.038	0.058
E_{h3}	5.76	3.56	0.280	0.80	104.8	0.062	0.062	0.086
F_{l1}	7.79	5.01	0.350	0.84	124.1	0.360	0.064	0.099
F_{h1}	6.56	3.74	0.072	0.97	87.5	0.038	0.057	0.061
G_{l1}	8.37	3.88	0.110	0.67	125.9	0.120	0.046	0.052
G_{l2}	9.52	7.82	0.220	0.55	185.0	0.650	0.082	0.106
H_{l1}	14.5	10.0	0.054	1.03	188.0	0.120	0.069	0.073
I_{l1}	30.4	22.8	0.170	1.10	254.8	0.480	0.075	0.090
I_{h1}	30.5	25.4	0.230	1.75	213.3	0.150	0.083	0.108
J_{l1}	35.8	20.9	0.070	1.21	214.3	0.150	0.058	0.063
J_{l2}	40.4	29.2	0.140	0.85	279.2	0.370	0.072	0.084

La tendencia general es que las TFEE en las simulaciones decrezcan con el tiempo, aunque, como se reporta en Avila-Reese et al. (2011a, ver Fig. 4), en general, las historias de la TFE, y por lo tanto las de la TFEE, son claramente episódicas. Es de remarcar que a bajos corrimientos al rojo ($z = 0$ y 0.33), todas las galaxias simuladas tengan TFEEs por debajo de la TFEE que tendrían si hubieran formado tods sus estrellas con una TFE constante[3] (línea segmentada horizontal). Esto significa que la M_s de estas galaxias se ensambló relativamente pronto, siendo las TFEs actuales menores que sus promedios en el pasado (*las galaxias entraron en una fase en que la FE esta apagada*). Para altos corrimientos al rojo, $z = 1.0$ y 1.5, las TFEEs de la mayoría de las simulaciones de alta resolución tienden a tener desde entonces valores cercanos a la línea TFE = const., lo que significa que estas galaxias se encuentran en su fase activa de FE y de ensamblaje de M_s. En general, en la Figura 3.1 se puede observar que los distintos experimentos

[3]Si la TFE = const. en el tiempo, entonces TFE/M_s= 1/[(1 – R)($t_H(z)$ – 1 Gyr)], donde $R = 0.4$ es el factor de reciclaje promedio de gas debido a la perdida de masa estelar, t_H es el tiempo cósmico, y 1 Gyr es restado para tomar en cuenta el inicio de la formación de la galaxia.

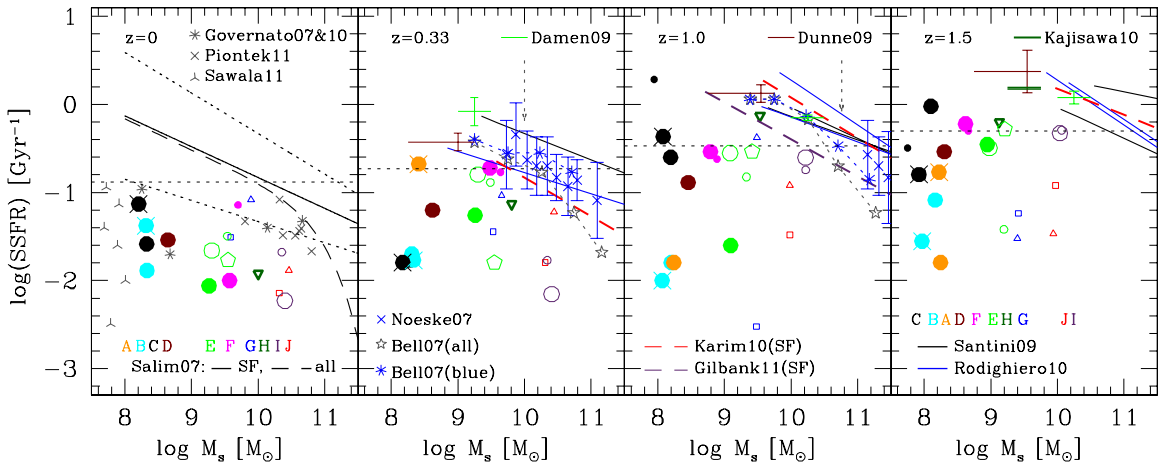

Figura 3.1: Tasas de formación estelar por unidad de masa estelar de la galaxia (tasa de formación estelar especifíca, TFEE) como función de la masa estelar M_S para $z = 0, 0.33, 1.0, 1.5$. A $z = 0$ se presenta los resultados reportados por Salim et al. (2007) para galaxias de toda la muestra en el SDSS (línea segmentada gris) y aquellas con formación estelar (línea sólida negra, y con línea punteada su respectiva dispersión $1 - \sigma$). Los asteriscos en azul y las estrellas en gris representan datos observacionales determinados por el CDFS para las galaxias azules y todas las galaxias de la muestra respectivamente, (Bell et al. 2007). Cruces con barras de error: datos observacionales reportados por Noeske et al. (2007b) que muestran la media y la desviación estandar de la muestra (AEGIS) para la TFEE en el rango donde la muestra es 95 % completa. Las líneas representan ajustes a observaciones dados por los autores indicados en los paneles. Los distintos símbolos en colores representan datos para diferentes modelos de galaxias (colores) obtenidos de simulaciones numéricas (H+ART), de alta (símbolos grandes) y baja (pequeños) resolución.

hechos al variar los parámetros sub-malla no son una fuente de cambios significantes y/o sistemáticos en la TFEE de las galaxias simuladas.

En cada panel de la Figura 3.1, se grafica también la compilación de inferencias observacionales descrita en la sección 2.1. Como se discutió anteriormente, los datos de la compilación obedecen el límite de completitud dado por los diferentes autores. En esta figura claramente se aprecia cómo las TFEEs de todas las galaxias simuladas caen por debajo de las determinaciones observacionales desde $z \approx 1.5$ hasta $z \approx 0$, especialmente cuando se les compara con las inferencias para galaxias reportadas como “star forming”. En el panel a $z = 0$ se presenta una compilación de resultados numéricos recientes (símbolos en color gris) que muestran el mismo problema que las simulaciones de nuestro trabajo.

Si solo consideramos nuestras simulaciones de alta resolución con $\epsilon_{\rm SF} = 0.5$, esti-

mamos que las TFEEs en el rango de masas $M_s \sim 10^8{-}10^{10}\ M_\odot$ son $\sim 5{-}10$ veces más bajas que los promedios inferidos por las observaciones a $z \approx 0$. Estas diferencias son del mismo orden o tal vez un poco menores a $z \approx 0.33$. A altos corrimientos al rojo ($z \approx 1.0{-}1.5$), la comparación se vuelve difícil de hacer por lo incompletas que se vuelven las muestras observacionales a las bajas masas. Es notable el desplazamiento sistemático de la relación TFEE–M_s de las galaxias observadas conforme z decrece: en promedio, la masa estelar típica, $M_{\rm quench}$, que cruza por debajo de la línea correspondiente al caso de la TFE constante a cada z (líneas horizontales segmentadas en la Figura 2.1) decrece con el tiempo. En otras palabras, mientras más bajo sea z, mas pequeñas en promedio son las galaxias que empiezan a apagar su FE (*Downsizing en la TFEE*). Es interesante ver que este mismo fenómeno, el del "downsizing" de la $M_{\rm quench}$, esta de acuerdo con el respectivo "downsizing" de la masa de transición de galaxias activas a pasivas que se encuentra a partir de modelos semi-empíricos en Firmani & Avila-Reese (2010): $\log M_{\rm tran}(z) = 10.30 + 0.55z$. *Para las galaxias simuladas, no hay evidencia de que este fenómeno ocurra*.

En la figura 3.2 mostramos la fracción de masa estelar, $f_s \equiv M_s/M_h$ para 4 épocas, $z = 0, 0.33, 1.0, 1.5$ de nuestras galaxias simuladas. Los resultados numéricos de otros autores a $z \approx 0$ también se grafican en el panel izquierdo (símbolos en color gris). Las curvas sólidas son el promedio de inferencias semi-empíricas (Behroozi, Conroy & Wechsler 2010; Conroy & Wechsler 2009; Firmani & Avila-Reese 2010) previamente discutidas en la sección 2.1.3. La barra de error en la Figura 3.2 indica el $\pm 1\sigma$ aproximado que resulta de considerar las incertidumbres estadísticas en las inferencias. El factor que más contribuye a tal incertidumbre viene de las suposiciones que se hacen para pasar de la luminosidad de una galaxia a su respectiva M_s (Behroozi, Conroy & Wechsler 2010).

Lo que observamos en la Figura 3.2 es que mientras menor es la masa, menor es también la f_s, tanto para las galaxias simuladas, como para las inferencias semi-empíricas. Sin embargo, las simulaciones numéricas confirman el problema que adolecen prácticamente todos los trabajos previos: sus fracciones de masa estelar (y bariónica) son muy altas con relación a las inferencias observacionales, por ejemplo, a $z \approx 0$, las diferencias son del orden de 5–10 veces; esto implica que el gas cae y se transforma en estrellas con demasiada eficiencia. Tal vez por eso mismo las TFEEs tardías observadas, desde $z \sim 1$, son altas, es decir, *la formación estelar en las galaxias pequeñas se retrasó por alguna razón con relación a lo que las simulaciones muestran*.

En esta misma dirección, es de notar que en las galaxias simuladas, F_s cambia muy poco en el rango de corrimientos al rojo aquí estudiados, mientras que las masas de los halos decrecen al incrementarse z. Por lo tanto se esperaría que la relación F_s–$M_{\rm v}$ se desplazará en promedio hacia el lado de las bajas masas conforme z crece. Claramente este comportamiento es contrario a las inferencias semi-empíricas.

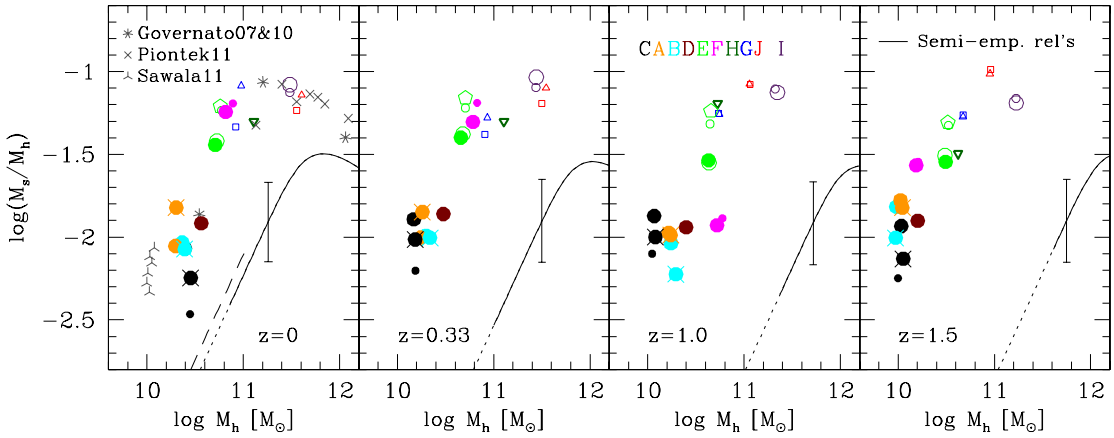

Figura 3.2: Fracciones de masa estelar f_S como función de la masa del halo M_h para $z = 0, 0.33, 1.0, 1.5$. Las líneas negras representan inferencias semi-empíricas reportadas por Firmani & Avila-Reese (2010). Los distintos símbolos en colores representan datos para diferentes modelos de galaxias (colores) obtenidos de simulaciones numéricas (H+ART), de alta (símbolos grandes) y baja (pequeños) resolución.

3.1.3. Discusión

En Avila-Reese et al. (2011a) estudiamos simulaciones de galaxias de alta resolución que tienen propiedades dinámicas y estructurales similares a las galaxias de campo de baja masa con las que se pueden comparar. Los principales resultados, de interés para este trabajo de tesis doctoral, se presentaron en la sección anterior y son tales que nos permiten concluir que:

- Las TFEEs a $z \sim 0$ y ~ 0.3 de las galaxias simuladas en el rango de masas $M_s \sim 10^8{-}10^{10}$ $M_\odot$ son $5{-}10$ veces menores que los valores medios inferidos por una gran muestra de observaciones de galaxias de campo (Figura 2.1). No obtuvimos una sola galaxia de alta resolución que tuviera una TFEE suficientemente alta para caer por encima del 1σ inferior reportado por Salim et al. (2007) para galaxias activas ("star-forming") a $z \sim 0$.

- La evolución de las relaciones TFEE–M_s (determinadas observacionalmente) muestra una clara tendencia de "downsizing" para la masa estelar típica, $M_{\rm quench}$, de galaxias que pasan de ser activas a pasivas. No hay evidencia de que tal tendencia se reproduzca en las simulaciones numéricas de galaxias.

- Las fracciones de masa estelar ($F_s \equiv M_s/M_{\rm v}$) de las galaxias simuladas son $5{-}10$ veces más grandes a $z \sim 0$ que las determinaciones actuales (semi-empíricas) de estas fracciones como función de M_s (Figure 3.2). A altos corrimientos al rojo las diferencias llegan incluso a ser más significativas.

Así, nuestras simulaciones numéricas confirman los problemas previamente encontrados con modelos semi-numéricos de evolución de galaxias de disco en el contexto del escenario ΛCDM(Firmani & Avila-Reese 2010): *en promedio, las galaxias de baja masa parecen ensamblar el grueso de su masa estelar mucho más temprano que lo que sugieren las inferencias observacionales y semi-empíricas vía las relaciones TFEE–M_s y F_s–M_s a corrimientos al rojo $z < 1$.*

El planteamiento y la resolución de los problemas del "downsizing" de la TFEE y de las fracciones estelares en el contexto del escenario jerárquico ΛCDM son de gran interés y relevancia en el campo. El abanico de posibilidades va desde un señalamiento a inconsistencias (¿sistemáticos?) en las inferencias observacionales actuales, hasta evidencias de necesidad de modificaciones a la física de los bariones incluida como parametrizaciones de la física no resuelta en los códigos cosmológicos bajo el escenario ΛCDM. El explorar algunas de estas posibilidades queda fuera del presente trabajo de tesis doctoral y se deja como trabajo a futuro.

3.2. Simulaciones numéricas de caja cosmológica

Las simulaciones numéricas de galaxias presentadas en Avila-Reese et al. (2011a) son en realidad resimulaciones de alta resolución de pocos objetos seleccionados especialmente para esto. Estas claramente nos permiten estudiar las propiedades de las galaxias hasta escala de cientos de parsecs, sin embargo no nos permiten hacer un estudio estadístico de las propiedades integradas de las galaxias. Es interesante saber si los potenciales problemas señalados en la sección anterior persisten o no cuando se analizan un gran número de simulaciones. Con este objetivo, en el artículo De Rossi et al. (2013) en el cual fui invitado a colaborar, analizamos las historias de TFE y ensamblaje de masas estelares, oscuras y gaseosas de una caja cosmológica entera (de 14 Mpc de lado).

3.2.1. Del código y la simulación cosmológica

La simulación fue realizada con el código GADGET-3, una actualización de GADGET-2 optimizada para simulaciones en paralelo (Springel & Hernquist 2003; Springel 2005). La versión de GADGET-3 usada aquí incluye el modelo multifase para el medio interestelar (MIE) y el esquema de retroalimentación por SNs de Scannapieco et al. (2005, 2006). Dicho esquema considera tanto supernovas tipo Ia como tipo II para la producción de energía y la química. Una de las ventajas de este código es el uso de un modelo de evolución química (Mosconi et al. 2001; Scannapieco et al. 2005) el cual determina la inyección de metales en el MIE. Bajo este esquema de inyección de energía y elementos pesados en las diferentes componentes del MIE, y dadas las propiedades termodinámicas locales, el modelo es capaz de generar vientos galácticos (ver De Rossi et al. 2013)

En este trabajo se estudió una población completa de galaxias tomadas de una caja cúbica de 14.3 Mpc de lado representando una "región de un campo típico" de un Universo ΛCDM con $\Omega_m = 0.3$, $\Omega_\Lambda = 0.7$, $\Omega_b = 0.045$, una normalización del espectro de potencias $\sigma_8 = 0.9$ y $H_0 = 100h$km s^{-1} Mpc^{-1} con $h = 0.7$. La simulación se corrió usando 2×230^3 partículas dando una resolución en masa de $8.4 \times 10^6 M_\odot$ y $1.3 \times 10^6 M_\odot$ para las componentes de materia oscura y gas respectivamente. Se identificaron las estructuras virializadas empleando la técnica estándar de "friends-of-friends", mientras que para el caso de las subestructuras se usó el algoritmo SUBFIND de Springel et al. (2001). La muestra principal, y que es de interés para los objetivos de este trabajo de tesis, se construyó usando solo galaxias centrales en cada halo de materia oscura. Para disminuir los posibles problemas con la resolución, se restringió el estudio a galaxias con $M_{\rm vir} \gtrsim 10^{10.3} M_\odot$, que corresponde a un total de partículas $N_{SUB} > 2000$ en las galaxias centrales. Así, cumpliendo con este criterio, en esta simulación de caja cosmológica se obtuvieron 214 + 46 y 187 + 22 galaxias centrales/satélites a $z = 0$ y $z = 2$, respectivamente.

Las principales propiedades de las galaxias simuladas se calcularon al "radio barióni-

co" (R_{bar}), definido como el radio que encierra el 83 por ciento de la masa bariónica de las galaxias. Para cada galaxia se estimaron la masa en estrellas (M_s), la masa en gas (M_g), la masa bariónica (M_b), y la TFE. Tomando en cuenta que los trazadores observacionales para la TFE son sensibles típicamente a períodos de $\sim$ 30–100 Myr, en este trabajo la TFE se calculó como el incremento en estrellas durante un período temporal de 100 Myr para obtener valores de la TFE promedio[4] en casos cuando esta procede de manera muy intermitente durante ciertas épocas. De igual manera, para cada halo se calculó su radio virial ($R_{\rm v}$) y las respectivas propiedades para las demás componentes hasta este radio: $M_s^{\rm v}$, $M_g^{\rm v}$, y $M_b^{\rm v}$.

Aunque la resolución es menor a la de las galaxias simuladas en Avila-Reese et al. (2011a) y el código y parámetros sub-malla son diferentes, esta simulación de caja nos proporciona estadística y la posibilidad de determinar historias promedio en función de las masas, algo que es útil para comparar con las observaciones. Vale la pena recalcar que aunque no se discutirá aquí, las galaxias formadas en esta caja cosmológica son tales que sus propiedades y correlaciones son consistentes con las inferidas observacionalmente para galaxias del Universo local (v. gr., de Rossi, Tissera & Pedrosa 2010; De Rossi, Tissera & Pedrosa 2012).

3.2.2. Resultados y comparación con el modelo paramétrico

El análisis de la simulación estuvo centrado principalmente para $z \lesssim 2$ debido a que a corrimientos al rojo más altos, el número de galaxias resueltas con $N_{sub} > 2000$ es muy bajo, y además las inferencias observacionales para las propiedades de galaxias de baja masa se vuelven imcompletas o poco robustas cuando las hay. Así, a continuación presentamos los resultados relevantes de De Rossi et al. (2013) en los que se comparan las propiedades de las galaxias simuladas con las inferencias del modelo paramétrico presentado en la Sección 2.3.

En la Figura 3.3 se muestran las TFEEs de las galaxias simuladas promediadas en "bines" de $logM_s$ como función de los valores promedio de $logM_s$ en cada bin. Las líneas verticales corresponden a la desviación estándar en torno a la media en cada bin de masa para la muestra total de galaxias. La línea horizontal segmentada en cada panel muestran la TFEE que tendrían las galaxias a esa época si estas hubieran formado sus estrellas con una TFE constante, tal como se discutió en la Sección 3.1.2. Así, en esta figura podemos identificar que las galaxias simuladas muestran que existe una correlación entre la TFEE y la M_s en todas los cuatro z's estudiados; le desviación estándar es ≈ 0.3 dex a $z = 0$ y no cambia significativamente a alto z para caulquier rango de masa. Además se pudo determinar que la pendiente de dicha correlación evoluciona con z, de tal manera que a alto z la relación se vuelve prácticamente plana (al hacer un ajuste lineal en el plano log-log, la

[4]Este es el mismo lapso de tiempo usado a lo largo de este trabajo para calcular el cambio en las propiedades generales de las galaxias.

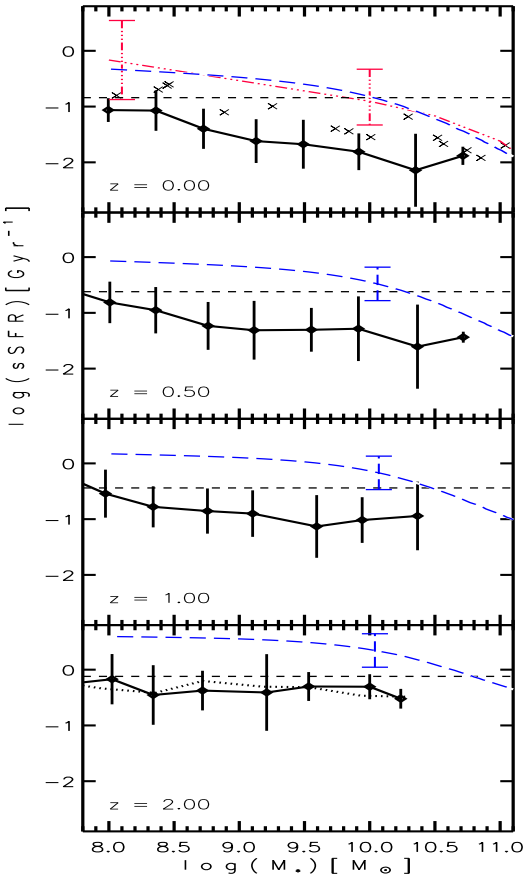

Figura 3.3: TFEE versus M_s a $z = 0$, 0.5, 1, y 2. El promedio de la relación y su dispersión 1σ se muestran con líneas sólidas negras. Las líneas horizontales segmentadas indican la TFEE a cada época que corresponden al caso de una TFE constante en su pasado: galaxias por encima (debajo) de esta línea de TFE constante se encuentran en una fase activa (pasiva) de FE. Las curvas segmentadas azules corresponden al modelo paramétrico presentado en la Sección 2.3. En $z = 0$ se muestra el ajuste a los datos observacionales de Salim et al. (2007) y su dispersión 1σ se muestra con las barras en color rojo. Las cruces representan una submuestra de las galaxias simuladas con altas TFEEs que estan en mejor acuerdo con las observaciones.

pendiente obtenida para la relación es ≈-0.4, -0.28, -0.20, y -0.06 a $z = 0$, 0.5, 1.0 y 2.0 respectivamente). También se observa que la media de las TFEEs de las galaxias simuladas es menor que las respectivas al caso de una TFEE constante (identificada por las líneas segmentadas horizontales) desde $z \sim 2$; esta diferencia se acentúa para las galaxias de mayor M_s en z's recientes. El promedio de la TFEE de toda la muestra a cada época decrece significativamente con z, cayendo del orden de un factor $\sim 10-15$ desde $z = 2$ hasta $z = 0$.

Las líneas segmentadas azules en la Figura 3.3 denotan los ajustes a las observaciones derivadas por el modelo paramétrico presentado en la Sección 2.3. Aquí se observa que las galaxias simuladas tienen TFEEs promedio más bajas que las inferidas por las observaciones, siendo las diferencia mayor conforme z decrece. Más aun, como ya se mencionó anteriormente, las simulaciones presentan TFEEs menores a la línea asociada con una TFE constante. Las diferencias con respecto a este caso se incrementan con la masa estelar y decrecen con el corrimiento al rojo, sugiriendo que la fase activa de FE en las galaxias simuladas tuvo lugar desde épocas muy tempranas, a $z > 1$. A pesar de esto, es importante recalcar que *las simulaciones si reproducen cualitativamente el incremento de la TFEE observado para las galaxias de baja masa a z's bajos (downsizing en la TFEE), además de predecir el aplanamiento de la correlación TFEE–M_s a altos corrimientos al rojo*.

El ensamblaje de la masa estelar en nuestras simulaciones se puede apreciar en la Figura 3.4 donde se muestran las curvas de ensamblaje de masa estelar para cuatro intervalos de masa de halo promedio. Aquí las barras de error denotan la desviación estándar asociada; las correspondientes líneas segmentadas se obtienen al considerar la masa estelar total dentro de $R_{\rm v}$ (en lugar de R_{bar}). De acuerdo con esta Figura las

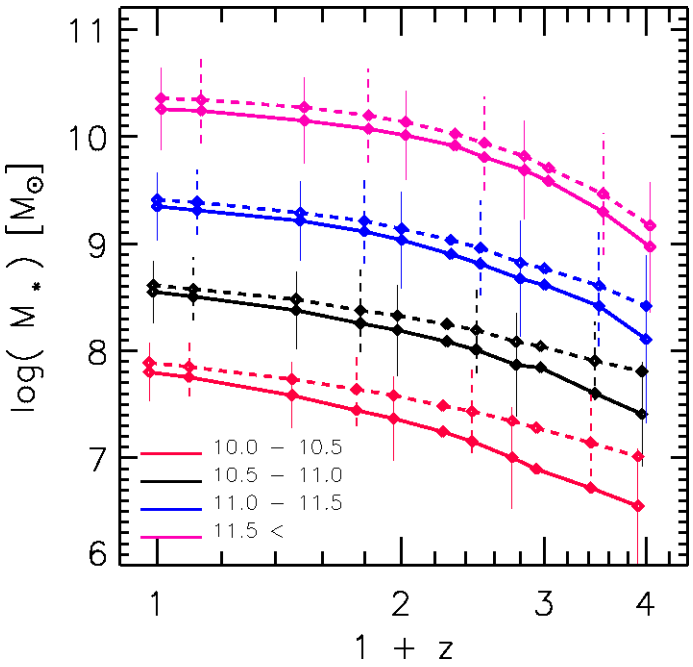

Figura 3.4: Historias de ensamblaje de masa estelar promedio (líneas sólidas) para las galaxias de la simulación de caja cosmológica (De Rossi et al. 2013) en 4 intervalos de masa de halo indicados en el panel. Líneas punteadas: los correspondientes promedios para la masa estelar total dentro de $R_{\rm v}$ (incluyendo satélites).

galaxias simuladas en el intervalo menor de masas tiende a mostrar un ensamblaje tardío, mientras que las más masivas (tipo Vía Láctea) se ensamblaron más temprano. Probablemente la eficiente retroalimentación por SNs introducida en el código actúa al punto de revertir el crecimiento jerárquico en M_s, sólo que el efecto es menor a lo que las observaciones implican: las galaxias simuladas siguen teniendo TFEE menores para sus masas estelares y fracciones estelares mayores que las observaciones (De Rossi et al. 2013).

El comportamiento descrito es más evidente si graficamos la evolución en z de las F_s promedio, Figura 3.5 (líneas sólidas). Como puede verse, a todas las épocas, F_s es sistemáticamente menor en galaxias formadas en halos de baja masa al día hoy, que en galaxias formadas en halos de mayor masa. De hecho, la evolución de la F_s aunque con una gran dispersión, es tal que para galaxias de baja masa, F_s decrece conforme z aumenta. Mientras que para galaxias de mayor masa, F_s no cambia significativamente desde $z \sim 2$.

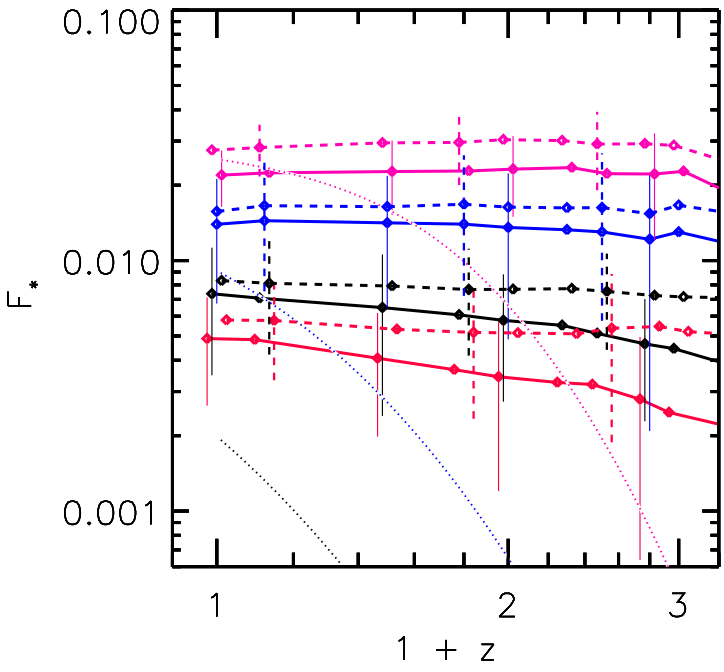

Figura 3.5: Evolución de las F_s promedio (líneas sólidas) para las galaxias de la simulación de caja cosmológica (De Rossi et al. 2013) en los 4 intervalos de masa de halo indicados en la figura 3.4. Las barras de error representan la dispersión 1σ de la población. Las líneas segmentadas muestran los correspondientes promedios para la F_s obtenidos al considerar la masa total dentro de $R_{\rm v}$ (incluyendo satélites). Las líneas punteadas son las inferencias derivadas usando el modelo paramétrico presentado en la Sección 2.3.

Estos nos sugiere que, *para las galaxias de mayor masa ($M_s > 10^{10} M_\odot$), M_s tiende a ensamblarse a una tasa similar que $M_{\rm v}$, mientras que por los sistemas de menor masa, M_s retrasa su ensamblaje con respecto a $M_{\rm v}$*.

Con respecto a la comparación con las inferencias empíricas basadas en el modelo paramétrico, en la Figura 3.5 graficamos la evolución de la F_s (líneas punteadas) asociada con galaxias que al día de hoy tienen $log(M_s/M_\odot) = 10.3$, 10.75, 11.25 y 11.75 (de abajo hacia arriba en la figura), los cusales son representativos de los rangos en masa estudiados en las simulaciones. Así, se observa quela evolución de la F_s inferida con el modelo paramétrico de desvía drásticamente del predicho por las simulaciones. Conforme la masa decrece, el modelo sugiere un retraso significativo del ensamblaje de la masa estelar con respecto del halo. Esta discrepancia puede ser explicada parcialmente por el hecho de que las historias de ensamblaje del halo usadas para contruir el modelo (Fakhouri, Ma & Boylan-Kolchin 2010, ver Fig. 7) decaen mucho menos rápido que las de los halos en esta simulación.

3.2.3. Discusión

Si bien en De Rossi et al. (2013) se realizó un estudio más profundo que el presentado aquí con respecto del ensamblaje de masas de galaxias simuladas en un escenario ΛCDM, sí es importante señalar que la comparación de dicha simulación cosmoógica con las inferencias semi-empíricas basadas en nuestro modelo paramétrico, nos permite extraer conclusiones bastante interesantes que son relevantes para el presente trabajo de investigación doctoral. En particular, podemos concluir que,

- En las simulaciones, la TFEE tiende a incrementarse si la M_s decrece (*downsizing en la TFEE*), pero a alto z, la relación se aplana. Esto reproduce el comportamiento cualitativo inferido por las observaciones. Sin embargo, los valores de la TFEEs en las simulaciones están muy por debajo de los medios en galaxias observadas, especialmente en el Universo local.

- En todos los z's estudiados, F_s decrece significativamente para valores de $M_{\rm v}$ bajos. Con respecto a la evolución de la relación F_s, se encontraron difeencias significativas entre las simulaciones y las inferencias semi-empíricas a bajas masas. De acuerdo con estas inferencias, para una dada $M_{\rm v}$, F_s tiende a disminuir si z crece, pero para las galaxias simuladas, la relación F_s–$M_{\rm v}$ no exhibe variaciones significativas desde $z \sim 2$, evidenciando un ensamblaje muy temprano de la masa estelar en las simulaciones.

- En los halos de mayor masa al día de hoy, la masa estelar promedio solo se incrementó ligeramente desde $z \sim 2$, mientras que para los halos más pequeños, el ensamblaje "tardío" de masa se desarrolla más rápido. En este sentido, aunque con una gran dispersión de por medio, la tendencia jerárquica (upsizing) del ensamblaje del halo

parece revertirse *moderadamente* a una tendencia tipo anti-jerárquica (downsizing) en el respectivo ensamblaje para la componente estelar.

- El ensamblaje de la masa estelar dentro de halos que crecen bajo un escenario ΛCDM inferido a partir de nuestro modelo paramétrico es capaz de reproducir la tendencia anti-jerárquica (downsizing) que muestran las observaciones. Las trazas evolutivas de la masa estelar en este modelo crecen mucho más rápido que las obtenidas en las simulaciones presentadas en este trabajo. Y aunque se ha señalado que las galaxias de más baja masa en las simulaciones experimentan un retraso en su ensamblaje de masa estelar con respecto al del halo en que viven, este es todavía muy pequeño como para reproducir los estudios observacionales actuales de galaxias de baja masa.

Finalmente, es importante enfatizar que, aunque con una tendencia moderada, *el modelo de retroalimentación por SN usado en este trabajo es capaz de invertir la tendencia de "upsizing" en el ensamblaje de masa de los halos (característica de los halos en el escenario ΛCDM), para llevarlo a un "downsizing" en el ensamblaje de la componente estelar (como el inferido por las observaciones).*

Capítulo 4

Historias de ensamblaje de galaxias enanas en simulaciones cosmológicas

Hasta ahora, hemos analizado como se comparan las propiedades de galaxias de baja masa observadas ($M_s \leq 3 \times 10^{10} M_\odot$) y sus inferencias semi-empíricas con los resultados de simulaciones cosmológicas a diferentes corrimientos al rojo. Esta comparación nos ha permitido identificar un potencial problema en los modelos y simulaciones para reproducir como es el ensamblaje de masa de estas galaxias. La pregunta es ¿Qué determina cómo se lleva a cabo el ensamblaje de las galaxias de baja masa?

Estudios recientes apuntan a que la masa del halo determina en gran medida las propiedades integradas de las galaxias. Sin embargo, para una masa de halo fija, es posible obtener galaxias con propiedades muy diversas. Así, es natural buscar otra variable que nos ayude a entender tal diversidad; las posibilidades pueden ser muchas: el momento angular del halo, el ambiente en el que viven, su historia de ensamblaje de masa, etc. En este capítulo, por medio de simulaciones cosmológicas de alta resolución estudiaremos esta última posibilidad.

4.1. Simulaciones de galaxias enanas aisladas formadas en halos de materia oscura fría con diferentes historias de ensamblaje de masa

A continuación se presenta el artículo González-Samaniego, A., et al. (2014a) que comparte el mismo título de esta sección pero en idioma inglés. En este se estudian las HEM de siete galaxias enanas simuladas con muy alta resolución ($\sim$60 parsecs) donde todas tienen $M_{\rm v} \approx 3 \times 10^{10} M_{\odot}$ a $z = 0$. Para esto se utilizó el código ART con hidrodinámica ya descrito en la sección 3.1. Los principales objetivos son (1) estudiar las HEM de las distintas componentes: halo, estrellas, y gas, y (2) explorar los efectos de las HEM de los halos tanto en el ensamblaje estelar/bariónico de las enanas simualadas como en sus propiedades al día de hoy.

Los resultados generales nos dicen que: a) El cociente M_s-$M_{\rm v}$ es ≈ 0.01 y permanece constante desde $z \sim 1$ (la HEM de las estrellas sigue muy de cerca la HEM del halo). Con un valor más pequeño a altos z's para aquellos halos que ensamblaron su masa después. b) La evolución de la fracción de gas, f_g, es episódica y más grande, la mayor parte del tiempo, que la fracción estelar. Lo anterior muestra que los vientos generados por las supernovas (SNs) juegan un papel importante en regular las fracciones de gas –y por lo tanto la TFE– de las enanas. c) Las historias de FE son episódicas con cambios en las TFE, medidas cada 100 Myr, de factores 2–10 en promedio. d) Aunque las enanas formadas en halos que se ensamblaron tardíamente muestran historias de FE mas extendidas, sus TFE al día de hoy están aún por debajo de las medidas para enanas aisladas en el Universo local. e) Los efectos de los bariones sobre la $M_{\rm v}$ son tales que a casi todo tiempo en la evolución del halo, $M_{\rm v}$ es 10–20 % más pequeña que la correspondiente $M_{\rm v}$ obtenida en simulaciones sin hidrodinámica.

Nuestros resultados sugieren que más que incrementar la magnitud de los vientos impulsados por SNs, procesos que reduzcan aún más la eficiencia de FE ayudarán a resolver los potenciales problemas que enfrentan las simulaciones de galaxias enanas en un escenario de MOF, tales como los pequeños valores predichos para la TFEE y los altos valores para las masas estelares al día de hoy.

4.2. Simulations of isolated dwarf galaxies formed in dark matter halos with different mass assembly histories

A. González-Samaniego[1], P. Colín[2], V. Avila-Reese[1], A. Rodríguez-Puebla[1], and O. Valenzuela[1]

The Astrophysical Journal, Volume 785, Issue 1, article id. 58, 15 pp. (2014)

Abstract

We present zoom-in *N*-body/hydrodynamics resimulations of dwarf galaxies formed in isolated cold dark matter (CDM) halos with *the same virial mass* ($M_{\rm v} \approx 2.5 \times 10^{10} M_{\odot}$) at redshift $z = 0$. Our goals are to (1) study the mass assembly histories (MAHs) of the halo, stellar, and gaseous components; and (2) explore the effects of the halo MAHs on the stellar/baryonic assembly of simulated dwarfs. Overall, the dwarfs are roughly consistent with observations. More specific results include: (1) the stellar-to-halo mass ratio remains roughly constant since $z \sim 1$, i.e., the stellar MAHs closely follow halo MAHs. (2) The evolution of the galaxy gas fractions, f_g, are episodic, showing that the supernova-driven outflows play an important role in regulating f_g and hence, the star formation rate, SFR; however, in most cases, a large fraction of the gas is ejected from the halo. (3) The star formation histories are episodic with changes in the SFRs, measured every 100 Myr, of factors 2–10 on average. (4) Although the dwarfs formed in late assembled halos show more extended SF histories, their $z = 0$ specific SFRs are still below observations. (5) The inclusion of baryons most of time reduces the virial mass by 10 %–20 % with respect to pure N-body simulations. Our results suggest that rather than increasing the strength of the supernova-driven outflows, processes that reduce the star formation efficiency could help to solve the potential issues faced by CDM-based simulations of dwarfs, such as low values of the specific SFR and high stellar masses.

4.3. Introduction

The Λ cold dark matter (ΛCDM) cosmology provides a robust theoretical background for understanding galaxy formation and evolution. The properties and evolution of galaxies predicted by the results of models and simulations based on the ΛCDM cosmology are encouraging, though several potential issues remain yet to be solved. One of these potential issues refers to the history and efficiency of the stellar mass assembly of low-mass galaxies, those with stellar masses $M_s \lesssim 10^{10}\ M_{\odot}$.

[1]Instituto de Astronomía, Universidad Nacional Autónoma de México, A.P. 70-264, 04510, México, D.F., México

[2]Centro de Radioastronomía y Astrofísica, Universidad Nacional Autónoma de México, A.P. 72-3 (Xangari), Morelia, Michoacán 58089, México

Several observational pieces of evidence show that low and intermediate redshift galaxies less massive than $M_s \sim (5-10) \times 10^9\ M_\odot$ have high specific star formation rates (sSFR $\equiv$ SFR/M_s), with larger values, on average, for less massive galaxies (e.g., Salim et al. 2007; Noeske et al. 2007a; Rodighiero et al. 2010; Karim et al. 2011; Bauer et al. 2011; Gilbank et al. 2011; Bauer et al. 2013). This shows that the smaller the galaxies, the later they assemble their stellar mass, on average, having younger stellar populations (downsizing in sSFR; see for reviews Fontanot et al. 2009; Firmani & Avila-Reese 2010). From an analysis of local galaxies, Geha et al. (2012) conclude that virtually all galaxies less massive than $M_s \approx 10^9\ M_\odot$ in the field show evidence of high recent star formation (SF) and have relatively young stellar populations. On the other hand, by applying a Bayesian analysis of the observed spectral energy distribution (SED) of low-mass galaxies ($M_s = 1.6-4.0 \times 10^9\ M_\odot$) at $0.2 < z < 1.4$ with synthetic SEDs, Pacifici et al. (2013) find that these galaxies have, on average, a rising SF history (SFH), contrary to massive galaxies for which the SF decreases with time (see also Pérez et al. 2013). Finally, it should be said that low-mass galaxies, specially dwarf galaxies, are susceptible to episodic (bursty) SFH; hence, any statistical inference of an average SFH could be biased (Bauer et al. 2013).

In agreement with the apparently late M_s assembly, several pieces of evidence show that low-mass galaxies have very low stellar and baryonic mass fractions, $F_s \equiv M_s/M_{\rm v}$ and $F_b \equiv M_b/M_{\rm v}$, respectively, where $M_{\rm v}$ is the virial halo mass: F_s and F_b exhibit a strong dependency on $M_{\rm v}$, decreasing as $M_{\rm v}$ gets smaller (e.g., Conroy, Gunn & White 2009; Guo et al. 2010; Behroozi, Conroy & Wechsler 2010; Behroozi, Wechsler & Conroy 2013b; Moster et al. 2010; Moster, Naab & White 2013; Rodríguez-Puebla et al. 2011; Rodríguez-Puebla, Avila-Reese & Drory 2013; Papastergis et al. 2012).

By applying the common recipes and schemes for SF and feedback, most semi-analytic models (e.g., Somerville et al. 2008; Fontanot et al. 2009; Santini et al. 2009; Liu et al. 2010; Bouché et al. 2010a; Weinmann et al. 2012) and high-resolution hydrodynamic simulations (e.g., Colín et al. 2010; Sawala et al. 2011; Avila-Reese et al. 2011b; De Rossi et al. 2013) predict, instead, that present-day low-mass galaxies, both satellites and centrals, are too red, passive, old, and efficient forming stars in the past, as compared to observations. In some recent works, it is discussed that these discrepancies can be reduced if a proper comparison of simulations with observations is used (Brook et al. 2012; Munshi et al. 2013) and/or when the H_2 formation process and a H_2-based SF scheme are taken into account (Kuhlen et al. 2012; Christensen et al. 2012; Munshi et al. 2013; Thompson et al. 2014).

As recently discussed in the literature, a key question for low-mass galaxies formed in the context of the ΛCDM cosmology is whether the assembly of their stellar and halo masses are closely related or the former is systematically detached from the latter (e.g., Conroy & Wechsler 2009; Firmani & Avila-Reese 2010; Leitner 2012; Behroozi, Wechsler & Conroy 2013b; Yang et al. 2012; Moster, Naab & White 2013; De Rossi et al. 2013). These works suggest that the stellar mass assembly inferred from the average observed galaxy population, as compared to the average theoretical halo mass assembly history (MAH), shows an opposite trend in the sense that while the assembly of less massive ΛCDM halos

Cuadro 4.1: Physical properties at z=0.

Name	$\log(M_{\rm v})$ ($M_\odot$)	$\log(M_s)^a$ ($M_\odot$)	$\log(M_g)$ ($M_\odot$)	$V_{\rm max}$ (km s^{-1})	${R_e}^b$ (kpc)	$R_{\rm v}$ (kpc)	${f_g}^c$	$M_{g,\rm cold}/M_g$	D / T^d	${z_{f,h}}^e$	SFR ($10^{-3} M_\odot$ yr^{-1})
Dw1	10.30	8.10	8.16	52.43	1.29	78.00	0.53	0.93	0.26	3.0	1.69
Dw2	10.46	8.35	8.27	49.59	1.57	79.16	0.45	0.47	0.33	2.3	0.87
Dw3	10.46	8.73	8.07	56.07	1.46	78.50	0.18	0.81	0.01	2.3	0.34
Dw4	10.38	8.38	8.61	52.87	1.14	73.64	0.63	0.67	0.19	1.9	1.08
Dw5	10.46	8.55	9.08	61.52	1.57	77.34	0.77	0.82	0.49	1.9	1.69
Dw6	10.46	8.44	8.93	50.63	4.16	78.00	0.76	0.98	0.66	1.9	13.7
Dw7	10.39	8.21	8.60	43.44	3.14	73.90	0.71	0.75	0.59	1.7	7.76

[a] Mass within $0.1R_{\rm v}$(the same applies for M_g).
[b] Radius that encloses half of the stellar mass within $0.1R_{\rm v}$.
[c] $f_g \equiv M_g/(M_g + M_s)$.
[d] Ratio of the mass contained in the high-angular momentum disk stars with respect to the total stellar mass.
[e] Redshift at which the given halo acquired one third of its present-day mass.

occurs earlier than the assembly of more massive ones, the stellar mass assembly occurs later as the galaxy gets smaller (see, e.g., Figure 4 in Firmani & Avila-Reese 2010). The complex baryonic physics of the galaxy evolution inside growing halos is summarized in this behavior.

Thus, some important questions worth exploring in detail in high-resolution simulations of central low-mass galaxies are: What are the MAHs of the halo, stars, and gas in these galaxies? How much do the stellar/baryonic mass assembly and the galaxy properties depend on the different (stochastic) halo MAHs? How episodic (bursty) could their SFHs be? How much do the physics of baryons affect the dark matter (DM) masses of the small halos at different epochs? These questions are addressed here using zoom N-body/hydrodynamics simulations of seven distinct low-mass halos and their corresponding central galaxies, all with similar present-day halo masses (2-3)$\times 10^{10} M_\odot$. The distinct halos are selected with the criterion of being relatively isolated in such a way that the central galaxies formed inside them can be associated with field dwarf galaxies. The study of subhalos/satellite galaxies have extra complications that are beyond the scope of the present work.

In Section 2, we describe the code and main parameters that will characterize the simulations. In Section 3 we present several results from the simulations as a function of the halo MAHs. The role that baryons play in the halo mass assembly is studied in Section 4. Section 5 is devoted to a discussion of the SF-driven outflows versus other processes that could delay the SF in low-mass galaxies (Section 5.1), the analysis of where the baryons are in the simulated galaxies (Section 5.2), and the episodic SFHs observed in the simulations (Section 5.3). Our conclusions are given in Section 6.

4.4. The method

4.4.1. Code, Star Formation, and Feedback

We perform numerical simulations with the adaptive mesh refinement (AMR) N-body/hydrodynamic ART code (Kravtsov, Klypin & Khokhlov 1997a; Kravtsov 2003a). This is one of the few cosmological codes that uses the Eulerian method to solve the hydrodynamical equations for gas trapped in the DM cosmic structures. Other widely used AMR codes are ENZO (Bryan & Norman 1997) and RAMSES (Teyssier 2002). The ART code incorporates a wide variety of physical processes, including: metal, atomic and molecular cooling, homogeneous UV heating, metal advection, SF, and thermal feedback. The cooling and heating rates, which take into account Compton heating/cooling, and the UV heating from a cosmological background radiation (Haardt & Madau 1996a) are tabulated for a temperature range of 10^2 K $< T < 10^9$ K, and a grid of densities, metallicities (from $Z = -3.0$ to $Z = 1.0$, in solar units), and redshifts using the CLOUDY code (Ferland et al. 1998a, version 96b4). We set the minimum temperature in the code to 300 K; because of the absence of gas self-shielding, such a low temperature is almost never reached in the simulated galaxies.

SF and feedback (subgrid physics) are implemented in the code as discussed in detail in Colín et al. (2010) and Avila-Reese et al. (2011b). Here, we use the same subgrid parameters as in Avila-Reese et al. (2011b) but with better resolution; the size of the cell at the maximum level of refinement (nominal resolution) is ≈ 60 pc at $z = 0$ and up to ≈ 25 pc at the highest redshifts. The actual resolution scale is probably closer to two to four times the size of the cell at the maximum level of refinement. Next, we summarize the subgrid schemes discussed in the above papers.

SF takes place in all those cells for which $T < T_{\rm SF}$ and $\rho_g > \rho_{\rm SF}$, where T and ρ_g are the temperature and density of the gas, respectively, and $T_{\rm SF}$ and $\rho_{\rm SF}$ are the temperature and density threshold, respectively. A stellar particle of mass $m_* = \epsilon_{\rm SF} m_g$ is placed in a grid cell *every time* these conditions are simultaneously satisfied, where m_g is the gas mass in the cell and ϵ_{SF} is a parameter that measures the *local* efficiency by which gas is converted into stars. No other criteria are imposed. We set $T_{\rm SF} = 9000$ K, $n_{\rm SF} = 6$ cm^{-3}, and $\epsilon_{\rm SF} = 0.5$ in all the hydrodynamics simulations analyzed in this paper, where $n_{\rm SF}$ is the density threshold in hydrogen atoms per cubic centimeter. Observational studies show that the SF rate across entire (local and high-z) galaxies as well as individual molecular clouds, depends on the mass of very dense gas ($n > 10^4$ cm^{-3}) within molecular cloud complexes, confined to sub-parsec narrow filamentary structures and compact cores (Lada et al. 2012; Lada, Lombardi & Alves 2010). As these authors remark, the key question for understanding what ultimately controls the SF is the one related to the local processes that produce the dense and cold gas component of the interstellar medium (ISM). Unfortunately, a density threshold of $n > 10^4$ cm^{-3} or more cannot be used in current cosmological simulations because structures with this density are not resolved. The value used here, in combination with the values of other subgrid parameters, is suitable for our resolution and

result in reasonable ISM properties at scales larger than $\sim$ 100 pc, as well as realistic structural and dynamical properties of the whole galaxy (see below; see also Colín et al. 2010; Avila-Reese et al. 2011b). On the other hand, for typical observed column densities averaged across whole giant molecular clouds ($\langle N \rangle > 10^{21}$ cm^{-2}), number densities corresponding to our resolution at $z = 0$ are $n > 5$ cm^{-3}.

Notice also that, because of our *deterministic* SF scheme, the gas density does not reach values much higher than the SF density threshold. Then, it turns out that an $\epsilon_{\rm SF}$ value of about 0.5 gives rise to a conversion of gas-into-stars efficiency[3] of about a few percent per free-fall time (for the chosen density threshold, it is about 20 Myr), *when* a strong and efficient thermal stellar feedback is present. These values are close to the value estimated for the giant molecular clouds in the Milky Way by Krumholz & Tan (2007a).

As in Colín et al. (2010) and Avila-Reese et al. (2011b), stellar particles in the simulations here also inject the energy from supernovae (SNe) and stellar winds in the form of heat into the gas cells in which they are born. Each star more massive than 8 $M_\odot$ is assumed to dump into the ISM, instantaneously, 2×10^{51} erg in the form of thermal energy; 10^{51} erg comes from the stellar wind and the other 10^{51} erg from the SN explosion. Moreover, the star is assumed to eject $1.3 M_\odot$ of metals.

If the resolution is not high enough and/or $n_{\rm SF}$ is too high, the cooling time, t_c, is comparable or less than the crossing time, t_s, (Stinson et al. 2006; Dalla Vecchia & Schaye 2012a), and most of the dumped energy is radiated away. It is then a common practice to avoid overcooling by delaying the cooling in the star-forming regions (e.g., Stinson et al. 2006; Colín et al. 2010; Agertz, Teyssier & Moore 2011; Hummels & Bryan 2012). We turn off the cooling for 40 Myr, after a stellar particle is born, *only* in the cell where the particle is located. Tests show that the structure of simulated galaxies is not sensitive to a factor of two variation on the value of this parameter (Colín et al. 2010). Yet, according to the formulae of the crossing and cooling times in Dalla Vecchia & Schaye (2012a) $t_s \ll t_c$ in the star-forming cells. These formulae can be applied here because the temperature reached by these cells is high, about 3×10^7K for the chosen parameters.[4] Thus, keeping the cooling on or turning it off temporarily is expected to produce similar results. In runs not shown here, we see that this is indeed the case.

It should be said that our density-based deterministic SF and thermal-driven feedback implementations, discussed in detail in Colín et al. (2010) and Avila-Reese et al. (2011b), have their particularities but, in general agree, with the common schemes applied to this kind of simulation in order to obtain present-day "realistic" galaxies (see for a recent review and comparison among several schemes and codes Scannapieco et al. 2012).

[3]This efficiency can be estimated as the ratio between the gas infall rate and the SFR in the SF cells.

[4]This temperature depends on the total number of SNe per solar mass, which in turn depend on $\epsilon_{\rm SF}$, the initial mass function, and the energy injected per SN.

4.4.2. The Numerical Simulations

We have simulated seven central galaxies with hydrodynamics. In six of the runs, the ΛCDM cosmological parameters are $\Omega_m = 0.3$, $\Omega_\Lambda = 0.7$, $\Omega_b = 0.045$, and $h = 0.7$. The fit of the ΛCDM power spectrum is taken from Klypin & Holtzman (1997a) and is normalized to $\sigma_8 = 0.8$, where σ_8 is the rms amplitude of mass fluctuations in 8 h^{-1}Mpc spheres. In one more simulation, the cosmological parameters are $\Omega_m = 0.27$, $\Omega_\Lambda = 0.73$, and $\Omega_b = 0.047$. The power spectrum for this latter simulation is the one used to run the "Bolshoi simulation" (Klypin, Trujillo-Gomez & Primack 2011) with $\sigma_8 = 0.82$.

The low-resolution N-body simulations from which halos were selected[5] are the same used in Avila-Reese et al. (2011b). These simulations were conducted with 128^3 DM particles in a periodic box of $10h^{-1}$Mpc on a side. As previously mentioned, because our goal is to study the impact of the halo MAH on the evolutionary properties of low-mass galaxies, all of our selected halos have about the same mass, around $2.5 \times 10^{10} M_\odot$ (see Table 1), but different MAHs. The halos were chosen to be isolated in the sense that no halo with a comparable or higher mass is within a sphere of radius of 1 Mpc. The simulations that include baryons were run with high resolution using the "zoom in" technique (Klypin et al. 2001a). They end up with about half a million DM particles inside the high-resolution zone, and the size of the finest grid cell is 60–30 pc proper. The number of resolution elements inside the virial radius, $R_{\rm v}$, of the halos of the simulated galaxies, on the other hand, is around 1.5 million. In order to compare the MAHs of halos with and without baryons, we also ran high-resolution N-body-only simulations for three of the simulated galaxies. These simulations were run using the N-body version of the ART code (Kravtsov, Klypin & Khokhlov 1997a) with comparable resolution to the hydrodynamic runs.

In ART, the grid is refined recursively as the matter distribution evolves. The runs use a DM or gas density criteria to refine. To make sure the dynamics is correctly followed, we consider a rather aggressive refinement. A cell is thus refined when its mass in DM exceeds $1.3\ m_p$ or the mass in gas is higher than $1.4 F_{b,U} m_p$, where m_p is the mass of the DM particle in the highest resolution region and $F_{b,U} = \Omega_b/\Omega_m$ is the universal baryon fraction. In the hydrodynamic simulations presented in this paper, the root grid of 128^3 cubic cells is immediately refined unconditionally to the third level, corresponding to an effective grid size of 1024^3.

Table 4.1 summarizes the main present-day properties of the seven simulated galaxies/halos. The halo mass, $M_{\rm v}$, is the mass within the virial radius, $R_{\rm v}$, defined as the radius that encloses a mean density equal to $\Delta_{\rm vir}$ times the mean density of the universe, where $\Delta_{\rm vir}$ is obtained from the spherical top-hat collapse model. The galaxy properties (M_s, stellar galaxy half-mass radius R_e, SFR, etc.) are computed within a sphere of $0.1 R_{\rm v}$ radius. This radius contains most of the stars and cold gas of the simulated central galaxy. The contamination of satellites or other substructures at this radius is negligible, and the central galaxies hardly extend beyond $0.1\ R_{\rm v}$. On the other hand, because the stellar mass

[5]The halos are located using a modified version of the bound density maxima (BDM) halo finder described in Klypin et al. (1999), run only on the dark matter particles.

density profiles decrease exponentially for most of the runs, the galaxy stellar mass does not differ significantly if we measure it at "aperture" radii smaller than $0.1R_{\rm v}$ by factors of 1.5–2. For example, for the runs Dw1–Dw5, 90 % of the stellar mass at $0.1R_{\rm v}$ is attained at $\sim 0.05\ R_{\rm v}$; for runs Dw6 and Dw7, 90 % of this mass is attained at $\sim 0.085\ R_{\rm v}$ (these late-assembling systems have the most extended stellar mass surface density profiles). If we measure M_s at half of our "apertureradius (0.05 $R_{\rm v}$ instead of $0.1R_{\rm v}$), then the masses would be ≈ 10 % smaller for runs Dw1–Dw5, and 35 %–40 % smaller for runs Dw6 and Dw7. Because observers measure the total luminosity (mass) with different surface brightness (SB) limits, these estimates give us an idea of how much could be different in our M_s with respect to observational inferences.

Our runs are sorted and numbered according to their $z_{f,h}$ value, the redshift at which the given halo reached one-third of its present-day mass; for similar $z_{f,h}$ values, an earlier mass assembly is determined from the visual inspection of the overall halo MAH. In this sense, the halo of run Dw1 forms earlier than the halo of run Dw2 and so on. *This should give us a preliminary idea of how the galaxy properties depend on the halo MAH*. We have chosen one-third instead of the standard one-half, because the MAHs of small halos are such that the fast growth phase, where more stochastic variations are expected, happens at earlier epochs or at smaller fractions of the present-day mass.

4.5. Results

4.5.1. Properties at $z = 0$

The seven present-day isolated halos, where the simulated galaxies form, have similar masses (see Table 4.1). The resulting galaxies at $z = 0$ display a range in stellar and gas masses that varies by factors between ~ 4 and 10, respectively. The main structural and dynamical properties of the simulated dwarfs are roughly consistent with those determined for dwarf galaxies (see for a discussion Avila-Reese et al. 2011b). Remarkably, at $z = 0$, all have nearly flat circular velocity profiles for radii larger than $\sim$2–3R_e (Figure 4.1). In Figure 4.2, we plot the maximum circular velocity, $V_{\rm max}$, the stellar effective radius R_e, the sSFR, and the galaxy cold gas-to-stellar mass ratio, $M_{\rm g,cold}/M_s$, as a function of M_s for the seven simulated dwarfs (solid colored circles), and compare them with some available observational information. The sizes of the circles increase with $z_{f,h}$.

According to panel (a), our dwarfs have lower stellar masses for their $V_{\rm max}$ as compared to extrapolations of the (inverse) stellar Tully–Fisher relation of massive galaxies (dashed line), but are consistent with the observations of dwarf galaxies (dots). The bending of the Tully–Fisher relation for galaxies below $V_{\rm max} \sim 100$ km s^{-1} has also been found in N-body/hydrodynamics simulations of a cosmological box by de Rossi, Tissera & Pedrosa (2010); it is explained by the strong effects of the SN-driven outflows in low-mass halos. There is no dependence of M_s or $V_{\rm max}$ on the halo formation epoch, $z_{f,h}$. Regarding R_e, in panel (b), we plot the extrapolation to low masses of the R_e–M_s relation of bigger disk-

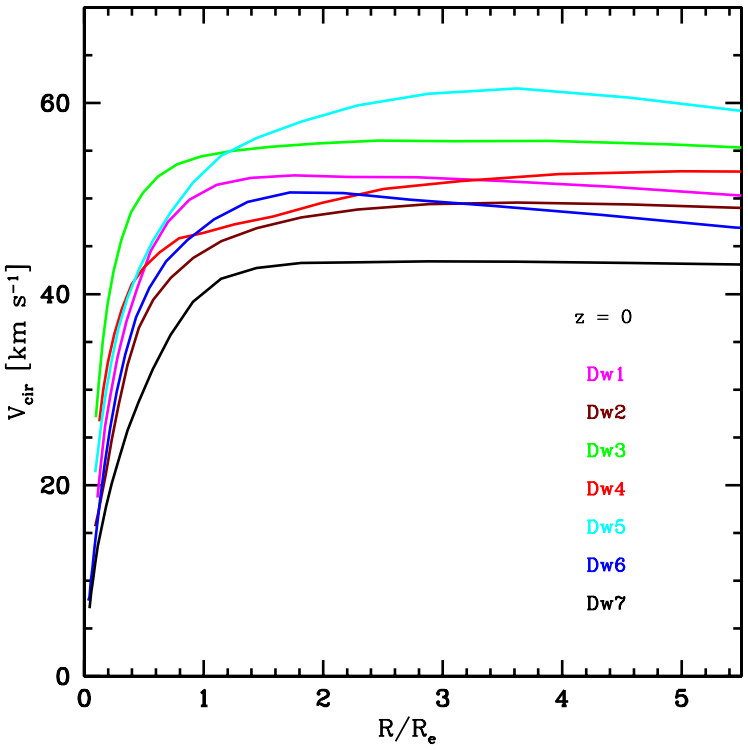

Figura 4.1: Circular velocity profile, $V_{\rm C}(R)$, at $z = 0$ for the different runs with the radius scaled in terms of the corresponding R_e.

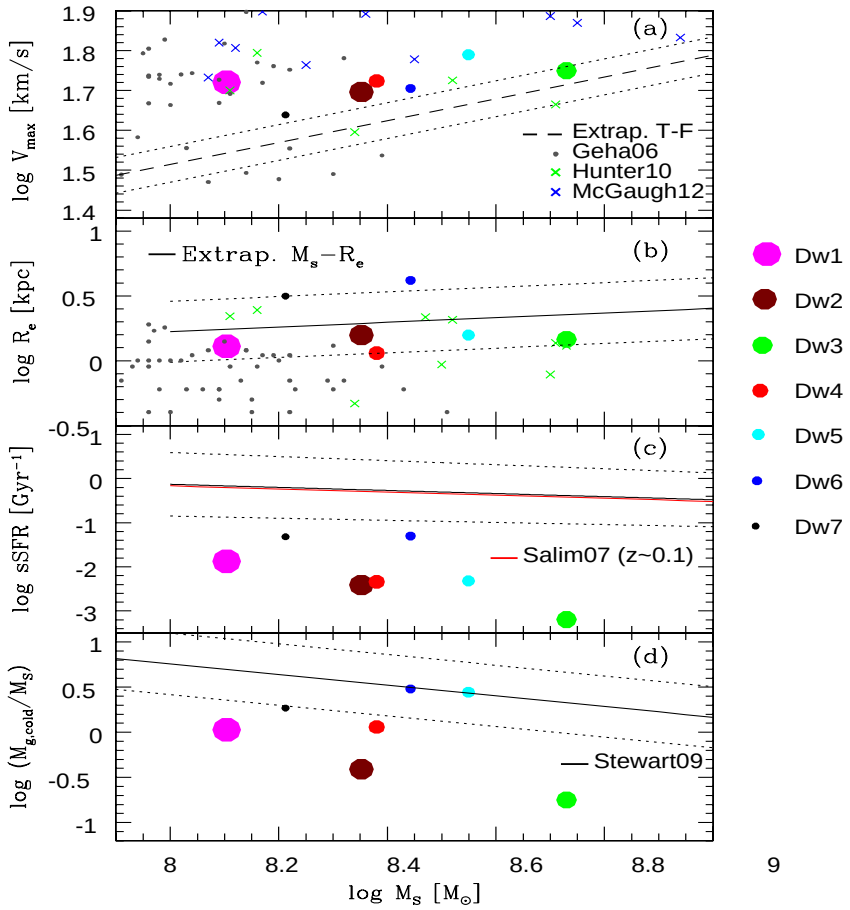

Figura 4.2: General properties at $z = 0$ for the different runs plotted as open circles, where sizes increase as a function of $z_{f,h}$. (a) Maximum circular velocity vs M_s; the dashed line represents the extrapolation of the stellar Tully–Fisher relation as reported in Avila-Reese et al. (2008), the small gray points correspond to observations of dwarf galaxies (Geha et al. 2006), green crosses are $GALEX$ observations of dwarfs reported by Hunter, Elmegreen & Ludka (2010), and blue crosses are compiled data by McGaugh (2012). (b) Stellar half-mass radius R_e vs. M_s; the solid line is the extrapolation to low masses of the fit to larger galaxies given by (Dutton et al. 2011), the dotted lines show the 84th and 16th percentiles of the distribution. (c) sSFR vs. M_s; the solid and dotted lines are the fit, including the scatter to a large star-forming galaxy sample from SDSS, as reported by Salim et al. (2007). (d) Gas fraction vs. M_s; the solid line and dotted lines are the analytical fit and its scatter to observations given by Stewart et al. (2009).

dominated galaxies from Sloan Digital Sky Survey (SDSS) reported in Dutton et al. (2011), as well as the measured effective radius of some late-type dwarf galaxies. The R_e values of the simulated galaxies are within those estimated for the dwarf galaxies, though the scatter for the latter is large. In several cases, the observed dwarfs are probably satellites. After a galaxy becomes a satellite, processes such as starvation and ram pressure are expected to quench the SF and stop the inside-out growth of the galaxy. Note that the two halos with the latest formation epochs, Dw6 and Dw7, have larger R_e, by at least a factor of two, than the rest of the simulated dwarfs. As these halos assemble their mass relatively late, they have had more time to acquire more angular momentum due to tidal torques during the linear regime.

According to panels (c) and (d), the simulated dwarfs have present-day sSFR's and cold gas-to-stellar mass ratios, $M_{\rm g,cold}/M_s$, smaller than the average ratios estimated for observed galaxies of similar stellar masses (see also Avila-Reese et al. 2011b; De Rossi et al. 2013). Note that the simulated galaxies with lower values of $z_{f,h}$ (i.e., galaxies that have experienced a relatively late assembly) tend to have, on average, higher values of sSFR and $M_{\rm g,cold}/M_s$ ratios, closer to observations. Besides, the stellar masses of the simulated dwarfs seem to be larger by ~ 0.5 dex than what semi-empirical inferences show for halos of similar masses (see Section 5.6 for a discussion).

Most of the gas in the simulated galaxies is cold ($T \leq 10^4$ K). In Table 4.1, the z=0 mass ratios of cold to total gas in the galaxy, $M_{\rm g,cold}/M_{\rm g}$, are reported. For Dw2, this fraction is only about 50 %, while for the rest, it is above $\sim 70\,\%$. On the contrary, most of the gas in the halo, between $0.1R_{\rm v}$and $R_{\rm v}$, is hot; in all cases, the ratio of hot to total gas is $\sim 99\,\%$, except for Dw6 which has a huge amount of cold gas in the halo. However, in this particular case, we have identified a couple of satellites in the halo that contain most of this cold gas.

The stellar structure of the simulated dwarfs varies from simulation to simulation but, in general, it is composed of a rotating disk and an extended low-angular momentum spheroid; the total mass surface density profiles roughly follow an exponential law or two exponential laws, with the outer one being shallower than the inner one. The mass contained in the high-angular momentum stellar disk is a fraction of the total stellar mass, which ranges from D/T ∼0.7–0.6 to ∼0.2–0.01 for runs with the latest and earliest halo MAHs, respectively. The values of D/T for the seven simulated galaxies are reported in Table 4.1. It is worth mentioning that the stellar structure of some observed dwarf galaxies seems to be dominated in mass by a kind of extended stellar halo with a surface density profile much flatter than the one of the inner disk (see, e.g., de Blok & Walter 2006; Barker et al. 2012; Bernard et al. 2012), likely a product of an early fast growth phase of galaxy formation (Stinson et al. 2009).

4.5.2. Mass assembly histories

The main results of the present work are reported in Figure 4.3, where the MAHs of different galaxy/halo components are shown for the seven simulated isolated dwarfs. The total MAHs (dark + baryonic mass contained within the virial radius $R_{\rm v}$; solid black lines)

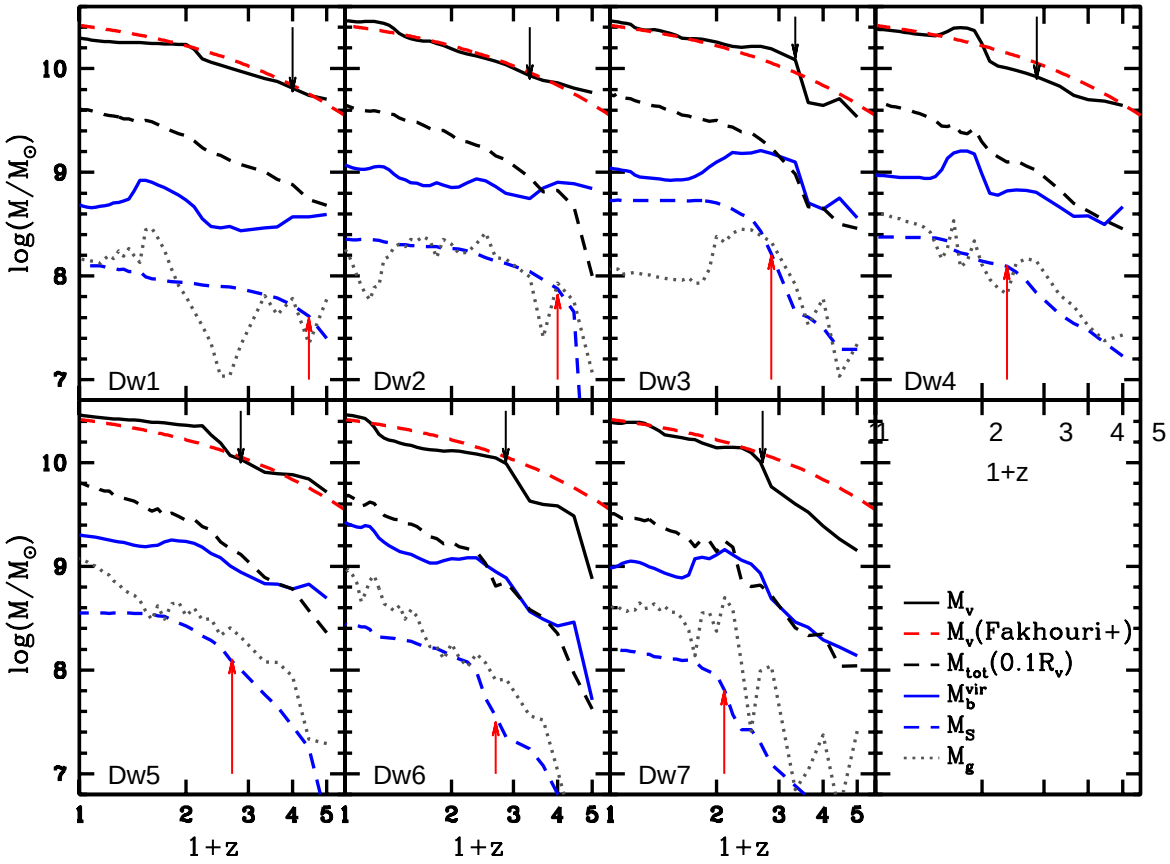

Figura 4.3: Different mass aggregation histories for the seven simulated galaxies. The solid black (blue) line represents the total (only baryonic) mass inside $R_{\rm v}$. The black (blue) dashed line represents the total (stellar) mass inside $0.1R_{\rm v}$, while the gas mass inside $0.1R_{\rm v}$is represented by dotted gray lines. For comparison, in each panel, we plot the average MAH of a halo of $\log(M_{\rm v}/M_{\odot}) = 10.4$ at $z = 0$ as given in Fakhouri, Ma & Boylan-Kolchin (2010) from an analysis of the Millennium Simulations(red dashed line). The black (red) arrow in each panel indicates the redshift at which 1/3 of the present day $M_{\rm v}$ (M_s) is attained.

are compared with the mean MAH of pure DM halos from the Millenium-2 simulation which, at $z = 0$, end up with the same mass as our runs ($M_{\rm v} \approx 2.5 \times 10^{10}\ M_{\odot}$, dashed red lines; Fakhouri, Ma & Boylan-Kolchin 2010). The black arrows indicate the redshift at which one-third of the present-day $M_{\rm v}$ was attained, $z_{f,h}$. For runs Dw1–Dw4, $M_{\rm v}$ attained a third of its present value earlier ($z_{f,h} \lesssim 2$) with a slower late mass growth than for runs Dw5–Dw7. The dashed black lines show the total MAHs (dark + baryonic) but for masses contained within $0.1R_{\rm v}$. The inner mass assembly roughly follows the assembly of the whole halo, though at earlier epochs ($z > 1$), the former is a bit delayed with respect to the latter in most runs.

The solid blue lines in Figure 4.3 show the MAHs of the baryon mass (gas + stars) within $R_{\rm v}$, $M_b^{\rm v}$. The shape of the virial baryon MAHs partially follows the ones of the total mass (solid black lines), with the former being more irregular and with periods of mass decrease, due to gas loss as a result of SN-driven outflows. These periods occur mostly after a major merger has happened (see, e.g., the mergers at $z \sim 1.1, 2.2,$ and 2.0 in the runs Dw1, Dw3, and Dw7, respectively, and the corresponding later drop of the baryon mass). We do not formally construct merger trees, where all of the progenitor subhalos of a descendant halo at a given time are identified. By major merger, we refer here to an increase in the halo MAH by 50 % (0.176 dex) or more between two consecutive snapshots (Δt ∼300–400 Myr). This increase may come in one or several progenitors, although the latter is less probable. In the literature, a major merger is defined usually as a merger between two progenitors with mass ratio $M_2/M_1 > 0.1$ (e.g., Fakhouri, Ma & Boylan-Kolchin 2010). Note that at earlier epochs, some of our MAHs increase by more than a factor of two, which means that a multiple halo merger event and fast smooth accretion has occurred. However, since $z \sim 1$ all of the halos hosting our dwarfs do not increase more than a factor of two between two consecutive snapshots.

We define the virial mass baryon fraction as $F_b^{\rm v} \equiv M_b^{\rm v}/M_{\rm v}$ and plot this fraction as a function of z for all of the runs in Figure 4.4 (solid black lines); the color lines correspond to baryon-to-total mass ratios inside 1.5, 2, 2.5, and 3 $R_{\rm v}$; the dotted line is for the commonly discussed *galaxy* mass baryon fraction, $F_b \equiv M_b/M_{\rm v}$, where M_b is the galaxy baryonic mass. All baryon fractions are normalized to the universal, $F_{b,U} \equiv \Omega_b/\Omega_m$, defined from the cosmological model used in each run. As can be seen from the plots, $F_b^{\rm v}$ decreases on average with time in all runs, except in run Dw6, showing that halos lose more and more baryons (gas) with time. Interestingly enough, this behavior extends to regions around the galaxy as far as $3R_{\rm v}$. For the early-assembled halos (Dw1–Dw3), the gas loss happens intensively early in the history of their evolution, while for halos assembled later (Dw5–Dw7), the gas loss is less intense overall, ending with higher $F_b^{\rm v}$ values than those corresponding to the early-assembled halos. In all cases, the virial mass baryon fractions are smaller than the universal one, by factors of 1.5–2 at high redshifts, increasing to 2–6 at $z = 0$. These factors are much smaller, especially at high z, than those obtained for the galaxy baryon fractions, which shows that large amounts of gas are actually not in the

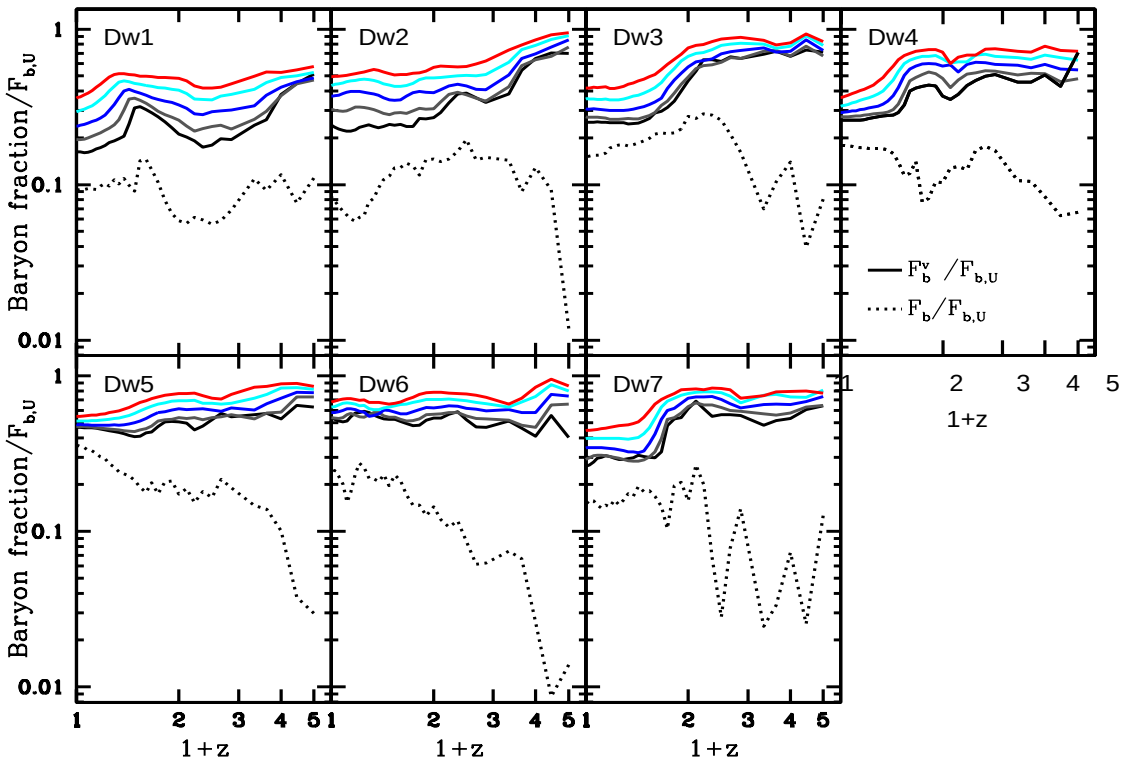

Figura 4.4: Virial mass baryon fraction, $F_b^{\rm v} \equiv M_b^{\rm v}/M_{\rm v}$, as a function of z for all of the runs (solid lines). From bottom to top, the color lines correspond to baryon-to-total mass ratios inside 1.5, 2, 2.5, and 3 $R_{\rm v}$. The dotted lines are for the galaxy mass baryon fractions, $F_b \equiv M_b/M_{\rm v}$. All of the baryon fractions are normalized to the universal one, $F_{b,U}$, defined from the cosmological model used in each run.

galaxy but in the halo.[6] This gas is mostly hot (see Table 4.1).

The dashed blue lines in Figure 4.3 show the galaxy stellar MAHs. It is quite remarkable that *the stellar mass assembly of our simulated dwarfs closely follows the halo mass assembly*, at least since $z \sim 1$ for all runs. The red arrows indicate the redshift when one-third of the present-day M_s is reached, $z_{f,s}$. In general, this redshift is close to the corresponding one for total virial mass, $z_{f,h}$ (black arrows). However, there is a slight trend for the early-assembled (late-assembled) halos to assemble their stellar mass earlier (later), $z_{f,h} \lesssim z_{f,s}$ ($z_{f,h} \gtrsim z_{f,s}$); that is, if the halo delays its mass assembly, the corresponding galaxy delays its assembly even more. Therefore, *an extended halo MAH helps to obtain a galaxy with late stellar mass assembly and higher SFRs at late epochs*. However, this dependence is actually weak for the galaxies analyzed here.

[6]Some of the baryons in the halo are stars but, as it is shown below, in most of the runs the amount of mass in stars that is outside the central galaxy is small, especially at low redshifts.

In Figure 4.5, we plot the galaxy stellar mass fraction, F_s, as a function of z for the seven runs (solid lines), as well as the halo stellar mass fraction defined as $F_s^{\rm v} \equiv M_s^{\rm v}/M_{\rm v}$ (dashed lines). For all runs, F_s *is almost constant with a value of around* 0.01 *since* $z = 1$. At $z > 1$, those halos that have a late assembly history decrease their F_s values with z. The virial stellar mass fraction, $F_s^{\rm v}$, is actually dominated by the central galaxy mass value; it is only at high redshifts where $F_s^{\rm v}$ is slightly larger than F_s, thus evidencing the presence of some satellites that are probably then accreted by the central galaxy. The most remarkable difference is for run Dw6 whose halo MAH grows by jumps (major mergers). It is expected, in this case, that the halo and posterior galaxy mergers shall produce those ups and downs in F_s.

The dotted lines in Figure 4.3 show the galaxy gas MAHs. Unlike the stellar MAHs, which always grow, the gas MAHs are irregular, with periods of increase and decrease. For runs with late-assembled halos (Dw4–Dw7), the galaxy gas mass, M_g, is mostly larger than the mass in stars, M_s, while for runs with early halo assembly (Dw1–Dw4), the gas loss events are stronger, so strong that there are intervals of time for which $M_g < M_s$; the most dramatic cases occur for Dw3 from $z \sim 1.5$ to $z = 0$ and for Dw1 at $1 \lesssim z \lesssim 2$. The difference between these two cases, however, is that in the latter one, the ejected gas is re-accreted later (as evidenced by the much more rapid gas growth rate, as compared with that of its halo), again increasing M_g, while in the former one, the gas is lost from the halo. This can be better appreciated in Figure 5.6 below.

4.5.3. Gas mass fractions and star formation rate histories

In Figure 5.6, the ratio between M_g and M_b= M_g + M_s (hereafter f_g, solid lines) and the halo gas fraction (the amount of gas that it is within 0.1 and 1 $R_{\rm v}$ relative to the total amount of gas within $R_{\rm v}$; dotted lines) are plotted as a function of z for the seven runs. It is important to remark that most of the gas in the galaxies is cold, while the gas outside the galaxies is mostly hot (see Table 4.1). One can clearly see that in the periods when f_g decreases (increases), the gas fraction outside the galaxy typically increases (decreases), which is clear evidence that *the strong SN-driven outflows play a major role in regulating the gas content of the simulated dwarfs*. However, there are some cases when the outflows are so strong, that the gas is completely lost and the regulation interrupted. This is the case of Dw3; at $z \sim 2$ (after a major merger), the gas fraction in the galaxy, f_g, starts to strongly decrease and it never substantially increases again because the gas fraction outside the galaxy (the reservoir) also decreases, due to the total gas ejection from the halo.

From Figure 5.6, one sees that the dwarfs formed in late-assembled halos tend to have higher gas fractions (see also Figure 4.2 and Table 4.1) and are less episodic than the dwarfs formed in early-assembled halos. These latter halos tend to have stronger changes in their virial baryon fractions, $F_b^{\rm v}$ (Figure 4.4), which are mostly due to gas ejection from the halo at early epochs, when the fast mass growth took place; the efficient consumption of gas into stars at early epochs in these halos (runs) also works in the direction of decreasing f_g. At $z \sim 0$, we then see that f_g in the galaxies formed inside early-assembled halos (Dw1–

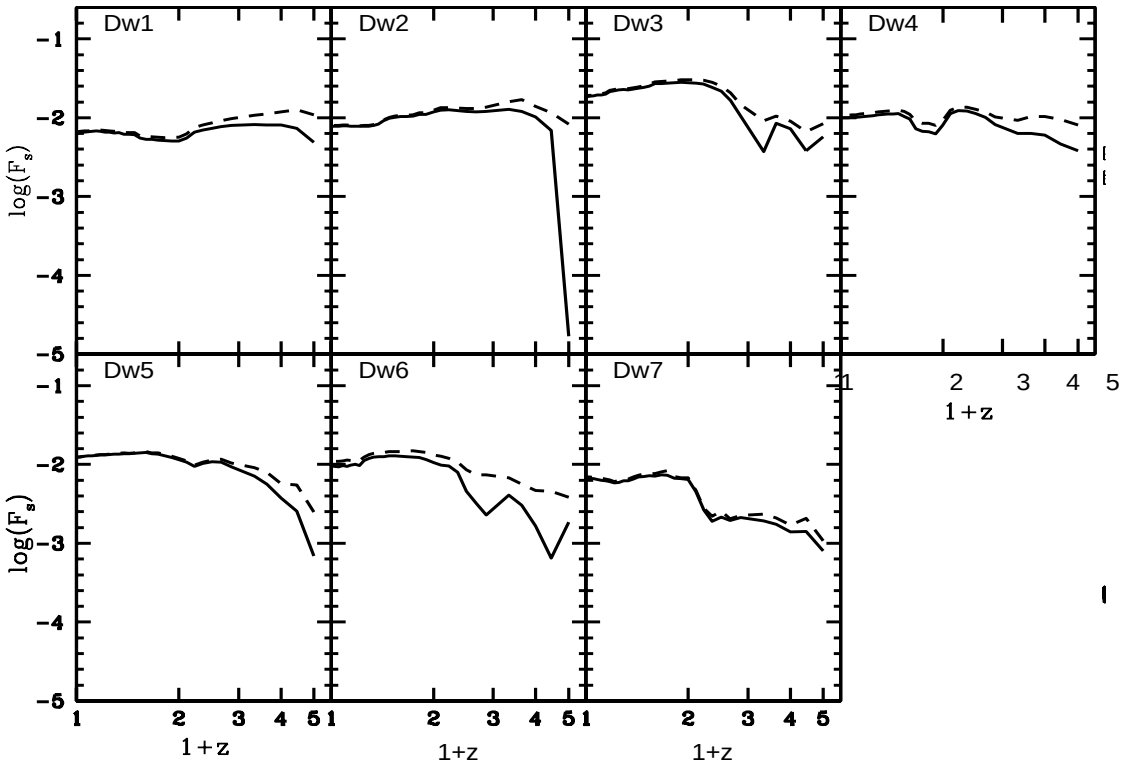

Figura 4.5: Evolution of $F_s = M_s/M_{\rm v}$. The solid line is for M_s inside $0.1R_{\rm v}$, while the dashed line is for M_s inside $R_{\rm v}$; there is almost no difference because most of the stellar mass is within the central galaxy ($0.1R_{\rm v}$).

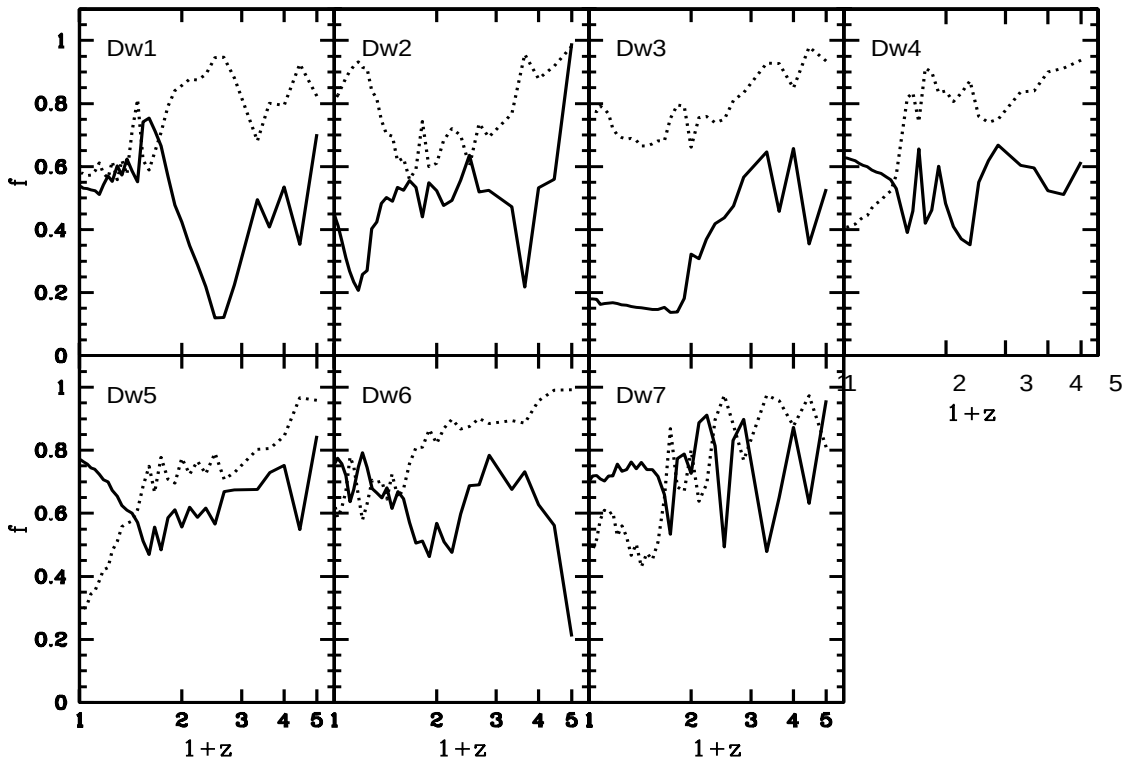

Figura 4.6: Evolution of the galaxy gas mass fraction, f_g, for the different runs (black solid lines). The dotted line refers to the mass fraction of gas in the halo (between $0.1R_{\rm v}$ and $1R_{\rm v}$) with respect to the total amount of gas within $R_{\rm v}$.

Dw3, $f_g < 0.6$) is lower than in galaxies formed inside late-assembled halos (Dw4–Dw7, $f_g > 0.6$).

In summary, the simulations show some systematic dependences of the gas mass and gas fraction on the halo MAH: *the earlier the halo is assembled, the earlier and more gas is converted into stars and ejected by the SN-driven outflows from the galaxy or even from the halo*. When the mass assembly process of the halo is more gradual, as opposed to an early fast assembly, the SN-driven outflows seem to be able to regulate the gas ejection and gas re-accretion processes. These processes, in turn, keep the galaxy with relatively high gas fractions, available for SF, so that a gradual increase in the galaxy stellar mass and fraction (M_s and F_s) with time is observed (see Figures 4.3 and 4.5).

The behavior of the galaxy gas mass fraction, f_g, with time is the result of several processes: cosmological gas accretion (proportional to the halo MAH) and cooling, transformation of the cold gas into stars, reheating and expansion of the gas due to the stellar (mainly SN) feedback, gas ejection, and re-accretion. The interplay of all of these processes produces the episodic M_g and f_g histories seen in Figures 4.3 and 5.6. Since stars form from the (cold) gas, episodic (bursty) SFR histories are expected for our simulated dwarfs.

The SFR histories for the seven dwarfs are shown in Figure 4.7. The SFR is measured as the amount of gas particles promoted to stellar particles inside 0.1 $R_{\rm v}$ during $\Delta t = 100$ Myr at a given z. The episodic character of the SFR histories is clearly reflected in the plots. The amplitudes of the burst and quiescent phases in periods of 100 Myr can vary by factors of $\sim$2–10, on average, with respect to the current average SFR in periods of 2 Gyr, though in some cases the SFR is completely quenched (see Section 4.7.3 for a discussion). In addition to the strong burstiness, one observes that the average SFH in most of the runs is composed of an early ($z \gtrsim 2$) period of high SFRs and then a significant decline at lower redshifts. This behavior is not followed by the SFHs of runs Dw6 and Dw7, those with the latest halo assemblies. In any case, *none of the seven simulated dwarfs can be considered an actively star-forming galaxy at* $z \sim 0$, contrary to what observations of local isolated dwarfs suggest (see the references in the Introduction).

4.6. Effects of baryons on halo mass assembly

The effects of the strong gas outflows on the halo MAH of our low-mass halos are not negligible. There are two main effects that work in the direction of reducing the total halo (dark + baryonic) mass. The trivial one is the direct loss of baryons from the halo, which reduces the total mass. The other effect is dynamical: due to the mass reduction by baryon losses and a possible expansion effect of the DM halo produced by the outflows, the gravitational potential of the halo becomes shallower than in the case with no galactic winds; thus, the ability of the halo to accrete matter becomes less efficient and the halo ends up with a lower total mass.

In order to explore the differences in the virial masses at different epochs, here we compare full N-body/hydrodynamics (H+ART) simulations with the corresponding N-body (ART)-only simulations. This exercise is performed for the runs Dw2, Dw5, and Dw7, for which we have run the corresponding N-body-only simulations using the same initial conditions and comparable (high) resolution. While Dw2 corresponds to an early-assembled halo with efficient SF and SN-driven outflows in the remote past, Dw6 and Dw7 correspond to late-assembled halos with respect to the average, having a more extended SFH.

In the upper panels of Figure 4.8, the ART (blue solid line) and the H+ART (black solid line) total virial MAHs are plotted. As expected, the ART MAHs lie above the H+ART ones at all times. We also plot the decomposition of the H+ART total virial MAHs into DM and baryonic matter, dashed and dotted lines, respectively; the latter has been shifted by +0.5 dex. The fractional difference in mass of the H+ART total virial MAHs with respect to the ART ones, $f_{\rm lost}$, is shown in the lower panels with solid lines. This fractional difference is the result of the above mentioned effects of baryons on the total virial MAHs, and it is defined as $f_{\rm lost} = [M_{\rm v}({\rm ART}) - M_{\rm v}({\rm H+ART})]/M_{\rm v}({\rm ART})$. The strong peaks seen in the plots should not be interpreted as strong mass differences. In fact, these peaks appear after mergers. In the H+ART simulations, mergers occur slightly later than the corresponding

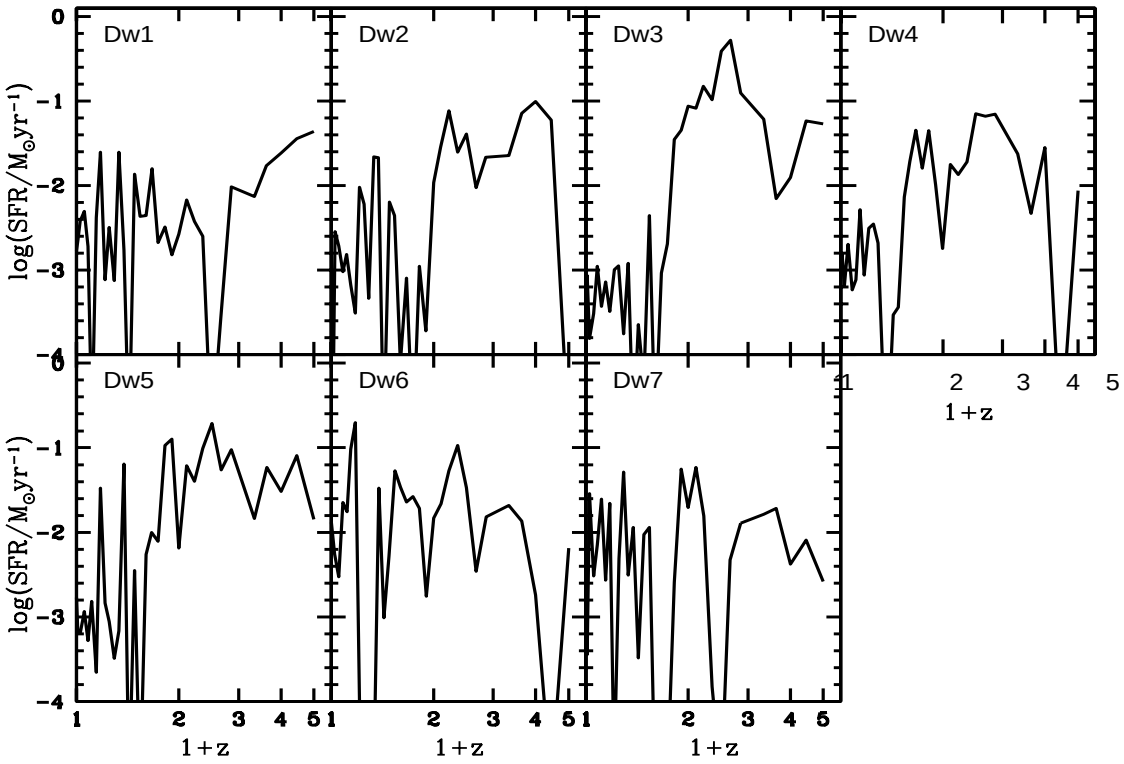

Figura 4.7: Star formation rate histories for all the runs.

mergers in the ART simulations, an effect related to the inclusion of the baryon physics on the dynamics of the system. Because of this delay, the fraction $f_{\rm lost}$ increases [$M_{\rm v}({\rm ART})$ increases with respect to $M_{\rm v}({\rm H+ART})$] until the merger also happens in the corresponding H+ART simulation, and then returns to, roughly, the value it had before the peak.

Excluding the peaks, we see that the fractional mass difference does not vary significantly or systematically with redshift, attaining values between 10 % and 20 % since $z = 2$; that is, *the baryonic effect on halos of virial masses ∼2–3×10^{10} $M_{\odot}$ decreases their masses (dark + baryons) by factors* 1.1–1.2. Note that the larger mass differences are typically reached after the mergers happen. In order to explore which is the contribution to the measured mass differences of the simple baryon losses (due to the SN-driven outflows), in Figure 4.8, we plot an estimate of those as: $f_{\rm lost}^{\rm bar} = [F_{b,U} M_{\rm v}({\rm ART}) - M_b^{\rm v}({\rm H+ART})]/M_{\rm v}({\rm ART})$ (red line). This fraction likely overestimates the effect because it is explicitly assumed that halos incorporate dark and baryonic matter with the same fraction as the universal one. According to Figure 4.8, most of the mass difference is due to the direct gas losses that result from the SN-driven winds. Note that the maximum value that the fractional mass difference can attain due to baryon losses is $F_{b,U}$, in the hypothetical case that all of the baryons are ejected or never reach the halo.

We confirm the results recently reported by Munshi et al. (2013) and Sawala et al. (2013), that at $z = 0$, the simulated low-mass galaxies have virial masses smaller than the counterpart pure N-body simulations. For the halo masses in the range of our simulations, these authors find differences of 20 %–25 %, which is roughly consistent with our results (10 %–18 %). *In addition, we also show that the differences remain of the same order since at least z ∼2–3*. The galaxy outflows are also expected to affect the halo inner mass distribution (e.g., Duffy et al. 2010; Bryan et al. 2013). Results related to this question will be presented elsewhere.

4.6.1. Corrections to the stellar-to-halo mass relation

The halo/subhalo mass functions obtained in N-body cosmological simulations (pure DM) will change if the effects of baryons are taken into account, especially at the low-mass side. It is expected that these differences will affect the inferences of the M_s–$M_{\rm v}$ relation obtained through statistical approaches as the abundance matching technique (AMT) and halo occupation model (HOM) (e.g., Munshi et al. 2013; Sawala et al. 2013). In the last few years many authors have inferred this relation at $z \sim 0$ and higher redshifts (see the Introduction for the references), which was used to compare with results from simulations and models of galaxy evolution. Of particular interest is this comparison for low-mass galaxies. In the following, we explore the change in the M_s–$M_{\rm v}$ relation after taking into account the correction in the halo/subhalo masses as well as other considerations.

In order to statistically infer the M_s–$M_{\rm v}$ relation down to low masses, we construct a galaxy stellar mass function (GSMF) similar to the one reported in Baldry, Glazebrook & Driver (2008). For this, we use the catalog used by these authors, namely, the SDSS DR4 version of the New York University Value-Added Galaxy Catalog (Blanton et al. 2005a,b),

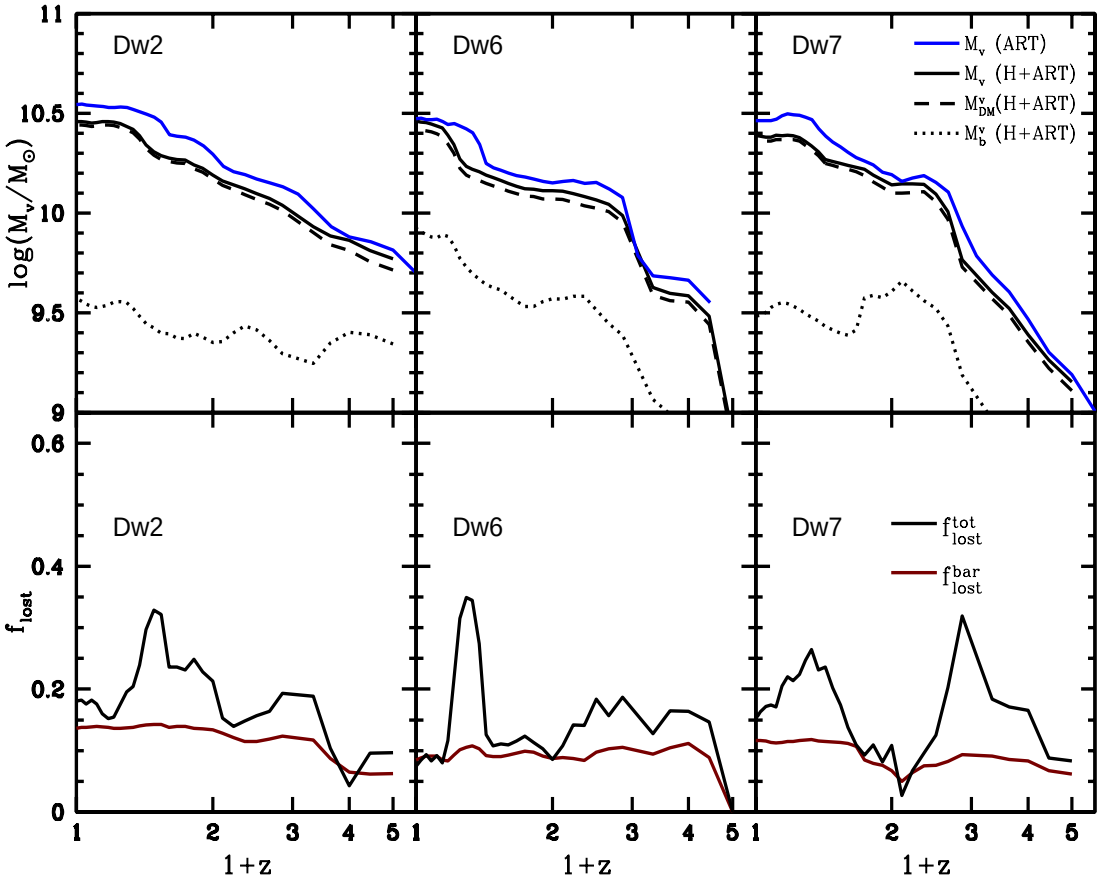

Figura 4.8: Comparison between the dark matter-only (ART) and the hydrodynamic (H+ART) simulations for the systems Dw2, Dw5, and Dw7. Upper panels: solid black (blue) line shows the total virial MAH in the H+ART (ART) simulation. The black dashed and dotted lines show the dark and baryonic matter components of the H+ART total virial MAHs, respectively; the latter has been shifted by +0.5 dex. Bottom panels: total and baryonic fractional differences in mass, $f^{\rm tot}_{\rm lost}$ and $f^{\rm bar}_{\rm lost}$, as defined in the text.

with their $V_{\rm max}$ volume correction and the stellar mass calculated from the g and i bands according to the Bell et al. (2003b) mass-to-luminosity ratios. The GSMF is close to the one reported by these authors but in the 10^9 to 3×10^{10} $M_\odot$ interval, our GSMF is slightly higher and less curved than in Baldry et al. (2008). In Figure 4.9 we plot the F_s–$M_{\rm v}$ relation obtained for this GSMF by applying the AMT as in Rodríguez-Puebla, Drory & Avila-Reese (2012, black solid line). The error bar in the panel indicates the typical uncertainty in the F_s determination due to systematical uncertainties, mainly the one in the stellar mass. We further take into account the effect of baryons on the halo mass discussed above by using the correction on $M_{\rm v}$ given in Sawala et al. (2013). As shown above, our results are consistent with this correction, at least at the masses studied here. After applying this correction to the halo/subhalo mass function and applying the AMT, we obtain the F_s–$M_{\rm v}$ relation plotted in Figure 4.9 with the dotted black line.

The common AMT inferences do not make a difference between the F_s–$M_{\rm v}$ relation of central and satellite galaxies. As shown in Rodríguez-Puebla et al. (2012, 2013), they are actually different. In order to constrain both relations, these authors used the AMT combined with the HOD model; the latter requires information about the observed two-point correlation function. Following Rodríguez-Puebla, Avila-Reese & Drory (2013), we calculate the F_s–$M_{\rm v}$ relation separately for centrals/halos and satellites/subhalos for the same total GSMF discussed above; the result for *centrals/halos*, is plotted in Figure 4.9 as the blue solid line, while the dotted blue line is for the case where $M_{\rm v}$ in the halo mass function is corrected for the effects of baryons. The latter relation will be used in Figure 4.10 of Section 4.7.1 for comparison with our simulated central dwarfs.

The short-dashed line in Figure 4.9 corresponds to the AMT result by Behroozi et al. (2013), who used a combined GSMF: from Moustakas et al. (2013) for large masses and from Baldry et al. (2008) for low masses. For the definition of halo mass, instead of the present-day halo mass or the mass at the accretion epoch in the case of subhalos, they use the maximum mass a halo/subhalo ever had (peak mass). Therefore, their halo mass function is expected to be slightly higher than the one used by us. This is partially why their F_s values for $M_{\rm v} \gtrsim 10^{11}$ $M_\odot$ are slightly below our corresponding AMT result (solid black line). The other reason is due to the small difference between our and the original Baldry et al. (2008) GSMF used by these authors (see above). The strong flattening of the F_s–$M_{\rm v}$ relation at masses below $\sim 10^{11}$ $M_\odot$ in Behroozi et al. (2013) is probably due to a correction for SB incompleteness applied by them but not described in the paper. In order to explore this question, we apply a correction to our GSMF for this incompleteness and for the SB–magnitude correlation by following the recipes given in Blanton et al. (2005a). The obtained F_s–$M_{\rm v}$ relation with the AMT lies above and becomes shallower at the low-mass side (red solid line) than the case without this correction (black solid line); at $M_{\rm v} = 3 \times 10^{10}$ $M_\odot$, F_s is already 0.5 dex higher after the (uncertain) SB corrections. However, we do not reproduce the strong bending reported in Behroozi et al. (2013). It seems that their SB corrections are stronger at low masses than those suggested by Blanton et al. (2005a).

We conclude that (1) correcting the halo/subhalo mass function by the effects of baryons does not significantly affect the F_s–$M_{\rm v}$ relation, at least down to $M_{\rm v} \sim 10^{10}$ $M_\odot$; (2) for

central galaxies, F_s is lower than the average case (conversely, for satellites, it is higher; see Rodríguez-Puebla, Drory & Avila-Reese (2012); (3) if the SB corrections are strong, the F_s–$M_{\rm v}$ relation could increase significantly at lower masses in such a way that the low-mass end of the GSMF would become very steep (see also Rodríguez-Puebla et al. 2012; Sawala et al. 2013).

4.7. Discussion

4.7.1. SF–driven outflows or delayed SF?

Despite the fact that the seven simulated dwarfs show structural and dynamical properties roughly consistent with observations, they have too low sSFR's and gas fractions as compared to the values estimated for local dwarfs (central or satellites), and presumably too high stellar masses as well (see below), a consequence of an efficient gas transformation into stars at early epochs. Overall, our analysis has shown that *the stellar mass growth of the dwarfs closely follows the mass growth of their halos*. In this sense, the dwarfs formed in those halos with a late mass assembly tend to have a late stellar mass assembly as well, with higher present-day SFR's and gas fractions. Thus, dwarfs formed in halos that assemble their masses later than the average have evolutionary signatures closer to observations; though, even in these cases, the simulated dwarfs are not as *active* and gas rich as observations suggest (see also Colín et al. 2010; Sawala et al. 2011; Avila-Reese et al. 2011b; De Rossi et al. 2013).

Gas outflows or supergalactic winds driven by stellar feedback (mainly SNe) have been commonly invoked as the mechanisms able to lower the stellar-to-halo mass ratio, F_s, and obtain the flattening of the faint-end of the GSMF. The effects of the SF-driven feedback (injected to the ISM as energy and/or momentum) are also expected to influence the thermal and hydrodynamic properties of the gas in such a way that the SFR history is affected by the feedback. Our hydrodynamical simulations include an efficient prescription for thermal feedback from stars and SNe (see Section 4.4.1).

According to the results presented in Section 4.5, the gas outflows in the simulations are strong, removing large fractions of baryons not only from the galaxies, but also from the halo, and producing episodic SFHs. However, in spite of it, our results do not agree with observational inferences as mentioned above. The question is *whether stronger SF-driven outflows (higher mass loading factors) should be allowed in order to solve the issues of the simulated galaxies or there is no more room for strong outflows in the simulations*.

In Figure 4.10, we plot the $z = 0$ stellar-to-halo (filled circles) and baryonic-to-halo (crosses) mass ratios versus the corresponding virial masses for the seven simulated central dwarfs. The blue dotted line with error bars corresponds to the F_s–$M_{\rm v}$ relation for central galaxies/distinct halos and its intrinsic scatter as inferred in Section 4.6.1 (Figure 4.9) by means of the AMT+HOD formalism, *taking into account the correction to the halo masses due to the effects of baryons*. The arrow indicates the factor by which F_s increases at

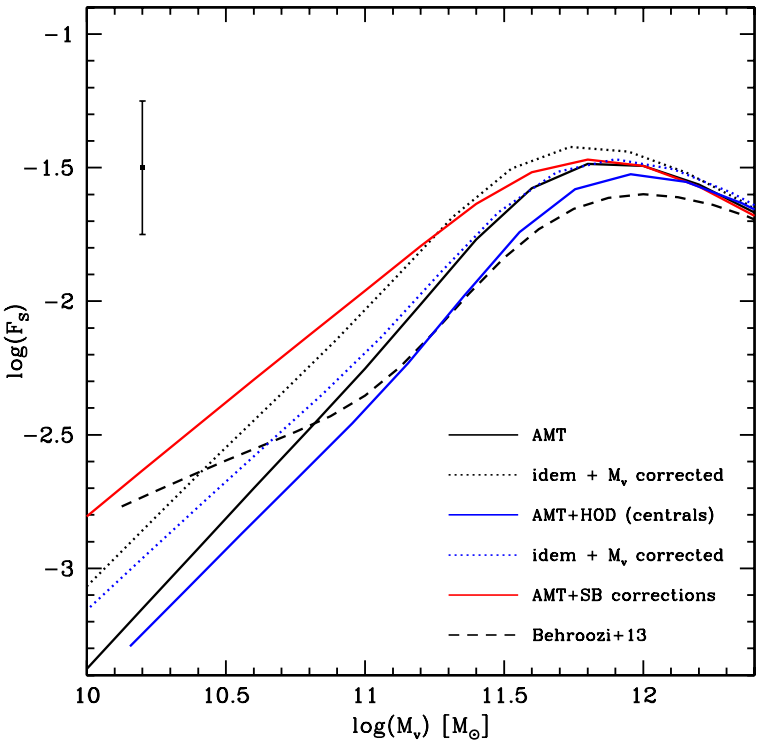

Figura 4.9: Different cases of semi-empirically inferred F_s–M_s relations: by means of the AMT (black line) and when the halo/subhalo mass function is corrected for the effects of baryons (dotted line); by means of the AMT+HOD, only for central galaxies/distinct halos (blue line) and when the correction for the effects of baryons is introduced (blue dotted line); again, by means of the AMT but correcting the GSMF for the (uncertain) SB issues (red solid line); see the text for details. The dashed line reproduces the AMT inferences by Behroozi et al. (2013). The error bar indicates the typical systematical uncertainty (mainly due to the M_s determination) of these inferences.

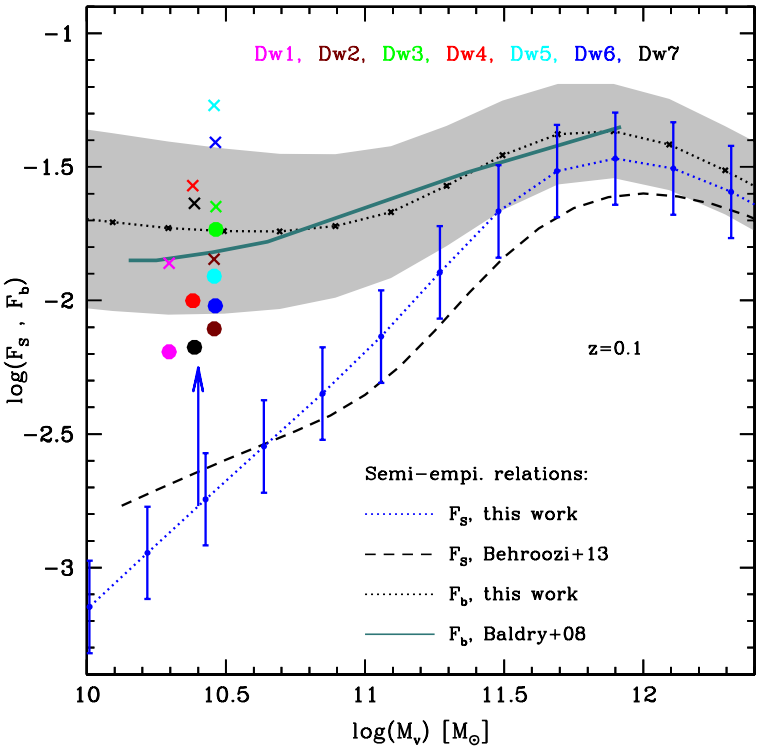

Figura 4.10: Stellar-to-halo (filled circles) and baryonic-to-halo (crosses) mass ratios vs. $M_{\rm v}$ for the seven simulated dwarfs. The blue dotted line with error bars corresponds to the F_s–$M_{\rm v}$ relation for central galaxies/distinct halos and its intrinsic scatter plotted in Figure 4.9. The arrow indicates the factor by which F_s increases at $\log(M_{\rm v}/M_\odot)$ = 10.4 if the (uncertain) corrections to the GSMF for SB issues are introduced (see Section 4.6.1). The dashed line corresponds to the F_s–$M_{\rm v}$ relation as inferred semi-empirically by Behroozi et al. (2013). Our inferences of the corresponding F_b–$M_{\rm v}$ relation and its 1σ scatter are represented by the dotted line and the gray shaded area (see the text for a description of how this is calculated). We also reproduce the mean F_b–$M_{\rm v}$ relation calculated by Baldry et al. (2008; green thick line).

$\log(M_{\rm v}/M_{\odot})$ = 10.4 if the (uncertain) corrections to the GSMF for SB issues are introduced (see section 4.6.1). The dashed line is for the average (central and satellites) relation reported in Behroozi et al. (2013). The simulated dwarfs are, on average, ~ 0.7 dex above the semi-empirical inferences.

What about the baryonic-to-halo mass ratio, F_b, versus $M_{\rm v}$? In order to calculate this relation, we add (see Section 4.6.1) information on the gas content to the galaxy catalog used here, thus constructing the corresponding galaxy baryonic mass function (GBMF), and applying the same AMT+HOD formalism mentioned above. For the gas content, we use the empirical M_g–M_s relation given in Stewart et al. (2009), including its scatter. The result obtained for central galaxies/distinct halos is plotted with the dotted line and gray area (1σ intrinsic scatter) in Figure 4.10. We also plot the inference by Baldry et al. (2008; green thick line), who used their GSMF, the empirical M_s–metallicity relation, and a model to infer from it the f_g–M_s relation, for obtaining the GBMF. By abundance matching this function with the CDM halo mass function, they calculated the mean F_b–$M_{\rm v}$ relation that we reproduce in Figure 4.10 (green thick line). For a given halo mass, the baryonic mass ratios, F_b, of our dwarfs are close to those inferred semi-empirically, unlike what happens with the stellar mass ratios, F_s. This result is consistent with the fact that the gas fractions of the simulated dwarfs are lower, on average, than what observations show (Figure 4.2).

The comparison shown in Figure 4.10 suggests that *there is not much room for more efficient SN-driven outflows (with higher mass loading factors) than those obtained in the simulations*; otherwise, the baryonic masses of the simulated dwarfs would be too low with respect to the semi-empirical inferences. Besides, more efficient outflows are not expected to help in keeping the SF at low redshifts active, as observations suggest for most low-mass galaxies, especially the isolated ones (cf. Salim et al. 2007; Geha et al. 2012; Pacifici et al. 2013). Instead, more gas would be ejected from the galaxy and halo, making a later re-accretion very unlikely (necessary to fuel SF) given the small and almost non-increasing gravitational potential of these low-mass halos (see Firmani, Avila-Reese & Rodríguez-Puebla 2010, for a discussion).

Therefore, the avenue for improving the simulations of low-mass galaxies, rather than increasing the strength of the SF-driven ejective feedback, should take into account processes that lower the SF efficiency at early epochs and delay the stellar mass assembly of the dwarfs with respect to their halo. This may be attained, for example, by (1) including the momentum transfer to the gas by the radiation field from young massive stars (radiation pressure) and the heating by local photoionization in the stellar feedback recipe (preventive feedback; e.g., Murray, Quataert & Thompson 2005; Brook et al. 2012; Hopkins, Quataert & Murray 2012; Wise et al. 2012; Agertz et al. 2013; Ceverino et al. 2013); or (2) by introducing an H_2-based SF scheme instead of a gas density threshold (Krumholz & Dekel 2012; Kuhlen et al. 2012; Christensen et al. 2012; Munshi et al. 2013; Thompson et al. 2014). It is known that H_2 formation depends on the gas metallicity; therefore, the SF should be less efficient in the past for the low–metallicity, low–mass galaxies.

Christensen et al. (2012) simulated a dwarf galaxy of halo mass similar to ours, where SF is triggered only in those regions where H_2 was formed (a scheme of H_2 metallicity–

dependent formation was implemented). They compared their results with a similar simulation but with the usual SF density threshold recipe with $n_{\rm SF} = 100\ {\rm cm}^{-3}$. They find that at high z, when the metallicities are low, both simulations show similar results (see their Figure 8), suggesting that a high $n_{\rm SF}$ value could emulate the H_2-driven SF implementation. We experimented with a $n_{\rm SF}$ value of 100 cm^{-3} in our Dw1 and Dw3 galaxies. The obtained dwarfs are unrealistic, with strongly peaked circular velocity profiles and stellar and gas masses at $z = 1$, larger than those presented in Section 3 (see also Colín et al. 2010). With about the same energy injection, specially at high redshift, the (strong) SN feedback is now unable to disperse and blow the gas out of the high-density lumps (comprised of the cells where SF proceeds and those around) and to avoid the SF runaway, as well as the formation of massive clumps that migrate to the center, making the galaxies very concentrated.

4.7.2. Where are the baryons?

Figure 4.4 shows that the total baryon mass fraction within the virial radius, $F_b^{\rm v}$ (solid black lines), is significantly lower than the universal baryon fraction, $F_{b,U}$, specially at lower redshifts. This fraction at radii larger than $R_{\rm v}$ is still smaller than $F_{b,U}$ (solid color lines, for radii up to 1.5, 2.0, 2.5, and 3.0 $R_{\rm v}$). In Figure 4.11, we show the spatial baryon mass fractions at different radii (spherical shells), $F_b(\Delta R) \equiv M_b(\Delta R)/M_{\rm v}(\Delta R)$, in units of $R_{\rm v}$ for the seven simulations. These fractions are evaluated at $z = 0$ (according to Figure 4.4, the results should be qualitatively similar at higher redshifts). The radii, in units of $R_{\rm v}$, at which ΔR is defined are between 0 and 0.1, 0.1 and 1, 1 and 1.5, 1.5 and 2, 2 and 2.5, and 2.5 and 3.0. The baryon fractions are normalized to the universal one.

From Figure 4.11, we identify four regimes for the baryon mass distribution with respect to the total one:

1. The baryon-to-total mass ratios inside 0.1 $R_{\rm v}$ tend to reach high values; this is the place where most baryons settle to form the galaxy. However, notice that, even in this region of high concentration, the baryon fraction is lower than the universal one for four of the dwarfs; the three for which the local baryon fraction is slightly higher than $F_{b,U}$, are those that assemble their mass later (as already discussed, these galaxies suffer less early gas loss). Thus, at 0.1 $R_{\rm v}$, DM dominates locally in all of the simulated dwarfs, something that agrees with dynamical studies within the optical radii of observed dwarfs.

2. The baryon-to-total mass ratios in the shell with radii from 0.1 $R_{\rm v}$ to 1 $R_{\rm v}$ are between 0.1 and 0.5 $F_{b,U}$; i.e., these are baryon-deficient regions because both a fraction of the baryons flowed to the center to form the galaxy and another larger fraction was blown away due to the galaxy feedback. As mentioned in Section 4.5.2 (see Figure 4.5), most baryons in the halo are in the form of hot gas. The virial temperature corresponding to halos of circular velocities $\lesssim 60$ km s^{-1} is actually very low; hence the halo gas in the simulations is hot due to the galaxy SN-driven feedback. Most of this gas is actually outflowing material.

3. The baryon-to-total mass ratios at radii larger than the virial radius are larger than those inside it but still lower than $F_{b,U}$, at least up to 2–3 $R_{\rm v}$. This means that the effects of the galaxy feedback extend out to these large radii, and gas is still outflowing here. Notice

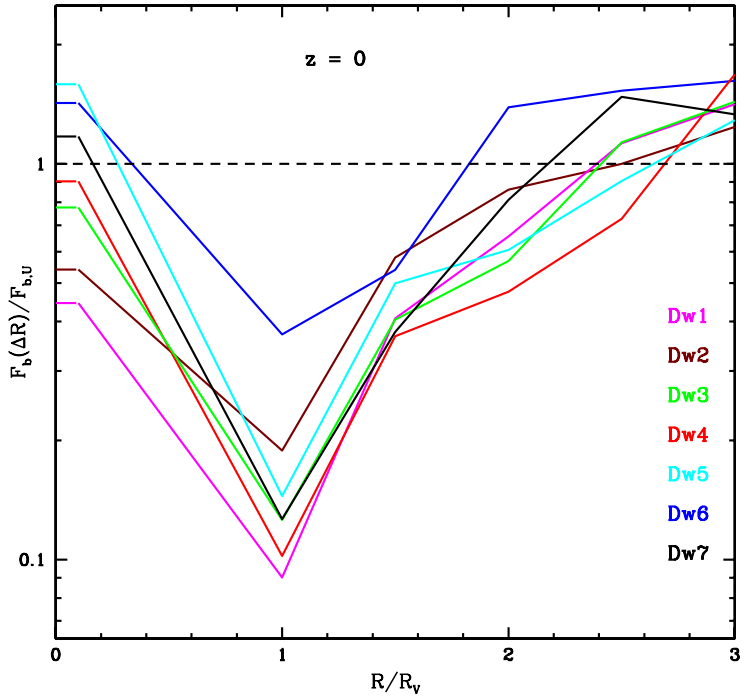

Figura 4.11: Different spatial baryon mass fractions (at $z = 0$), $F_b(\Delta R) \equiv M_b(\Delta R)/M_{\rm v}(\Delta R)$, where ΔR are radius intervals in unities of $R_{\rm v}$ between 0 and 0.1, 0.1 and 1, 1 and 1.5, 1.5 and 2, 2 and 2.5, and 2.5 and 3.0.

that 2–3 $R_{\rm v}$ correspond to 100–150 kpc $\rm h^{-1}$ in physical scales.

4. Only at radii as large as 2–3 $R_{\rm v}$, the baryon-to-total mass ratios become close to the universal baryon fraction, and at still larger radii, there is even an excess of baryons with respect to the universal average. This excess can be explained as the accumulation of baryons swept out by the galaxy outflows.

4.7.3. Episodic star formation

According to Figure 4.7, the history of the SFR of the simulated dwarfs is episodic, with strong ups and downs, even with periods of time in which it is completely quenched. In an attempt to quantify the average amplitude of the bursty SFR behavior, we compute the logarithmic standard deviation of the SFR (measured every $\Delta t = 100$ Myr) with respect to its mean in a period of 2 Gyr, $\sigma_{\rm LgSFR}$. The results for the seven dwarfs are plotted in Figure 4.12. For this exercise, we use the stellar age histogram as a proxy for the SFH; as we keep record of the birth time of each stellar particle, we use this to compute the amount of mass in stars inside the galaxy in time bins of 100 Myr width, from the oldest to the youngest stellar particle.[7]

From Figure 4.12, we observe that the logarithmic amplitude of the 100 Myr episodes of the SFR oscillates between $\sigma_{\rm LgSFR} = \pm 0.3$ and ± 1 dex for all of the runs and at different cosmic epochs. There is not a monotonic trend of $\sigma_{\rm LgSFR}$, calculated in periods of 2 Gyr, with cosmic time. For most runs, the degree of burstiness attains a maximum at early epochs, then decreases, and after 5–6 Gyr, it increases again, just to show a fall in the last bin. This behavior is more pronounced for galaxies in early assembled halos. The fact that the SFR changes in 100 Myr periods by factors of 2–10, on average, in our simulated galaxies is partially explained by the effects of stellar feedback, which likely acts at the level of the whole galaxy, heating and ejecting the gas from it. As a consequence, the global SFR is decreased or quenched until gas infalls and cools again. The bursty SFH can also be due to the small number of SF regions in the dwarfs; since these regions are intrinsically stochastic, a low number of them also implies a somewhat stochastic global SFR. In general, our results are qualitatively similar to the ones found by other authors, which also report a bursty behavior in the SFR of dwarf simulated galaxies (e.g., Stinson et al. 2007; Teyssier et al. 2013). In Teyssier et al. (2013), the extreme fluctuations in the SFR reach amplitudes of a factor of ~ 10.

It is difficult to evaluate whether the bursty nature of the SFHs of our simulated dwarfs is consistent with the SFHs of observed dwarf galaxies because, from the observational point of view, the number and amplitude of the SF episodes are not well constrained. Only limited and/or indirect inferences have been obtained. From observations of the Local Group dwarf galaxies, Mateo (1998) found that the most recent SF episodes last from 10 to 500 Myr in

[7] We have decided to use 100 Myr to be consistent with the analysis done in Figure 4.7, where the "instantaneous" SFRs were computed using this period of time. However, we have checked that the global results regarding the measured SFRs do not change significantly if Δt is assumed to be larger (200 Myr) or smaller (50 Myr) than our assumed value.

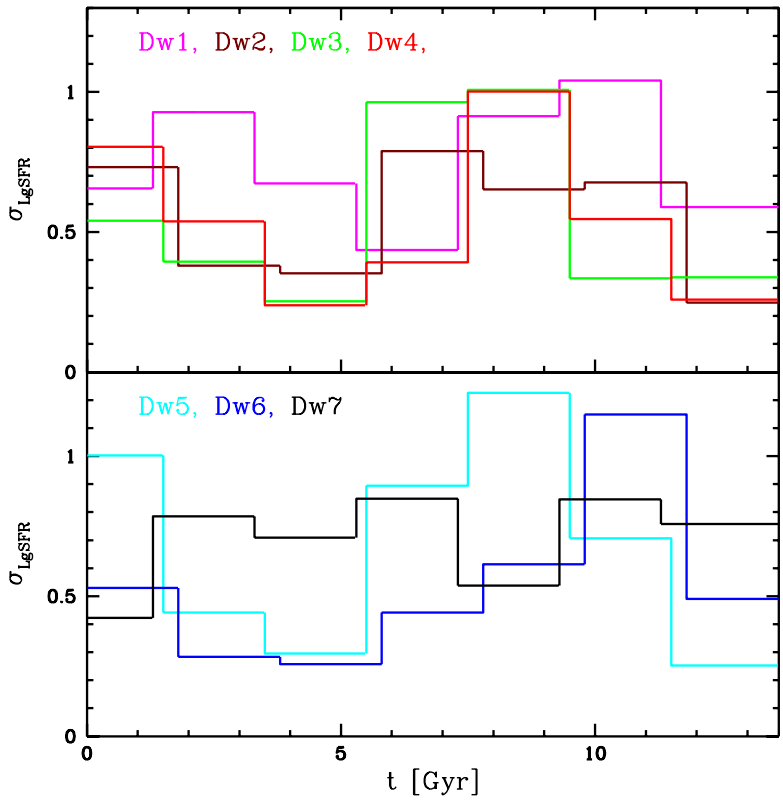

Figura 4.12: Logarithmic standard deviation of the SFR measures in periods of $\Delta t = 100$ Myr with respect to the mean SFR in a period of 2 Gyr, σ_{LgSFR}, as a function of cosmic time for the seven runs divided in the two panels. An "archeological" SFR history is used to compute σ_{LgSFR}.

both irregular and early-type dwarfs. On the other hand, based on the 11HUGS sample, and by assuming that bursts occur with equal probability in all the sample galaxies, Lee et al. (2009) found that the SFR in the burst mode is ~ 4 times greater than in the quiescent mode. They also estimated that the bursts, assumed to last $\sim$ 100 Myr (Weisz et al. 2008), occur every 1–2 Gyr, and the fraction of stars formed in the bursts is, on average, $23\,\%$. For a sample of eighteen nearby starburst dwarfs, McQuinn et al. (2010) reported that their recent SFRs are more than two times higher than the SFR averaged over the past 6 Gyr.

In a detailed study of 60 dwarfs from the ACS nearby galaxy survey treasury, Weisz et al. (2011) showed that SFHs are so complex that they cannot be explained by simple SFH models, like single bursts, constant SFRs, or exponentially declining SFRs. The above mentioned observational estimates confirm that dwarf galaxies have an episodic SFH, in general (see also Bauer et al. 2013, for an extensive discussion). However, the amplitude and frequency of the SFR episodes seem to be lower than those measured in our simulated dwarfs. More observational work is necessary in order to quantitatively evaluate how episodic the SFHs of dwarf galaxies are. If the conclusion that the simulated dwarfs have SFHs similar to or burstier than the ones inferred for observed galaxies holds, *this then indicates that the intensity of the SN-driven global outflows in the simulations cannot be stronger*; otherwise, the SFHs would show even more frequent and more intense galactic SFR episodes.

4.7.4. Numerical resolution

In order to determine the effect of resolution in our results, we ran galaxies Dw1 and Dw3 with less resolution: the cell size at the maximum level of refinement is twice as large ($\sim$ 109 pc), and the mass of the DM particle m_p is eight times higher than in the runs presented above. The two runs with lower resolution, $\mathrm{Dw1_{lres}}$ and $\mathrm{Dw3_{lres}}$, end with galaxy properties and evolutionary trends similar to runs Dw1 and Dw3, respectively, showing that we have found resolution convergence, at least in regards to the aspects studied here. For example, the stellar mass fractions at $z = 0$ in $\mathrm{Dw1_{lres}}$ and $\mathrm{Dw3_{lres}}$ are $\log(F_s)$=-2.2 and –1.7, respectively, very similar to those obtained in the runs Dw1 and Dw3; the gas fractions also do not vary by more than 5 % between the simulations with the two resolutions; the circular velocity profiles are again flat at large radii, with small changes in its maximum, $V_{\rm max}(\mathrm{Dw1_{lres}}, \mathrm{Dw3_{lres}})$ = (55.5, 54.6) km s^{-1} versus $V_{\rm max}$(Dw1, Dw3) = (52.0, 56.1) km s^{-1}. Moreover, the halo, baryonic, and stellar MAHs look similar.

4.8. Conclusions

High-resolution zoom simulations of seven central dwarf galaxies formed in isolated halos, which today attain the same virial (dark + baryonic) mass, $\log(M_{\rm v}/M_\odot)\approx 10.4$, were performed with the N-body/hydrodynamics code ART, including standard prescriptions for SF and SF-driven thermal feedback. All simulated dwarfs have nearly flat rotation cur-

ves, with some of them also having a significant stellar disk component. They roughly agree with observations in the $V_{\rm max}$–M_s and R_e–M_s relations. However, their sSFRs and gas fractions are lower than the observational determinations, and their stellar masses are too high as compared to semi-empirical inferences of F_s=M_s/$M_{\rm v}$; on the other hand, their baryonic masses (stars + gas) seem to be in agreement with these kind of inferences. The seven runs were classified according to their halo MAHs, from those that assemble their masses, on average, earlier to those that do it later (from Dw1 to Dw7, respectively). We then explored how the properties and mass assembly of the different galaxy/halo components of the dwarf systems depend on the halo MAHs. Our main conclusions are as follows.

- Stellar mass assembly of the central dwarfs closely follows their halo mass assembly; the ratio F_s is ≈ 0.01 and constant since $z \sim 1$ for all of the simulated galaxies, and at higher redshifts, the dwarfs formed in the late-assembled halos tend to have even smaller F_s values. The baryons within the virial radius roughly follow the assembly of the whole halo but there are periods when baryons are lost due to the SN-driven outflows; as a result, the $F_b^{\rm v}$=$M_b^{\rm v}$/$M_{\rm v}$ ratio systematically decreases with time, from values 1.5–2 times smaller than the universal baryon fraction at $z \sim 4$ to values 2–6 times smaller at $z = 0$. For the early-assembled halos, the SN-driven gas loss happens intensively early in the evolution, while for halos that assemble their mass later, the gas loss is less intense overall, ending these systems with higher $F_b^{\rm v}$ values than those assembled earlier. The mentioned behaviors of the baryon content with respect to total mass extend roughly up to $3R_{\rm v}$ (100–150 kpc $\rm h^{-1}$ from the galaxy in physical scales), showing a high efficiency of the gas outflows in the simulations.

- Assembly histories of the gas of the dwarfs are episodic, with periods of increase and decrease. The dwarfs formed in late-assembled halos have higher gas fractions, f_g=M_g/M_b, than those formed in early-assembled halos; the early SF-driven outflows remove more gas from the latter than the former. When the galaxy f_g decreases, one typically sees an increase in the gas fraction in the halo (this gas is much hotter, while the gas in the galaxy is dominantly cold). This shows that the strong SN-driven outflows play a major role in regulating the gas content—and therefore the SFR—of the simulated dwarfs, at least for those in which the corresponding halo assembling happens more gradually. However, there are also periods, mostly in the early-assembled halos, when the gas fractions in both the galaxy and halo decrease, since the gas is completely expelled from the halo.

- SFHs of the simulated dwarfs are quite episodic with average variations of the SFR (measured every 100 Myr) of factors 2–10 with respect to the mean, measured in periods of 2 Gyr. The average SFH in most of the runs is composed of an early ($z \gtrsim 2$) period of high SFRs and then a significant decline at lower redshifts; the exceptions are the two dwarfs formed in the latest-assembled halos (Dw6 and Dw7). However, even in these cases, the SFHs do not show the late active SF regime of observed isolated dwarfs.

- The effect of baryons on the total virial mass of the simulated halos is to reduce it by 10 %–20 % with respect to that obtained in the N-body only simulations; this effect is seen from at least since $z \sim 2$. Most of the difference is caused by the loss of baryons from the halo due to the SN-driven outflows. A smaller contribution comes from the gravitational potential being less deep, due to gas loss, and the halos are less capable of accreting mass. The abundance matching and halo occupation model carried out with a corrected halo/subhalo mass function by the effects of baryons gives a slightly higher F_s–M_s relation at lower masses than in the case when no correction is applied.

In summary, we conclude that the "cosmological" halo MAHs have a non-negligible influence on stellar and baryonic mass assembly of the dwarfs that form in their centers. In spite of the strong SF-driven feedback effects (mainly the SN-driven outflows), the mass assembly of galaxies roughly follows the one of their halos. Since, in the hierarchical ΛCDM scenario, low-mass halos are assembled early, then low-mass galaxies are expected to have an early stellar mass assembly and small sSFRs at late epochs. Our results indeed show that the simulated galaxies, even those that form in late-assembled halos, have lower sSFRs and gas contents, and larger stellar masses for their halo masses than observations and semi-empirical inferences show. Yet, the baryonic masses of the simulated dwarfs seem to agree with the semi-empirical inferences. Thus, rather than further increasing the strength of the ejective SN-driven feedback, possible avenues to solve the issues of simulated low-mass galaxies are to introduce subgrid processes that delay the atomic gas transformation into molecular gas, and/or to take into account the effects of preventive feedback (produced by, e.g., radiation pressure of massive stars and local photoionization), which reduces the conversion efficiency of gas into stars.

After the completion of this paper, several works have appeared in the arXiv, showing that the introduction of preventive feedback may indeed delay the SF in simulated galaxies (Kannan et al. 2014; Sales et al. 2014; Hopkins et al. 2013; Trujillo-Gomez et al. 2013). In particular, in the papers by Hopkins et al. (2013) and Trujillo-Gomez et al. (2013), some of their simulated galaxies, which include radiation-pressure feedback (the former authors include also photo-ionization and photo-electric heating), in addition to the SN feedback, are low-mass galaxies run to $z = 0$. As these authors show, the inclusion of preventive feedback delays the SF and decouples the assembly of the galaxy from that of its DM halo in low-mass galaxies, helping produce dwarfs with smaller M_s-to-$M_{\rm v}$ ratios and higher values of gas fraction and sSFR at late epochs.

Acknowledgements

We are grateful to Dr. Peter Behroozi for providing us his data plotted in Figures 4.9 and 4.10, in electronic form. A.G. acknowledges a PhD fellowship provided by DGEP-UNAM. V.A. and A.G. acknowledge CONACyT grant (Ciencia Básica) 167332-F, and A.V. acknowledges PAPIIT-UNAM grant IA100212 for partial support.

Capítulo 5

Ensamblaje de las galaxias en el escenario jerárquico ΛWDM

En los Capítulos 3 y 4 hemos visto cómo es que las galaxias de baja masa simuladas baja la cosmología ΛCDM, a pesar de tener una serie de propiedades estructurales que comparan muy bien con las observaciones, presentan dificultades para reproducir el "downsizing" en la TFEE que caracteriza a las galaxias de baja masa, y el ensamblaje tardío de su masa. Estos dos aspectos, que son resultados propiamente empíricos, parecen representar un reto para las simulaciones numéricas de galaxias. Como ya se discutió ampliamente en los capítulos anteriores, en años recientes se ha propuesto que la respuesta está en la física de los bariones cuando se lleva a cabo el proceso de ensamblaje de las galaxias. En particular, se ha propuesto que el feedback (vía distintos mecanismos astrofísicos) puede jugar un papel fundamental en el retraso del ensamblaje de masa estelar de las galaxias de baja masa. En el capítulo anterior ya discutimos este escenario y planteamos que en particular, un feedback eyectivo no parece ser una respuesta satisfactoria. También se ha planteado que el retraso en la formación de H_2 en el MIE puede ser responsable de tal ensamblaje tardío. Todos estos son mecanismos astrofísicos que como dijimos, están asociados con la gastrofísica. Sin embargo, es válido plantearse como hipótesis si una modificación en el escenario cosmológico subyacente, en este caso la cosmología ΛCDM, puede explicar las propiedades empíricas arriba planteadas. En este capítulo abordaremos dicho estudio.

Así, a continuación se presenta el artículo *"Simulations of galaxies formed in warm dark matter halos of masses at the filtering scale"* que esta por enviarse a una revista para su arbitraje, por lo cual el texto se encuentra en idioma inglés. Mi contribución en este trabajo estuvo centrada principalmente en el análisis de las simulaciones y su visualización. Como el título lo menciona, allí abordamos el análisis del ensamblaje de galaxias de baja masa para un escenario en el que la partícula oscura es "tibia" ($m_p = 1.2$ y 3 kevs). El objetivo central de este trabajo, más que radicar en el estudio de la formación de estructuras en un escenario con un masa de partícula en especial, está orientado al

estudio de galaxias a la “masa de corte” (masa de filtrado), es decir, galaxias cuya masa corresponde justo a la masa en la que el espectro de potencias cae abruptamente con respecto al definido por la cosmología ΛCDM. A esta masa ya se deberían de notar claramente los efectos del cambio de escenario cosmológico (a masas mayores el espectro de potencias es prácticamente igual y no se observarían mayores diferencias), y justo esto es lo que se encuentra reportado en el presente capítulo, en el que, entre otras cosas, encontramos que:

Las galaxias a escalas del filtrado (que para nuestro caso corresponde a una masa de partícula térmica de 1.2 KeV) con relación a sus contrapartes ΛCDM: ensamblan sus masas de halo y estelar más tarde, teniendo edades estelares pesadas por masa entre 1.4 y 2.8 Gyr menores; tienen valores de $V_{\max}$ $20-60\,\%$ menores y curvas de rotación más suaves, así como distribuciones de estrellas mucho menos concentradas al centro y radios efectivos más grandes por factores 1.3–3. Por otro lado, las enanas formadas en halos al día de hoy 20-30 veces la masa de filtrado (que para nuestro caso corresponde a una masa de partícula térmica de 3.0 KeV) tiene propiedades y evolución ya muy similares a las de sus contrapartes ΛCDM. Si la masa de la partícula térmica queda restringida a valores > 3 KeV, sólo los halos menores al día de hoy que $\sim 2\times10^{9}\,M_{\odot}$ son afectados, lo cual implica que los efectos encontrados aquí de la cosmología ΛWDM sobre las galaxias afectarían a enanas de masas estelares menores de $\sim 10^{7}-10^{6}\,M_{\odot}$. Aunque las observaciones son escasas, preliminarmente se puede decir que estos efectos van en la dirección necesaria para lograr acuerdo con las mismas.

5.1. Simulations of galaxies formed in warm dark matter halos of masses at the filtering scale

P. Colín[1], V. Avila-Reese[2], A. González-Samaniego[2], and H. Velázquez[3]

To be submitted in September 2014 to *The Astrophysical Journal*

Abstract

We present zoom-in N-body/Hydrodynamics simulations of dwarf central galaxies formed in Warm Dark Matter (WDM) halos that end up today with masses around the half-mode filtering scale, M_f, and $\sim 20-30$ times M_f. The results of these simulations are compared with those obtained from the corresponding simulations in the Cold Dark Matter (CDM) cosmology. The dwarfs formed in halos of masses $\sim 20-30\times M_f$ have roughly similar properties and evolution than their CDM counterparts; on the contrary, those formed in halos of masses $\sim M_f$, are systematically different from their CDM counterparts. As compared to the CDM dwarfs, they assemble the dark and stellar masses later, having mass-weighted stellar ages 1.4–4.8 Gyr younger; their circular velocity profiles are shallower, with maximal velocities 20–60 % lower; their stellar distributions are much less centrally concentrated and with larger effective radii, by factors 1.3–3. The WDM dwarfs at the filtering scale have disk-like structures, and end in most cases with higher gas fractions and lower stellar-to-total mass ratios than their CDM counterparts. The late halo assembly, low halo concentrations, and the absence of satellites of the former with respect to the latter, are at the basis of the differences.

5.2. Introduction

The Λ cold dark matter (ΛCDM) cosmology provides the most accepted background for studying the process of cosmic structure formation in the Universe. The predictions of the ΛCDM-based scenario of structure formation are fully consistent with observations of the large-scale structure of the present and past Universe, including the anisotropies in the cosmic microwave background radiation (see Frenk & White 2012, for a review). However, doubts have been cast on whether observations of matter distribution at small –dwarf galactic and subgalactic– scales are consistent with the predictions of the ΛCDM scenario (see for recent reviews e.g., Weinberg et al. 2013; Del Popolo et al. 2014). Currently, it is

[1]Centro de Radioastronomía y Astrofísica, Universidad Nacional Autónoma de México, A.P. 72-3 (Xangari), Morelia, Michoacán 58089, México

[2]Instituto de Astronomía, Universidad Nacional Autónoma de México, A.P. 70-264, 04510, México, D.F., México

[3]Instituto de Astronomía, Universidad Nacional Autónoma de México, A. P. 877, Ensenada BC 22800, México

matter of great debate whether the potential problems are real or consequence of observational biases and/or still poorly understood astrophysical processes at small scales. If they are confirmed, introducing variations to the ΛCDM cosmology will appear as a feasible solution.

From the point of view of initial conditions for the cosmic structure formation, ΛCDM is the simplest model. For the ΛCDM model: (1) the cut-off scale in the linear mass power spectrum of perturbations due to free streaming, $\lambda_{\rm fs}$, is many orders of magnitude smaller than the resolution reached by current numerical cosmological simulations of galactic halos so that in practice $\lambda_{\rm fs} = 0$ and hierarchical cosmic structure formation proceeds at all scales; (2) the relic thermal velocities of the CDM particles, $v_{\rm th}$, are very small, so in practice $v_{\rm th}$=0 is assumed; (3) since CDM particles are non-baryonic, they do not interact electromagnetically, and are assumed to have a negligible self-interaction cross section, $\sigma_{\rm SI} = 0$, constituting the CDM then a pure collisionless fluid; and (4) the statistical distribution of the primordial overdensity perturbations is assumed to be Gaussian. Therefore, the relaxation of any of the above listed assumptions implies necessarily the introduction of free parameters in the initial conditions of cosmic structure formation; for example, values of $\lambda_{\rm fs}$, $v_{\rm th}$, $\sigma_{\rm SI}$, or the skewness and kurtosis in the primordial density perturbations distribution.

More than a decade ago, high-resolution N-body cosmological simulations were performed to explore how substructure, inner density profiles and shapes of halos were affected when one or several of the ΛCDM assumptions listed above were relaxed. Concretely, in these simulations were introduced: (a) a cut-off in the power spectrum and/or non-negligible thermal velocities in the dark particles (in concordance with the Λ warm dark matter, ΛWDM, cosmology; Colín, Avila-Reese & Valenzuela 2000; Avila-Reese et al. 2001; see also, Bode, Ostriker & Turok 2001, Knebe et al. 2002); (b) a non-negligible self-interaction with constant and velocity-dependent particle cross sections (Yoshida et al. 2000; Colín et al. 2002, see also Spergel & Stenihardt 2000; Firmani et al. 2000); (c) and a non-Gaussian initial perturbations, positively or negatively skewed (Avila-Reese et al. 2003).

Among alternative cosmologies, the most popular is the ΛWDM one with a power spectrum filtered at scales corresponding to dwarf galaxies. As N-body simulations show, in this case the amount of substructure in Milky Way-sized halos is considerably reduced (e.g., Colín, Avila-Reese & Valenzuela 2000; Bode, Ostriker & Turok 2001; Knebe et al. 2002; Macciò & Fontanot 2010; Kennedy et al. 2014), the abundance of low-circular velocity halos hosting dwarf galaxies is lowered (e.g., Zavala et al. 2009; Papastergis et al. 2011), and, although the halos/subhalos do not present shallow cores at the scales of astrophysical interest, they are less concentrated and with lower maximum circular velocities than their CDM counterparts (Avila-Reese et al. 2001; Colín, Valenzuela & Avila-Reese 2008; Lovell et al. 2012; Schneider et al. 2012a; Anderhalden et al. 2013). These and other effects make the ΛWDM model an appealing alternative for alleviating the potential problems of the ΛCDM model at small scales, while conserving its successes at larger scales.

The main constraint to the ΛWDM scenario comes from the comparison of the results

of WDM hydrodynamics simulations in the quasi-linear regime with the Ly-α flux power spectrum of high-redshift quasars (Narayanan et al. 2000; Viel et al. 2005), though these comparisons are not free of uncertainties and limitations (see e.g., de Vega, Salucci & Sanchez 2014). Depending on the nature of the WDM particle, thermal, sterile neutrino, etc., a lower limit to its mass, $m_{\rm WDM}$, can be stablished from the Ly-α forest analysis, which implies an upper limit to the damping scale in the mass power spectrum. Several updated estimates were presented recently in the literature (e.g., Viel et al. 2013). Based on the constrains of the latter authors (for a thermal relic particle, $m_{\rm WDM}$ should be $\gtrsim 3.3$ keV at the 2σ level), Schneider et al. (2014) conclude that the upper limit in the damping is at so small scales that the allowed ΛWDM models would not be already able to solve the potential problems of ΛCDM.

So far, most studies on galaxy properties in the ΛWDM scenario were based on dark-matter-only simulations or a combination of these kind of simulations with semi-analytic models (for the latter see e.g., Macciò & Fontanot 2010; Menci, Fiore & Lamastra 2012; Kang, Macciò & Dutton 2013). However, by their own nature, these approaches can not take into account the effects of the non-linear baryonic physics on the evolution and dynamics of the halos, which can be important. Thus, inferences based on the analysis of dark-matter-only simulations (and, perhaps, semi-analytic models) are necessarily limited when comparing with observations (see e.g. Kang, Macciò & Dutton 2013). It is then important to go beyond those techniques and perform full N-body + hydrodynamical simulations. An interesting question than one can ask is how much differ the evolution and properties of galaxies formed in the ΛWDM scenario from those formed in the ΛCDM one. At this point, it is important to recognize that the dark-matter structure evolution is expected to be very similar in both scenarios at scales much larger than the filtering one, with differences appearing gradually at scales approaching this scale.

The so-called half-mode wavelength or its corresponding mass, M_f, is commonly chosen as the relevant *filtering* scale at which WDM halo abundance and properties start to significantly deviate from the CDM case (see for the exact definition and references Section 5.3). In this paper, we present a set of zoom-in N-body/hydrodynamical simulations of (dwarf) galaxies formed in a WDM scenario in halos with masses $\lesssim M_f$ and $\sim 20M_f$, and compare them with their CDM counterparts. Recently, Herpich et al. (2014, see also Libeskind+2013) reported WDM simulations of this kind but for three halos of masses significantly larger than the filtering masses corresponding to their WDM particle masses ($m_{\rm WDM}$= 1, 2, and 5 keV). This is very likely the reason why the evolution of their WDM galaxies did not differ significantly from the CDM counterparts. After completion of our study, it appeared a preprint by Governato et al. (2014), where the authors present a simulation of *one* dwarf galaxy formed in a $\sim 10^{10}$ M$_\odot$ halo, both in WDM and CDM cosmologies. For the WDM cosmology, $m_{\rm WDM}$=2 keV was used, which implies that their system is ~ 2 times larger than the filtering mass.

Here, our main goal is to explore the evolution and properties of dwarf galaxies formed in *halos of masses similar to* M_f. These are expected to be among the most abundant halos in a WDM scenario; below $\sim 0.5M_f$, the halo mass function strongly decreases, and

the structures, rather than virialized halos, are isolated 3D enhancements not assembled hierarchically (Angulo, Hahn & Abel 2013). Although our halos with mass $\sim M_f$ consist of halos with virial masses $\sim 2-4\times10^{10}$ M$_\odot$, the evolution and properties of these systems *are expected to be generic of structures of mass* $\sim M_f$*, regardless of the value of the WDM particle mass*.

In Section 2, the cosmological background and the used WDM models are presented. The details of the code and simulations performed here are given in Section 3. The properties and evolution of the simulated WDM dwarf galaxies and their corresponding CDM ones are presented in Section 4. A summary of the results and further discussion are presented in Section 5.

5.3. The cosmological models

The cosmological background used in our numerical simulations is a flat, low-density model with $\Omega_m = 0.3$, $\Omega_b = 0.045$, $\Omega_\Lambda = 0.7$, and $h = 0.7$. For the CDM initial power spectrum, $P(k)_{CDM}$, we adopt the approximation by Klypin & Holtzman (1997b), which was obtained as a direct fit of the power spectrum calculated using a Boltzmann code. For the scales studied in this paper, and even larger ones, this approximation is very accurate. In the case of WDM, the power spectrum at large scales is essentially that of the CDM, but at small scales the power is systematically reduced due to the free-streaming damping. The transfer function $T^2_{WDM}(k)$ describes such a deviation from the CDM power spectrum,

$$P_{WDM}(k) = T^2_{WDM}(k) P_{CDM}(k). \tag{5.1}$$

The CDM or WDM power spectra are normalized to $\sigma_8 = 0.8$, a value close to that estimated from the *Planck* mission (Planck Collaboration et al. 2013b); σ_8 is the rms of $z = 0$ mass perturbations estimated with the top-hat window of radius $8h^{-1}$Mpc.

The free-streaming of collisionless particles erase dark matter perturbations below a scale given by the properties of the dark matter particle. Here, we will refer to the case of fully thermalized particles at decoupling as *thermal relics*. A simple analysis gives an estimate of the comoving length at which thermal particles diffuse out (e.g., Kolb & Turner 1990; Schneider et al. 2012a):

$$\lambda_{fs} \simeq 0.4 \left(\frac{m_{\rm WDM}}{\rm keV}\right)^{-4/3} \left(\frac{\Omega_{WDM} h^2}{0.135}\right)^{1/3} [h^{-1}{\rm M}_\odot]. \tag{5.2}$$

However, in order to calculate the whole processed power spectrum, the coupled Boltzmann relativistic system of equations for the various species of matter and radiation should be numerically solved. Here, we adopt the WDM transfer function given in Viel et al. (2005):

$$T_{WDM}(k) = \left[1 + (\alpha k)^{2.0\nu}\right]^{-5.0/\nu}, \tag{5.3}$$

where $\nu = 1.12$ and the parameter α is related to $m_{\rm WDM}$, Ω_{WDM}, and h through

$$\alpha = a \left(\frac{m_{\rm WDM}}{1{\rm keV}}\right)^b \left(\frac{\Omega_{WDM}}{0.25}\right)^c \left(\frac{h}{0.7}\right)^d h^{-1}{\rm Mpc}, \tag{5.4}$$

with $a = 0.049$, $b = -1.11$, $c = 0.11$, $d = 1.22$. In eq. (5.3), α is a characteristic scale length that can be related to an effective free-streaming scale, $\lambda_{\rm fs}^{\rm eff} \equiv \alpha$ (e.g., Schneider et al. 2012a). The corresponding effective free-streaming mass is then:

$$M_{\rm fs} = \frac{4\pi}{3}\bar{\rho}\left(\frac{\lambda_{\rm fs}^{\rm eff}}{2}\right)^3, \tag{5.5}$$

where $\bar{\rho}$ is the present-day background density. The primordial density perturbations below $M_{\rm fs}$ are expected to be completely erased, while perturbations with masses up to thousand times $M_{\rm fs}$ can be significantly affected by the damping process. It is common, on the other hand, to define a characteristic scale below which the linear WDM power spectrum start to deviate significantly from the CDM one (Sommer-Larsen & Dolgov 2001; Avila-Reese et al. 2001). Following Avila-Reese et al. (2001), we define the half-mode wavenumber, $k_{\rm hm}$, for which $T^2_{WDM}(k) = 0.5$; i.e., where the value of the power spectrum of the WDM model is half that of the corresponding CDM one. The associated half-mode *filtering* mass is given by:

$$M_f = \frac{4\pi}{3}\bar{\rho}\left(\frac{\lambda_{\rm hm}}{2}\right)^3, \tag{5.6}$$

where $\lambda_{\rm hm} = 2\pi/k_{\rm hm}$ is the comoving half-mode length.[4] This filtering mass scale, which is much larger than $M_{\rm fs}$, is where one expects the abundance and properties of the halos to start to significantly deviate from the CDM case (Colín, Valenzuela & Avila-Reese 2008; Smith & Markovic 2011; Menci, Fiore & Lamastra 2012; Schneider et al. 2012a; Benson et al. 2013; Angulo, Hahn & Abel 2013). At masses around M_f, the abundance of halos already falls below, by a factor of ~ 2, that of the corresponding CDM one, reaching its relatively shallow peak at $\sim 0.5\, M_f$. Thus, the most abundant halos in the WDM cosmogony are those of masses around to M_f.

Structures of masses close to M_f can be unambiguously defined as approximately spherical virialized objects that resemble those seen in CDM simulations, albeit with some differences; for instance, they are less concentrated (e.g., Avila-Reese et al. 2001; Angulo, Hahn & Abel 2013). Moreover, halos of masses $\gg M_f$ are expected to assemble hierarchically, sharing the same properties as their CDM counterparts. Systems of masses several times smaller than M_f but larger than $M_{\rm fs}$ can be defined as "protohalos", that is halos that are not fully formed, but show clear isolated 3D enhancements (Angulo, Hahn & Abel 2013). At masses close to $M_{\rm fs}$, these authors report structures that appear as clear failures of their halo finder algorithm, these include outer caustics of large halos and dense sheets and filaments, where the collapse of a further axis has just started.

[4]Note that some authors define the half-mode wavenumber as $T_{WDM}(k) = 0.5$ (e.g., Schneider et al. 2012a), which implies a smaller M_f than in our case.

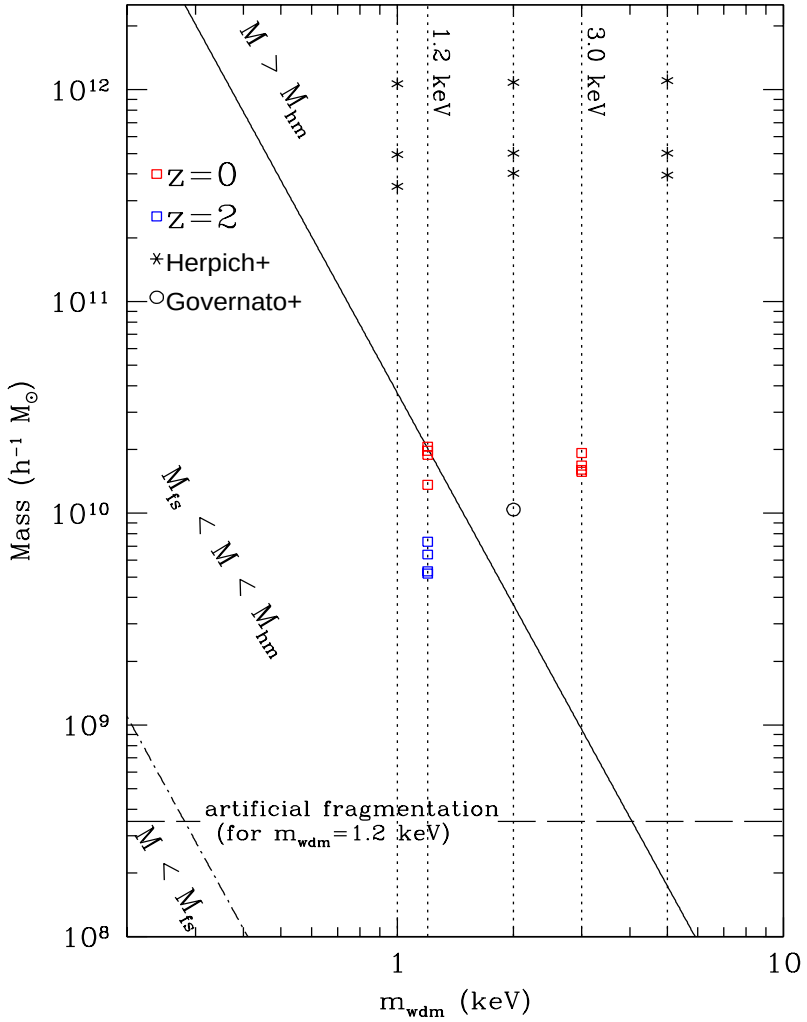

Figura 5.1: The free-streaming and half-mode (filtering) mass scales as a function of the thermal relic particle mass, $m_{\rm WDM}$ (for a sterile neutrino particle, see eq. 5.7). The squares show where our simulations lie at $z = 0$ (red) and at $z = 2$ (blue; only for the 1.2 keV case). Even at $z = 2$ our simulations are far from the artificial fragmentation scale for a filtering corresponding to 1.2 keV (horizontal dashed line). The starred symbols and the open circle correspond to the simulations presented in Herpich et al. (2014) and Governato et al. (2014) at $z = 0$.

Following Schneider et al. (2014), in Fig. 5.1, we show the dependence of M_f and $M_{\rm fs}$ on the thermal WDM particle mass $m_{\rm WDM}$. For a given $m_{\rm WDM}$ and at any epoch, objects located well above the solid line ($M = M_f$) are halos assembled hierarchically, as in the CDM cosmogony. Objects of masses close to M_f, on the other hand, can be considered "normal" halos. However, their early assembly is already affected by the filtering at small scales; for example, they form later than their CDM counterparts. The objects that Angulo, Hahn & Abel (2013) define as "protohalos" start to apear as the mass decreases below M_f and dominate the population when $M \ll M_f$. In these "protohalos", the hierarchical assembly fails notoriously (e.g., Schneider et al. 2012a). Finally, below the dot-dashed line ($M = M_{\rm fs}$), no structure formation is expected. However, in N-body simulations it is possible to find structures smaller than $M_{\rm fs}$ but they are actually artificial (see e.g., Avila-Reese et al. 2001; Bode, Ostriker & Turok 2001; Götz & Sommer-Larsen 2003; Knebe et al. 2003; Wang & White 2007; Schneider et al. 2012b; Angulo, Hahn & Abel 2013).

In Fig. 5.1 we plot our eight simulated systems (presented below) with red squares as well as those simulated by Herpich et al. (2014) (starred symbol; their M_{200} masses were multiplied by 1.24 in order to pass to our definition of virial masses). These masses are at $z = 0$; we also plot the virial masses of our simulated systems at $z = 2$ (blue squares). The horizontal dashed line corresponds to the mass scale where spurious structures would form in our simulations with $m_{\rm WDM}$=1.2 keV (for $m_{\rm WDM}$=3 keV, it is at a smaller mass) due to numerical fragmentation, according to the criterion given by Wang & White (2007). This criterion depends on the filtering scale and the resolution of the numerical simulation. As can be seen, our halos lie above the dashed line even at high redshifts.

The relations show in Fig. 5.1 are for thermal relic particles. Popular candidates for WDM are also the sterile and right-handed neutrinos, particles proposed to never been in thermal equilibrium (Dodelson & Widrow 1994; Shi & Fuller 1999; Abazajian, Fuller & Patel 2001; see Boyarsky, Ruchayskiy & Shaposhnikov 2009 for a review). Viel et al. (2005) provided a relation between the sterile neutrino mass and the mass of the thermal relic particle such that the transfer function for the sterile neutrino can be calculated according to eq. (5.3). The relation is given by

$$m_{\nu_s} = 4.43 \text{ keV}(m_{\rm WDM}/1 \text{ keV})^{4/3}(\Omega_{WDM}h^2)^{-1/3}. \quad (5.7)$$

Thus, for a given cosmological background, we can use Fig. 5.1 also for the case of the sterile neutrino, after going from $m_{\rm WDM}$ to m_{ν_s}. Another particle candidate for WDM is the gravitino (e.g., Pagels & Primack 1982; Ellis, Kim & Nanopoulos 1984; Moroi, Murayama & Yamaguchi 1993). Weakly interacting massive particles (WIMPs, the most favored candidates for CDM), if produced in non-thermal processes, can also have large free-streaming lengths and emulate the power spectrum of WDM (e.g., Lin et al. 2001; He et al. 2013).

Finally, thermal WDM particles are expected to have a relic velocity dispersion, which could affect the inner structure of halos due to the Liouville theorem limit for the phase density (Hogan & Dalcanton 2000). However, this velocity dispersion is very small for reasonable mass candidates ($\sim$ 3.0 keV) and even for thermal particle masses as low as

$m_{\rm WDM} \sim 1$ keV it does not affect significantly the inner structure of WDM halos (Avila-Reese et al. 2001; Colín, Valenzuela & Avila-Reese 2008; Macciò et al. 2012). Therefore, we assume a zero thermal velocity dispersion, $v_{\rm th}$=0, in our simulations.

5.4. The code and the simulations

We have carried out a set of N-body/hydrodynamics simulations of low-mass halos using the zoom-in technique in both the ΛWDM cosmology and its counterpart the ΛCDM one. The simulations were run using the Adaptive Refinement Tree (ART) N-body/hydrodynamical code (Kravtsov, Klypin & Khokhlov 1997b; Kravtsov 2003b). The code includes gas cooling, star formation (SF), stellar feedback, advection of metals, and a UV heating background source. The cooling and heating rates incorporate Compton heating/cooling, atomic and molecular cooling, UV heating from a cosmological background radiation (Haardt & Madau 1996b), and are tabulated for a temperature range of $10^2 < T < 10^9$ K and a grid of densities, metallicities, and redshifts using the CLOUDY code (Ferland et al. 1998b, version 96b4).

The SF and feedback processes (subgrid physics) are implemented in the code as discussed in detail in Colín et al. (2010) and Avila-Reese et al. (2011a). Below, we give a brief summary. The SF takes place in those cells for which $T < T_{\rm SF}$ and $\rho_g > \rho_{\rm SF}$, where T and ρ_g are the temperature and density of the gas, respectively, and $T_{\rm SF}$ and $\rho_{\rm SF}$ are the temperature and density threshold, respectively. Here, we use the same values of the $T_{\rm SF}$ and $n_{\rm SF}$ parameters as in Avila-Reese et al. (2011a); namely, 9000 K and 6 cm^{-3}, respectively, where $n_{\rm SF}$ is the density threshold in hydrogen atoms per cubic centimeter; see Avila-Reese et al. (2011a), as well as Colín et al. (2010) and González et al. (2014) (hereafter G+2014), for a discussion on the choice of these values, in particular $n_{\rm SF}$. A stellar particle of mass $m_* = \epsilon_{\rm SF}\ m_g$ is placed in a grid cell every time the above conditions are simultaneously satisfied, where m_g is the gas mass in the cell and $\epsilon_{\rm SF}$ is a parameter that measures the local efficiency by which gas is converted into stars. As in Avila-Reese et al. (2011a), we set $\epsilon_{\rm SF} = 0.5$.

We use the "explosive" stellar thermal feedback recipe, according to which each star more massive than 8 M$_\odot$ injects instantaneously into the cell, where the particle is located, $E_{\rm SN+Wind} = 2 \times 10^{51}$ erg of *thermal* energy; half of this energy is assumed to come from the type-II SN and half from the shocked stellar winds. This energy provided by the stellar feedback raises the temperature of the cell to values $\gtrsim 10^7$ K; the precise value depends on the assumed initial mass function (IMF), the amount of energy assumed to be dumped by each massive star, and the value of the $\epsilon_{\rm SF}$ parameter. On the other hand, each 8M$_\odot$ ejects 1.3M$_\odot$ of metals. For the assumed Miller & Scalo (1979) IMF, a stellar particle of 10^5 M$_\odot$ produces 749 type-II SNe.

In our previous works, we have delayed the radiative cooling for some time (typically between 10 and 40 Myr) in those cells where young stellar particles are, in order to avoid overcooling due to, for instance, resolution limitations. However, at the current resolution

Cuadro 5.1: Physical properties of WDM runs at z = 0

Name	log($M_{\rm v}$) ($M_\odot$)	log(M_s)[a] ($M_\odot$)	log(M_g) ($M_\odot$)	$V_{\rm max}$ (km s^{-1})	R_e[b] (kpc)	$R_{\rm v}$ (kpc)	f_g[c]	$M_{g,cold}/M_g$	D/T[d]	$z_{f,h}$[e]	T[f] (Gyr)
$m_p = 0.0$ keV (CDM)											
Dw3	10.46	8.73	8.07	56.07	1.02	78.50	0.18	0.81	0.01	2.30	9.67
Dw4	10.38	8.38	8.61	52.87	0.80	73.64	0.63	0.67	0.19	1.90	8.90
Dw5	10.46	8.55	9.08	61.52	1.10	77.34	0.77	0.82	0.49	1.90	8.79
Dw7	10.39	8.21	8.60	43.44	2.20	73.90	0.71	0.75	0.59	1.70	6.79
Dwn1	10.63	8.90	9.23	63.71	2.83	89.77	0.68	0.91	0.66	2.10	6.84
Dwn2	10.58	8.72	9.13	62.73	1.25	84.20	0.72	0.86	0.57	1.50	9.45
$m_p = 1.2$ keV (WDM$_{1.2}$)											
Dw3	10.43	8.74	8.92	47.87	2.03	75.24	0.60	0.86	0.43	1.85	4.89
Dw5	10.29	7.80	8.28	37.57	1.51	68.86	0.76	0.56	0.46	1.86	6.42
Dwn1	10.47	8.43	8.29	43.23	3.61	78.79	0.42	0.42	0.65	1.85	5.48
Dwn2	10.45	8.41	9.00	49.34	3.85	76.60	0.80	0.80	0.73	1.50	6.26
$m_p = 3.0$ keV (WDM$_{3.0}$)											
Dw3	10.36	8.67	6.27	50.83	0.86	72.54	0.004	0.00	0.00	2.60	9.69
Dw4	10.35	8.21	7.75	48.07	0.80	72.50	0.26	0.20	0.14	2.10	10.09
Dw5	10.44	8.47	9.07	58.23	1.44	76.23	0.80	0.87	0.55	2.10	7.95
Dw7	10.38	7.99	8.73	42.80	3.08	73.23	0.85	0.60	0.78	1.60	5.69

[a] Mass within $0.1R_{\rm v}$(the same applies for M_g);
[b] Radius that encloses half of the stellar mass within $0.1R_{\rm v}$;
[c] $f_g \equiv M_g/(M_g + M_s)$;
[d] Ratio of the mass contained in the high-angular momentum disk stars with respect to the total stellar mass;
[e] Redshift at which the given halo acquired one third of its present-day mass;
[f] Stellar mass-weighted average age.

reached by our simulations and for the typical densities found in the SF cells (~ 10 cm^{-3}), which in turn depend on $n_{\rm SF}$, the cooling time is actually much larger than the crossing time (Dalla Vecchia & Schaye 2012b). Thus, for the simulations used in this study, switching-off the cooling temporarily is expected to have only a minor effect on the properties of the simulated galaxies. We have carried out some tests and verified that this is the case. However, we decided to keep in the code this cooling delay when running the ΛWDM simulations because some of the corresponding CDM galaxies, to be compared with the WDM ones, were run with this prescription (G+2014).

5.4.1. The zoom-in simulations

The aim of this paper is to explore the evolution of galaxies formed in WDM halos of masses around the half-mode (filtering) scale M_f. As discussed in Section 5.3, M_f (see eq. 5.6) is a characteristic scale, where the properties and abundance of the WDM halos start to depart significantly from those of their CDM counterparts.

According to eqs. (5.6) and (5.3), a half-mode mass of 2×10^{10} h^{-1}M$_\odot$ is associated

to a thermal relic particle of $m_{\rm WDM} = 1.2$ keV (see Fig. 5.1). In G+2014, a set of seven zoom-in ΛCDM N-body/hydrodynamics simulations that end up with around this mass were analyzed with the aim at exploring the effects of different halo mass assembly histories (MAHs) on the evolution and properties of central dwarf galaxies. These low-mass simulated galaxies have enough resolution (see below) so that an analysis of their internal structural properties can be done with some confidence. Therefore, in order to study systems at the half-mode mass scale and compare them with the CDM results, we carry out here zoom-in simulations of some of the G+2014 runs but using the WDM power spectrum corresponding to $m_{\rm WDM} = 1.2$ keV (case $\rm WDM_{1.2}$ hereafter). We also carry out simulations of the same systems for a WDM power spectrum corresponding to $m_{\rm WDM} = 3$ keV (case $\rm WDM_{3.0}$ hereafter), in order to explore whether the properties of simulated galaxies in halos much more massive than M_f tend to be similar to those of galaxies formed in CDM halos. For this case, M_f= 9.6×10^8 $h^{-1}\rm M_\odot$ and thus, the simulated systems are about 20-30 times M_f.

The ΛWDM simulations performed here have the same random seed and box size as the ΛCDM simulations in G+2014. Therefore, all the target WDM halos/galaxies here have their CDM counterpart simulations. The box used in G+2014 has $L_{box} = 10$ h^{-1}Mpc per side and a root grid of 128^3 cells. We first set the multiple-mass species initial conditions with the code PMstartM (Klypin et al. 2001b) and then run a low–mass resolution simulation with the N-body ART code (Kravtsov, Klypin & Khokhlov 1997b). A spherical region of radius three times the virial radius $R_{\rm v}$ of the selected halo is chosen. The virial radius is defined as the radius that encloses a mean density equal to Δ_{vir} times the mean density of the universe, where Δ_{vir} is obtained from the spherical top-hat collapse model. The Lagrangian region corresponding to the $z = 0$ spherical volume is identified at $z = 50$ and resampled with additional small-scale waves (Klypin et al. 2001b). The new zoom-in simulation is then run with the hydrodynamical/N-body version of ART. The number of DM particles in the high-resolution zone changes from halo to halo but it is between 500 thousand and one million. The mass per particle m_p in the highest resolution region is 6.6×10^4 $h^{-1}\rm M_\odot$ and increases for the DM N-body only runs to 7.8×10^4 $h^{-1}\rm M_\odot$.

In ART, the grid is refined recursively as the matter distribution evolves. The runs use a DM or gas density criteria to refine. In the CDM runs presented in G+2014, the cell is refined when its mass in DM exceeds $1.3\ m_p$ or the mass in gas is higher than $1.4 F_U m_p$, where $F_U \equiv \Omega_b/\Omega_m$ is the universal baryon fraction. For the WDM runs, we have decided to use a less aggressive refinement (it acts as a softening of very small structures) in an attempt to eliminate artificial fragments[5], which are known to arise due to the finite number of particles and the resolved cut-off of the power spectrum (see above for references). Thus, we refine cells only until they reach a mass eight times the previous value of $1.3\ m_p$ in DM or $1.4 F_U m_p$ in gas. To make sure that the less aggressive refinement does not introduce significant differences in the simulations, we resimulated some of the CDM runs with the

[5]Although our target halos/galaxies have masses at $z \sim 0$ much larger than the scale where fake structures would form (see Fig. 5.1), the artificial fragments could affect our results at very high redshifts.

less aggressive refinement setting. A comparison between the CDM halos/galaxies obtained with the aggressive and soft refinements was done for some of the dwarfs and roughly the same evolution and properties were obtained. In the Appendix, we show and discuss the case for run Dw3.

As in G+2014, in the hydrodynamical simulations presented in this paper, the root grid of 128^3 cubic cells is immediately refined unconditionally to the third level, corresponding to an effective grid size of 1024^3. Although we formally set the maximum refinement level to 11, which implies a minimum cell size of 55 comoving pc, this is not reached in practice in the WDM runs with $m_{\rm WDM} = 1.2$ keV. In general, the number of cells inside $R_{\rm v}$ depends on the mass of the halo/galaxy, cosmology, and on the kind of refinement that was used, but it is roughly about one million and reduces by a factor of eight or so for the less aggressive refinement.

As mentioned above, we focus on WDM systems that have masses around M_f and much larger than M_f, as well as on their CDM counterparts. From G+2014 we have selected the CDM systems named there as Dw3, Dw4, Dw5 and Dw7, each one with a different halo MAH but with about the same present-day virial masses, $M_{\rm v} \approx 2 \times 10^{10}\ h^{-1}{\rm M}_\odot$. Unfortunately, the halo finder[6] could not identify the halos corresponding to dwarfs Dw4 and Dw7 in the WDM simulation with $m_{\rm WDM} = 1.2$ keV. Therefore, only the systems Dw3 and Dw5 have been simulated in all cosmologies: CDM and WDM with $m_{\rm WDM} = 1.2$ and 3 keV. The systems Dw4 and Dw7 were run in WDM with $m_{\rm WDM} = 3$ keV, in which case the corresponding M_f is much smaller than the masses of the simulated objects. In order to have more WDM systems of masses around M_f, we have identified in the 1.2 keV WDM box two more distinct halos, around these masses, and performed the corresponding zoom-in hydrodynamical simulations (dwarfs Dwn1 and Dwn2). The CDM simulations for these systems with the aggressive refinement were also run for comparison.

In Table 1, we present all the runs studied in this paper and summarize their main present-day properties. The WDM runs are shown in Fig. 5.1. For comparison, the runs presented in Herpich et al. (2014) and in Governato et al. (2014) are also plotted in this figure. Our simulations are the only ones that lie around the filtering scale M_f at present-day. The galaxy properties (M_s, stellar galaxy half-mass radius R_e, SFR, etc.) are computed within a sphere of $0.1R_{\rm v}$ radius. We notice that the $R_e$values reported in Table 1 of G+2014 were erroneously boosted by a factor $1/h$; the values presented in Table 1 here are the correct ones. This radius 0.1 $R_{\rm v}$ contains essentially all the stars and cold gas of the simulated central galaxy. The contamination of satellites or other substructures at this radius is negligible. On the other hand, because the outer stellar mass density profiles decrease strongly with radius in most of the runs, the galaxy stellar mass would not differ significantly had we measure it at "aperture" radii slightly smaller than $0.1R_{\rm v}$ by, for example, 20-50 %. The disk-to-total ratio (D/T) is found using a kinematic decomposition of the stellar galaxy into an spheroid and a disk. The mass of the spheroid, M_{sph}, is defined as two times the mass

[6]We use a variant of the bound density maxima (BDM) halo finder algorithm of Klypin et al. (1999), kindly provided by A. Kravtsov, and run it on the dark matter particles in order to identify the dark matter halos or subhalos. The central galaxy is then centered at the position of the corresponding most massive halo.

of the stellar particles inside $0.1R_{\rm v}$ that have negative spin values (counter-rotate), it is thus implicitly assumed that the spin distribution of the spheroid is symmetric around zero. The D/T is then defined as $(M_s - M_{sph})/M_s$.

5.5. Results

5.5.1. General properties

All of our zoom-in simulations are for *distinct* halos that at the present epoch end up with virial masses of $\approx 1.5 - 3 \times 10^{10}\ h^{-1}{\rm M}_{\odot}$; the dwarf galaxies inside these halos are therefore *centrals*. Those halos of masses around M_f (runs $\rm WDM_{1.2}$) are devoid of substructures and have mass distributions less concentrated than their CDM and $\rm WDM_{3.0}$ counterparts. In Fig. 5.2, we plot the 2D stellar and gaseous distributions at $z = 0$ for dwarf Dw3 in the $\rm WDM_{1.2}$ (top) and CDM (bottom) runs. Projections in the face-on (first and third columns) and edge-on (second and fourth columns) planes of the galaxy are shown. The FITS images of these projections were obtained with TIPSY[7]. In these images, the galaxy disk lies on the plane perpendicular to the angular momentum vector of the gas cells that are within a sphere of radius $0.15R_{\rm v}$, centered on the center of mass of the stellar particles. We use then the DS9 visualization program[8] to create the images by color coding the density of the respective components within a fixed range of values for a fair comparison between the panels.

From a visual inspection of Fig. 5.2, we see that the $\rm WDM_{1.2}$ dwarf galaxy has a more extended and less centrally concentrated stellar mass distribution than in the CDM case. Indeed, the R_e of the former is 2 times larger than the one of the latter (see Table 1). Moreover, the former has a more disk-like structure than the latter. Indeed, we measure a disk-to-total mass ratio, D/T, of 0.43 vs 0.01 (Table 1). A more pronounced disk-like structure for the former than for the latter is also seen in the gas distribution. The $\rm WDM_{1.2}$ dwarf at the half-mode mass is gas rich (f_g=0.60) and it has an extended and a low-surface density gaseous disk, unlike the CDM case, where the dwarf is gas poor (f_g=0.18) and has a compact gas distribution. The spatial temperature distribution of the gas is also quite different: in the CDM case the gas in the galaxy is colder than the one in the dwarf at the half-mode mass scale, while the gas in the corona is hotter.

According to Table 1, the present-day dwarfs Dw3, Dw5, Dwn1 and Dwn2, formed in halos of masses around M_f, are systematically more extended (larger R_e), have a lower stellar mass and maximum circular velocities, $V_{\rm max}$, and, in most of cases, end up with a higher gas fractions than their CDM counterparts. These differences are likely a consequence of *the later assembly, lower concentrations and absence of mergers of the halos at the filtering mass*. However, due to the complex and non-linear subgrid physics, small variations in the non-linear evolutionary processes can also produce large differences and

[7]http://www-hpcc.astro.washington.edu/tools/tipsy/tipsy.html
[8]http://ds9.si.edu/site/Home.html

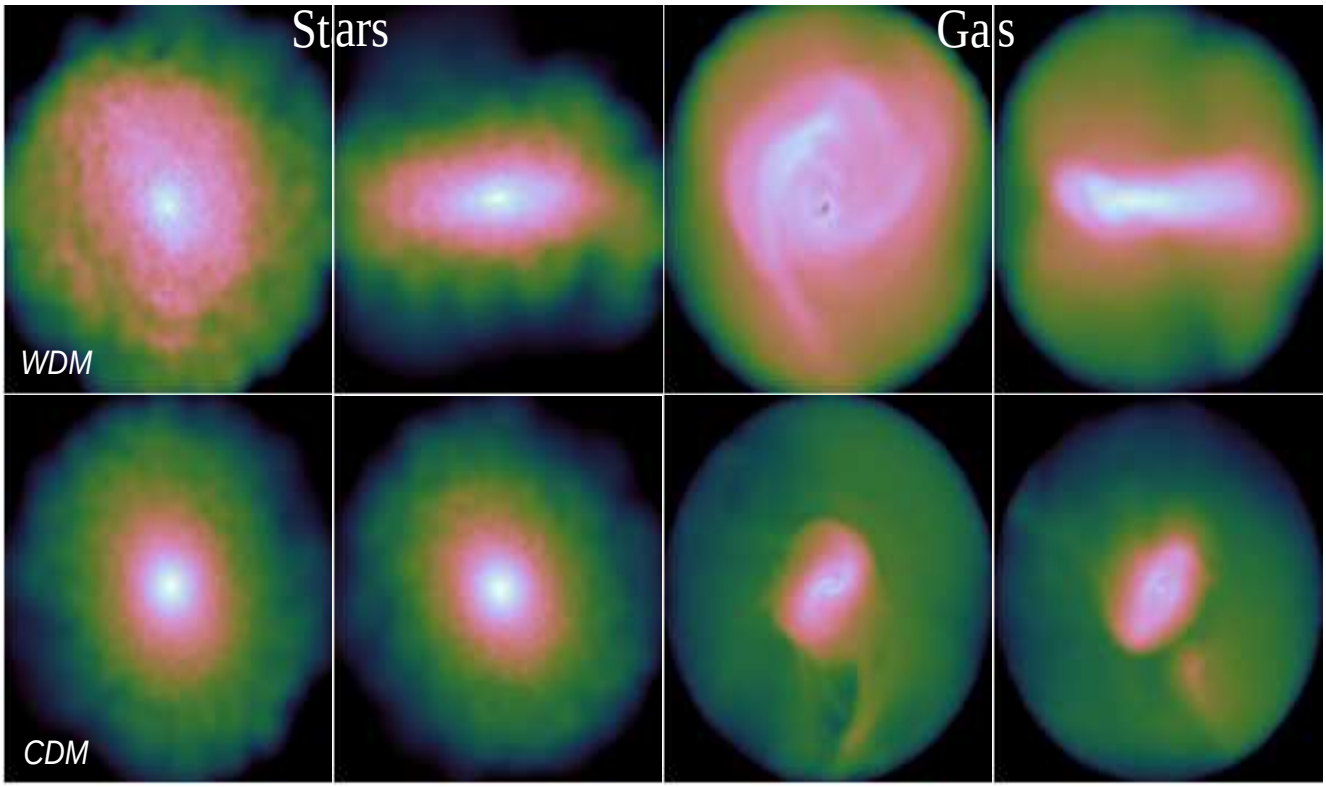

Figura 5.2: Stellar (two leftmost panels) and gas (two rightmost panels) projected distributions at $z = 0$ for the dwarf Dw3 in the $\mathrm{WDM}_{1.2}$ (top) and CDM (bottom) runs within a sphere of radius 0.15 R_{v}. The first and third (second and fourth) columns are projections in the face-on (edge-on) planes of the galaxy. The $\mathrm{WDM}_{1.2}$ run clearly show a more extended gaseous and stellar structure than its CDM counterpart.

shifts in the galaxy properties at any given epoch. This is why we have simulated several systems to verify that the found differences between dwarfs formed in halos of masses around M_f and their CDM counterparts are systematical and not due to small variations in a particular case. Moreover, although the systems with masses much larger than M_f (runs $\mathrm{WDM}_{3.0}$) show some differences with respect to their CDM counterparts, these differences are already small and do not follow a systematical trend as in the case of the $\mathrm{WDM}_{1.2}$ runs. For example, in some $\mathrm{WDM}_{3.0}$ runs f_g, R_e or D/T are larger in the $\mathrm{WDM}_{3.0}$ runs than in their CDM counterparts, while in others they are smaller. This very likely means that the differences are due to small variations in the non-linear evolution rather than due to the (small) differences in the initial power spectrum. Yet, $V_{\rm max}$ is systematically lower in all $\mathrm{WDM}_{3.0}$ runs, but not by much as seen in the case of the $\mathrm{WDM}_{1.2}$ ones. *The depth of the gravitational potential of the systems seems to be the main property systematically affected by the filtering in the power spectrum of fluctuations.*

Radial distributions

Following, we explore in more detail the present-day inner structure and dynamics of the simulated dwarfs. Solid lines in Fig. 5.3 show the total circular velocity profiles, $V_c(r)$, and their decompositions into DM, stars and gas (gray, blue and cyan lines, respectively) for the systems of mass around M_f (runs $\mathrm{WDM}_{1.2}$, upper panels) and of mass $20-30\times M_f$ (runs $\mathrm{WDM}_{3.0}$, lower panels). For each run, the corresponding CDM one is also shown with dashed lines with the same color coding as for the WDM runs. For those dwarfs formed in halos at the filtering scale, the total profiles (magenta lines) are *shallower in the center than their CDM counterparts and with values of* $V_{\rm max}\sim 20-60\,\%$ *lower*. The differences remain even for the systems in the $\mathrm{WDM}_{3.0}$ runs, though these differences are small, showing that the systems formed in halos much larger than M_f tend to be similar to those formed in the CDM scenario.

The stellar $V_c(r)$ components (blue lines) of the $\mathrm{WDM}_{1.2}$ runs are significantly lower and less peaked than those of their CDM counterparts. In all simulations, the halo component is the dominant one, at least from radii larger than $\sim\ 0.1-0.7\ R_e$. The circular velocities of the gaseous component (cyan lines) tend also to be less peaked in the $\mathrm{WDM}_{1.2}$ runs than in the CDM ones. However, while in the CDM case their inner contributions to the total circular velocity lie below that of the stellar component, except for dwarf Dw7, in the case of the $\mathrm{WDM}_{1.2}$ runs, the $V_c(r)$ of the gaseous component is similar or dominates at all radii over the stellar one, except in the inner region of dwarf Dw3 ($\mathrm{WDM}_{1.2}$ dwarfs are more gaseous than their CDM counterparts, see also Table 1). In any case, the baryonic (stellar + gaseous) contribution to the total $V_c(r)$ is more important and *more centrally concentrated* in all the CDM runs than in the $\mathrm{WDM}_{1.2}$ ones. Therefore, the circular velocities of the WDM systems of masses around M_f are shallower than the CDM ones mainly because *less centrally concentrated baryonic galaxies form in the former simulations* (see also Fig. 5.4 below).

On the other hand, $V_{\rm max}$ is significantly lower in the $\mathrm{WDM}_{1.2}$ runs than in the CDM

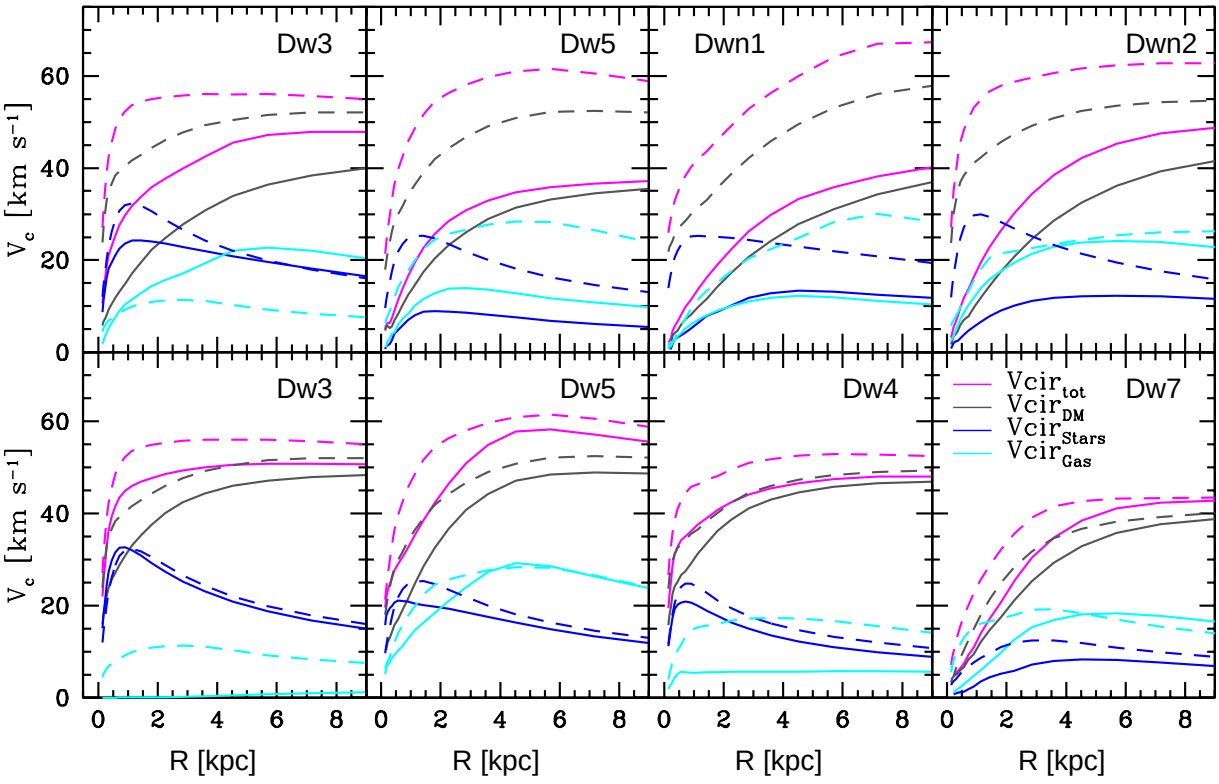

Figura 5.3: Circular velocity profiles and their decomposition for the WDM runs (solid lines) and their CDM counterparts (dashed lines) at $z = 0$. In the upper panels are plotted the profiles for the systems of masses around the filtering scale M_f and in the lower panels for those systems of masses 20 to 30 times M_f. We denote with magenta, gray, blue, and cyan lines the total, halo, stellar, and gaseous circular velocities, respectively.

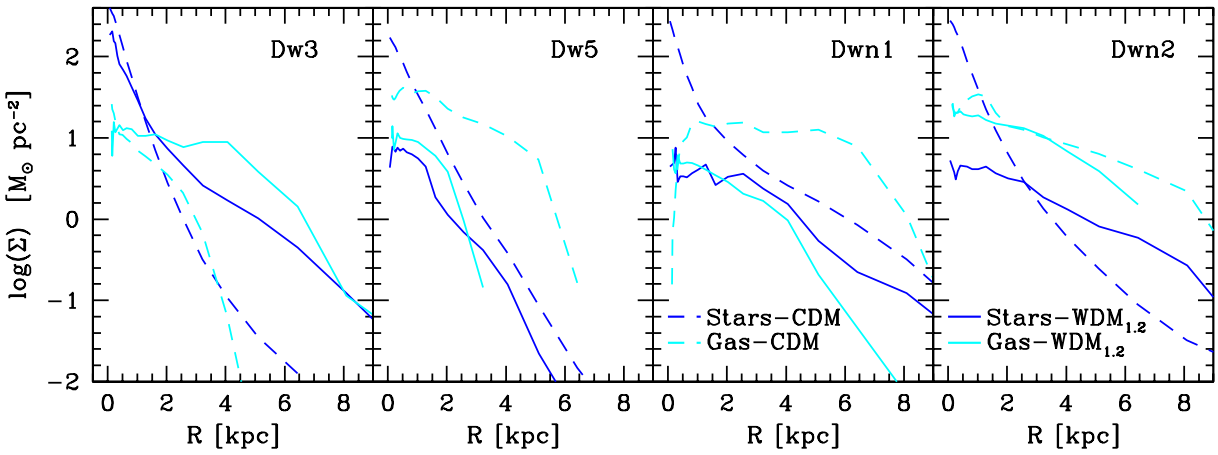

Figura 5.4: Stellar (blue lines) and gas (cyan lines) surface density profiles of the $\mathrm{WDM}_{1.2}$ dwarfs (solid lines), compared to their CDM counterparts (dashed lines).

ones mainly because the corresponding pure DM halos are already less concentrated in the WDM case than in the CDM one (e.g, Avila-Reese et al. 2001; Lovell et al. 2012). However, the astrophysical processes in both cases are also expected to produce different effects on the inner dynamics of the galaxy-halo systems, which could increase/reduce the differences in $V_{\rm max}$, as well as in the innermost dynamics of the galaxy-halo systems (for instance, the formation or not of shallow cores). We will study in detail this question elsewhere (Avila-Reese et al., in prep.).

In Fig. 5.4, the stellar (blue) and cold gas (cyan) surface density (SD) profiles of the $\mathrm{WDM}_{1.2}$ runs (solid lines) are compared to those of their CDM counterparts (dashed lines). The SDs profiles of the $\mathrm{WDM}_{3.0}$ dwarfs are roughly similar to those of their CDM counterparts, so we do not show them. The most noticeable difference in the stellar SD profiles between the $\mathrm{WDM}_{1.2}$ runs and the corresponding CDM ones is that *the inner regions of the former are significantly lower than those of the latter*. While the CDM dwarfs have a central peaked stellar density, reminiscent of a bulge-like structure, in the $\mathrm{WDM}_{1.2}$ ones a flattened SD is seen, except in run Dw3; though, even in this case, the CDM dwarf has a more peaked SD (see also Fig. 5.3). Regarding the gas SD profiles, for the CDM dwarfs, they tend to be more extended than the stellar ones and of lower SDs in the center, while for the $\mathrm{WDM}_{1.2}$ dwarfs, the gas SD profiles roughly follow the stellar ones, except for run Dw3. The CDM dwarfs have higher baryonic (stars+gas) SDs in the center than the dwarfs formed in halos at the filtering scale.

The differences in the stellar SD profiles between the $\mathrm{WDM}_{1.2}$ and CDM runs, specially in the inner regions, could be the result of many effects. One of them might be the angular momentum of the halos in which galaxies form. We have measured the halo (dark matter

particles only) spin parameter[9] λ for all the runs at $z = 0$ with the following results: runs Dw3 and Dw5 have a lower spin parameter in the CDM runs than in the $WDM_{1.2}$ ones (0.015 and 0.007 vs. 0.033 and 0.012, respectively) but for runs Dwn1 and Dwn2 we found the contrary, that CDM runs have a higher spin parameter (0.072 and 0.083 versus 0.032 and 0.037, respectively). The last two runs, specially Dwn2, have a relatively late merger in the CDM simulations that could affect the spin parameter, although these mergers happened more than ~ 4 Gyr ago. We have also measured the spin parameter by using the alternative definition of λ introduced in Bullock et al. (2001). Although the values of λ are different, the trend is the same: runs Dwn1 and Dwn2 have larger values in the CDM simulations, and Dw3 and Dw5 have smaller values. In summary, it is not clear that the halo spin parameter is the reason why the stellar distribution is less concentrated in the WDM runs than in the CDM ones. We plan to study in detail elsewhere (Avila-Reese et al in prep) the question of the spin parameter in WDM and CDM, both in DM-only and hydrodynamical simulations.

The mechanism responsible for the stellar-SD profile differences between the $WDM_{1.2}$ and CDM dwarfs can be traced probably to the merging history of the central galaxies (Herpich et al. 2014). The satellite interactions/mergers in the case of CDM simulations drive gas to the center, where SF proceeds efficiently, producing a cuspy stellar structure. The stellar specific angular momentum is also more likely to decrease in the galaxies that suffered mergers since the angular momentum of these merging galaxies can cancel each other (Cloet-Osselaer et al. 2014). These processes do not happen in the $WDM_{1.2}$ dwarfs because they are practically devoid of satellites. Besides, the galaxy assembly starts later than in the CDM halos, being the disks more gaseous and less susceptible of secular evolutionary processes.

In summary, dwarfs formed in halos of masses around M_f have a quite different dynamical history and structural inner properties when compared to their CDM counterparts, whereas dwarfs formed in a WDM cosmology but in halos with a mass much larger than M_f, tend to be similar to the corresponding CDM dwarfs. The latter is in agreement with the simulation results of Herpich et al. (2014).

5.5.2. Mass assembly histories

In Fig. 5.5 we plot the virial MAHs of the $WDM_{1.2}$ (upper panels) and $WDM_{3.0}$ (lower panels) runs along with their corresponding CDM counterparts (black solid and dashed lines, respectively). As can be seen, the halos around the filtering mass M_f start to assemble later and end up with masses slightly smaller than the corresponding CDM ones. However, afterwards the former grow faster than the latter, specially in the runs Dw3 and Dw5. Thus, the epoch at which half or one-third of the present-day virial mass is acquired is not very different between the two cosmologies (see Table 1). The WDM halos of scales $20 - 30 \times$

[9]The spin parameter is defined as $\lambda = \frac{J|E|^{1/2}}{GM^{5/2}}$, where J, M and E are the total angular mometum, mass, and energy. This latter quantity is computed, assuming that the halo is virialized, as -K, where K is the kinetic energy, respectively.

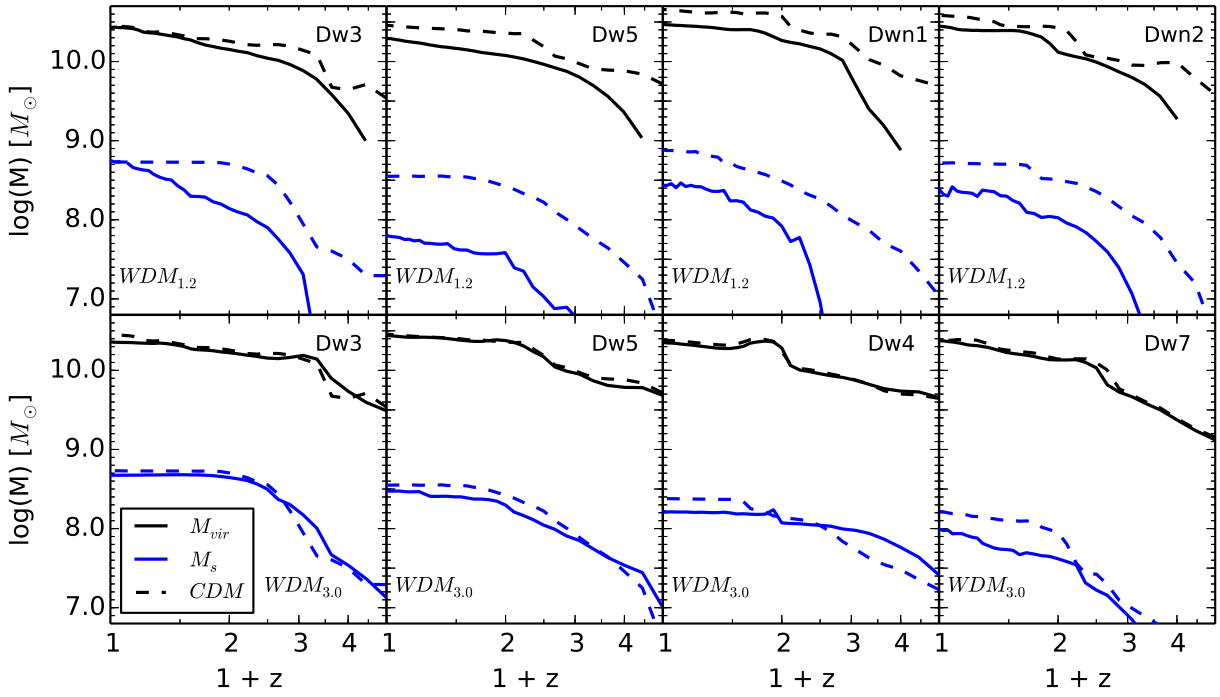

Figura 5.5: Mass assembly histories for the simulated dwarf galaxies. In the upper panels we show the MAHs for the $\mathrm{WDM}_{1.2}$ runs, while in the lower panels are the MAHs of the $\mathrm{WDM}_{3.0}$ runs (solid lines). In each case, the MAHs of the corresponding CDM runs are also plotted (dashed lines). We denote with black lines the total (virial) MAHs and with blue lines the galaxy stellar MAHs. The MAHs of the dwarfs formed in halos around M_f ($\mathrm{WDM}_{1.2}$ runs) differ significantly from their CDM counterparts.

M_f assemble their masses practically in the same way as they do in the CDM scenario.

The blue solid and dashed lines in Fig. 5.5 show the stellar MAHs of the WDM and CDM simulated dwarf galaxies, respectively. In G+2014, it was shown that the stellar MAHs of dwarfs follow roughly their halo MAHs in the CDM simulations; i.e., the M_s-to-$M_{\rm v}$ ratio is roughly constant, at least up to $z \sim 2$ (with variations of $0.1 - 0.4$ dex). Here, for the $\mathrm{WDM}_{1.2}$ dwarfs we find that from $z \gtrsim 2$ to ~ 1 the M_s-to-$M_{\rm v}$ ratio significantly increases; from $z \sim 1$ to 0, this ratio continues increasing (except in run Dw5) but only slightly. The early fast increase occurs because at earlier epochs the $\mathrm{WDM}_{1.2}$ baryonic galaxies are in their active growth phase. Thus, the stellar mass assembly of the dwarfs at the filtering scale shows a decoupling from the assembly of their halos, unlike what happens with the dwarfs in the CDM case. At $z = 0$, the M_s-to-$M_{\rm v}$ ratios of all $\mathrm{WDM}_{1.2}$ galaxies are $2 - 4$ times lower than their CDM counterparts except for the dwarf Dw3 in which case they are similar. As expected, the differences are much smaller when compared to the $\mathrm{WDM}_{3.0}$ runs; at $z = 0$, the maximum difference, which amounts a factor of 1.6, is found for the dwarf Dw7. In general, the M_s-to-$M_{\rm v}$ ratio remains close to the CDM one at all redshifts. Thus, a systematical effect of the filtering of the power spectrum on the galaxies

is that *they end up with lower M_s-to-$M_{\rm v}$ ratios as the mass of system becomes closer to the filtering scale M_f.*

The dwarf galaxies formed in halos of masses around M_f assemble their stellar masses with a delay with respect to their CDM counterparts. For example, the assembly of half of the present-day M_s for dwarf Dw5 happens 1.3 Gyr later in the $\rm WDM_{1.2}$ cosmology. For the dwarfs formed in halos much larger than M_f, the stellar MAHs are close to those of the CDM counterparts, with minimum differences in the half-mass assembly epochs.

The galaxy baryon (stars + gas) MAHs, $M_b(z)$, of the simulated galaxies follow moderately the halo MAHs, with some intermittence, both in the WDM and CDM simulations. However, the $\rm WDM_{1.2}$ runs show more intermittent histories than the CDM ones, due to more pronounced periods of gas infall/outflow onto/from the halos. This is likely because the $\rm WDM_{1.2}$ halos accrete baryons in a more regular way than the CDM halos, as well as are able to blowout the gas more efficiently due their lower concentrations and $V_{\rm max}$. The baryon-to-halo mass ratios, M_b-to-$M_{\rm v}$, of the former are slightly lower than those of the latter at all epochs, excepting for run Dw3 at $z \lesssim 0.7$. At $z = 0$, the M_b-to-$M_{\rm v}$ ratios are $1.1 - 3.5$ times lower for the $\rm WDM_{1.2}$ galaxies than for the CDM counterparts, though for the run Dw3, this ratio is higher in the former case.

5.5.3. Gas fraction and star formation histories

In Fig. 5.6, we plot the change with redshift of the *galaxy* gas fractions (f_g=M_g/M_b, solid lines) for the $\rm WDM_{1.2}$ and $\rm WDM_{3.0}$ runs, upper and lower panels, respectively. The dashed lines show the change with redshift of the fraction of gas outside the galaxy but within the *halo*, the "halo" gas fraction $F_{g,h}$. This is defined as the ratio of the gas mass contained in the spherical shell of radii between $0.1R_{\rm v}$ and $R_{\rm v}$ to the gas mass in the whole halo. As in the case of the CDM simulations (see Fig. 6 in G+2014), the two gas fractions oscillate, and in periods where f_g decreases (increases) typically $F_{g,h}$ increases (decreases). This is mainly due to the interplay among gas accretion onto the galaxy, SF and SN-driven outflows from the galaxy. It seems that this interplay is stronger in the CDM simulations than in the systems with mass around M_f ($\rm WDM_{1.2}$). This can be appreciated by comparing the upper and lower panels, where the latter are for the $\rm WDM_{3.0}$ runs, which tend to be similar to the CDM ones (see Fig. 6 in G+2014).

The galaxy gas fractions in the $\rm WDM_{1.2}$ runs are, at all epochs, higher than those found in their CDM runs counterparts, probably as a consequence of the later galaxy assembly of the former runs. The values of f_g at $z = 0$ are shown in column eighth of Table 1. We see that the f_g values of the WDM dwarfs formed in halos of scales around M_f are relatively high.

In Fig. 5.7 we plot the "archeological" SF histories of our WDM runs (solid lines) compared to their CDM counterparts (blue dashed lines). For illustration purposes, since the SF histories are strongly intermittent, they were smoothed with a top-hat filter of 500 Myr width. The original histories were built with 0.1 Gyr bins. This is computed, for any given time t [Gyr], identifying all galaxy stellar particles at $z = 0$ born within the time

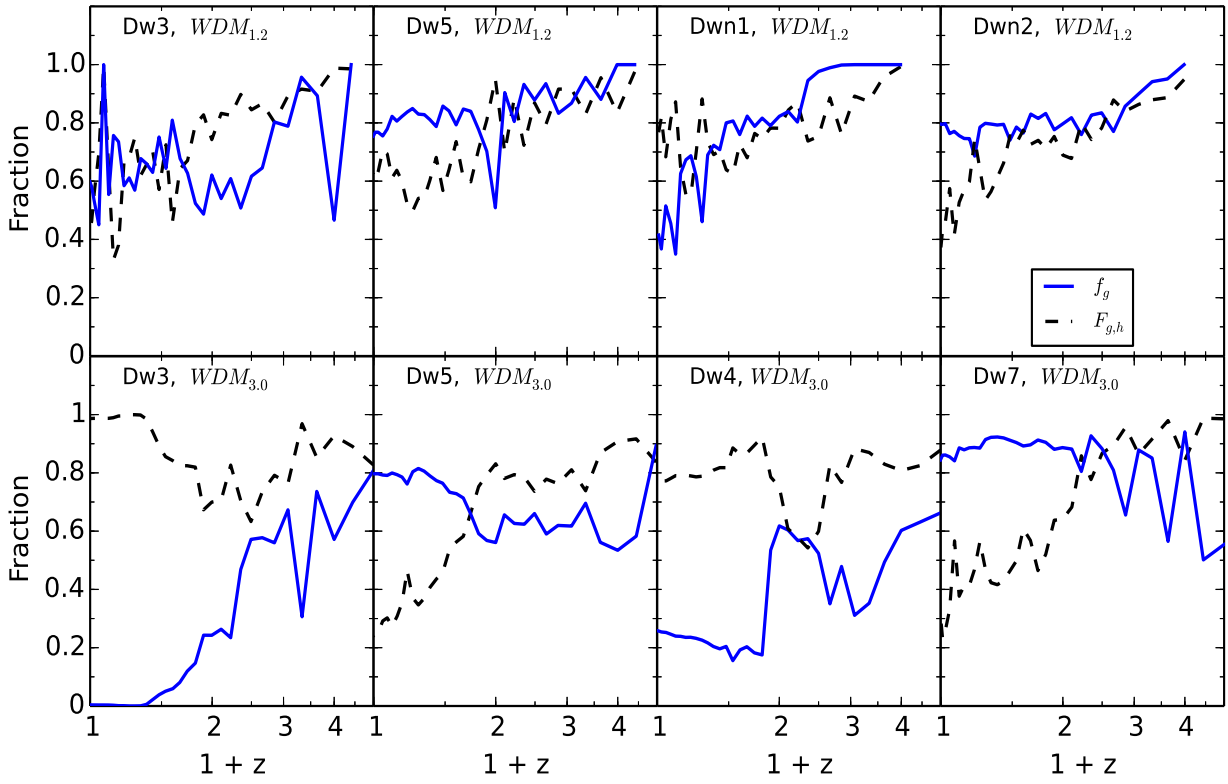

Figura 5.6: Evolution of the galaxy gas mass fraction, f_g, for the different runs (blue solid lines). The dashed line refers to the ratio between the gas mass in the halo, the gas in the spherical shell of radii $0.1R_{\rm v}$ and $1R_{\rm v}$, and the total gas mass within $R_{\rm v}$. In the upper panels we show the results for the $\rm WDM_{1.2}$ runs and in the lower panels for the $\rm WDM_{3.0}$ runs. These latter present similar results as their corresponding CDM runs. This is not the case for the $\rm WDM_{1.2}$ runs.

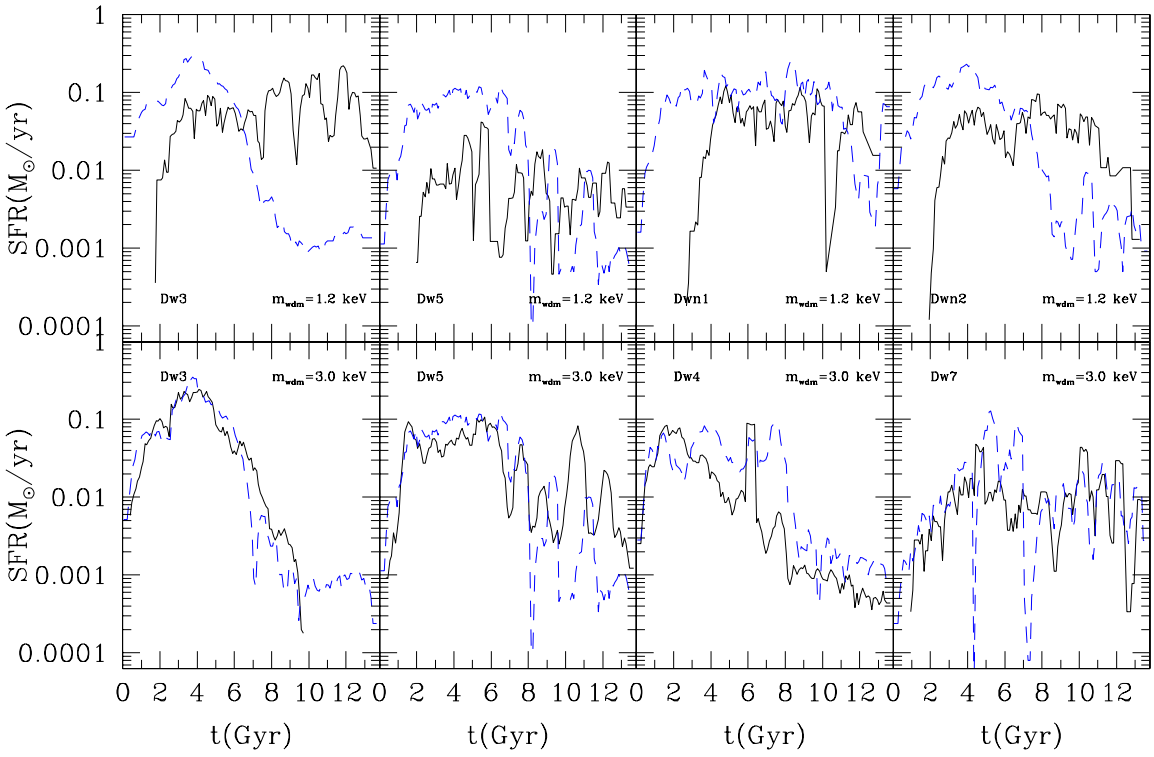

Figura 5.7: Archaeological SF rate histories for the $\mathrm{WDM}_{1.2}$ (upper panels) and $\mathrm{WDM}_{3.0}$ (lower panels) runs presented in this paper (black solid lines). In each panel, the corresponding CDM SF histories are also shown (dashed blue lines). In the x-axis runs the cosmic time. The histories were smoothed with a top-hat filter of 500 Myr width; see text for details about how the SF histories were calculated.

interval [$t - 0.1$,t] Gyr; the SFR at this time is then simply the mass of these particles divided by 0.1 Gyr.

As expected from the later halo assembly, the SF in systems of masses around M_f starts later than in the CDM counterparts. Besides, the former present *more sustained SF histories at later epochs than the CDM dwarfs*, for which the SFR tends to fall in the last Gyrs. This implies that the specific SFRs (SFR/M_s) of the WDM galaxies of scales around M_f tend to be higher at late epochs than those of the CDM counterparts. The fact that the $\mathrm{WDM}_{1.2}$ galaxies assemble later and have lower central gas surface densities than the CDM ones likely explains their less efficient but more sustained SF histories. As in the CDM runs (see a discussion in G+2014), the SF histories in the WDM runs are also episodic. For those systems around the filtering mass M_f, the SF is sometimes even more bursty than their CDM counterparts.

To highlight the differences in the stellar populations between the dwarfs in the $\mathrm{WDM}_{1.2}$ runs and their CDM counterparts, in Fig. 5.8 we plot the cumulative (archaeological) SF histories. Solid lines are for the $\mathrm{WDM}_{1.2}$ dwarfs, while dashed lines are for the CDM counterparts. One clearly sees that the stellar populations of present-day $\mathrm{WDM}_{1.2}$ dwarfs are formed on average significantly later than those of the CDM dwarfs, with $20\,\%$ of their

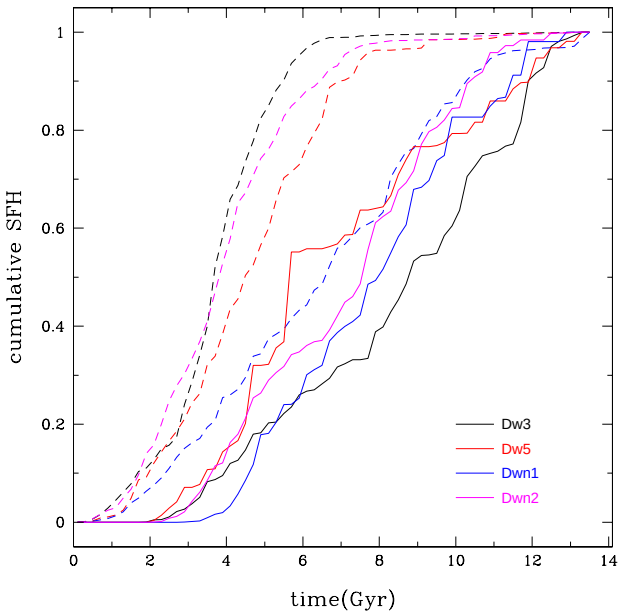

Figura 5.8: Cumulative SF histories of the $\mathrm{WDM}_{1.2}$ runs (solid lines) and their CDM counterparts (dashed lines). Different dwarfs are identified with different colors. The $\mathrm{WDM}_{1.2}$ runs clearly form most of their present-day stars much later than their CDM counterparts.

stars being formed in the last ~ 4 Gyr; in contrast, the CDM dwarfs, have formed already 80 % of their stars between ~ 7.5 and 9 Gyr ago (Dwn1 reaches this fraction later, ~ 4.6 Gyr ago). The galaxy Dw3 is the one that most differs in its SF history (black lines), when compared $\mathrm{WDM}_{1.2}$ with CDM, and Dwn1 is the one that shows the most similar history (blue lines).

We have calculated also the mass-weighted "archeological" ages of all runs and report them in the last column of Table 1. This age is the result of multiplying the age of each galaxy stellar particle at $z = 0$ by its mass fraction contribution (the particle mass divided by M_s), and summing these terms for all the particles. *The dwarfs of scales around M_f are between ~ 1.4 and 4.8 Gyrs younger than their CDM counterparts.* The largest difference is for the dwarf Dw3 and the smallest for Dwn1 (see above). The mass-weighted ages of the $\mathrm{WDM}_{3.0}$ dwarfs are similar or slightly smaller (by ~ 1 Gyr) than the CDM counterparts. In summary, *central dwarf galaxies in the WDM scenario are expected to have younger stellar populations on average than their CDM counterparts,* the younger the closer their virial masses is to the filtering scale.

5.6. Summary and Discussion

We have presented the first N-body/hydrodynamics (zoom-in) simulations of galaxies formed in distinct WDM halos of masses close to the filtering scale M_f (runs $\mathrm{WDM}_{1.2}$). Galaxies formed in WDM halos 20–30 times more massive than M_f were also simulated (runs $\mathrm{WDM}_{3.0}$). In a WDM cosmology, the halos of masses around M_f are close to the peak of the halo mass function; at masses a factor of $\sim 2-3$ lower, the halo mass function declines sharply due to the damping of the initial power spectrum of fluctuations (e.g., Schneider et al. 2012b; Angulo, Hahn & Abel 2013). Most of structures ~ 3 times smaller than M_f at $z = 0$ already do not appear to be virialized spherical overdensities (halos) and they did not assemble hierarchically.

Our results show that the WDM galaxies formed at scales around M_f have disk-like structures and circular velocity profiles that gently increase and then flattens. These dwarfs are quite different in several aspects from their CDM counterparts, which assembled hierarchically. The galaxies formed in halos $\sim 20-30$ times M_f, instead, are very similar in properties and evolution to their CDM counterparts, in agreement with the results of Herpich et al. (2014). Therefore, *the properties and evolution of WDM galaxies differ more from those of the CDM galaxies as the mass get closer to the filtering scale.* In summary, the WDM dwarf galaxies formed in halos with a mass around M_f differ from their CDM counterparts in that:

1. they assemble their stellar masses later (Fig. 5.5), with archaeological SF histories shifted to younger stellar populations (Fig. 5.8; on average, the WDM dwarfs have mass-weighted ages 1.4–4.8 Gyr younger than the CDM ones, see also Governato et al. 2014);

2. their $V_{\rm max}$ values are 20–60 % lower;

3. they have significantly lower central stellar SDs and larger R_e values, by factors of 1.3–3 (Fig. 5.4);

4. their $V_c(r)$ profiles are shallower, being this mainly because the baryonic (stars + gas) components are shallower (Fig. 5.3);

5. on average, they have higher gas fractions and lower stellar masses (and thus lower M_s-to-$M_{\rm v}$ ratios).

5.6.1. WDM galaxy formation

If the Ly-α power spectrum constrains WDM models to be made of relic particles with masses above ≈ 3 keV (Viel et al. 2013), then the corresponding filtering scale at $z = 0$ should be $\lesssim 1.5\times10^9$ $\mathrm{M}_\odot$. In the CDM cosmology, the distinct halos of 1.5×10^9 $\mathrm{M}_\odot$have $V_{\rm max}$ values of ~ 20 km/s and their stellar masses are expected to be $\lesssim 10^7-10^6$ $\mathrm{M}_\odot$ (M_s-to-$M_{\rm v}$ ratios $\lesssim 7-0.7\times10^{-3}$), depending on the used subgrid physics (e.g., Sawala et al.

2010; Munshi et al. 2013; Cloet-Osselaer et al. 2014; Sawala et al. 2014b,a; Governato et al. 2014).

Applying our results to these small dwarfs, form in halos at the filtering scale of 1.5×10^9 $M_\odot$, the corresponding $V_{\rm max}$ and $M_s/M_{\rm v}$ ratio would be around 12 km/s and 0.005, respectively. On the other hand, we would expect these WDM dwarfs to have higher gas fractions, lower central stellar SDs and later SF histories than the corresponding CDM ones.

Unfortunately, current observations of field dwarf galaxies of masses and circular velocities as small as those corresponding to halos of masses $\sim 10^9$ $M_\odot$ are so limited that they can not be used to distinguish between the CDM and the WDM with $m_{\rm WDM} \approx 3$ keV cosmogony. The few and uncertain observations of central (field) very small dwarfs point out that practically all of them are star-forming and gaseous rich galaxies (e.g., Geha et al. 2006, 2012), with late SF histories (e.g., Weisz et al. 2014; Cole et al. 2014), and with $V_{\rm max}$ values for a given M_s smaller than those inferred or simulated in the CDM scenario (e.g, Ferrero et al. 2012; Rodríguez-Puebla, Avila-Reese & Drory 2013), thus favoring the WDM scenario. However, as several authors have shown, these potential disagreements in the CDM scenario, in particular those related to the too-high $V_{\rm max}$ and $M_s/M_{\rm v}$ values, could be solved also by plausible changes/improvements in the subgrid physics; for example, by introducing a metallicity-dependent H_2 molecule formation process (Kuhlen et al. 2012; Christensen et al. 2012) or by introducing preventive/early mechanisms of feedback besides of increasing the strength of the ejective SN-driven feedback (Hopkins, Quataert & Murray 2012; Hopkins et al. 2013; Munshi et al. 2013; Trujillo-Gomez et al. 2013; Stinson et al. 2013; Agertz et al. 2013).

Along this venue, Governato et al. (2014) (see also a recent review by Brooks 2014) argue that the effects of the SF-driven feedback overcome those of the initial power spectrum regarding the inner dark matter and stellar mass distributions. This conclusion is based on only one zoom-in simulated dwarf in both CDM and WDM cosmologies. For the latter, the filtering corresponds to a relic particle of mass 2 keV, which means that the filtering mass is $M_f = 5.7 \times 10^9$ $M_\odot$ (see Fig. 5.1). The present-day virial mass of their dwarf is $\approx 1.4 \times 10^{10}$ $M_\odot$ (after correcting by a factor of 1.23 as one goes from M_{200} to $M_{\rm v}$); that is, this system is ≈ 2 times larger than the filtering mass. For this particular object, the dark-matter only simulations in the CDM and WDM cosmologies show that their $V_c(r)$ profiles are actually not too different from each other (see their Fig. 6). In our case, the dark-matter only simulations of the four systems (to be presented elsewhere, Avila-Reese et al. in preparation) have different halo mass distributions in the $\rm WDM_{1.2}$ and CDM runs; in particular, their $V_{\rm max}$ values and $V_c(r)$ profiles are very different. So, the damping in the power spectrum has significant effects at the level of pure dark matter. This, along with the significant differences between the CDM and WDM runs regarding the assembly histories (which are also seen in the Governato et al. 2014 dwarf), lead us to conclude that *the effects of the damping of the power spectrum in the WDM cosmology strongly affect the evolution, properties, and dynamics of the halos (galaxies) of masses around the filtering scale*. However, the astrophysical effects are also important. These effects on the properties and dynamics of the $z = 0$ dwarf galaxies could affect the predictions based on dark-matter

only results as those, for example, based on the WDM circular velocity function (e.g., Zavala et al. 2009; Klypin et al. 2014; Papastergis et al. 2014).

Future observational studies of central (field) dwarf galaxies will be crucial for constraining the nature of dark matter. In addition to the inner dynamics, we have also found important differences between CDM and WDM dwarfs in their SF histories, stellar SD profiles (specially in the central regions), and gas fractions.

It should be said that resolution issues are likely affecting our results regarding the earliest stages ($z > 3$) of the WDM galaxy assembly, where virial masses get closer to the scale of artificial fragmentation of filaments and to the free-streaming scale. Very high-resolution simulations, including baryons, suggest that structures around the free-streaming scale are smooth and dense filaments able to capture gas that can cool efficiently and form stars (Gao & Theuns 2007; Gao, Theuns & Springel 2014). Thus, the smallest (earliest) baryonic structures in a WDM cosmology are expected to be filament-like; certainly, the formation of stars (the first ones) in this environment is different from that in a virialized halo (see Gao & Theuns 2007). SF may efficiently proceed in these filaments before they disappear into the more familiar halo-like structures, so that a non-negligible fraction of stars in the $z = 0$ galaxy may have formed early in these filaments. Hence, our result that the fraction of stars formed during the first 2–4 Gyr in the $\mathrm{WDM}_{1.2}$ runs is negligible (Fig. 5.8) could be an underestimation due to our inability to adequately resolve and follow the physics of the gas in the first smallest filaments (their masses should be of the order of the corresponding free-streaming mass, $\sim 2 \times 10^6\ h^{-1}\mathrm{M}_\odot$).

We end the discussion by asking whether our simulated dwarfs with m_{WDM}=1.2 keV are in agreement with observations. In Avila-Reese et al. (2011a) and in G+2014 we studied the properties and evolution of CDM low-mass galaxies, some of which (Dw3, Dw4, Dw5 y Dw7) were also studied here. These CDM galaxies with total masses around $1 - 5 \times 10^{10}$ $h^{-1}\mathrm{M}_\odot$ are relatively realistic in structural and dynamical properties; however, they have lower specific SF rates, too high M_s-to-M_{v} ratios and lower gas fractions than the observed ones, showing that they form most of their stars too early. The $\mathrm{WDM}_{1.2}$ dwarfs simulated here *with the same subgrid physics* have delayed SF histories, form less stars, and have more gas than their CDM counterparts. However, when compared to observed galaxies of similar stellar masses, they are too extended. In any case, a WDM model with m_{WDM}=1.2 keV seems to be in conflict with the last Ly-α forest constraints (Viel et al. 2013).

Acknowledgements

VA and AG acknowledge CONACyT grant (Ciencia Básica) 167332-F. AG acknowledges a PhD fellowship provided by DGEP-UNAM

Appendix

As mentioned in Section 3.1, the CDM dwarfs were run with the same refinement setting used in G+2014. Moreover, to try to reduce the appearance and growth of spurious fragments, a less aggressive refinement was used in the WDM runs. This, however, means that WDM dwarfs are slightly less resolved than their CDM counterparts; that is, the halo/galaxy ends up with less resolution elements. To show that no significant differences appear when this setting (resolution) is used, we run some of our CDM simulations with this soft refinement. In Fig. 5.9, we compare the cumulative SFH (upper panel) and circular velocity (lower panel) of the CDM run of Dw3 with the aggressive refinement (black solid lines) with the corresponding quantities of the less aggressive setting (red dotted lines). The difference between the two runs in $V_{\rm max}$ amounts only to $\sim 2\,\%$, while in the cumulative SFH the major differences are seen during the stage of active star formation, in the first $\sim$ 5 Gyr. On the other hand, the late star formation seems to be sensitive to the details of the used resolution. Yet, we certainly believe this should not be much of concern because the amount of mass in stars formed in this relatively quiet star forming phase is small; in general, the stellar mass M_s in the less resolved run is only $17\,\%$ higher than the corresponding one with the aggressive refinement setting.

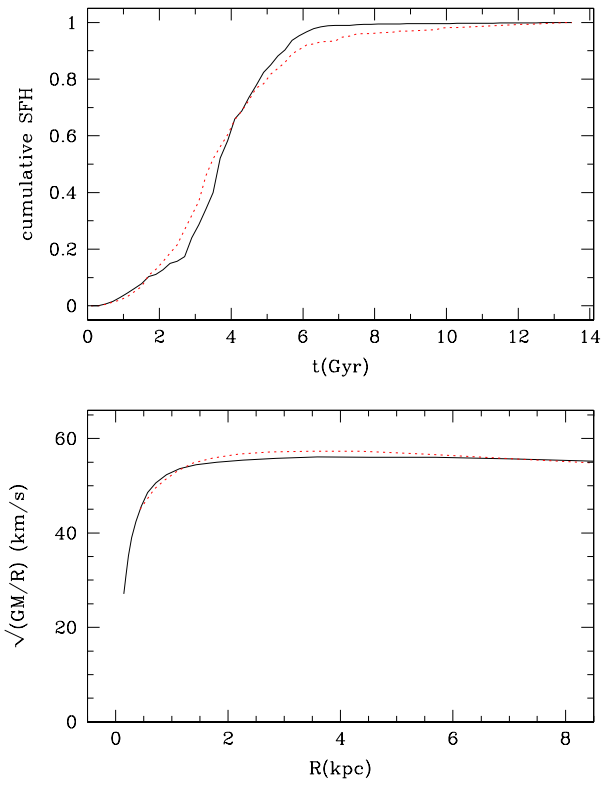

Figura 5.9: A comparison of the CDM runs of dwarf Dw3 with aggressive (black solid lines) and soft (red dotted lines) refinements is presented. In the upper panel we show the comparison regarding the cumulative SF history while in the lower panel the comparison is with respect to the circular velocity.

Capítulo 6

Formación estelar en las galaxias

Hasta aquí hemos estudiado como se lleva a cabo el ensamblaje de masa de las galaxias de baja masa y su relevancia en las propiedades integradas de las mismas. Pero claramente hemos mostrado que uno de los retos para caracterizar mejor estos procesos radica en entender en sí mismo el proceso de *formación estelar* (FE) a escalas que aún no se pueden resolver en las simulaciones cosmológicas actuales. Así, para entender como procede la FE en las nubes moleculares (NMs), es necesario estudiar las propiedades del MIE y sus posibles correlaciones con las estructuras colapsadas que eventualmente formarán estrellas.

En años recientes han aparecido en la literatura teorías (Krumholz & McKee 2005, KM05; Padoan & Nordlund 2011, PN11; Hennebelle & Chabrier 2011, HC11) que tratan de describir la dependencia de la TFE de los principales parámetros físicos de las NMs, a decir, el cociente de energía cinética entre la energía gravitacional, caracterizado pr el parámetro virial α (KM05), el número de Mach turbulento $\mathcal{M}_{\rm s}$, el número de Mach Alfvénico $\mathcal{M}_{\rm A}$ y el cociente de los modos solenoidales entre los modos compresivos inyectados a la turbulencia, caracterizados estos por el así llamdo *parámetro-b* (Federrath et al., 2008). Una revisión detallada de estas teorías se encuentra en Federrath & Klessen (2012, FK12).

Estas tres recientes teorías parten de la hipótesis fundamental de que los movimientos supersónicos no-térmicos constituyen turbulencia isotrópica que, mientras localmente induce compresiones que pueden llegar a ser inestables gravitacionalmente y colapsen, globalmente produzca una presión turbulenta que puede oponerse a la autogravedad de los núcleos densos que se forman en las NMs. Más aún, dos de éstas teorías (KM05 y PN11) dependen de la suposición de que núcleos densos que son subsónicos y que a su vez tienen masa superior a su masa de Jeans juegan un papel fundamental en el proceso de formación estelar. Estas dos suposiciones han sido ya cuestionadas en un estudio basado en simulaciones numéricas hidrodinámicas (HD) sin campo magnético, Vazquez-Semadeni et al., 2008). En este contexto es importante verificar sí estas suposiciones básicas para entender la formación estelar son auto consistentes en simulaciones numéricas ahora en el

caso magnetohidrodinámico. Y tratando de ir un poco más allá, también será importante poner a prueba las prediciones que de la TFE hacen estas teorías. En el presente capítulo se estudian a detalle todos estos aspectos por medio de simulaciones magnetohidrodinámicas (MHD) en un medio turbulento. Al final del mismo se discute brevemente cual podría ser el impacto de estos estudios en el ensamblaje de masa estelar de las galaxias.

6.1. Pruebas a hipótesis y predicciones de teorías de formación estelar

A continuación se presenta el artículo González-Samaniego, A., et al. (2014b) que comparte el mismo título de esta sección pero en idioma inglés. En este se presentan simulaciones numéricas MHD de un medio isotérmico y turbulento (supersónico) con autogravedad, diseñadas para probar varias hipótesis que frecuentemente se asumen en teorías de formación estelar. Se consideran tres simulaciones, cada una con diferente tamaño físico, número de Mach sónico $\mathcal{M}_{\rm s}$, y parámetro de Jeans J[1], pero tales que las tres tienen el mismo valor para el parámetro virial y siguen las relaciones de escala de Larson.

Los resultados generales nos dicen que: (1) en el medio así simulado no se producen estructuras que sean a la vez subsónicas y super-Jeans[2]; (2) la fracción de estructuras super-Jeans de menor escala se incrementa cuando la autogravedad empieza a actuar, y la producción de núcleos muy densos vía solo por turbulencia es muy baja. Esto implica que la autogravedad no solo influye en el colapso de los núcleos inestables gravitacionalmente, sino que también es responsable de su formación. (3) También encontramos que las regiones más densas tienden a tener una convergencia más fuerte del campo de velocidades, implicando un influjo neto hacia las regiones centrales. (4) Contrario al caso no-magnético (simulación puramente hidrodinámica, HD), encontramos que la simulación MHD con los valores más bajos de $\mathcal{M}_{\rm s}$ y J (5 y 2 respectivamente) no produce ninguna región colapsada durante varios millones de años (correspondientes a más de tres tiempos de caída libre de la simulación), esto a pesar de ser tanto super-Jeans como magnéticamente supercrítica. Atribuimos este resultado al efecto combinado del soporte térmico y magnético.

Finalmente comparamos resultados de nuestras simulaciones HD y MHD con las predicciones para la eficiencia de la formación estelar por tiempo de caída libre (EFE_{ff}) de las teorías de FE mencionadas anteriormente (KM05, PN11, y HC11), usando expresiones descritas recientemente por Federrath & Klessen (FK12) para el caso MHD. En ambos

[1]El parámetro de Jeans J representa el tamaño físico en unidades de la longitud de Jeans, $J \equiv L/L_J$.

[2]Una estructura se denomina super-Jeans si es tal que alcanza en su evolución una masa $\mathcal{M}$ superior a su masa de Jeans $\mathcal{M}_{\rm J}$, lo cual en principio provocaría que, ante ausencia de algún agente no gravitacional que provea soporte, dicha estructura eventualmente se colapse.

casos, el HD y el MHD, encontramos que las predicciones teóricas para la EFE_{ff} tienden a ser más grandes que las medidas en las simulaciones. En el caso MHD, ninguna de las teorías captura la supresión del colapso a bajos valores de J debido al soporte adicional del campo magnético.

Nuestros resultados sugieren que un flujo isotérmico y continuamente turbulento no representa correctamente el flujo del medio en las NMs reales, y que las teorías que asumen este régimen estarán perdiendo un aspecto fundamental de las propiedades del MIE. Finalmente, sugerimos que un escenario más realista puede ser el del colapso gravitacional jerárquico.

6.2. Testing assumptions and predictions of star-formation theories

Alejandro González-Samaniego[13], Enrique Vázquez-Semadeni[1], Ricardo F. González[1], and Jongsoo Kim[4]

Monthly Notices of the Royal Astronomical Society, Volume 440, Issue 3, p.2357-2374, (2014)

Abstract

We present numerical simulations of isothermal, magnetohydrodynamic (MHD), supersonic turbulence, designed to test various hypotheses frequently assumed in star formation (SF) theories. This study complements our previous one in the non-magnetic (HD) case. We consider three simulations, each with different values of its physical size, rms sonic Mach number $M_{\rm s}$, and Jeans parameter J, but so that all three have the same value of the virial parameter and conform with Larson's scaling relations. As in the non-magnetic case, we find that (1) no structures that are both subsonic and super-Jeans are produced; (2) that the fraction of small-scale super-Jeans structures increases when self-gravity is turned on, and the production of very dense cores by turbulence alone is very low. This implies that self-gravity is involved not only in the collapse of Jeans-unstable cores, but also in their formation. (3) We also find that denser regions tend to have a stronger velocity convergence, implying a net inwards flow towards the regions' centres. Contrary to the non-magnetic case, we find that the magnetic simulation with lowest values of $M_{\rm s}$ and J (respectively, 5 and 2) does not produce any collapsing regions for over three simulation free-fall times, in spite of being both Jeans-unstable and magnetically supercritical. We attribute this result to the combined thermal and magnetic support. Next, we compare the results of our HD and MHD simulations with the predictions from the recent SF theories by Krumholz & McKee, Padoan & Nordlund, and Hennebelle & Chabrier, using expressions recently provided by Federrath & Klessen, which extend those theories to the magnetic case. In both the HD and MHD cases, we find that the theoretical predictions tend to be larger than the $\rm SFE_{ff}$ measured in the simulations. In the MHD case, none of the theories captures the suppression of collapse at low values of $J_{\rm eff}$ by the additional support from the magnetic field. We conclude that randomly driven isothermal turbulence may not correctly represent the flow within actual clouds, and that theories that assume this regime may be missing a fundamental aspect of the flow. Finally, we suggest that a more realistic regime may be that of hierarchical gravitational collapse.

[1]Centro de Radioastronomía y Astrofísica, Universidad Nacional Autónoma de México, Apdo. Postal 3-72, Morelia, 58089, México

[3]Instituto de Astronomía, Universidad Nacional Autónoma de México, A.P. 70-264, 04510, México, D.F., México

[4]Korea Astronomy and Space Science Institute, 61-1, Hwaam-dong, Yuseong-gu, Daejon 305-764, Korea

6.3. Introduction

Theories of star formation (SF) necessarily rely on assumptions about the structure of the molecular clouds (MCs) where the stars form. One of the most common of such assumptions is that the observed supersonic linewidths observed within MCs constitute supersonic turbulence (Zuckerman & Evans 1974b), and that this turbulence causes a net pressure that provides support against the clouds' self-gravity, maintaining them in approximate virial equilibrium (e.g., Larson 1981b; Myers & Goodman 1988b; Blitz 1993). The notion of turbulent pressure as an agent of support against self-gravity was first introduced by Chandrasekhar (1951) and later the scale-dependence of the turbulent support was also considered (e.g., Bonazzola et al. 1987; Vazquez-Semadeni & Gazol 1995).

It is important to note that, in order for the non-thermal motions to be able to provide support against self-gravity, the turbulent velocity field must be essentially random. This property is actually extremely difficult to measure observationally, because one normally has information about only *one* component of the vector velocity field (the one along the line of sight), and moreover one does not have information about the spatial structure of that component along the line of sight. Thus, most measurements of the velocity structure in MCs refer to the *magnitude* of the velocity, which in turn is most commonly interpreted in terms of the non-thermal kinetic energy in the clouds, and its relative importance in the clouds' virial balance, in particular in relation to the clouds' gravitational energy (e.g., Mac Low & Klessen 2004; McKee & Ostriker 2007, and references therein). Statistical quantities, such as the kinetic energy *spectrum* in MCs (see, e.g., the review by Elmegreen & Scalo 2004), give the distribution of the kinetic energy over the range of size scales present in the turbulent motions. However, this distribution is still obtained by averaging over the cloud's volume, so no spatial information on the velocity field structure is provided by it.

Studies of the radial velocity gradient (e.g. Goldsmith & Arquilla 1985; Goodman et al. 1993; Phillips 1999; Caselli et al. 2002; Rosolowsky 2007; Imara & Blitz 2011; Imara, Bigiel & Blitz 2011; Li et al. 2012) provide a crude approximation to the spatial structure of the radial component of the velocity field across MCs. It must be noted that such gradients are most often interpreted as rotation, although in principle they might equally be interpreted as shear, expansion, or contraction. In fact, Brunt (2003) has pointed out that a principal component analysis of the clouds is inconsistent with that expected for uniform rotation, and instead interprets the inferred principal components of the velocity dispersion as large-scale chaotic turbulence (see also Brunt, Heyer & Mac Low 2009). Moreover, the possibility that the clouds are undergoing global contraction has been advocated by various recent studies (Vázquez-Semadeni et al. 2007, 2009; Heitsch & Hartmann 2008; Ballesteros-Paredes et al. 2011a,b), in which case the gradients might be interpreted as the signature of this contraction. Thus, determination of the velocity field's topology in MCs is a very important challenge for our understanding of their structure.

Another universal notion concerning SF is that, in MCs and their substructure, there

exists a linewidth–size relation of the form (Larson 1981b)

$$\delta v_\ell \propto \ell^\kappa, \tag{6.1}$$

and it is widely believed that such scaling relation originates as a consequence of the existence of a turbulent cascade, which produces a kinetic energy spectrum of the form $E(k) \propto k^{-n}$. Indeed, this form of the energy spectrum implies that the typical velocity difference across scales $\ell \sim 1/k$ is $\delta v_\ell \propto \ell^{(n-1)/2}$ (see, e.g., Vazquez-Semadeni et al. 2000). Thus, a spectral slope $n = 5/3$ directly implies $\delta v_\ell \propto \ell^{1/3}$, close to the value $\kappa \approx 0.38$ initially observed by Larson (1981b), while $n = 2$ implies $\delta v_\ell \propto \ell^{1/2}$, as determined by most later studies (see, e.g., the review by Blitz 1993, and references therein).

Larson (1981b) also advanced a scaling relation between mean density and size, of the form

$$\langle \rho \rangle \propto \ell^\lambda, \tag{6.2}$$

with $\lambda \sim -1$. Relations (6.1) and (6.2) are almost universally thought to be a manifestation of near virial equilibrium in the clouds, as originally proposed by Larson (1981b) himself. However, the density–size relation has been questioned by a number of authors (e.g., Kegel 1989; Scalo 1990), in particular as it may be the result of an observational selection effect. Moreover, Ballesteros-Paredes et al. (2011a) have recently pointed out that the linewidth–size relation is in general not universally verified, and that it might also be a consequence of the same selection effects. Indeed, high-mass star-forming clumps typically exhibit larger linewidths for their size than those implied by the Larson (1981b) relation (e.g., Caselli & Myers 1995; Plume et al. 1997; Shirley et al. 2003; Gibson et al. 2009; Wu et al. 2010). Yet, Ballesteros-Paredes et al. (2011a) showed that, when the massive cores have mass determinations independent from virial estimates, it is found that their linewidth, size, and column density follow the general relation found by Heyer et al. (2009), namely

$$\delta v_\ell \propto \Sigma^{1/2} \ell^{1/2}. \tag{6.3}$$

The latter authors interpreted this scaling as evidence of virial equilibrium in clouds without constant column density, although Ballesteros-Paredes et al. (2011a) noted that this may just as well be interpreted as evidence of free-fall in the clouds and their substructures.

Within the context of the linewidth–size relation, equation (6.1), it is well known that such a relation implies that at some particular scale, termed the 'sonic scale' ($\lambda_{\rm s}$), the turbulent velocity dispersion is equal, on average, to the sound speed in the medium. Thus, a number of authors (e.g., Padoan 1995; Vázquez-Semadeni, Ballesteros-Paredes & Klessen 2003; Krumholz & McKee 2005; Federrath et al. 2010) have assumed that stars form in cores that have sizes equal to or smaller than the sonic scale, if they contain more than one thermal Jeans mass, since in these cores the main support is thermal. In principle, such cores can proceed to collapse without significant turbulent support nor fragmentation. Clumps larger than this scale are assumed to be globally supported against their self-gravity by turbulence, since they exhibit scaling relations like relation (6.3), and thus are interpreted as

being near virial equilibrium. Nevertheless, within the clumps, the turbulence is assumed to induce local compressions that constitute smaller scale clumps and cores. However, if MCs are in a global state of gravitational collapse, as proposed by Vázquez-Semadeni et al. (2007, 2009), Heitsch & Hartmann (2008) and Ballesteros-Paredes et al. (2011a), then the observed linewidths may not reflect supporting turbulent motions, but rather the infall velocities themselves. In this case, the notion that the structures that collapse are the subsonic, super-Jeans cores may not apply.

In a previous paper (Vázquez-Semadeni et al. 2008b, hereafter Paper I), we presented a numerical study designed to test the hypotheses mentioned above, using simulations of supersonic, isothermal, hydrodynamic driven turbulence. We considered three simulations with different physical box sizes, rms Mach numbers ($M_{\rm s}$), and Jeans numbers ($J = L/L_{\rm J}$, with L the numerical box size and $L_{\rm J}$ the Jeans length), but such that the ratio $M_{\rm s}/L_{\rm J}$ remained constant, thus assuring that the boxes followed Larson-type scaling relations (Larson 1981b). We found, among other results, that (a) there appeared to exist a negative correlation between the mean density and the mean velocity divergence of isolated subregions in the flow, suggesting that the velocity field is not completely random in overdense regions, but is characterized by a net convergence (negative divergence) of the velocity. The fact that the flow within the clumps has a net negative divergence instead of being fully random implies that not all of the flow's kinetic energy is available for support against the self-gravity of the clump. (b) Clumps or subboxes of the numerical box with subsonic velocity tended to be Jeans *stable*, although significant gravitational collapse did occur in the simulations. This suggested that the main collapsing structures are large-scale, supersonic clumps, rather than small-scale, subsonic ones. (c) The SF efficiency per free-fall time of the various simulations, $\mathrm{SFE_{ff}}$, scaled with $M_{\rm s}$ roughly in agreement with the theoretical prediction by Krumholz & McKee (2005, hereafter KM05), within the (relatively large) uncertainties.

Since the publication of Paper I, two new theories have appeared (Hennebelle & Chabrier 2011; Padoan & Nordlund 2011), in addition to that by KM05, which attempt to describe the dependence of the star formation rate (SFR) on the main physical parameters of the clouds, namely the ratio of kinetic to gravitational energy, characterized by the *virial parameter* α (KM05), the rms turbulent Mach number $M_{\rm s}$, the Alfvénic Mach number $M_{\rm A}$, and the ratio of solenoidal to compressive modes injected to the turbulence, measured by the so-called *b-parameter* (Federrath, Klessen & Schmidt 2008b). All of those theories start from considering the fraction of the mass in a turbulent cloud above a certain critical density, as computed from the probability density function (PDF) of the density field, expected to have a lognormal form (Vazquez-Semadeni 1994; Padoan, Nordlund & Jones 1997; Passot & Vázquez-Semadeni 1998). The main difference between the theories resides mainly in how this 'star-forming fraction' is selected. Specifically, KM05 assumed that stars form from clumps that simultaneously satisfy the conditions of being *subsonically turbulent* (i.e. have sizes below the sonic scale) and of having a density large enough that their Jeans length is equal to or smaller than the sonic scale, as described above. Padoan & Nordlund (2011, hereafter PN11) further included magnetic support to compute the appropriate density cutoff, while Hennebelle & Chabrier (2011, hereafter HC11) took a scale-dependent

'turbulent support' into account, as well as the fact that material at different densities evolve on different time-scales, given by their corresponding free-fall times. A detailed review on how each theory determines this fraction is provided by Federrath & Klessen (2012b, hereafter FK12).

It can thus be seen that all three of these recent theories indeed rely on one of the fundamental assumptions discussed above, namely that the supersonic non-thermal motions constitute isotropic turbulence that, while locally inducing compressions that can become Jeans-unstable and collapse, globally produce a turbulent pressure that can oppose the clumps' self-gravity. Moreover, two of these theories (KM05 and PN11) rely on the assumption that simultaneously subsonic and super-Jeans cores play a fundamental role in the process of SF. Both of these assumptions were questioned, in the non-magnetic case, in Paper I. It is thus important to test whether these assumptions are verified, at least in numerical simulations designed for that purpose. It is worth pointing out that one theory not assuming turbulent support, but rather generalized gravitational collapse, has been presented by Zamora-Avilés, Vázquez-Semadeni & Colín (2012).

The assumption that the non-thermal motions in MCs consist of turbulence that can oppose self-gravity extends beyond theories for the SFR. In particular, theories for the mass spectrum of the clouds themselves as well as the dense cores within them have often relied on this assumption. For example, Hennebelle & Chabrier (2008) developed a theory for the stellar initial mass function (actually, for the core mass function in MCs) that relied on the competition between turbulent support and self-gravity, and, more recently, Hopkins (2012a,b, 2013) has combined this with an excursion-set formalism in order to obtain the mass function of gravitationally bound objects (with respect to thermal, turbulent and rotational support) both at large and small scales.

In this paper, we continue the study performed in Paper I, now in the magnetohydrodynamic (MHD) case, aimed at testing the hypotheses that the bulk motions in the clumps can provide support against self-gravity, and that clumps that are simultaneously subsonic and super-Jeans are produced by turbulent compressions. We also use our driven-turbulence simulations to test the predictions of the various theories for the SFR. The plan of the paper is as follows: In Sec. 6.4, we discuss the control parameters for our numerical simulations and the cases we have considered. Next, in Sec. 6.4.2, we present the results from the simulations, and in Sec. 6.6, we discuss them in the context of previous results, including our non-magnetic ones, as well as their implications. Finally, in Sec. 6.7, we present a summary and some conclusions.

6.4. The models

6.4.1. Control parameters

Our simulations of supersonic, isothermal, magnetized, and self-gravitating turbulence may be described in terms of three dimensionless parameters, namely the rms turbulent

Cuadro 6.1: Run parameters.

Name	L (pc)	n_0 (cm^{-3})	M (M$_\odot$)	$L_{\rm J}$ (pc)	J	$t_{\rm ff}$ (Myr)	$t_{\rm grav}$ (Myr)	β	$v_{\rm A}$	$v_{\rm rms}$ (km s^{-1})	$J_{\rm eff}$ (km s^{-1})	Resolution	Driving
Ms5J2	1	2000	115.8	0.5	2	2.5	2	0.086	0.967	1.	0.91	512	Sol.
Ms10J4	4	500	1853	1	4	5	4	0.021	1.934	2.	0.95	512	Sol.
Ms15J6	9	222.22	9382	1.5	6	7.5	6	0.0095	2.901	3.	1.02	512	Sol.
Ms15J6C-128	9	222.22	9382	1.5	6	7.5	6	0.0095	2.901	3.	1.02	128	Comp.
Ms15J6C-256	9	222.22	9382	1.5	6	7.5	6	0.0095	2.901	3.	1.02	256	Comp.
Ms15J6C-512	9	222.22	9382	1.5	6	7.5	6	0.0095	2.901	3.	1.02	512	Comp.

Mach number $M_{\rm s}$, the Jeans number J, and the mass-to-magnetic flux ratio (in units of its critical value), μ. In this paper, we employ the same normalization as in Vázquez-Semadeni et al. (2005). The rms turbulent Mach number is given by $M_{\rm s} = v_{\rm rms}/c_{\rm s}$, where $v_{\rm rms}$ is the rms turbulent velocity dispersion and $c_{\rm s}$ is the isothermal sound speed. The Jeans number is defined by $J = L/L_{\rm J}$, where L is the numerical box size and

$$L_{\rm J} = \left(\frac{\pi c_{\rm s}^2}{G\rho}\right)^{1/2} \tag{6.4}$$

is the Jeans length at density ρ and isothermal sound speed $c_{\rm s}$. The magnetic flux ϕ is defined as

$$\phi \equiv \int_A \mathbf{B} \cdot d\mathbf{S}, \tag{6.5}$$

where A is a cross-sectional area across the region over which the flux is to be evaluated. The critical value of the mass-to-magnetic flux ratio for a cylindrical geometry is given by (Nakano & Nakamura 1978)

$$\left(\frac{M}{\phi}\right)_{\rm crit} = \frac{1}{\sqrt{4\pi^2 G}} \approx 0.16\, G^{-1/2}. \tag{6.6}$$

This is the relevant criterion for our Cartesian simulations, since the column density is the same along all flux tubes in the initial conditions, as in a cylindrical configuration. A spherical criterion, such as that given by Shu (1992), would apply for a configuration in which the column density is lower for flux tubes intersecting a spherical cloud near its poles.

It is important to note that collapsing clouds must have $J > 1$ and $\mu > 1$, while clumps with $J > 1$ and $\mu < 1$ are gravitationally bound but will only contract for a while, and then oscillate around a stable magnetostatic state (Vázquez-Semadeni et al. 2011). Finally, structures with $J < 1$ are Jeans-stable and must re-expand after being formed by a transient turbulent compression, regardless the value of μ.

Two other frequently used parameters for describing a magnetized plasma are the so-called 'plasma β' and the Alfvénic Mach number, $M_{\rm A} \equiv v_{\rm rms}/v_{\rm A}$. The former is given by $\beta = P_{\rm th}/P_{\rm mag}$, where $P_{\rm th} = c_{\rm s}^2\rho$ and $P_{\rm mag} = B^2/8\pi$. It can be easily shown that, for

a cubic numerical box of size L, and for uniform initial density and magnetic fields, β is related to the normalized mass-to-flux ratio and the Jeans number by

$$\beta = \frac{2}{\pi^2}\left(\frac{\mu}{J}\right)^2, \tag{6.7}$$

where we have assumed that the critical mass-to-flux ratio is given by the cylindrical expression, equation (6.6). Similarly, the Alfvénic Mach number is related to the nondimensional parameters by

$$M_{\rm A} = \sqrt{\frac{\beta}{2}} M_{\rm s} = \frac{\mu M_{\rm s}}{\pi J}. \tag{6.8}$$

This implies that all three of our simulations have $M_{\rm A} \approx 1.03$.

Also, from equation (6.7), we see that the critical value of β (that is, the value of β that corresponds to $\mu = 1$) is $\beta_{\rm cr} = 2/(\pi^2 J^2)$, and thus we have, in general,

$$\mu = (\beta/\beta_{\rm cr})^{1/2}. \tag{6.9}$$

In addition, we assume the same magnitude of the magnetic field in all our runs. This is motivated by the observation that the magnetic field strength is roughly independent of density for densities below $\sim 10^3 {\rm cm}^{-3}$, with magnitudes of a few tens of μG (see fig. 1 of Crutcher et al. 2010).

A separate argument is the following. Consider the definition of the Alfven speed $v_{\rm A}$, that is,

$$v_{\rm A}^2 = \frac{B_0^2}{4\pi\rho}, \tag{6.10}$$

which, in terms of the Alfvenic Mach number $M_{\rm A}$, reads

$$B_0^2 = 4\pi\rho\left(\frac{\Delta v}{M_{\rm A}}\right)^2, \tag{6.11}$$

where Δv is the three-dimensional velocity dispersion. Then, inserting the Larson relations (6.1) and (6.2), we see that B_0, which is proportional to $\rho\,\Delta_v^2 = $ cst., should be taken constant in our constant-$M_{\rm A}$ numerical simulations.

6.4.2. Numerical simulations

As mentioned in Sec. 6.3, we consider a suite of three main numerical simulations of randomly driven, isothermal, self-gravitating, ideal MHD turbulence with different rms Mach numbers $M_{\rm s}$ and physical sizes L, chosen in such a way as to keep the ratio $M_{\rm s}/J$ constant. This implies that the mean density and rms Mach number of the simulations satisfy Larson's (1981) scaling relations with their physical size, so that the smaller ones can be considered to be a part of the larger ones. The simulations were performed with a resolution of 512^3 zones, using a total variation diminishing scheme (Kim et al. 1999) with

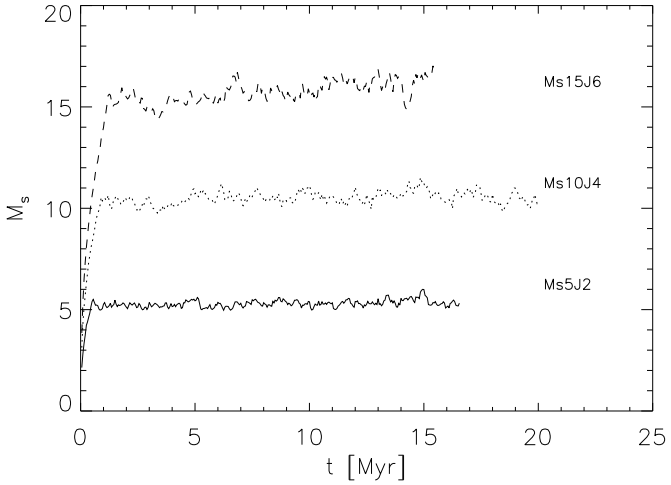

Figura 6.1: Evolution of the turbulent Mach number $M_{\rm s}$ for each of our simulations.

periodic boundary conditions. The initial conditions in all simulations have uniform density and magnetic field strength. The turbulence is driven in Fourier space with a spectrum

$$P(k) = k^6 \exp\left[-\frac{8k}{k_{\rm pk}}\right], \tag{6.12}$$

where $k_{\rm pk} = 2(2\pi/L)$ is the energy-injection wavenumber. The driving in the main simulations is purely rotational (or 'solenoidal'), and a prescribed rate of energy injection is applied in order to approximately maintain the rms Mach number near a nominal value, which characterizes each run (Fig. 6.1).

The restriction that the simulations satisfy Larson's (1981) relations means that each simulation's sonic Mach number must scale as $M_{\rm s} \propto L^{1/2}$ and its mean density as $\langle n \rangle \propto L^{-1}$. Specifically, we choose box sizes $L = 1$, 4, and 9 pc, and corresponding densities $n = 2000$, 500, and $222 {\rm cm}^{-3}$. We choose a temperature $T = 11.4$ K, implying an isothermal sound speed of $c_{\rm s} = 0.27$km/s, and we set the turbulence driving as to produce rms Mach numbers $M_{\rm s} = 5$, 10, and 15, respectively. The runs are respectively labelled Ms5J2, Ms10J4, and Ms15J6.

Table 6.1 summarizes these parameters, together with the Jeans number J, and other physical quantities characterizing our runs, such as their mass M, Jeans length $L_{\rm J}$, free-fall time $t_{\rm ff}$, the time at which gravity is turned on, $t_{\rm grav}$, and their *rms* velocity dispersion, $v_{\rm rms}$. Note that, because the density–size relation implies a constant column density, all of our simulations have the same initial, uniform column density, of $N = 6.2 \times 10^{21}$ cm^{-2}.

In addition to these runs, three other runs were performed in order to test for convergence and for the effect of compressible, rather than solenoidal, driving. These all have a

nominal rms Mach number $M_{\rm s} = 15$ and Jeans number $J = 6$, so that they correspond to run Ms15J6. These runs had a 100 % compressible forcing, and were performed at resolutions of 128^3, 256^3, and 512^3. They are also indicated in Table 6.1, with mnemonic names.

An important parameter of the simulations is the so-called *virial parameter*, α, defined as the ratio of twice the kinetic energy to the magnitude of the gravitational energy (Bertoldi & McKee 1992) and which, for a spherical geometry, reads:

$$\alpha \equiv \frac{2E_{\rm k}}{\mid E_{\rm g} \mid} \approx \frac{M\sigma^2}{GM^2/L} = \frac{3}{4\pi^2}\frac{M_{\rm s}^2}{J^2}. \tag{6.13}$$

The last equality gives α in terms of the nondimensional parameters J and $M_{\rm s}$. For the nominal values of these parameters for our simulations, we see that all three of our simulations have a nominal value of $\alpha \approx 0.475$.[5]

The choice of magnetic parameters for our runs requires some further discussion. Observational results (e.g. Myers & Goodman 1988b; Crutcher et al. 2010) suggest that the magnetic field strength is roughly independent of density for densities below $\sim 10^3 {\rm cm}^{-3}$, with magnitudes of a few tens of μG. We thus choose a constant magnetic field strength for all three simulations, since their mean densities are comparable to or below this threshold. Moreover, since the simulations all have the same initial column density, this choice implies that they all have the same mass-to-flux ratio (recall that, for uniform conditions and cylindrical geometry, $M/\phi = N/B$). We thus choose the same initial uniform field strength, $B = 30.3$ μG for all three simulations, which implies that they have the same normalized mass-to-flux ratio, $\mu = 1.3$.

6.5. Results

6.5.1. Fraction of subsonic, super-Jeans structures

As in Paper I, we measure the fraction of structures in the simulations that are simultaneously subsonic and super-Jeans. We do this as a function of structure size because in the adopted isothermal regime, there is no inherent physical size scale for a given density enhancement, and its 'size' is a completely arbitrary, observer-defined quantity (for example, through a density-threshold criterion). Of course, larger structures will in general be more massive and, because they in general have density profiles that resemble Bonnor–Ebert spheres (Ballesteros-Paredes, Klessen & Vázquez-Semadeni 2003; Gómez et al. 2007), they will eventually appear more massive than the Jeans mass associated with their mean density. On the other hand, larger structures will tend to have larger velocity dispersions, as

[5] FK12 propose to use a cell-to-cell estimator for the virial parameter instead of equation (6.13), which is based on global flow parameters. We discuss in Appendix 6.7 our reasons not to use their suggested prescription.

dictated by the fact that the turbulent kinetic energy spectrum in general decays with increasing wavenumber (i.e., the kinetic energy content decreases with decreasing size scale). Thus, sufficiently small structures should appear subsonic in general. The question is then whether, on average, there is a range of scales within a turbulent supersonic flow where the structures appear both subsonic and super-Jeans.

We consider two types of regions in the simulations: either cubic subboxes (or 'cells') of fixed sizes that fill up the numerical box, or dense clumps defined by a density threshold criterion. The subboxes are independent of the local density structure, and constitute just a subdivision of the numerical box, thus providing us with a very large statistical sample in the case of sizes significantly smaller than the numerical box. Also, they can have average densities larger or smaller than the mean density of the numerical simulation. We consider subboxes of sizes 2, 4, 8, 16, 32, 64, and 128 grid zones per side.

On the other hand, the clumps are exclusively overdense regions, and their shapes are dictated by the local density structure. Thus, the sample of these structures contains much fewer elements than the subbox sample. As in Paper I, we then define the clumps' size as the cubic root of their volume V, assuming they are spherical, so that $L = (3V/4\pi)^{1/3}$, and produce a logarithmic histogram with size bins of the form $[2^n, 2^{n+1}]\Delta x$, for $n = 1, \ldots$,6, where Δx is the grid cell size. Finally, also following our procedure in Paper I, we identify both kinds of structures at two different times in each run: just before the gravity is turned on, at which the density distribution is only due to turbulent effects, and at a time around two *global* free-fall times after gravity is turned on, at which the density structure is influenced by both turbulence and gravity. Note that, when we speak of 'super-Jeans' structures at the times when self-gravity has not been turned on yet, we simply mean that their masses are larger than the corresponding Jeans mass at the structure's mean density and temperature.

Figs 6.2 and 6.3, respectively, show the fractions of subsonic (*solid lines* and *triangles*) and of super-Jeans structures (*dotted lines* and *diamonds*) for subboxes and clumps, as a function of their sizes. In both figures, the top panels present the results from run Ms5J2, the middle panels from run Ms10J4, and bottom panels from run Ms15J6. The results computed before (resp. after) self-gravity is turned on are shown in the left-hand (resp. right-hand) panels. In Fig. 1, the fraction of subboxes is shown in logarithmic scale because the total number of subboxes is very large for the smallest sizes, and thus the subsonic and super-Jeans fractions can be very small.

It is important to note that, similarly to the case of the non-magnetic simulations presented in Paper I, we have found no structures (either cells or cores) that are *simultaneously* subsonic and super-Jeans at any of the size scales we considered in this work. In Figs 6.2 and 6.3, when both the subsonic and the super-Jeans curves show non-zero values at a given scale, these correspond to *different* structures, that are *either* subsonic or super-Jeans, but no structure among the ones we sampled has both properties simultaneously.

In addition, no significant effect is observed in the fraction of subsonic structures at a given scale upon the inclusion of self-gravity. On the other hand, the fraction of super-Jeans structures as a function of scale exhibits a clear change after self-gravity is turned on.

However, the effect is different for the subboxes and the clumps. For the former, the range of scales at which super-Jeans cells exist is stretched towards *small* scales when self-gravity is on. Instead, for clumps, *no super-Jeans structures exist in the absence of self-gravity*, and when it is included, super-Jeans clumps appear at *large* scales.

We conclude from this section that, similarly to the non-magnetic case studied in Paper I, simultaneously subsonic and super-Jeans structures are uncommon also in driven, MHD supersonic, isothermal turbulent flows. We discuss some implications of these results in Sec. 6.6.

6.5.2. Velocity convergence

A second nearly universal assumption about the non-thermal motions in molecular clouds and their substructure is that they consist of random turbulence, which provides an isotropic, 'turbulent' pressure, in a similar manner to thermal motions and pressure. In Paper I, we tested this hypothesis by computing the mean divergence in subboxes of size equal to the physical size of the small-scale simulation within the largest scale simulation, and plotting it against the mean density of the regions. In that paper, we found that there exists a negative correlation between the mean divergence of the flow and the mean density of the subboxes, suggesting that, on average, overdense regions are characterized by a net convergence of the velocity field within them. Such a velocity field structure has a reduced capability of countering the self-gravity of the structures, and in fact may be *caused* by it. We now test whether this result persists in the MHD case.

As in Paper I, we subdivide the large-scale simulation, Ms15J6, into cells of size equal to that of run Ms5J2, and compute the mean density and mean divergence of the velocity field for each cell. The divergence is computed by dotting the Fourier transform of the velocity field with the corresponding wavevector $\mathbf{k}$.

Fig. 6.4 shows the two-dimensional histogram of the cells in the $\{-\nabla \cdot \mathbf{v}, \log n\}$ space, at three different times during the simulation. The left and middle panels, respectively, show the histogram at $t = 3$ and 6 Myr, which, respectively, correspond to 1 and 2 $t_{\rm turb}$, where $t_{\rm turb} \equiv L/v_{\rm rms} = 3$ Myr is the turbulent crossing time (see Table 6.1). Both of these correspond to times before self-gravity was turned on. The right-hand panel shows the histogram at $t = 13.5$ Myr, which corresponds to one free-fall time after gravity was turned on. The contours are drawn at levels 1/14, 1/7, 2/7,. . ., 6/7 of the maximum. We find in all cases that the contours show an elongated shape, and the straight solid lines show least-squares fits through the data points. The fitted slope has values of $\sim 0.16 \pm 0.033$ at time $t = 3$ Myr, $\sim 0.26 \pm 0.035$ at $t = 6$ Myr, and $\sim 0.16 \pm 0.33$ at $t = 13.5$ Myr, with corresponding correlation coefficients 0.21, 0.31, and 0.22. The uncertainties reported are the 1σ errors of the fit. However, given the low correlation coefficients, and the fact that the earliest and latest distributions exhibit approximately the same slope, the slopes can be considered to be the same before and after turning self-gravity on, ~ 0.19, with the main difference being that the distribution of points in this diagram becomes more elongated in the presence of self-gravity, as evident from the larger extent to higher densities of the

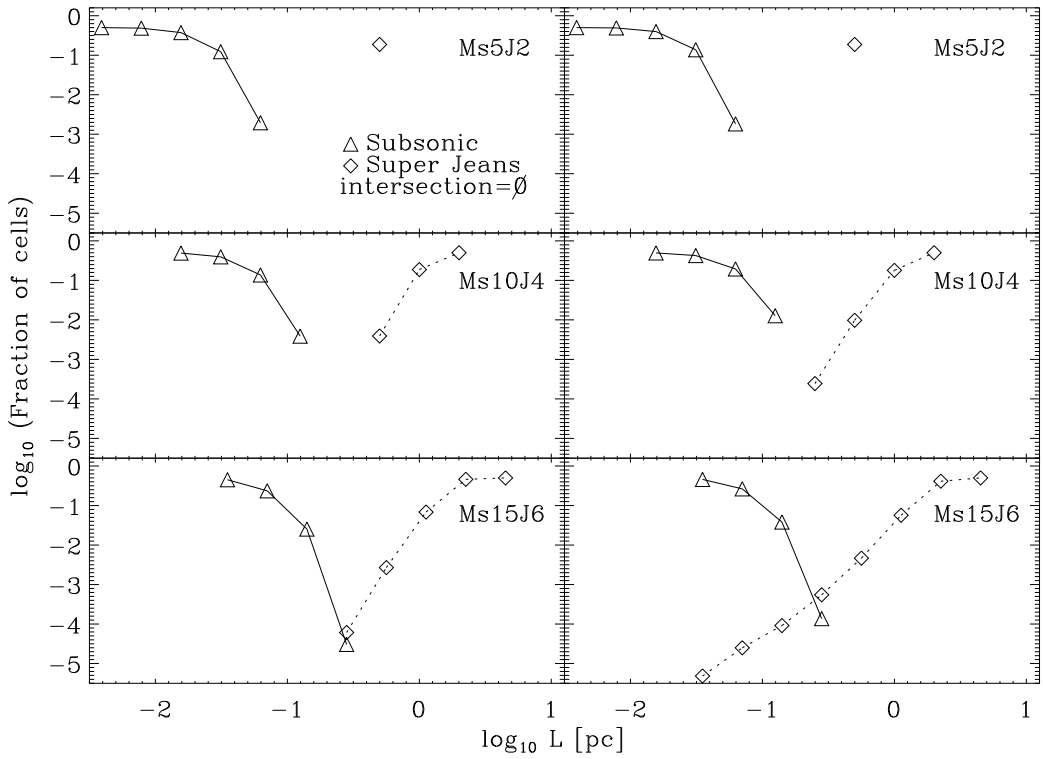

Figura 6.2: Fraction of subsonic (triangles, solid lines) and super-Jeans (diamonds, dotted lines) subboxes (in logarithmic scale) for runs Ms5J2 (top panels), Ms10J4 (middle panels), and Ms15J6 (bottom panels), as a function of subbox size. The left-hand panels show the fractions shortly before the time $t_{\rm grav}$ when self-gravity is turned on. The right-hand panels show the fractions at approximately one free-fall time after $t_{\rm grav}$. The fraction of subboxes that are both subsonic and super-Jeans is zero at all subbox sizes, and thus cannot be shown in this figure.

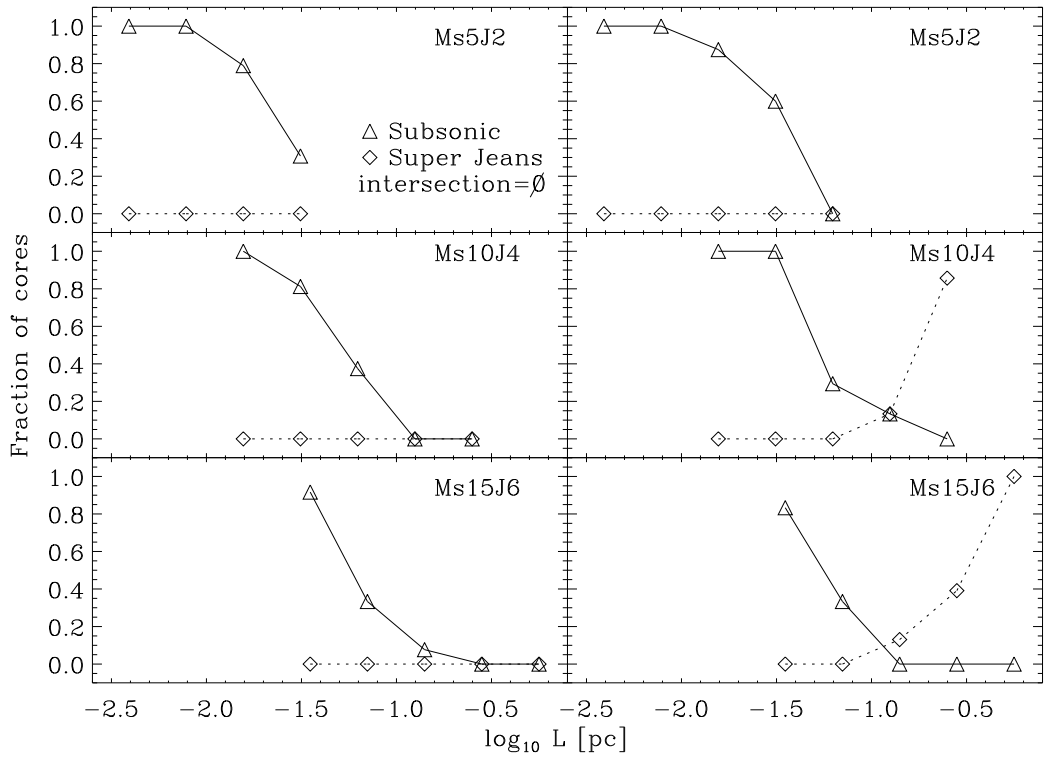

Figura 6.3: Fraction of simultaneously subsonic (triangle, solid lines) and super-Jeans (diamonds, dotted lines) clumps in runs Ms5J2, Ms10J4, and Ms15J6, as a function of clump sizes. The clumps are defined as connected regions above a certain density threshold. The ensemble of clumps was created by considering thresholds 32, 64, 128, and 256 times the mean density n_0. The fraction of clumps that are both subsonic and super-Jeans is zero at all clump sizes considered.

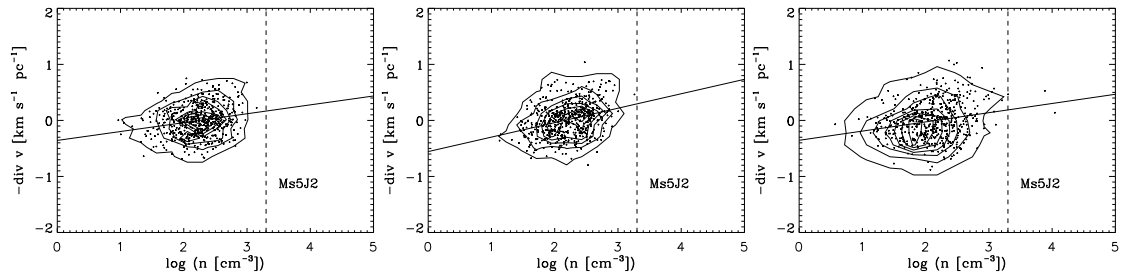

Figura 6.4: Negative mean velocity divergence *versus* mean density for subboxes of the large-scale simulation Ms15J6. The left and middle panels show the two-dimensional histograms of the subboxes in this plane at two times before self-gravity is turned on, namely $t = 3$ Myr, corresponding to 1 $t_{\rm turb}$ (left-hand panel) and $t = 6$ Myr (2 $t_{\rm turb}$; middle panel). The right-hand panel shows the histogram at $t = 13.5$ Myr, corresponding to one free-fall time after gravity was turned on. The straight solid lines show least-squares fits through the data points, and have slopes 0.16 (left-hand panel), 0.26 (middle panel), and 0.16 (right-hand panel), with respective correlation coefficients of 0.21, 0.31, and 0.22. The contours are drawn at increments of 1/7th of the maximum. The dashed vertical lines show the mean density of the small-scale simulation Ms5J2.

lowest contour in this case (right-hand panel of Fig. 6.4).

Compared to our result from Paper I in the non-magnetic case, in which we had found slopes ranging from 0.35 to 0.5, the present MHD simulations exhibit a weaker dependence of $\nabla \cdot \mathbf{v}$ on n. One possible explanation for this would be that the magnetic field converts a larger fraction of the converging motions into vortical ones than do the pure hydrodynamical non-linear interactions (Vazquez-Semadeni, Passot & Pouquet 1996; Vázquez-Semadeni, Cantó & Lizano 1998; Robertson & Goldreich 2012). To test this possibility, in Fig. 6.5 we show the two-dimensional histograms in the $\nabla \times \mathbf{v}$ – $\langle n \rangle$ space for the subboxes of run Ms15J6 in both the non-magnetic case (left-hand panel, from Paper I) and in the magnetic case studied in this paper (right-hand panel). Contrary to the aforementioned expectation, it is seen that the range of $\nabla \times \mathbf{v}$ values is in fact similar in the magnetic and non-magnetic cases. This suggests that the decrease in the slope of the $\nabla \cdot \mathbf{v}$ – $\langle n \rangle$ correlation is *not* due to a more efficient transformation of compressive motions into rotational motions inside the dense regions in the presence of the magnetic field, but rather, simply to a stronger average opposition to the turbulent compressions due to the added pressure from the magnetic field (e.g., Molina et al. 2012).

In any case, a net correlation is still observed between density and velocity convergence, supporting the result from Paper I that density enhancements in a turbulent flow must on average contain a net convergent component of the velocity field which, rather than opposing gravitational contraction, contributes to it, or is driven by it, even in the presence of a magnetic field of magnitude typical of molecular clouds. It is important to mention that

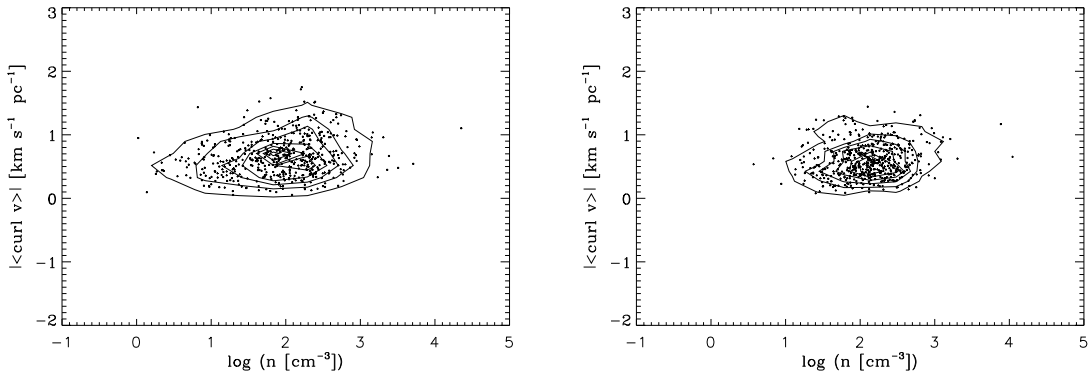

Figura 6.5: Magnitude of the velocity curl *versus* mean density for subboxes of the large-scale simulation Ms15J6 in the non-magnetic case (left-hand panel; from Paper I) and in the magnetic case (right-hand panel; this paper). The range of $\nabla \times \mathbf{v}$ values is seen to be very similar in both cases, while the density range is seen to be significantly shorter in the magnetic case.

we do not find any significant change in the distributions showed in Fig. 6.4 with the action of self-gravity, as can be seen by comparing the left and middle panels of Fig. 6.4 with the right one. In this figure, we plotted a line showing the density of simulation Ms5J2 and, similar to that in Paper I, we find that self-gravity appears to be necessary for the production of regions dense enough as to fall on the same Larson density–size relation (same intercept) as their parent structure, while turbulence alone seems essentially incapable of doing it.

6.5.3. SF efficiency per free-fall time in constant-virial parameter structures

As in Paper I, we now use our numerical simulations to assess the dependence of the 'star formation efficiency per free-fall time', $\mathrm{SFE_{ff}}$,[6] on the turbulent rms Mach number.

To measure $\mathrm{SFE_{ff}}$ in our simulations, we compute the evolution of the total mass in collapsed regions. Operationally, we define a collapsed region as a connected region with density above a threshold density $n_{\rm thr} = 1000\ n_0$, where n_0 is the mean density, given in Table 6.1 for each one of the runs. As explained in Paper I, this is a sufficiently high density that it cannot be reached by turbulent compressions alone, and thus it has to be the

[6]Note that KM05 called this quantity the 'star formation *rate* per free-fall time', and this nomenclature has become common in the literature. However, this is actually somewhat misleading, since the $\mathrm{SFE_{ff}}$ is obtained by integrating the SFR over a free-fall time and then dividing by the total mass, giving the fraction of the gas mass converted into stars over one free-fall time, thus being an efficiency, not a rate. At best, it can be considered an *average* SFR over a free-fall time, with mass normalized to the system mass. Thus, we prefer to call it the star formation efficiency per free-fall time.

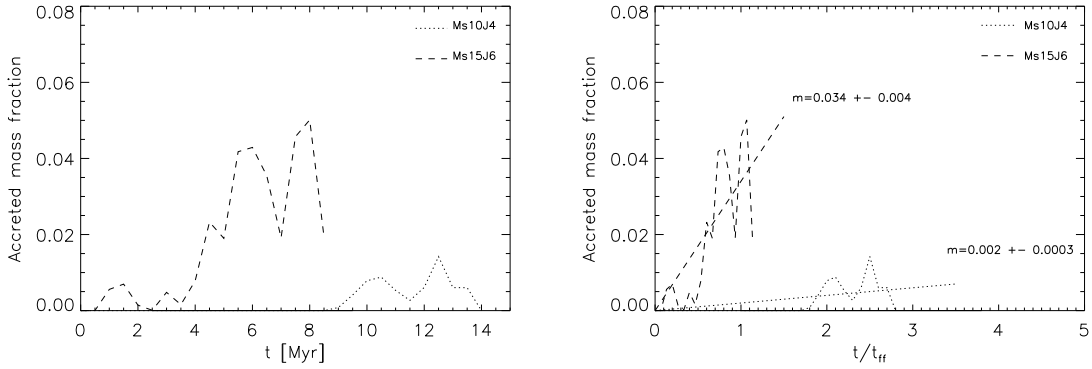

Figura 6.6: Fraction of mass accreted into collapsed objects as function of time in units of Myr (left-hand panel) and of the free-fall time $t_{\rm ff}$ (right-hand panel) for the simulations Ms10J4 and Ms15J6. Run Ms5J2 is not shown in this figure because there is no accreted mass in this simulation. The average $\mathrm{SFE_{ff}}$ is computed by fitting a least-squares line to the plot of accreted mass versus time in units of $t_{\rm ff}$.

result of a local gravitational collapse event.[7] It was shown in Paper I that using a threshold $n_{\rm thr} = 500\ n_0$ does not significantly alter the results.

Fig. 6.6 shows the accreted mass fraction as function of time for runs Ms10J4 and Ms15J6, starting from the time at which gravity was turned on in each case. Run Ms5J2 is not shown in this figure because, contrary to the non-magnetic case, no gravitational collapse occurs in this simulation. When the time is written in units of the simulation free-fall time, the slope of this curve gives $\mathrm{SFE_{ff}}$. In the right-hand panel of Fig. 6.6, the dashed and dotted lines show least-squares fits to the evolution of the accreted mass for runs Ms15J6 and M10J4, respectively, with their slopes indicated. We observe that $\mathrm{SFE_{ff}} = 0.002 \pm 0.0003$ for run Ms10J4 and $\mathrm{SFE_{ff}} = 0.034 \pm 0.004$ for run Ms15J6, where the indicated uncertainties are the 1-σ errors of the linear fit, due to the noisiness of the accreted mass graphs and the scarcity of collapsed objects. These values are shown, as a function of the corresponding rms Mach number of the simulations, by the solid line and triangles in the *right-hand panel* of Fig. 6.7. Note that $\mathrm{SFE_{ff}} = 0$ for run Ms5J2, and thus this run is off the plot.

As discussed in Sec. 6.4.2 and in Appendix 6.7, FK12 have suggested that the virial

[7]Note that sink particles are not implemented in the version of the code used in this paper. Therefore, a gravitational collapse event simply leads to the accumulation of all the mass involved in it in a few grid cells. Also, this implies that the 'collapsed object', defined by $n_{\rm thr}$, does not have a strictly constant mass, because it can oscillate around its equilibrium state, and thus have a variable mass above $n_{\rm thr}$. Resolution is not a concern here, because we are only concerned with the total collapse mass, and not about how it is distributed into fragments, which would be the affected outcome of the collapse in the case of insufficient resolution (Truelove et al. 1997).

parameter be measured directly from the simulation data, rather than from the global run parameters. Upon doing that, they obtained values of α up to an order of magnitude larger than the nominal, global ones. As discussed in the appendix, it is unclear to us how realistic these values are, and thus which one is a better choice but, as simple test, we show in the bottom panels of Fig. 6.7 the model predictions assuming $\alpha = 4.75$, i.e., a value 10 times larger than the nominal one, to obtain a feel for the $\mathrm{SFE_{ff}}$ predicted by the models in this case. It is seen that, for the non-magnetic case, the larger value of $\alpha_{\rm vir}$ implies somewhat smaller values of the $\mathrm{SFE_{ff}}$, ameliorating the discrepancy between the predicted and measured values of the $\mathrm{SFE_{ff}}$, although still the only model that captures the *trend* of $\mathrm{SFE_{ff}}$ *versus* $M_{\rm s}$ (the multi-free-fall KM05 model) differs by nearly an order of magnitude from the simulation measurement. In the case of the PN11 and HC11 models, although agreeing in absolute value with the measurement of the $\mathrm{SFE_{ff}}$ at low $M_{\rm s}$, exhibit the opposite trend with $M_{\rm s}$, and so they are off the measured value by nearly an order of magnitude at the highest value of $M_{\rm s}$. On the other hand, in the magnetic case, the change in α introduces almost no variation in the model predictions for the $\mathrm{SFE_{ff}}$ in the magnetic case, and the discrepancy with the simulation measurements remains.

6.5.4. Absence of collapse in run Ms5J2

As already mentioned above, no collapse occurred in run Ms5J2, in spite of it being both Jeans unstable, with a Jeans length equal to half the simulation box size, and magnetically supercritical, with a mass-to-flux ratio 1.3 times critical (cf. Table 6.1). This is illustrated in Fig. 6.8, which shows the evolution of the maximum density in the three runs (top panels), and also for their non-magnetic counterparts from Paper I. It is seen that run Ms5J2 has not produced collapsed regions even after three and a half free-fall times, and that run Ms10J4 takes nearly two free-fall times to develop a collapse, while run Ms15J6 produces it immediately after self-gravity is turned on.

In order to understand this behaviour, we consider the combined effect of the two supporting agents, thermal pressure and magnetic field, in a virial balance calculation. As is well known, the virial equilibrium for a uniform-density spherical mass of radius R in hydrostatic equilibrium, supported by thermal pressure and the magnetic field, is (see, e.g., Shu 1992)

$$3\int PdV + \frac{1}{8\pi}\int B^2 dV - \frac{3}{5}\frac{GM^2}{R} = 0, \tag{6.14}$$

which leads to an equilibrium, 'magneto-thermal Jeans radius'[8]

$$R_{\rm J,mt} = \left[\frac{5c_{\rm s}^2(3+1/\beta)}{4\pi G\rho}\right]^{1/2}, \tag{6.15}$$

[8]FK12 also use this quantity, although they omit the factor of 3 in the thermal contribution, because they added in quadrature the Alfvén velocity and the sound speed to obtain total thermal+magnetic pressure in the medium. Instead, we obtain the extra factor of 3 because we consider the virial balance of the cloud.

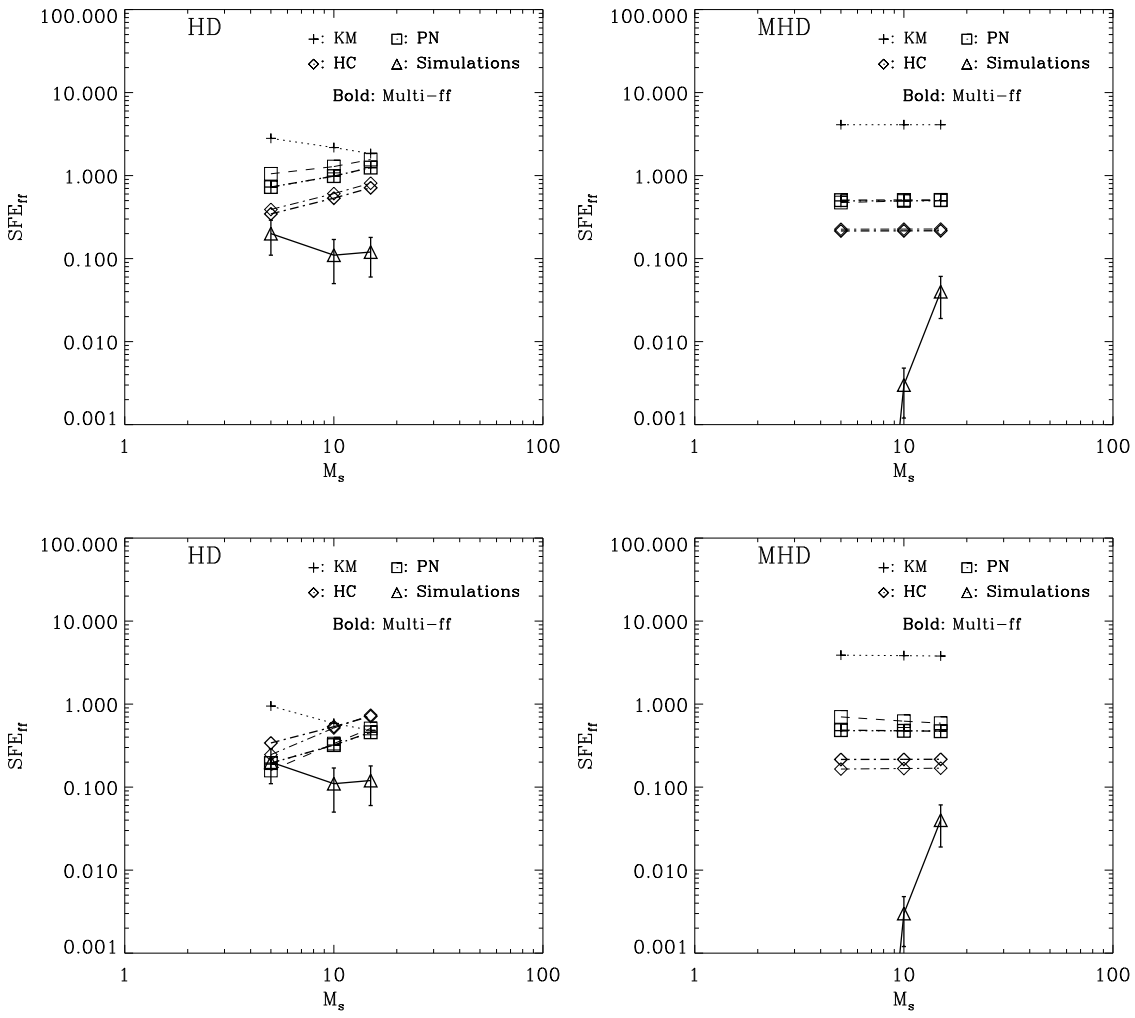

Figura 6.7: *Top-left panels:* $\mathrm{SFE_{ff}}$ *versus* rms Mach number for the three non-magnetic simulations from Paper I (which used the same values of the parameters as the ones presented here, except for the absence of the magnetic field), and for the predictions from the theories by KM05, PN11, and HC11, in both their original as well as their 'multi-free-fall' modes (shown in bold lines and symbols), according to the expressions given by FK12 in the non-magnetic limit ($\beta \rightarrow \infty$). The error bars in the values for the simulation data indicate 3σ errors. *Top-right panels:* same as the left-hand panel, but showing the results from the magnetic simulations Ms10J4 and Ms15J6, as well as the predictions from the six models, according to the extension to the magnetic case proposed by FK12. Run Ms5J2 in the magnetic case produced no collapsed objects, and is indicated by the line going off the plot down and to the left from the point for run Ms10J4. *Bottom panels:* same as the respective top panels, but showing the model predictions assuming a value of the α parameter 10 times larger than the nominal one, to consider the possible effect of measuring it directly from the simulation, as done by FK12.

where we have used the isothermal equation of state $P = c_{\rm s}^2 \rho$, the definition of the Alfvén speed, equation (6.10), and the fact that $\beta = 2(c_{\rm s}/v_{\rm A})^2$. We then can see that the magneto-thermal Jeans radius is a factor $f = [(3 + 1/\beta)/3]^{1/2}$ times larger than the pure thermal value, which corresponds to $\beta \rightarrow \infty$. In turn, we can thus define the *magneto-thermal Jeans parameter* $J_{\rm eff} = J/f$, which is given in the last column of Table 6.1 for the three runs. Specifically, it is 0.91, 0.95, and 1.02 for runs Ms5J2, Ms10J4, and Ms15J6, respectively. Thus, although the difference between the three cases is only $\sim 10\,\%$, this parameter is indeed minimum for run Ms5J2, for which it appears that the global magnetic support is enough to prevent collapse at least over more than three simulation free-fall times. Correspondingly, at $J_{\rm eff} \approx 0.95$, magnetic support is able to delay the occurrence of collapse for nearly two free-fall times for run Ms10J4, while at $J_{\rm eff} \approx 1.02$ for run Ms15J6, magnetic support seems to already make essentially no difference with respect the non-magnetic case.

6.5.5. Effects of resolution and type of driving

The results discussed so far refer to simulations performed at a fixed resolution of 512^3 and with solenoidal driving, following the scheme used in Paper I. It is important, however, to test whether they are affected by the numerical resolution and whether they hold in the presence of compressible driving. In this section, we discuss the results from a few additional simulations designed to test this.

In Fig. 6.9, we show the fraction of subsonic and of super-Jeans subboxes (cf. Fig. 6.2) in the numerical box for the compressible runs. Fig. 6.10 shows the corresponding result for the cores in these simulations. It is seen that at all three resolutions, the compressible runs also do not exhibit simultaneously subsonic and super-Jeans structures, neither subboxes of the simulation nor clumps selected as density enhancements above a certain density threshold. Thus, this result from the solenoidal simulations continues to hold when the forcing is fully compressible. Of course, we cannot rule out that, at higher resolution, such structures may appear, but we defer higher resolution simulations to a future study, and perhaps using an adaptive-mesh code. So, here we can only report that, up to our highest resolution, such structures do not appear, regardless of the compressibility of the driving applied.

Fig. 6.11 shows the two-dimensional histograms of the cells in the $\{-\nabla\cdot\mathbf{v}, \log n\}$ space for the three compressively driven runs, before (left-hand panels) and after (right-hand panels) having turned self-gravity on. While the correlations are poorly defined at the low resolutions, it can be seen that, for the highest resolution run Ms15J6C-512, the distribution is qualitatively very similar to that for the solenoidally driven run Ms15J6 (cf. Fig. 6.4). In particular, the fitted slopes for run Ms15J6C-512 are 0.16 ± 0.031 and 0.31 ± 0.034, with correlation coefficients 0.22 and 0.38, for the distributions before and after turning self-gravity on, respectively, thus spanning a very similar range to that observed in run Ms15J6.

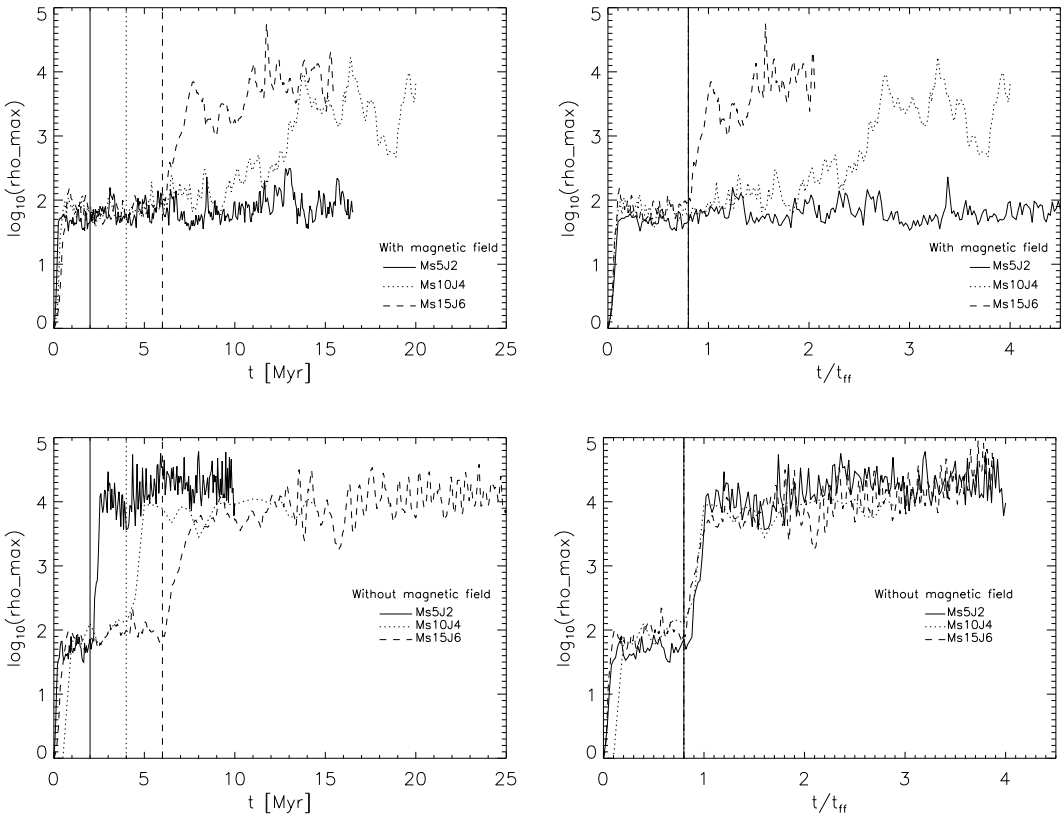

Figura 6.8: Maximum density as function of time for the three magnetic simulations in this paper (top panels), and for their non-magnetic counterparts from Paper I (bottom panels). The left-hand panels show the time in Myr, while the right-hand panels show it in terms of the simulation free-fall time. The vertical lines show the time $t_{\rm grav}$ when self-gravity is turned on for each simulation, which is the same in units of the free-fall time for the three runs.

Moreover, the scatter in the distributions is also similar, so we conclude that this result is also independent of whether the driving is solenoidal or compressible.

Finally, Fig. 6.12 shows the mass accretion histories for the three compressible runs, and least-squares fits to them, with their associated slopes and uncertainties. Fig. 6.13 shows the predictions of the various SFR models assuming fully compressible driving ($b = 1$) and virial parameter $\alpha = 0.475$ (middle) or $\alpha = 4.75$ (right). As in the case for the solenoidal run Ms15J6, it is seen again that the models overpredict the $\mathrm{SFE_{ff}}$ produced by our models, even when α is multiplied by a factor of 10, to mimic the larger values obtained directly by the simulations by FK12.

We conclude from this section that the nature of the driving (solenoidal or compressible) does not introduce any significant changes to our results. However, we cannot rule out that, at higher resolution, cores that are simultaneously subsonic and super-Jeans may appear.

6.6. Discussion

6.6.1. Comparison with previous work

Absence of simultaneously subsonic and super-Jeans structures, and the turbulent driving

Our result that no simultaneously subsonic and super-Jeans regions (either arbitrary subboxes of the simulations or dense cores) seem to appear in the simulations is qualitatively identical to our non-magnetic results from Paper I. In that paper, we speculated that the presence of the magnetic field might allow for the formation of subsonic, super-Jeans structures because of the 'cushioning' effect of the magnetic field, which might reduce the velocity difference between the converging flows that form the clumps. However, the fact that the absence of these structures persists suggests that, perhaps, the cushioning simultaneously causes the clumps to attain lower peak densities, with both effects tending to cancel each other out.

The absence of simultaneously subsonic and super-Jeans structures in our isothermal, driven-turbulence, magnetized simulations, in spite of their ubiquitous observed existence in actual molecular clouds, suggests that perhaps some other feature of our simulations is not sufficiently realistic. One possible candidate is the very nature of the velocity field in our simulations, which consists of randomly driven supersonic turbulence, in which the clumps are in fact the density fluctuations produced by the supersonic compressions in this turbulent regime, and the driving is applied at the largest scales in the numerical box. This continuous-driving setup is intended to model the turbulence driven into clouds and their substructure mostly by supernova explosions in the ambient ISM. Another important candidate is the isothermal effective equation of state, which is one of the assumptions we are testing, but which indeed may not be sufficiently realistic, since MCs may well contain a mixture of atomic and molecular gas phases (e.g., Li & Goldsmith 2003).

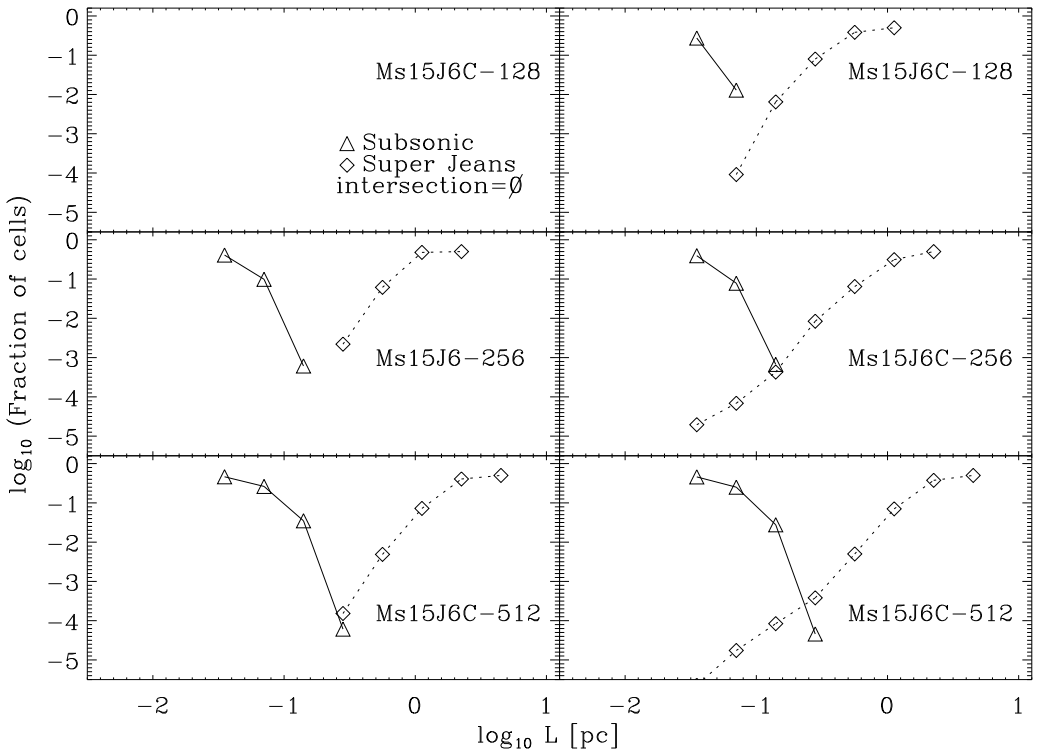

Figura 6.9: Fraction of simultaneously subsonic (triangles, solid lines) and super-Jeans (diamonds, dotted lines) subboxes (in logarithmic scale) for the compressible-driving runs Ms15J6C-128 (top panels), Ms15J6C-256 (middle panels), and Ms15J6C-512 (bottom panels), as a function of the subbox size. The left-hand panels show the fractions shortly before the time $t_{\rm grav}$ when self-gravity is turned on. The right-hand panels show the fractions at approximately one free-fall time after $t_{\rm grav}$. The fraction of subboxes that are both subsonic and super-Jeans is zero at all subbox sizes, and thus cannot be shown in this figure.

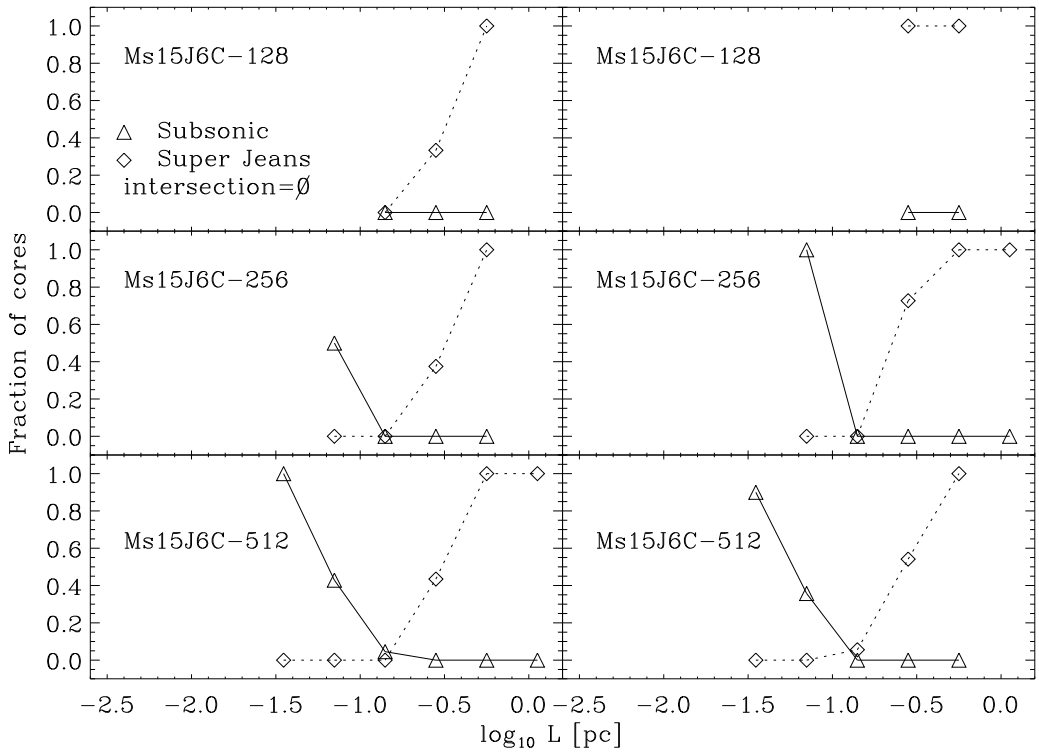

Figura 6.10: Fraction of simultaneously subsonic (triangle, solid lines) and super-Jeans (diamonds, dotted lines) clumps in the compressively driven runs Ms15J6C-128, Ms15J6C-256, and Ms15J6C-512, as a function of clump sizes. The clumps are defined as connected regions above a certain density threshold. The ensemble of clumps was created by considering thresholds 32, 64, 128, and 256 times the mean density n_0. The fraction of clumps that are both subsonic and super-Jeans is zero at all clump sizes considered.

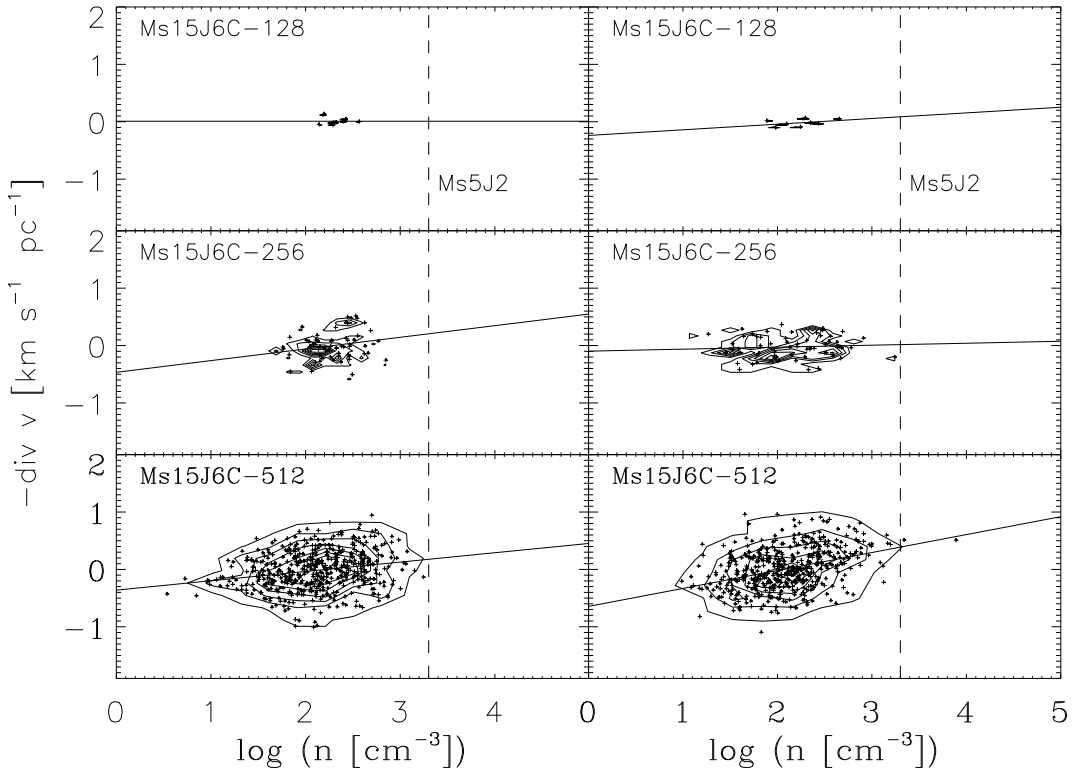

Figura 6.11: Negative mean velocity divergence *versus* mean density for subboxes of the large-scale simulation with compressible forcing, Ms15J6C, at the three resolutions we considered. The left-hand panels show the two-dimensional histograms of the subboxes in this plane at time $t = 6$ Myr, before self-gravity is turned on, corresponding to 2 $t_{\rm turb}$ after the start of the simulations (left-hand panel). The right-hand panels show the histogram at $t = 13.5$ Myr, corresponding to one free-fall time after gravity was turned on. The contours are drawn at increments of 1/7th of the maximum. The straight solid lines show least-squares fits through the data points. For the high-resolution run Ms15J6C-512, the fits have slopes 0.16 ± 0.031 (left-hand panel) and 0.31 ± 0.034 (right-hand panel), with correlation coefficients 0.22 and 0.38, respectively. The dashed vertical lines show the mean density of the small-scale simulation Ms5J2.

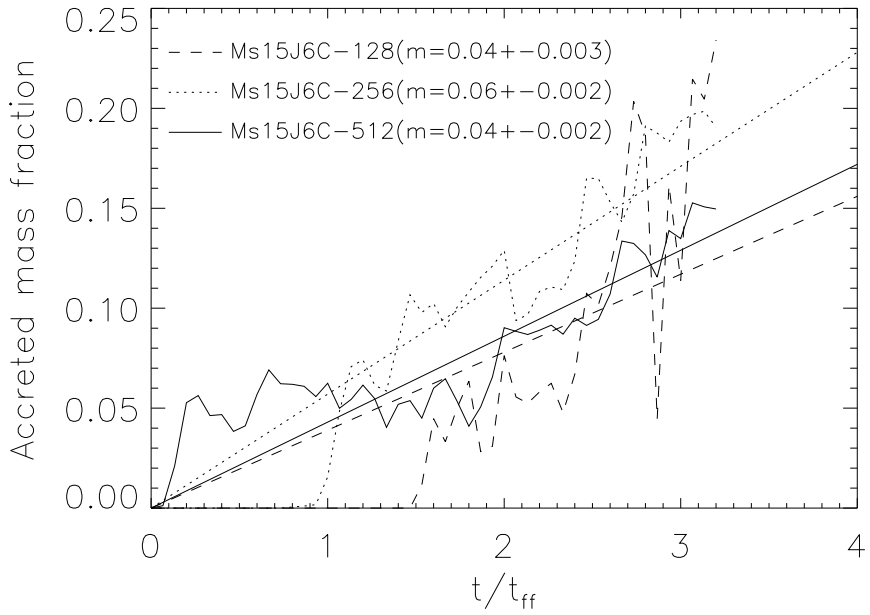

Figura 6.12: Fraction of mass accreted into collapsed objects as function of time in units of the free-fall time $t_{\rm ff}$ for the compressive-forcing simulations Ms15J6C-128, Ms15J6C-256, and Ms15J6C-512. The straight lines show least-squares fits to the accretion histories, with the indicated fitted slopes.

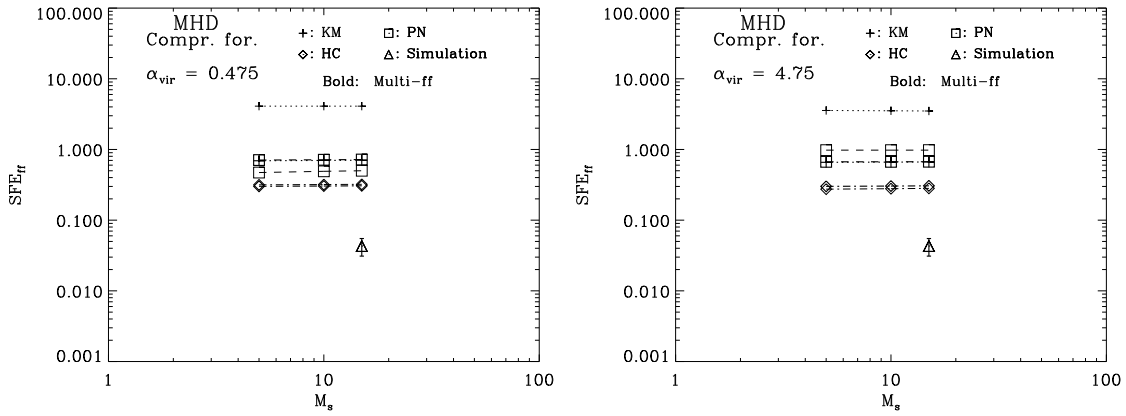

Figura 6.13: *Left-hand panel:* $\mathrm{SFE_{ff}}$ for the various models assuming a fully compressible forcing ($b = 1$) and $\alpha = 0.475$, and the $\mathrm{SFE_{ff}}$ for run Ms15J6C-512, with its associated 3σ uncertainty. *Right-hand panel:* same as the middle panel, but with the model predictions calculated assuming $\alpha = 4.75$.

Within this context, our three simulations, with their successively smaller physical scales, larger mean densities, and respective forcings applied at the largest scales available within each one, are intended to represent a hierarchy of nested turbulent density fluctuations. However, as already pointed out in Paper I, the equivalence between each run and a turbulent density fluctuation of the same size within a larger scale run is not perfect. While in each simulation the driving produces a zero net velocity divergence, Fig. 6.4 shows that this is not the case in high-density regions within run Ms15J6 that have the same size as run Ms5J2, as those regions tend to have, on average, a net velocity convergence. The same situation was encountered in Paper I. Moreover, it has recently been argued that the motions in numerical simulations of molecular cloud formation, even in the presence of stellar feedback, are dominated by hierarchical gravitational contraction (i.e. of collapses within collapses; Hoyle 1953; Field, Blackman & Keto 2008; Vázquez-Semadeni et al. 2009), rather than by random, isotropic turbulence, again suggesting that the motions in the clouds are not equivalent to the random, supersonic turbulent we use in the present simulations, in spite of it being a standard procedure (for a recent example, see Federrath & Klessen 2012b). Moreover, there have been suggestions that this kind of simulations may produce cores that are systematically more dynamic than observed (André, Basu & Inutsuka 2009). In a future study, we plan to search for such structures in numerical simulations of hierarchical, chaotic gravitational contraction and fragmentation (e.g., Vázquez-Semadeni et al. 2007, 2011; Heitsch & Hartmann 2008; Hennebelle et al. 2008; Banerjee et al. 2009; Heitsch, Ballesteros-Paredes & Hartmann 2009; Clark et al. 2012).

The star formation efficiency per free-fall time

The values of the $\mathrm{SFE_{ff}}$ obtained in Sec. 6.5.3, including the absence of collapse in run Ms5J2, can be compared with the non-magnetic results from Paper I. The values of $\mathrm{SFE_{ff}}$ we obtained, of 0.002 for run Ms10J4 and of 0.034 for Ms15J6, are significantly smaller than those obtained for the corresponding runs in Paper I for the non-magnetic case, which were ~ 0.11 and ~ 0.12, respectively. The $\mathrm{SFE_{ff}}$ for the present simulations, as well as for the non-magnetic runs from Paper I, are plotted as a function of M_{s} in both panels of Fig. 6.7.

The strong reduction in the $\mathrm{SFE_{ff}}$ observed in the magnetic runs indicates that the presence of a moderately supercritical magnetic field is able to strongly reduce the $\mathrm{SFE_{ff}}$ when the magneto-thermal Jeans parameter (cf. Sec. 6.5.4) is sufficiently small, in agreement with previous results (e.g., Passot, Vazquez-Semadeni & Pouquet 1995; Ostriker, Gammie & Stone 1999; Vázquez-Semadeni et al. 2005; Nakamura & Li 2005; Price & Bate 2008; Federrath & Klessen 2012b, 2013). The most dramatic difference occurs in the case of run Ms5J2, which in the magnetic case did not produce any collapse, at least for over four free-fall times (cf. Fig. 6.8). Instead, the corresponding non-magnetic run from Paper I had in fact the largest $\mathrm{SFE_{ff}}$ of all runs in that paper. This implies that the *combined* thermal and magnetic support must be considered in order to determine the stability of a region since, as mentioned in Sec. 6.5.4, run M5J2 is diagnosed to be unstable by either the Jeans or the mass-to-flux criteria taken separately.

The $\mathrm{SFE_{ff}}$ of our simulations can also be compared to the predictions from the theories by KM05, PN11, and HC11. A useful summary of the predictions from these theories, as well as simple extensions to the magnetic case, has been recently given by FK12. Specifically, the expressions for $\mathrm{SFE_{ff}}$ as a function of the virial parameter α, the rms Mach number, M_{s}, the *plasma beta*, β, and the *forcing parameter*, b (which parametrizes the relative strength of compressible and solenoidal forcing) according to the three theories and to the multi-free-fall variant of each one, are given in Table 1 and equations 4, 31, and 39 of FK12. The assumed values of various parameters are described in sec. 2.5 of that paper, and we use the best-fitting values given in their table 3.

Some other parameters are characteristic of our simulations. Specifically, we use the nominal values of M_{s} and β for each run as indicated in our Table 6.1, while, as explained in Sec. 6.4.2, all of our runs have a nominal value of $\alpha \approx 0.475$. Finally, since our main simulations use purely solenoidal forcing, we take $b = 1/3$ (Federrath, Klessen & Schmidt 2008b). It is important to note that FK12 warn that their proposed extension of the six theories to the magnetic case is applicable only for super-Alvénic flows, with $M_{\mathrm{A}} \gtrsim 2$. Since our simulations all have $M_{\mathrm{A}} \approx 1$, they are slightly outside of the applicability range, and thus, moderate deviations are to be expected.

The predictions from all three theories, in both their original and 'multi-free-fall' modes (a total of six theoretical models), according to the expressions provided by FK12, are also plotted in Fig. 6.7, together with the values of the $\mathrm{SFE_{ff}}$ derived from the simulations (cf. Sec. 6.5.3). The *left panel-hand* shows the results for the six theories in the non-magnetic

(or 'hydro') case ($\beta \to \infty$) and for the simulations from Paper I, while the *right-hand panel* shows the magnetic (or MHD) case, for the values of β corresponding to our runs (Table 6.1). It is seen that, in general, both the magnitude of the $\mathrm{SFE_{ff}}$ and its trend with M_s is missed by the theoretical predictions. In the non-magnetic case, only the HC11 theory, in both its original and multi-free-fall forms, matches the magnitude of the simulation $\mathrm{SFE_{ff}}$ for $M_\mathrm{s} = 5$, but not for $M_\mathrm{s} = 10$ and 15, since it predicts an increasing trend with M_s, while the simulations exhibit a globally decreasing trend. This trend is only predicted by the original KM05 theory which, however, is off in magnitude by nearly an order of magnitude. All other theories, including the multi-free-fall KM05 one, exhibit increasing trends with M_s.

In the magnetic case, we see that none of the theories, as modified by FK12 to include magnetic pressure, match the results from the simulations, neither in absolute magnitude of the $\mathrm{SFE_{ff}}$ nor in the trend with M_s. In particular, while our simulations show a strong trend towards collapse suppression at lower M_s with fixed α, the theoretical models all tend to remain at roughly constant $\mathrm{SFE_{ff}}$. This suggests that the procedure used by FK12 to include the magnetic field, consisting in simply substituting the sound speed by the sum in quadrature of the sound and the Alfvén speeds to determine the width of the density PDF and the effective Jeans length, does not capture the effect of the decrease of J_eff at low M_s exhibited by our simulations.

This conclusion, however, cannot be considered as definitive since, as mentioned above, the Alvénic Mach number of our simulations, $M_\mathrm{A} \approx 1$, is slightly outside the range of applicability of the magnetically extended theories, as stated by FK12 ($M_\mathrm{A} \gtrsim 2$). However, it appears unlikely that a difference by a mere factor of 2 in the Alfvénic Mach number will change the behaviour in as drastic a manner as to go from complete collapse suppression to an independence of $\mathrm{SFE_{ff}}$ from M_s, as shown in the *right-hand panel* of Fig. 6.7. Moreover, note that the values we have chosen for our parameters attempt to mimic the values observed in real regions of the size scales represented by the simulations. If anything, it can be argued that the magnetic field strength is somewhat excessive in the case of the larger scale simulations (Ms10J4 and Ms15J6). However, the chosen magnetic field strength appears to be typical for a region of mean density $n_0 \sim 2000\mathrm{cm}^{-3}$ (see, e.g. Crutcher et al. 2010), as is the case of run Ms5J2. Therefore, run Ms5J2 may be representative of real regions with the same physical conditions, even if it does not fall on the range of the applicability of the magnetically extended theories. In any case, further testing appears necessary in order to more precisely attest the accuracy of the theoretical models and their range of applicability.

6.6.2. Implications

Our results have important implications for our understanding of the role of turbulence in the support of, and regulation of SF in, molecular clouds. Our simulations have been set up to represent clouds obeying Larson's (1981) linewidth–size and density–size scaling relations, so that all three of them have the same value of the virial parameter α, and with the kinetic energy corresponding mostly to turbulent motions that counteract the cloud's self

gravity. For such a sequence of clouds, Krumholz & Tan (2007b) have argued that, for a variety of molecular objects, the $\mathrm{SFE_{ff}}$ is approximately constant, at a value $\mathrm{SFE_{ff}} \sim 2\,\%$, independently of density, and thus, for clouds obeying both of equations (6.1) and (6.2), independently of Mach number as well. Note, however, that this conclusion by Krumholz & Tan (2007b) is inconsistent with equation 30 of KM05, which is a fit to the numerical results from their theory and predicts, at constant α, a scaling $\mathrm{SFE_{ff}} \propto M_{\mathrm{s}}^{-0.32}$, as also pointed out in section 3.2 of Elmegreen (2007).

In Paper I, we showed that our non-magnetic simulations were marginally consistent, within their uncertainties, with the $\mathrm{SFE_{ff}} \sim M_{\mathrm{s}}^{-0.32}$ dependence given by KM05. However, our magnetic simulations from this paper suggest that this dependence is strongly modified upon the introduction of a constant magnetic field strength, and in a way that does not agree with KM12's extension of the KM05 theory to the magnetic case, nor with the other two theories, in neither of their variants. This disagreement may be attributed to the fact that the Alfvénic Mach number of our simulations (≈ 1 in all three runs) does not fall in the range where the extension to the magnetic case proposed by FK12 applies. On the other hand, since the required increment in our values of M_{A} to fall in the applicability range is of only a factor of a few, it does not appear likely that the drastic observed discrepancy can be attributed to this.

6.7. Summary and conclusions

In this paper, we have presented numerical simulations of randomly driven, supersonic, magnetized, and isothermal turbulent flows, commonly believed to represent the flow within molecular clouds. Our simulations are the magnetized counterparts of the simulations presented in Paper I, and have allowed us, among other things, to determine whether, and to what extent, the conclusions reached in that paper extend to the magnetized case. Our main conclusions are as follows.

- We have used numerical simulations of continuously driven, isothermal turbulence as a sort of 'reductio ad absurdum' test of these hypotheses, showing that they lead to results that are inconsistent with the hypotheses. In particular, using random turbulent driving in a box causes the clumps to have a non-random flow, but rather having a net convergent component, so that the clumps cannot be modelled by a simple rescaled box with random driving.

- As in Paper I, we do not find any simultaneously subsonic and super-Jeans structures (neither regular subboxes of the numerical box nor dense clumps) in our simulations. In Paper I, we argued that perhaps our failure there to find such structures was due to the neglect of the magnetic field there, but the fact that we do not find them even in the magnetized case strongly suggests that they form only very rarely, if at all, in the kind of flows that we have simulated here, i.e., continuously and randomly driven, strongly supersonic, isothermal turbulent flow. On the other hand, since such

structures are routinely observed in real molecular clouds (see, e.g. Goodman et al. 1998; Caselli et al. 2002; André, Basu & Inutsuka 2009), our result suggests that this type of flow may not be representative of the flow within molecular clouds. A viable alternative is the type of hierarchical, chaotic gravitational fragmentation, consisting of collapses within collapses, and seeded by turbulence, that has been discussed in other studies (e.g. Clark & Bonnell 2005; Vázquez-Semadeni et al. 2009; Heitsch, Ballesteros-Paredes & Hartmann 2009; Ballesteros-Paredes et al. 2011a), to which we plan to apply the same tests in a future study. Another viable alternative is that, rather than being isothermal, the flow in MCs may be thermally bistable, containing a mixture of atomic and molecular gas that may aid in the formation of these structures.

- Also as in Paper I, we have found that the turbulent density enhancements ('clumps') tend to have a net negative velocity divergence, although the typical magnitude of the convergence at a given overdensity is decreased with respect to the non-magnetic case. Nevertheless, the fact that this result persists indicates that a turbulent box with totally random turbulent velocity field (thus with a zero mean divergence) is not an exact match for the type of flow that develops inside the clumps, which contain a non-zero net velocity convergence.

  A crucial implication of the presence of a net convergent component in the non-thermal motion within the clumps is that the energy contained in these motions is not available for support against gravity, a fact which needs to be accounted for in theories relying on this support.

- Contrary to its non-magnetic counterpart in Paper I, which had the highest $\mathrm{SFE_{ff}}$, run Ms5J2 did not produce any collapsing objects over more than four global free-fall times. We attributed this result to the fact that this run had the lowest value of the magneto-thermal Jeans parameter, J_{eff}, among our simulations. Instead, run Ms15J6, which only had a value $J_{\mathrm{eff}} \sim 12\,\%$ larger than run Ms5J2, did not exhibit any delay in its development of collapsing regions compared to the non-magnetic case. Therefore, it appears that the transition from total to non-existent inhibition of the collapse is a very sharp function of this parameter. Of course, we cannot rule out the possibility that collapse will occur in run Ms5J2 after a sufficiently long time, but in any case, it can be concluded that the inhibition of gravitational collapse by the combined effect of thermal pressure and the magnetic field for this run is very strong.

- We compared the dependence of the $\mathrm{SFE_{ff}}$ in our simulations (measured as the slope of the collapsed mass versus time in units of the free-fall time) on the turbulent Mach number M_{s} against the predictions of the theories by KM05, PN11, and HC11, in both their original form, and as modified by FK12 to include the magnetic pressure (thus forming a set of six theoretical models in total). We compared our results against the analytic expressions provided by FK12 for each of the six models, finding that in general they fail to reproduce both the absolute magnitudes of the $\mathrm{SFE_{ff}}$

we obtain, as well as the trend with $M_{\rm s}$, in both the magnetic and non-magnetic cases. In particular, the suppression of collapse in run Ms5J2 is missed by all magnetic models.

- The failure of the theories in the magnetic case may be explained because the Alvénic Mach number of our simulations, $M_{\rm A} \approx 1$, is too small by at least a factor of 2 to fall in the range where FK12 suggest their implementation of the effects of the magnetic field into the theories should apply. However, since the discrepancy between the predictions of the theories and the results of our simulations are large even at the qualitative level (complete suppression of collapse in the smallest, densest simulation), it is possible that the failure is an indication of a deeper problem with the theories.

- We suggest instead that the observed discrepancies in the magnitude of $\mathrm{SFE_{ff}}$ and its dependence on $M_{\rm s}$ originate from the fact that the assumptions of the theories are not verified in the flow realized in the simulations. First, the velocity field in subregions of the simulation is not a scaled-down version of the flow implemented in the simulations as a whole: while the latter is a fully random turbulent flow with zero net convergence, in subregions of the numerical boxes, the flow naturally develops, on average, a globally converging topology. This contradicts the assumption in the HC11 theory that, at each scale, turbulence provides additional support against collapse, since the converging component of the flow we have observed implies that at least a fraction of the kinetic energy *collaborates* with the collapse, rather than impeding it. Secondly, the KM05 and PN11 theories assume that the collapsing objects are clumps that are simultaneously subsonic and super-Jeans, while our simulations suggest that this is not the dominant collapse mechanism.

In conclusion, our results seem to cast doubt on the premises of the current SF theories and on simulations of randomly driven turbulence as accurate representations of the physical conditions in molecular clouds and their clumps. The fact that the motions in the clumps have a net convergent nature implies that, far from providing support against gravity, they will collaborate with it. Of course, as noted in Paper I, our analysis cannot discriminate between the convergent motions being produced by turbulence or gravity, and in reality it is likely that both agents contribute. In the near future, we plan to apply similar tests to a different kind of flow, suggested by numerical simulations of the formation and evolution of entire giant molecular clouds, in which the regime that develops seems to be dominated by gravity at all scales, and evolves through hierarchical, chaotic gravitational fragmentation.

Acknowledgements

We are glad to acknowledge fruitful discussions with Christoph Federrath. AG-S was supported in part by CONACyT grant 102488 to EV-S. RFG acknowledges support from

grants PAPPIT IN117708 and IN100511-2. The numerical simulations were performed on the cluster KanBalam of DGTIC at UNAM, and the high-performance computing cluster, POLARIS, at the Korea Astronomy and Space Science Institute.

Appendix: On the calculation of the virial parameter α

Instead of the estimator given by equation (6.13), which is based on global flow parameters, FK12 have advocated using an estimator computed from the full computational domain, given by

$$\alpha = \frac{\sum_i M_i v_i^2}{\left| \sum_i M_i \phi_i \right|}, \tag{6.16}$$

where M_i is the mass of the ith cell, v_i is the magnitude of the flow velocity in that cell, and ϕ_i is the gravitational potential there. FK12 argue that, because the flow develops highly inhomogeneous, irregularly shaped, and fractal-like density structures, this estimator better represents the potential generated by the actual density distribution.

However, some additional considerations are important as well. First is the issue that in a periodic box, the Poisson equation is actually computed as (see, e.g., Weinberg 1972; Peebles 1980; Alecian & Leorat 1988)

$$\nabla^2 \phi = 4\pi G(\rho - \rho_0), \tag{6.17}$$

in order to avoid the well-known Jeans' swindle; that is, the fact that the underlying equilibrium state in the Jeans gravitational instability analysis is only truly self-consistent when the mean density is zero. Equation (6.17) means that, in the simulations, the gravitational potential arises from the distribution of density *fluctuations*, rather than from the full density distribution.

In practice, this means that, in the simulation, underdense regions are characterized by positive values of the gravitational potential. In turn, this will cause the total sum of the gravitational term to be decreased, in fact explaining why FK12 obtained values of α up to an order of magnitude larger than that obtained with the global parameters. This is correct with respect to the simulations, although it reminds us that the large-scale gravitational potential in the simulations is somewhat unrealistic, especially if the simulation intends to represent an entire cloud. Its accuracy increases if the modelled region is intended to represent a small fraction of a much larger volume at the same mean density, as is the case, for example, of simulations of cloud *formation* within a much larger volume (e.g., Vázquez-Semadeni et al. 2007).

Secondly, the larger values of α obtained with the estimator (6.16) seem to accomplish the opposite result of FK12's motivation to use it in the first place: the presence of large

local density enhancements should result in a more tightly bound medium, which would in turn result in *smaller* values of α, contrary to the larger values obtained from the estimator.

Moreover, in order to fully capture the binding of the local, dense structures, the local α parameter should be computed by taking the velocities referred to the local centres of mass of the clumps. In other words, if the intention of an α estimator is to reasonably represent local excursions to low values of α, it must take into account not just the local value of the gravitational energy (the denominator), but also the local value of the kinetic energy (the numerator). But this must be done by removing the bulk velocity of a local density enhancement, a consideration that is not included in the estimator (6.16), and which in practice is very difficult to accomplish, because the average bulk velocity to subtract depends on the size scale of the clump.

The fact that FK12 tended to find *larger*, rather than smaller values of the α parameter when computing it directly from the simulation means that it was dominated by the effect of the modified Poisson equation, rather than by the presence of strong local density enhancements. Nevertheless, this is indeed more representative of the actual gravitational potential in the simulations, due to the modified form of the Poisson equation.

As a compromise, in the body of the paper, we compute the α parameter from the global parameters, but also show the predictions from the models when α is multiplied by a factor of 10, which is the maximum typical enhancement found by FK12, in order to obtain an estimate of the modification that can be expected to occur in the model predictions due to the computation of α directly from the simulations. In general, we find that the modifications are very small.

Capítulo 7

Conclusiones generales

La presente tesis doctoral estuvo enmarcada en el estudio de diferentes aspectos de la formación y evolución de galaxias, en particular las de masas menores a 10^{10} $M_\odot$ en estrellas al día de hoy, así como de ingredientes claves de estos procesos, en particular el de la formación estelar (FE) a pequeñas escalas. El contexto global para el estudio de la formación y evolución de galaxias lo provee el así llamado modelo cosmológico ΛCDM, mismo que se usó a lo largo de esta tesis. No obstante, se presentaron también los resultados recientes logrados por nuestro grupo con simulaciones numéricas de galaxias enanas en el modelo ΛWDM; esto último debido a que, como lo mostramos en varias partes de la tesis, la cosmología ΛCDM podría enfrentar ciertas controversias a pequeñas escalas, al menos cuando se usa la "gastrofísica" (sub-malla) estándard. A lo largo de la tesis se han seguido distintas estrategias para estudiar el cómo se forman y evolucionan las galaxias, ya sea a través de un modelo paramétrico semi-empírico, el cual nos permitió una visión global y unificada, así como de (re)simulaciones de N-cuerpos/hidrodinámica de alta resolución de galaxias de baja masa. Por otra parte, hemos utilizado simulaciones magneto-hidrodinámicas para estudiar las propiedades físicas del medio interestelar que determinan el proceso de FE en nubes moleculares.

Las conclusiones principales de los diferentes trabajos realizados en esta tesis se encuentran al final de cada Capítulo. De ellas extraemos algunas de las principales lecciones que hemos aprendido y que responden a varias de las preguntas formuladas en la Introducción.

• El modelo paramétrico presentado en el Capítulo 2, una vez constreñido con un enorme cuerpo de "observables", evidenció con claridad el comportamiento promedio de las galaxias conectadas a sus halos de ΛCDM: mientras que las galaxias formadas en halos de masas actuales $M_{\rm v} \approx 2-3\times10^{12}$ $M_\odot$ (masas estelares actuales $M_s = 5-8\times10^{10}$ $M_\odot$) tienen historias de crecimiento de M_s cercanas a las de sus halos, las galaxias más y menos masivas desvían sistematicamente su ensamblaje estelar del oscuro. Mientras más masivas, más temprano se estanca el crecimiento de M_s, en particular por FE in situ (se apagan) mientras que mayor es el crecimiento tardío de $M_{\rm v}$ ("downsizing" arqueológico). Al con-

trario, en las galaxias menos masivas, el ensamblaje promedio de sus halos se estanca más temprano mientras menos masivo es, mientras que el ensamblaje estelar se "activa" más tardíamente, de tal modo que a menor masa hoy, mayor es la tasa de FE específica ("downsizing" en TFEE), al menos hasta masas actuales $M_s \sim 10^8$ $\mathrm{M}_\odot$. Estos comportamientos se deben a que la eficiencia de FE (G_{SFE}=TFE/$\dot{M}_b$) en los halos cambia drásticamente con la masa y el tiempo hacia masas grandes y pequeñas. Son los halos de masas $\sim 10^{12}$ $\mathrm{M}_\odot$ actualmente los que la mayor parte de su historia tienen altas eficiencias, mientras que halos muy masivos, bajan sus eficiencias drásticamente a medida que crecen; al contrario, halos poco masivos, tiene eficiencias muy bajas en el pasado y sólo recientemente se van "activando", más tardíamente mientras más pequeños son. A nivel de la densidad de tasa de FE global (por unidad de volumen comóvil) sorprendentemente encontramos que las galaxias de $M_s \approx 1 - 3 \times 10^{10}$ $\mathrm{M}_\odot$ (halos de $M_s \approx 3 - 10 \times 10^{11}$ $\mathrm{M}_\odot$) son las que más contribuyen a todas las épocas estudiadas (hasta $z \sim 5$).

Los resultados semi-empíricos obtenidos en el Capítulo 2 plantean la pregunta acerca de qué procesos astrofísicos, dependientes de M_{v} y la época, son capaces de producir el comportamiento de la eficiencia de FE descrito. En particular, estudiamos el rol que puede jugar la fase de encendido de cuásar en los halos masivos. Nuestro estudio nos muestra que se ve favorecida la propuesta de que es la retroalimentación del cuasar el que puede producir el apagado de las galaxias, las más masivas más temprano. Por otro lado, vimos que las historias de FE individuales (promedio) inferidas pueden ser descritas por el modelo usual τ (crecimiento y declinación exponencial posterior) para las galaxias masivas y de masas intermedias. No obstante, galaxias al día de hoy menos masivas que $M_s \sim 10^{10}$ $\mathrm{M}_\odot$ tienen historias crecientes todo el tiempo, más pronunciadas mientras menor es la masa. Los modelos τ no aplican para ellas. La gran pregunta es ¿Qué puede producir el "retraso" de sus historias de FE? ¿Qué predicen las simulaciones cosmológicas de N-cuerpos/hidrodinámica con la gastrofísica sub-malla estándar? ¿Estarían de acuerdo con el comportamiento de "downsizing" en TFE inferido semi-empíricamente con nuestro modelo? ¿Cómo es la historia de FE de las galaxias poco masivas?

• Los Capítulos 3 y 4 se abocaron a explorar las preguntas arriba formuladas, usando para ello simulaciones cosmológicas de muy alta resolución para galaxias de baja masa en el escenario cosmológico ΛCDM. Los principales resultados fueron:

- Se encontró que las simulaciones numéricas de alta resolución de galaxias tienen problemas en reproducir el "downsizing" de la TFEE que caracteriza de manera importante a las galaxias de baja masa, y el ensamblaje de masa estelar retrasado que se infiere del enfoque semi-empírico.

- Nuestras simulaciones numéricas de muy alta resolución confirman los problemas previamente encontrados con modelos semi-numéricos de evolución de galaxias de disco en el contexto del escenario ΛCDM: *en promedio, las galaxias de baja masa parecen ensamblar el grueso de su masa estelar mucho más temprano que lo que sugieren las inferencias observacionales y semi-empíricas vía las relaciones TFEE–M_s y M_s–M_{v} a corrimientos al rojo $z < 1$.*

- Con simulaciones numéricas que incluían una mejor implementación para emular las propiedades del medio interestelar, y que implicaban un "feedback" efectivo muy potente, se pudo reproducir un "downsizing" moderado, pero no lo suficientemente fuerte como para explicar las inferencias empíricas y semi-empíricas.

- A pesar de que un "feedback" eyectivo potente (aún sin comprobarse observacionalmente) ayuda a desviar el ensamblaje de masa de las galaxias del respectivo ensamblaje del halo en el que viven, encontramos que no se puede invocar efectos aún mayores; en nuestras simulaciones la cantidad de bariones dentro del radio virial está en acuerdo con las respectivas inferencias semi-empíricas, así como las fracciones de gas de las galaxias simuladas reproducen las observaciones. Un feedback eyectivo produciría menos masa estelar pero también fracciones bariónicas (y de gas) demasiado pequeñas, en desacuerdo con las inferencias semi-empíricas y algunas observaciones directas.

- El ensamblaje de masa estelar de las galaxias enanas centrales sigue muy de cerca el ensamblaje de sus halos. Los bariones dentro del radio virial regularmente siguen el ensamblaje del halo pero existen períodos cuando los bariones se pierden debido a los vientos impulsados por SNs; como resultado, la fracción bariónica dentro de los halos, $F_b^{\rm v}$=$M_b^{\rm v}/M_{\rm v}$, sistemáticamente decrece con el tiempo, de valores 1.5–2 veces menores que la fracción bariónica universal a $z \sim 4$ a valores 2–6 más pequeños a $z = 0$.

- Las historias de ensamblaje del gas de las galaxias enanas son episódicas, con períodos de crecimiento y decrecimiento. Las enanas formadas en halos ensamblados tardíamente tienen mayores fracciones de gas, f_g=M_g/M_b, que aquellas formadas en halos ensamblados de manera temprana. Cuando la f_g galáctica decrece, se observa un incremento en la fracción de gas en el halo (esta gas es típicamente caliente, mientras que el gas en la galaxia es de manera dominate frío). Esto muestra que los fuertes vientos impulsados por la retroalimentación por SNs juegan un papel principal en regular el contenido de gas—y por lo tanto las SFR—de las galaxias enanas simuladas, al menos para aquellas en las cuales el correspondiente ensamblaje del halo ocurre de manera gradual. Sin embargo, también existen períodos, principalmente en los halos ensamblados tempranamente, cuando las fracciones de gas decrecen tanto en la galaxia como en el halo, ya que el gas es expulsado completamente del halo.

- Las historias de FE de las galaxias enanas simuladas son episódicas con variaciones promedio de la tasa de formación estelar (medidas cada 100 Myr) de factores de 2–10 con respecto al promedio, medido en períodos de cada 2 Gyr. Esto parece estar de acuerdo con resultados observacionales recientes (v.gr. Kauffmann 2014).

- El efecto de la física bariónica es capaz de reducir la masa virial total de los halos simulados en un 10 %–20 % con respecto al obtenido en las simulaciones de solo

N-cuerpos; este efecto se ve desde al menos $z \sim 2$. La diferencia es causada principalmente por la pérdida de bariones debida a los vientos causados por la retroalimentación de SNs.

- Como en el escenario jerárquico ΛCDM los halos de baja masa se ensamblan tempranamente, entonces se espera que las respectivas galaxias tengan un ensamblaje de masa estelar también temprano y pequeñas sSFRs a épocas tardías. Nuestras resultados muestran que las galaxias simuladas, aún aquellas que se forman en halos ensamblados tardíamente, tienen sSFRs y contenidos de gas más bajos que los observados en galaxias del mismo tamaño, así como masas estelares mayores para las masas de sus halos que las inferidas por relaciones semi-empíricas. Pero, las masas bariónicas de las galaxias enanas simuladas parecen estar de acuerdo con las inferencias semi-empíricas. Así que, más que incrementar aún más la magnitud de la retroalimentación (eyectiva) por SNs, para resolver los conflictos ya señalados de las simulaciones de galaxias de baja masa, se deben considerar otras alternativas que introduzcan procesos sub-malla que retrasen la transformación de gas atómico en gas molecular, y/o tomar en cuenta los efectos de una retroalimentación "preventiva" (producida por ejemplo, por presión de radiación de estrellas masivas y fotoionización local), lo cual reduciría la eficiencia de conversión de gas a estrellas en el pasado, dejando gas abundante para una FE tardía.

• En el Capítulo 5 se presentaron resultados de simulaciones de algunas de las galaxias enanas del Capítulo 4 (mismas masas de halo a $z = 0$) pero introduciendo un filtrado en el espectro de potencias a escalas que corresponden al de los objetos simulados y otra que corresponde a 20–30 veces las escalas de estos objetos. De esta manera exploramos cómo influye el cambiar de la cosmología ΛCDM a la ΛWDM en las propiedades y evolución de galaxias formadas en escalas cercanas al filtrado del espectro de potencias y en escalas ya 20-30 veces mayores a ese filtrado.

Encontramos que las galaxias a escalas del filtrado (que para nuestro caso corresponde a una masa de partícula térmica de 1.2 KeV) con relación a sus contrapartes ΛCDM: ensamblan sus masas de halo y estelar más tarde, teniendo edades estelares pesadas por masa entre 1.4 y 2.8 Gyr menores; tienen valores de $V_{\rm max}$ $20 - 60\,\%$ menores y curvas de rotación más suaves, así como distribuciones de estrellas mucho menos concentradas al centro y radios efectivos más grandes por factores 1.3–3. Por otro lado, las enanas formadas en halos al día de hoy 20-30 veces la masa de filtrado (que para nuestro caso corresponde a una masa de partícula térmica de 3.0 KeV) tiene propiedades y evolución ya muy similares a las de sus contrapartes ΛCDM. Si la masa de la partícula térmica queda restringida a valores > 3 KeV, sólo los halos menores al día de hoy que $\sim 2 \times 10^9$ $\mathrm{M}_\odot$ son afectados, lo cual implica que los efectos encontrados aquí de la cosmología ΛWDM sobre las galaxias afectarían a enanas de masas estelares menores de $\sim 10^7 - 10^6$ $\mathrm{M}_\odot$. Aunque las observaciones son escasas, preliminarmente se puede decir que estos efectos van en la dirección necesaria para lograr acuerdo con las mismas.

• En el Capítulo 6 se presentaron simulaciones numéricas magnetohidrodinámicas de flujos turbulentos supersónicos e isotérmicos con el objetivo de estudiar las hipótesis comúnmente usadas en las distintas teorías de formación estelar, así como algunas de sus predicciones. En particular, se estudió la eficiencia de la tasa de formación estelar en nubes moleculares y su comparación con las predicciones de las teorías actuales al respecto. Las principales conclusiones son:

- Hemos encontrado que usando turbulencia implementada aleatoriamente en una caja que trata de emular propiedades de las nubes moleculares, causa que los grumos dentro de ella no tengan un flujo aleatorio, sino más bien una componente convergente neta, de tal manera que los "grumos" no pueden ser modelados por una simple caja re-escalada que incluya un flujo aleatorio. Esto contradice la hipótesis en la teoría de HC11 que asume que, a cada escala, la turbulencia provee soporte adicional contra el colapso, ya que la componente convergente del flujo que hemos observado implica que al menos una fracción de la energía cinética *colabora* con el colapso, en lugar de impedirlo.

- En nuestras simulaciones magnetohidrodinámicas no encontramos estructuras que fueran al mismo tiempo subsónicas y super-Jeans. Esto nos sugiere que la formación de dichas estructuras es muy rara, sí es que se llegan a formar en el tipo de flujos que hemos simulado. Lo anterior contradice las teorías de KM05 y PN11 que asumen que los objetos colapsados son grumos que son simultáneamente subsónicos y super-Jeans. Por otro lado, como tales estructuras son comúnmente observadas en nubes moleculares reales (ver, e.g. Goodman et al. 1998; Caselli et al. 2002; André, Basu & Inutsuka 2009), nuestros resultados apuntan de nuevo a que este tipo de flujo no es representativo de los flujos dentro de las nubes moleculares.

- Así, encontramos que las hipótesis que comúnmente se hacen para explicar el proceso de formación estelar en nubes moleculares, tales como que los movimientos no-térmicos observados en las NMs constituyen turbulencia isótropica que globalmente produce una presión que se opone al colapso de subestructuras, no se verifican en simulaciones magneto-hidrodinámicas diseñadas para ese fin.

- En general, nuestros resultados de la formación estelar en nubes moleculares sugieren que *un flujo isotérmico y continuamente turbulento no representa correctamente el flujo del medio en las NMs reales, y que las teorías que asumen este régimen estarán perdiendo un aspecto fundamental de las propiedades del MIE. Finalmente, sugerimos que un escenario más realista puede ser el del colapso gravitacional jerárquico, que ha sido discutido en otros estudios (e.g. Clark & Bonnell 2005; Vázquez-Semadeni et al. 2009; Heitsch, Ballesteros-Paredes & Hartmann 2009; Ballesteros-Paredes et al. 2011a).*

Es estimulante darnos cuenta de los grandes progresos que ha habido en el estudio de la formación y evolución de galaxias en años recientes. Sin embargo, *los resultados de*

la investigación doctoral presentados aquí nos señalan que existen varios preguntas aún por responder en esta área, en particular, por lo que respecta a galaxias de baja masa. El poder responderlas no parece ser una empresa fácil de lograr, sin embargo, esto en sí mismo representa un reto para trabajos futuros y nos plantea objetivos muy definidos por alcanzar. Poner restricciones claras al papel que juega el feedback asociado a distintos procesos astrofísicos en el ensamblaje de masa de las galaxias de baja masa es uno de estos objetivos. Caracterizar de manera robusta en que momento, cómo, y porqué se desvía el ensamblaje de masa de las galaxias del respectivo de los halos en los que viven es otro de las áreas de trabajo en lo inmediato. Sin duda, las simulaciones numéricas de alta resolución serán la herramienta básica para tales estudios; así, caracterizar el grado de realismo a detalle de las galaxias simuladas vía su comparación con las observaciones es un trabajo que queda aún por hacer y en el cual estamos ya trabajando. Solo a partir de esto es que podremos avanzar en la consecución de dichos objetivos.

Bibliografía

Abazajian K., Fuller G. M., Patel M., 2001, Phys. Rev. D, 64, 023501

Agertz O., Kravtsov A. V., Leitner S. N., Gnedin N. Y., 2013, ApJ, 770, 25

Agertz O., Teyssier R., Moore B., 2011, MNRAS, 410, 1391

Alecian G., Leorat J., 1988, A&A, 196, 1

Anderhalden D., Schneider A., Macciò A. V., Diemand J., Bertone G., 2013, J. Cosmology Astropart. Phys., 3, 14

André P., Basu S., Inutsuka S., 2009, The formation and evolution of prestellar cores, Chabrier G., ed., Cambridge University Press, p. 254

Angulo R. E., Hahn O., Abel T., 2013, MNRAS, 434, 3337

Avila-Reese V., 2006, ArXiv Astrophysics e-prints

Avila-Reese V., Colín P., González-Samaniego A., Valenzuela O., Firmani C., Velázquez H., Ceverino D., 2011a, ApJ, 736, 134

Avila-Reese V., Colín P., González-Samaniego A., Valenzuela O., Firmani C., Velázquez H., Ceverino D., 2011b, ApJ, 736, 134

Avila-Reese V., Colín P., Piccinelli G., Firmani C., 2003, ApJ, 598, 36

Avila-Reese V., Colín P., Valenzuela O., D'Onghia E., Firmani C., 2001, ApJ, 559, 516

Avila-Reese V., Firmani C., Hernández X., 1998, ApJ, 505, 37

Avila-Reese V., Zavala J., Firmani C., Hernández-Toledo H. M., 2008, AJ, 136, 1340

Baldry I. K., Glazebrook K., Brinkmann J., Ivezić Ž., Lupton R. H., Nichol R. C., Szalay A. S., 2004, ApJ, 600, 681

Baldry I. K., Glazebrook K., Driver S. P., 2008, MNRAS, 388, 945

Ballesteros-Paredes J., Hartmann L. W., Vázquez-Semadeni E., Heitsch F., Zamora-Avilés M. A., 2011a, MNRAS, 411, 65

Ballesteros-Paredes J., Klessen R. S., Vázquez-Semadeni E., 2003, ApJ, 592, 188

Ballesteros-Paredes J., Vázquez-Semadeni E., Gazol A., Hartmann L. W., Heitsch F., Colín P., 2011b, MNRAS, 416, 1436

Banerjee R., Vázquez-Semadeni E., Hennebelle P., Klessen R. S., 2009, MNRAS, 398, 1082

Barker M. K., Ferguson A. M. N., Irwin M. J., Arimoto N., Jablonka P., 2012, MNRAS, 419, 1489

Bauer A. E., Conselice C. J., Pérez-González P. G., Grützbauch R., Bluck A. F. L., Buitrago F., Mortlock A., 2011, MNRAS, 417, 289

Bauer A. E., Drory N., Hill G. J., Feulner G., 2005, ApJ, 621, L89

Bauer A. E. et al., 2013, MNRAS, 434, 209

Behroozi P. S., Conroy C., Wechsler R. H., 2010, ApJ, 717, 379

Behroozi P. S., Wechsler R. H., Conroy C., 2013a, ApJ, 762, L31

Behroozi P. S., Wechsler R. H., Conroy C., 2013b, ApJ, 770, 57

Behroozi P. S., Wechsler R. H., Wu H.-Y., Busha M. T., Klypin A. A., Primack J. R., 2013, ApJ, 763, 18

Bell E. F., McIntosh D. H., Katz N., Weinberg M. D., 2003a, ApJ, 585, L117

Bell E. F., McIntosh D. H., Katz N., Weinberg M. D., 2003b, ApJS, 149, 289

Bell E. F., Zheng X. Z., Papovich C., Borch A., Wolf C., Meisenheimer K., 2007, ApJ, 663, 834

Benson A. J., Bower R. G., Frenk C. S., Lacey C. G., Baugh C. M., Cole S., 2003, ApJ, 599, 38

Benson A. J. et al., 2013, MNRAS, 428, 1774

Bernard E. J., Ferguson A. M. N., Barker M. K., Irwin M. J., Jablonka P., Arimoto N., 2012, MNRAS, 426, 3490

Bernardi M., Meert A., Sheth R. K., Vikram V., Huertas-Company M., Mei S., Shankar F., 2013, MNRAS, 436, 697

Bertoldi F., McKee C. F., 1992, ApJ, 395, 140

Blanton M. R., Lupton R. H., Schlegel D. J., Strauss M. A., Brinkmann J., Fukugita M., Loveday J., 2005a, ApJ, 631, 208

Blanton M. R. et al., 2005b, AJ, 129, 2562

Blitz L., 1993, in Protostars and Planets III, Levy E. H., Lunine J. I., eds., pp. 125–161

Bluck A. F. L., Conselice C. J., Buitrago F., Grützbauch R., Hoyos C., Mortlock A., Bauer A. E., 2012, ApJ, 747, 34

Bode P., Ostriker J. P., Turok N., 2001, ApJ, 556, 93

Bonazzola S., Heyvaerts J., Falgarone E., Perault M., Puget J. L., 1987, A&A, 172, 293

Borch A. et al., 2006, A&A, 453, 869

Bouché N. et al., 2010a, ApJ, 718, 1001

Bouché N. et al., 2010b, ApJ, 718, 1001

Bower R. G., Benson A. J., Malbon R., Helly J. C., Frenk C. S., Baugh C. M., Cole S., Lacey C. G., 2006, MNRAS, 370, 645

Bower R. G., Vernon I., Goldstein M., Benson A. J., Lacey C. G., Baugh C. M., Cole S., Frenk C. S., 2010, MNRAS, 407, 2017

Boyarsky A., Ruchayskiy O., Shaposhnikov M., 2009, Annual Review of Nuclear and Particle Science, 59, 191

Boylan-Kolchin M., Springel V., White S. D. M., Jenkins A., 2010, MNRAS, 406, 896

Brook C. B., Stinson G., Gibson B. K., Wadsley J., Quinn T., 2012, MNRAS, 424, 1275

Brunt C. M., 2003, ApJ, 584, 293

Brunt C. M., Heyer M. H., Mac Low M.-M., 2009, A&A, 504, 883

Bruzual G., 2007, in Astronomical Society of the Pacific Conference Series, Vol. 374, From Stars to Galaxies: Building the Pieces to Build Up the Universe, A. Vallenari, R. Tantalo, L. Portinari, & A. Moretti, ed., pp. 303–+

Bruzual G., Charlot S., 2003, MNRAS, 344, 1000

Bryan G. L., Norman M. L., 1997, in Astronomical Society of the Pacific Conference Series, Vol. 123, Computational Astrophysics; 12th Kingston Meeting on Theoretical Astrophysics, Clarke D. A., West M. J., eds., p. 363

Bryan S. E., Kay S. T., Duffy A. R., Schaye J., Dalla Vecchia C., Booth C. M., 2013, MNRAS, 429, 3316

Bullock J. S., Dekel A., Kolatt T. S., Kravtsov A. V., Klypin A. A., Porciani C., Primack J. R., 2001, ApJ, 555, 240

Bundy K. et al., 2006, ApJ, 651, 120

Bundy K., Fukugita M., Ellis R. S., Targett T. A., Belli S., Kodama T., 2009, ApJ, 697, 1369

Cano-Díaz M., Maiolino R., Marconi A., Netzer H., Shemmer O., Cresci G., 2012, A&A, 537, L8

Caselli P., Myers P. C., 1995, ApJ, 446, 665

Caselli P., Walmsley C. M., Zucconi A., Tafalla M., Dore L., Myers P. C., 2002, ApJ, 565, 331

Ceverino D., Klypin A., Klimek E., Trujillo-Gomez S., Churchill C. W., Primack J., Dekel A., 2013, ArXiv e-prints

Chabrier G., 2003, PASP, 115, 763

Chandrasekhar S., 1951, Royal Society of London Proceedings Series A, 210, 26

Chen Y.-M., Wild V., Kauffmann G., Blaizot J., Davis M., Noeske K., Wang J.-M., Willmer C., 2009, MNRAS, 393, 406

Christensen C., Quinn T., Governato F., Stilp A., Shen S., Wadsley J., 2012, MNRAS, 425, 3058

Cicone C. et al., 2014, A&A, 562, A21

Cimatti A., Daddi E., Renzini A., 2006, A&A, 453, L29

Clark P. C., Bonnell I. A., 2005, MNRAS, 361, 2

Clark P. C., Glover S. C. O., Klessen R. S., Bonnell I. A., 2012, MNRAS, 424, 2599

Cloet-Osselaer A., De Rijcke S., Vandenbroucke B., Schroyen J., Koleva M., Verbeke R., 2014, MNRAS, 442, 2909

Cole A. A., Weisz D. R., Dolphin A. E., Skillman E. D., McConnachie A. W., Brooks A. M., Leaman R., 2014, ArXiv e-prints

Colín P., Avila-Reese V., Valenzuela O., 2000, ApJ, 542, 622

Colín P., Avila-Reese V., Valenzuela O., Firmani C., 2002, ApJ, 581, 777

Colín P., Avila-Reese V., Vázquez-Semadeni E., Valenzuela O., Ceverino D., 2010, ApJ, 713, 535

Colín P., Valenzuela O., Avila-Reese V., 2008, ApJ, 673, 203

Conroy C., Gunn J. E., White M., 2009, ApJ, 699, 486

Conroy C., Wechsler R. H., 2009, ApJ, 696, 620

Conselice C. J., Mortlock A., Bluck A. F. L., Grützbauch R., Duncan K., 2013, MNRAS, 430, 1051

Cowie L. L., Songaila A., Hu E. M., Cohen J. G., 1996, AJ, 112, 839

Croton D. J., 2009, MNRAS, 394, 1109

Crutcher R. M., Wandelt B., Heiles C., Falgarone E., Troland T. H., 2010, ApJ, 725, 466

Daddi E., Cimatti A., Renzini A., Fontana A., Mignoli M., Pozzetti L., Tozzi P., Zamorani G., 2004, ApJ, 617, 746

Daddi E. et al., 2009, ApJ, 694, 1517

Dalla Vecchia C., Schaye J., 2012a, MNRAS, 426, 140

Dalla Vecchia C., Schaye J., 2012b, MNRAS, 426, 140

Damen M., Förster Schreiber N. M., Franx M., Labbé I., Toft S., van Dokkum P. G., Wuyts S., 2009a, ApJ, 705, 617

Damen M., Labbé I., Franx M., van Dokkum P. G., Taylor E. N., Gawiser E. J., 2009b, ApJ, 690, 937

de Blok W. J. G., Walter F., 2006, AJ, 131, 343

De Lucia G., Blaizot J., 2007, MNRAS, 375, 2

De Rossi M. E., Avila-Reese V., Tissera P. B., González-Samaniego A., Pedrosa S. E., 2013, MNRAS, 435, 2736

de Rossi M. E., Tissera P. B., Pedrosa S. E., 2010, A&A, 519, A89+

De Rossi M. E., Tissera P. B., Pedrosa S. E., 2012, A&A, 546, A52

de Vega H. J., Salucci P., Sanchez N. G., 2014, MNRAS, 442, 2717

Del Popolo A., Lima J. A. S., Fabris J. C., Rodrigues D. C., 2014, J. Cosmology Astropart. Phys., 4, 21

Dodelson S., Widrow L. M., 1994, Physical Review Letters, 72, 17

Drory N., Alvarez M., 2008, ApJ, 680, 41

Drory N., Salvato M., Gabasch A., Bender R., Hopp U., Feulner G., Pannella M., 2005, ApJ, 619, L131

Duffy A. R., Schaye J., Kay S. T., Dalla Vecchia C., Battye R. A., Booth C. M., 2010, MNRAS, 405, 2161

Dutton A. A., van den Bosch F. C., 2009, MNRAS, 396, 141

Dutton A. A., van den Bosch F. C., Dekel A., 2010, MNRAS, 405, 1690

Dutton A. A. et al., 2011, MNRAS, 410, 1660

Elbaz D. et al., 2007, A&A, 468, 33

Ellis J., Kim J. E., Nanopoulos D. V., 1984, Physics Letters B, 145, 181

Elmegreen B. G., 2007, ApJ, 668, 1064

Elmegreen B. G., Scalo J., 2004, ARA&A, 42, 211

Fakhouri O., Ma C.-P., Boylan-Kolchin M., 2010, MNRAS, 406, 2267

Federrath C., Klessen R. S., 2012a, ApJ, 761, 156

Federrath C., Klessen R. S., 2012b, ApJ, 761, 156

Federrath C., Klessen R. S., 2013, ApJ, 763, 51

Federrath C., Klessen R. S., Schmidt W., 2008a, ApJ, 688, L79

Federrath C., Klessen R. S., Schmidt W., 2008b, ApJ, 688, L79

Federrath C., Roman-Duval J., Klessen R. S., Schmidt W., Mac Low M.-M., 2010, A&A, 512, A81

Ferland G. J., Korista K. T., Verner D. A., Ferguson J. W., Kingdon J. B., Verner E. M., 1998a, PASP, 110, 761

Ferland G. J., Korista K. T., Verner D. A., Ferguson J. W., Kingdon J. B., Verner E. M., 1998b, PASP, 110, 761

Ferreras I. et al., 2014, MNRAS, 444, 906

Ferrero I., Abadi M. G., Navarro J. F., Sales L. V., Gurovich S., 2012, MNRAS, 425, 2817

Field G. B., Blackman E. G., Keto E. R., 2008, MNRAS, 385, 181

Firmani C., Avila-Reese V., 2010, ApJ, 723, 755

Firmani C., Avila-Reese V., Rodríguez-Puebla A., 2010, MNRAS, 404, 1100

Fontana A. et al., 2004, A&A, 424, 23

Fontana A. et al., 2006, A&A, 459, 745

Fontanot F., De Lucia G., Monaco P., Somerville R. S., Santini P., 2009, MNRAS, 397, 1776

Frenk C. S., White S. D. M., 2012, Annalen der Physik, 524, 507

Gallazzi A., Brinchmann J., Charlot S., White S. D. M., 2008, MNRAS, 383, 1439

Gao L., Theuns T., 2007, Science, 317, 1527

Gao L., Theuns T., Springel V., 2014, ArXiv e-prints

Geha M., Blanton M. R., Masjedi M., West A. A., 2006, ApJ, 653, 240

Geha M., Blanton M. R., Yan R., Tinker J. L., 2012, ApJ, 757, 85

Genel S., Bouché N., Naab T., Sternberg A., Genzel R., 2010, ApJ, 719, 229

Gibson D., Plume R., Bergin E., Ragan S., Evans N., 2009, ApJ, 705, 123

Gilbank D. G. et al., 2011, MNRAS, 414, 304

Goldsmith P. F., Arquilla R., 1985, in Protostars and Planets II, Black D. C., Matthews M. S., eds., pp. 137–149

Gómez G. C., Vázquez-Semadeni E., Shadmehri M., Ballesteros-Paredes J., 2007, ApJ, 669, 1042

González V., Bouwens R., Illingworth G., Labbé I., Oesch P., Franx M., Magee D., 2014, ApJ, 781, 34

González V., Labbé I., Bouwens R. J., Illingworth G., Franx M., Kriek M., 2011, ApJ, 735, L34

González-Samaniego A., Colín P., Avila-Reese V., Rodríguez-Puebla A., Valenzuela O., 2014, ApJ, 785, 58

Goodman A. A., Barranco J. A., Wilner D. J., Heyer M. H., 1998, ApJ, 504, 223

Goodman A. A., Benson P. J., Fuller G. A., Myers P. C., 1993, ApJ, 406, 528

Götz M., Sommer-Larsen J., 2003, Ap&SS, 284, 341

Governato F. et al., 2014, ArXiv e-prints

Guo Q., White S., Li C., Boylan-Kolchin M., 2010, MNRAS, 404, 1111

Haardt F., Madau P., 1996a, ApJ, 461, 20

Haardt F., Madau P., 1996b, ApJ, 461, 20

Hayward C. C. et al., 2014, ArXiv e-prints

He Y. Q., Xia X. Y., Hao C. N., Jing Y. P., Mao S., Li C., 2013, ApJ, 773, 37

Heitsch F., Ballesteros-Paredes J., Hartmann L., 2009, ApJ, 704, 1735

Heitsch F., Hartmann L., 2008, ApJ, 689, 290

Hennebelle P., Banerjee R., Vázquez-Semadeni E., Klessen R. S., Audit E., 2008, A&A, 486, L43

Hennebelle P., Chabrier G., 2008, ApJ, 684, 395

Hennebelle P., Chabrier G., 2011, ApJ, 743, L29

Herpich J., Stinson G. S., Macciò A. V., Brook C., Wadsley J., Couchman H. M. P., Quinn T., 2014, MNRAS, 437, 293

Heyer M., Krawczyk C., Duval J., Jackson J. M., 2009, ApJ, 699, 1092

Hogan C. J., Dalcanton J. J., 2000, Phys. Rev. D, 62, 063511

Hopkins P. F., 2012a, MNRAS, 423, 2016

Hopkins P. F., 2012b, MNRAS, 423, 2037

Hopkins P. F., 2013, MNRAS, 430, 1653

Hopkins P. F., Bundy K., Hernquist L., Ellis R. S., 2007, ApJ, 659, 976

Hopkins P. F., Cox T. J., Younger J. D., Hernquist L., 2009, ApJ, 691, 1168

Hopkins P. F., Keres D., Onorbe J., Faucher-Giguere C.-A., Quataert E., Murray N., Bullock J. S., 2013, ArXiv e-prints

Hopkins P. F., Quataert E., Murray N., 2012, MNRAS, 421, 3522

Hopkins P. F., Richards G. T., Hernquist L., 2007, ApJ, 654, 731

Hoyle F., 1953, ApJ, 118, 513

Huang S., Haynes M. P., Giovanelli R., Brinchmann J., Stierwalt S., Neff S. G., 2012, AJ, 143, 133

Hummels C. B., Bryan G. L., 2012, ApJ, 749, 140

Hunter D. A., Elmegreen B. G., Ludka B. C., 2010, AJ, 139, 447

Ilbert O. et al., 2013, A&A, 556, A55

Imara N., Bigiel F., Blitz L., 2011, ApJ, 732, 79

Imara N., Blitz L., 2011, ApJ, 732, 78

Kajisawa M. et al., 2009, ApJ, 702, 1393

Kajisawa M., Ichikawa T., Yamada T., Uchimoto Y. K., Yoshikawa T., Akiyama M., Onodera M., 2010, ApJ, 723, 129

Kang X., Macciò A. V., Dutton A. A., 2013, ApJ, 767, 22

Kannan R. et al., 2014, MNRAS, 437, 2882

Karim A. et al., 2011, ApJ, 730, 61

Kauffmann G., 2014, MNRAS, 441, 2717

Kegel W. H., 1989, A&A, 225, 517

Kennedy R., Frenk C., Cole S., Benson A., 2014, MNRAS, 442, 2487

Kim J., Ryu D., Jones T. W., Hong S. S., 1999, ApJ, 514, 506

Klypin A., Gottlöber S., Kravtsov A. V., Khokhlov A. M., 1999, ApJ, 516, 530

Klypin A., Holtzman J., 1997a, ArXiv Astrophysics e-prints

Klypin A., Holtzman J., 1997b, ArXiv Astrophysics e-prints

Klypin A., Karachentsev I., Makarov D., Nasonova O., 2014, ArXiv e-prints

Klypin A., Kravtsov A. V., Bullock J. S., Primack J. R., 2001a, ApJ, 554, 903

Klypin A., Kravtsov A. V., Bullock J. S., Primack J. R., 2001b, ApJ, 554, 903

Klypin A. A., Trujillo-Gomez S., Primack J., 2011, ApJ, 740, 102

Knebe A., Devriendt J. E. G., Gibson B. K., Silk J., 2003, MNRAS, 345, 1285

Knebe A., Devriendt J. E. G., Mahmood A., Silk J., 2002, MNRAS, 329, 813

Knebe A. et al., 2013, MNRAS, 428, 2039

Kolb E. W., Turner M. S., 1990, The early universe.

Komatsu E. et al., 2009, ApJS, 180, 330

Kormendy J., Ho L. C., 2013, ARA&A, 51, 511

Kravtsov A., Vikhlinin A., Meshscheryakov A., 2014, ArXiv e-prints

Kravtsov A. V., 2003a, ApJ, 590, L1

Kravtsov A. V., 2003b, ApJ, 590, L1

Kravtsov A. V., Klypin A. A., Khokhlov A. M., 1997a, ApJS, 111, 73

Kravtsov A. V., Klypin A. A., Khokhlov A. M., 1997b, ApJS, 111, 73

Kravtsov A. V., Nagai D., Vikhlinin A. A., 2005, ApJ, 625, 588

Krumholz M. R., Dekel A., 2012, ApJ, 753, 16

Krumholz M. R., McKee C. F., 2005, ApJ, 630, 250

Krumholz M. R., Tan J. C., 2007a, ApJ, 654, 304

Krumholz M. R., Tan J. C., 2007b, ApJ, 654, 304

Kuhlen M., Krumholz M. R., Madau P., Smith B. D., Wise J., 2012, ApJ, 749, 36

Labbé I. et al., 2013, ApJ, 777, L19

Lada C. J., Forbrich J., Lombardi M., Alves J. F., 2012, ApJ, 745, 190

Lada C. J., Lombardi M., Alves J. F., 2010, ApJ, 724, 687

Larson R. B., 1981a, MNRAS, 194, 809

Larson R. B., 1981b, MNRAS, 194, 809

Lee J. C., Kennicutt, Jr. R. C., Funes S. J. J. G., Sakai S., Akiyama S., 2009, ApJ, 692, 1305

Lee K.-S. et al., 2012, ApJ, 752, 66

Leitner S. N., 2012, ApJ, 745, 149

Li C., White S. D. M., 2009, MNRAS, 398, 2177

Li D., Goldsmith P. F., 2003, ApJ, 585, 823

Li J., Wang J., Gu Q., Zhang Z.-y., Zheng X., 2012, ApJ, 745, 47

Lin W. B., Huang D. H., Zhang X., Brandenberger R., 2001, Physical Review Letters, 86, 954

Lintott C. et al., 2011, MNRAS, 410, 166

Liu L., Yang X., Mo H. J., van den Bosch F. C., Springel V., 2010, ApJ, 712, 734

López-Sanjuan C. et al., 2013, A&A, 553, A78

Lotz J. M. et al., 2008, ApJ, 672, 177

Lovell M. R. et al., 2012, MNRAS, 420, 2318

Mac Low M.-M., Klessen R. S., 2004, Reviews of Modern Physics, 76, 125

Macciò A. V., Fontanot F., 2010, MNRAS, 404, L16

Macciò A. V., Paduroiu S., Anderhalden D., Schneider A., Moore B., 2012, MNRAS, 424, 1105

Madau P., Dickinson M., 2014, ArXiv e-prints

Madau P., Ferguson H. C., Dickinson M. E., Giavalisco M., Steidel C. C., Fruchter A., 1996, MNRAS, 283, 1388

Mandelbaum R., Seljak U., Kauffmann G., Hirata C. M., Brinkmann J., 2006, MNRAS, 368, 715

Maraston C., 2005, MNRAS, 362, 799

Maraston C., Daddi E., Renzini A., Cimatti A., Dickinson M., Papovich C., Pasquali A., Pirzkal N., 2006, ApJ, 652, 85

Marchesini D., van Dokkum P. G., Förster Schreiber N. M., Franx M., Labbé I., Wuyts S., 2009, ApJ, 701, 1765

Mateo M. L., 1998, ARA&A, 36, 435

Maulbetsch C., Avila-Reese V., Colín P., Gottlöber S., Khalatyan A., Steinmetz M., 2007, ApJ, 654, 53

McGaugh S. S., 2012, AJ, 143, 40

McKee C. F., Ostriker E. C., 2007, ARA&A, 45, 565

McQuinn K. B. W. et al., 2010, ApJ, 721, 297

Menci N., Fiore F., Lamastra A., 2012, MNRAS, 421, 2384

Miller G. E., Scalo J. M., 1979, ApJS, 41, 513

Molina F. Z., Glover S. C. O., Federrath C., Klessen R. S., 2012, MNRAS, 423, 2680

More S., van den Bosch F. C., Cacciato M., Skibba R., Mo H. J., Yang X., 2011, MNRAS, 410, 210

Moroi T., Murayama H., Yamaguchi M., 1993, Physics Letters B, 303, 289

Mosconi M. B., Tissera P. B., Lambas D. G., Cora S. A., 2001, MNRAS, 325, 34

Moster B. P., Naab T., White S. D. M., 2013, MNRAS, 428, 3121

Moster B. P., Somerville R. S., Maulbetsch C., van den Bosch F. C., Macciò A. V., Naab T., Oser L., 2010, ApJ, 710, 903

Moustakas J. et al., 2013, ApJ, 767, 50

Muñoz-Gutíerrez M. A., 2010, Cálculo y disección por masas de la historia de la densidad de tasa de formación estelar cósmica, Asesor: Avila-Reese V., ed., Tesis de Licenciatura, Facultad de Ciencias, UNAM, p. 131 páginas

Munshi F. et al., 2013, ApJ, 766, 56

Murray N., Quataert E., Thompson T. A., 2005, ApJ, 618, 569

Mutch S. J., Croton D. J., Poole G. B., 2013, MNRAS, 435, 2445

Myers P. C., Goodman A. A., 1988a, ApJ, 326, L27

Myers P. C., Goodman A. A., 1988b, ApJ, 326, L27

Nakamura F., Li Z.-Y., 2005, ApJ, 631, 411

Nakano T., Nakamura T., 1978, PASJ, 30, 671

Narayanan V. K., Spergel D. N., Davé R., Ma C.-P., 2000, ApJ, 543, L103

Noeske K. G. et al., 2007a, ApJ, 660, L47

Noeske K. G. et al., 2007b, ApJ, 660, L43

Oliver S. et al., 2010, MNRAS, 405, 2279

Ostriker E. C., Gammie C. F., Stone J. M., 1999, ApJ, 513, 259

Pacifici C., Kassin S. A., Weiner B., Charlot S., Gardner J. P., 2013, ApJ, 762, L15

Padoan P., 1995, MNRAS, 277, 377

Padoan P., Nordlund Å., 2011, ApJ, 730, 40

Padoan P., Nordlund A., Jones B. J. T., 1997, MNRAS, 288, 145

Pagels H., Primack J. R., 1982, Physical Review Letters, 48, 223

Panter B., Jimenez R., Heavens A. F., Charlot S., 2007, MNRAS, 378, 1550

Papastergis E., Cattaneo A., Huang S., Giovanelli R., Haynes M. P., 2012, ApJ, 759, 138

Papastergis E., Giovanelli R., Haynes M. P., Shankar F., 2014, ArXiv e-prints

Papastergis E., Martin A. M., Giovanelli R., Haynes M. P., 2011, ApJ, 739, 38

Passot T., Vázquez-Semadeni E., 1998, Phys. Rev. E, 58, 4501

Passot T., Vazquez-Semadeni E., Pouquet A., 1995, ApJ, 455, 536

Peebles P. J. E., 1980, The large-scale structure of the universe

Peng Y.-j., Lilly S. J., Renzini A., Carollo M., 2014, ApJ, 790, 95

Pérez E. et al., 2013, ApJ, 764, L1

Pérez-González P. G. et al., 2008, ApJ, 675, 234

Phillips J. P., 1999, A&AS, 134, 241

Planck Collaboration et al., 2013a, ArXiv e-prints

Planck Collaboration et al., 2013b, ArXiv e-prints

Plume R., Jaffe D. T., Evans, II N. J., Martín-Pintado J., Gómez-González J., 1997, ApJ, 476, 730

Pozzetti L. et al., 2010, A&A, 523, A13+

Price D. J., Bate M. R., 2008, MNRAS, 385, 1820

Riess A. G. et al., 2009, ApJS, 183, 109

Robertson B., Goldreich P., 2012, ApJ, 750, L31

Rodighiero G. et al., 2010, A&A, 518, L25+

Rodríguez-Puebla A., 2013, La conexión galaxia-halo y su evolución, Asesor: Avila-Reese V., ed., Tesis de Doctorado, Instituto de Astronomía, UNAM, p. 249 páginas

Rodríguez-Puebla A., Avila-Reese V., Drory N., 2013, ApJ, 767, 92

Rodríguez-Puebla A., Avila-Reese V., Firmani C., Colín P., 2011, RevMexAA, 47, 235

Rodriguez-Puebla A., Avila-Reese V., Yang X., Foucaud S., Drory N., Jing Y. P., 2014, ArXiv e-prints

Rodríguez-Puebla A., Drory N., Avila-Reese V., 2012, ApJ, 756, 2

Rosolowsky E., 2007, ApJ, 654, 240

Sales L. V., Marinacci F., Springel V., Petkova M., 2014, MNRAS, 439, 2990

Salim S. et al., 2007, ApJS, 173, 267

Salimbeni S., Fontana A., Giallongo E., Grazian A., Menci N., Pentericci L., Santini P., 2009, in American Institute of Physics Conference Series, Vol. 1111, American Institute of Physics Conference Series, G. Giobbi, A. Tornambe, G. Raimondo, M. Limongi, L. A. Antonelli, N. Menci, & E. Brocato, ed., pp. 207–211

Santini P. et al., 2009, A&A, 504, 751

Sawala T., Frenk C. S., Crain R. A., Jenkins A., Schaye J., Theuns T., Zavala J., 2013, MNRAS, 431, 1366

Sawala T. et al., 2014a, ArXiv e-prints

Sawala T. et al., 2014b, ArXiv e-prints

Sawala T., Guo Q., Scannapieco C., Jenkins A., White S., 2011, MNRAS, 413, 659

Sawala T., Scannapieco C., Maio U., White S., 2010, MNRAS, 402, 1599

Scalo J., 1990, in Astrophysics and Space Science Library, Vol. 162, Physical Processes in Fragmentation and Star Formation, Capuzzo-Dolcetta R., Chiosi C., di Fazio A., eds., pp. 151–176

Scannapieco C., Tissera P. B., White S. D. M., Springel V., 2005, MNRAS, 364, 552

Scannapieco C., Tissera P. B., White S. D. M., Springel V., 2006, MNRAS, 371, 1125

Scannapieco C. et al., 2012, MNRAS, 423, 1726

Schiminovich D. et al., 2007, ApJS, 173, 315

Schneider A., Anderhalden D., Macciò A. V., Diemand J., 2014, MNRAS, 441, L6

Schneider A., Smith R. E., Macciò A. V., Moore B., 2012a, MNRAS, 424, 684

Schneider A., Smith R. E., Macciò A. V., Moore B., 2012b, MNRAS, 424, 684

Sheth R. K., Tormen G., 2002, MNRAS, 329, 61

Shi X., Fuller G. M., 1999, Physical Review Letters, 82, 2832

Shirley Y. L., Evans, II N. J., Young K. E., Knez C., Jaffe D. T., 2003, ApJS, 149, 375

Shu F. H., 1992, Physics of Astrophysics, Vol. II. University Science Books

Smith R. E., Markovic K., 2011, Phys. Rev. D, 84, 063507

Somerville R. S. et al., 2008, ApJ, 672, 776

Sommer-Larsen J., Dolgov A., 2001, ApJ, 551, 608

Speagle J. S., Steinhardt C. L., Capak P. L., Silverman J. D., 2014, ArXiv e-prints

Springel V., 2005, MNRAS, 364, 1105

Springel V., Hernquist L., 2003, MNRAS, 339, 289

Springel V., White S. D. M., Tormen G., Kauffmann G., 2001, MNRAS, 328, 726

Stewart K. R., Bullock J. S., Wechsler R. H., Maller A. H., 2009, ApJ, 702, 307

Stinson G., Seth A., Katz N., Wadsley J., Governato F., Quinn T., 2006, MNRAS, 373, 1074

Stinson G. S., Brook C., Macciò A. V., Wadsley J., Quinn T. R., Couchman H. M. P., 2013, MNRAS, 428, 129

Stinson G. S., Dalcanton J. J., Quinn T., Gogarten S. M., Kaufmann T., Wadsley J., 2009, MNRAS, 395, 1455

Stinson G. S., Dalcanton J. J., Quinn T., Kaufmann T., Wadsley J., 2007, ApJ, 667, 170

Teyssier R., 2002, A&A, 385, 337

Teyssier R., Pontzen A., Dubois Y., Read J. I., 2013, MNRAS, 429, 3068

Thomas D., Maraston C., Bender R., Mendes de Oliveira C., 2005, ApJ, 621, 673

Thompson R., Nagamine K., Jaacks J., Choi J.-H., 2014, ApJ, 780, 145

Tonini C., Maraston C., Devriendt J., Thomas D., Silk J., 2009, MNRAS, 396, L36

Truelove J. K., Klein R. I., McKee C. F., Holliman, II J. H., Howell L. H., Greenough J. A., 1997, ApJ, 489, L179

Trujillo-Gomez S., Klypin A., Colin P., Ceverino D., Arraki K., Primack J., 2013, ArXiv e-prints

van den Bosch F. C., Aquino D., Yang X., Mo H. J., Pasquali A., McIntosh D. H., Weinmann S. M., Kang X., 2008, MNRAS, 387, 79

Vazquez-Semadeni E., 1994, ApJ, 423, 681

Vázquez-Semadeni E., Ballesteros-Paredes J., Klessen R. S., 2003, ApJ, 585, L131

Vázquez-Semadeni E., Banerjee R., Gómez G. C., Hennebelle P., Duffin D., Klessen R. S., 2011, MNRAS, 414, 2511

Vázquez-Semadeni E., Cantó J., Lizano S., 1998, ApJ, 492, 596

Vazquez-Semadeni E., Gazol A., 1995, A&A, 303, 204

Vázquez-Semadeni E., Gómez G. C., Jappsen A. K., Ballesteros-Paredes J., González R. F., Klessen R. S., 2007, ApJ, 657, 870

Vázquez-Semadeni E., Gómez G. C., Jappsen A.-K., Ballesteros-Paredes J., Klessen R. S., 2009, ApJ, 707, 1023

Vázquez-Semadeni E., González R. F., Ballesteros-Paredes J., Gazol A., Kim J., 2008a, MNRAS, 390, 769

Vázquez-Semadeni E., González R. F., Ballesteros-Paredes J., Gazol A., Kim J., 2008b, MNRAS, 390, 769

Vázquez-Semadeni E., Kim J., Shadmehri M., Ballesteros-Paredes J., 2005, ApJ, 618, 344

Vazquez-Semadeni E., Ostriker E. C., Passot T., Gammie C. F., Stone J. M., 2000, Protostars and Planets IV, 3

Vazquez-Semadeni E., Passot T., Pouquet A., 1996, ApJ, 473, 881

Vergani D. et al., 2008, A&A, 487, 89

Viel M., Becker G. D., Bolton J. S., Haehnelt M. G., 2013, Phys. Rev. D, 88, 043502

Viel M., Lesgourgues J., Haehnelt M. G., Matarrese S., Riotto A., 2005, Phys. Rev. D, 71, 063534

Wang J., White S. D. M., 2007, MNRAS, 380, 93

Wang L., Jing Y. P., 2010, MNRAS, 402, 1796

Wechsler R. H., Bullock J. S., Primack J. R., Kravtsov A. V., Dekel A., 2002, ApJ, 568, 52

Weinberg D. H., Bullock J. S., Governato F., Kuzio de Naray R., Peter A. H. G., 2013, ArXiv e-prints

Weinberg S., 1972, Gravitation and Cosmology: Principles and Applications of the General Theory of Relativity

Weinmann S. M., Pasquali A., Oppenheimer B. D., Finlator K., Mendel J. T., Crain R. A., Macciò A. V., 2012, MNRAS, 426, 2797

Weisz D. R. et al., 2011, ApJ, 739, 5

Weisz D. R., Dolphin A. E., Skillman E. D., Holtzman J., Gilbert K. M., Dalcanton J. J., Williams B. F., 2014, ApJ, 789, 147

Weisz D. R., Skillman E. D., Cannon J. M., Dolphin A. E., Kennicutt, Jr. R. C., Lee J., Walter F., 2008, ApJ, 689, 160

Wise J. H., Abel T., Turk M. J., Norman M. L., Smith B. D., 2012, MNRAS, 427, 311

Wu J., Evans, II N. J., Shirley Y. L., Knez C., 2010, ApJS, 188, 313

Yabe K., Ohta K., Iwata I., Sawicki M., Tamura N., Akiyama M., Aoki K., 2009, ApJ, 693, 507

Yang X., Mo H. J., van den Bosch F. C., Zhang Y., Han J., 2012, ApJ, 752, 41

Yoshida N., Springel V., White S. D. M., Tormen G., 2000, ApJ, 544, L87

Zamora-Avilés M., Vázquez-Semadeni E., Colín P., 2012, ApJ, 751, 77

Zavala J., Jing Y. P., Faltenbacher A., Yepes G., Hoffman Y., Gottlöber S., Catinella B., 2009, ApJ, 700, 1779

Zheng X. Z., Bell E. F., Papovich C., Wolf C., Meisenheimer K., Rix H.-W., Rieke G. H., Somerville R., 2007, ApJ, 661, L41

Zuckerman B., Evans, II N. J., 1974a, ApJ, 192, L149

Zuckerman B., Evans, II N. J., 1974b, ApJ, 192, L149